Spring 2002

Modeling Aspects of Magnetic Actuators and Magnetic Suspension Systems

V. Dale Bloodgood Jr.
Old Dominion University

MODELING ASPECTS OF MAGNETIC ACTUATORS AND MAGNETIC SUSPENSION SYSTEMS

by

V. Dale Bloodgood, Jr.
B.S.M.E. December 1995, Old Dominion University
M.S.E.M. December 1998, Old Dominion University

A Dissertation Submitted to the Faculty of
Old Dominion University in Partial Fulfillment of the
Requirement for the Degree of

DOCTOR OF PHILOSOPHY

ENGINEERING MECHANICS

OLD DOMINION UNIVERSITY
May 2002

Approved by:

Colin P. Britcher (Director)

Thomas E. Alberts (Member)

Donald L. Kunz (Member)

W. Stephen Gray (Member)

Nelson J. Groom (Member)

ABSTRACT

MODELING ASPECTS OF MAGNETIC ACTUATORS
AND MAGNETIC SUSPENSION SYSTEMS

V. Dale Bloodgood, Jr.
Old Dominion University, 2002
Director: Dr. Colin P. Britcher

This dissertation is a study of new modeling techniques developed for magnetic suspension systems. The techniques discussed are modifications of magnetic circuit theory and fundamental eddy current models. The techniques are compared against experimental test results and finite element data. The information gained from the experimental testing is used to provide insight into magnetic bearing design.

A small-gap modeling technique called extended circuit theory is developed that incorporates information about the system gained from finite element data, or experimental data, to be included in the analytic model. The variations between the classical magnetic circuit model and the finite element model are used to develop performance coefficients, which are in turn incorporated into the extended circuit model. The coefficients modify the classical theory to account for magnetomotive force loses, flux leakage and flux fringing. The theory is developed from fundamental principles. The techniques used to determine, and predict, the coefficients are discussed. The use of this method in optimal bearing design is also discussed.

The extended circuit model is verified against experimental test results of a family of magnetic actuators. The actuators consist of a "C-shaped" stator and a flat armature. The pole separation distance was varied along with the location of the biasing permanent

magnets and the windings. The permanent magnets were placed either on the pole faces, in the center of the armature, or at both locations, and the windings were wound on poles of the stator or on the back of the stator, resulting in a total of 22 design permutations. The experimental performance of each design is analyzed and efficiency trends are discussed.

The diffusive model for eddy currents is analyzed along with the lumped parameter model to explore the "half-order" behavior of eddy currents commonly observed in experimental testing. A fractional order eddy current model is developed and compared against finite element data and experimental test results. The models developed are based on a frequency dependent resistance. The implications of using fractional order modeling techniques, along with control considerations, are discussed.

This dissertation is dedicated to my all of my family and friends.

ACKNOWLEDGMENTS

This research was conducted with the support of the NASA Graduate Student Researchers Program under Grant number NGT-1-52171, the Virginia Space Grant Consortium's Aerospace Graduate Research Fellowship Program, and the Old Dominion University Aerospace Engineering Department. Additional support was provided by Dan Moerder and the Guidance and Controls branch at NASA Langley Research Center.

I would like to acknowledge the efforts of my academic advisor Dr. Colin P. Britcher and my NASA advisor Nelson J. Groom. Without their help I would not be where I am today. I would also like to thank Dr. Donald L. Kunz and Dr. W. Stephen Gray for serving on my dissertation committee, and a special thanks goes to Dr. Thomas E. Alberts, who instructed me throughout my Bachelors, Masters, and PhD degree programs.

TABLE OF CONTENTS

LIST OF TABLES

LIST OF FIGURES

NOMENCLATURE

$A_{A,fe,g}$	Area of armature, iron cross section, pole area (m^2)
B	Magnetic flux density (Tesla or Wb/m^2)
E	Electric field intensity (N/Coulomb or V/m)
F	Force vector (N)
H	Magnetic field intensity (A/m)
I	Current (A)
J	Polarization (T)
$L_{A,fe,g}$	Magnetic bearing flux path length in armature, iron, air gap (m)
m	Magnetic moment ($A \cdot m^2$)
M	Magnetization vector (A/m)
N	Number of turns
p	Magnetic monopole strength (A·m)
P	Permeance ($T \cdot m^2/A$)
P_m	Magnetic pressure (N/m^2)
R	Reluctance ($A/T \cdot m^2$)
T_q	Torque (N·m)
T_{ij}	Maxwell's stress tensor
δ	Eddy current skin depth (m)
v	Volume (m^3)
φ	Magnetic flux ($T \cdot m^2$)
$\mu_{A,fe,g,0}$	Permeability of armature, iron, air gap, of free space (H/m)
μ_r	Relative permeability
σ	Conductivity $(\Omega \cdot m)^{-1}$
σ_m	Magnetic tension (N/m^2)
κ	Reluctance ratio
τ_m	Magnetic shear stress (N/m^2)
ω	Frequency (rad/s)

1. INTRODUCTION

One of the first documented investigations into magnetic suspension was credited to Samuel Earnshaw, who in 1842 proved that stable equilibrium of a suspended object along three axes in a static magnetic field is not possible [Earnshaw, 1842]. The first use of magnetic suspension is generally considered to have been in 1937 when Holmes and Beams at the University of Virginia successfully levitated a steel ball [Holmes, 1937, Beams, 1937]. Using feedback controlled DC electromagnets they actively suspended a rotating steel ball beneath an electromagnet with rotational speeds of 60,000 rpm, eventually reaching a maximum speed of 2.7×10^7 rpm.

The research effort by Holmes and Beams was not focused on magnetic suspension; rather, they were trying to develop a new technique for material testing. The magnetic suspension aspect was simply a necessary means to an end. Historically, this has been the driving force behind the development of magnetic suspension systems, and many see this as still being true today. That being said, it should be realized that the majority of the current research dealing with magnetic suspension is not simply an exercise in science but a necessary step in the further development of new technologies.

It will be shown in Section 2 that the underlying mathematical models of magnetic suspension leads toward two somewhat different categorizations. Systems are classified as small-gap systems, where the suspension height is small compared to the characteristic dimension, and large-gap systems, where the suspension height is large compared to the characteristic dimension. Within each of these categories a further subdivision exists,

The reference model for this work is *Applied Mechanics Reviews*.

that of the static components (DC field characteristics) and the dynamic components (eddy-currents). Typically, these two components can be analyzed independently. The overall effectiveness of any design is highly dependent on the accurate modeling of both the dynamic and static components.

The research discussed in this dissertation concerns the improved development of both static and dynamic modeling techniques. The static modeling method discussed is limited to small-gap systems like magnetic bearings. The dynamic modeling techniques that are developed are applicable to both small-gap and large-gap systems.

1.1. Small-Gap Systems and Magnetic Bearings

The best example of a small-gap system would be that of a magnetic bearing. A typical magnetic bearing will have a very small air gap thickness as compared to the cross sectional area of the air gap. This results in the magnetic field being well defined, or focused, on specified areas of the affected surfaces.

1.1.1. Historical Survey

The development of magnetic bearings dates back to the 1937 experiment of Holmes and Beams, discussed previously. They used an AC resonance circuit to actively suspend the steel ball. The system worked by tuning the circuit such that as the air gap increased the inductance of the electromagnetic system moved toward resonance at the excitation frequency, thus increasing the current to the coil and producing a restoring force. These AC resonant circuits in combination with the power amplifiers available of the day,

consisting of vacuum tubes and magnetic amplifiers, did not provide enough stiffness or damping for practical applications of magnetic bearings. The hardware limitations that plagued the early investigations faded in the early 1950's with the invention of the transistor by Bell Laboratories. The transistor made active control practical and ushered in a new era, where control algorithms could vary the stiffness and damping of the rotors to attain the desired performance characteristics [Swann, 1988].

These advancements led to a large research effort into satellite and other space based applications throughout the 1960's. The first prototype systems designed for space use were delivered to Goddard Space Flight Center (GSFC) in 1970 from the Cambridge Thermionic Corporation. They developed two magnetically suspended rotors for attitude control systems using active control. However, even though the technology had proven feasible, the 3 kg weight of the rotor and the 40Watt power consumption proved impractical.

The problem with the early designs was that the weight of the magnetic bearings was much more than conventional bearings and they required a significant power source that conventional bearings did not. This problem led to the development of hybrid designs consisting of permanent magnets and electromagnets [Swann, 1988]. The permanent magnets provide a steady-state bias flux for suspension and the electromagnets provide the necessary stability and control. This combination resulted not only in a lower power bearing, but also in a lighter bearing because less iron is needed in the magnetic circuit.

Combining the permanent magnets and electromagnets also served to linearize the system with respect to control current.

Commercial systems for industry began appearing in the 1970's. The first commercial use of magnetic bearings occurred in 1975 in thread spinning equipment. The first company devoted to the manufacture of magnetic bearings was S2M, which began in 1976. They have continued to develop their product line and are currently producing turbomachinery, serial products, machine tools, and other specialty items [S2M, 2001]. The requirements for space based systems were more stringent than land based systems. The first use of an active magnetic bearing in space occurred in 1983. The European SpaceLab used active magnetic bearings to suspend a vacuum pump. In 1986 magnetic bearings were used in an attitude control system in the SPOT satellite [Gautheir, 1987].

The first international conference dedicated to magnetic bearings was held in Zurich Switzerland in June 1988, the 1st International Symposium on Magnetic Bearings [Schweitzer, 1988]. In the same year a workshop was held at NASA Langley Research Center which discussed all aspects of magnetic suspension systems [Keckler, 1993]. Another workshop was held at NASA Langley Research Center in September 1990 [Groom, 1992(a)]. This workshop spawned a second set of international conferences, the International Symposia on Magnetic Suspension Technology. The first symposium in this series was held in August 1992 [Groom, 1992(b)]. The two sets of conferences have been continuing on an alternating bi-annual schedule ever since. The growth of all the various aspects of magnetic bearings is well documented in these conference

proceedings. For more information on the history of magnetic bearings, from the 1930's to the late 1980's, it is recommended that the reader see [Swann, 1988].

1.1.2. Applications of Magnetic Bearings

Magnetic bearings have many advantages over conventional contact bearings. The rotating shaft is free of mechanical contact which results in lower maintenance cost and longer life. The rotational speeds attainable with magnetic bearings are several orders of magnitude higher than conventional bearings. Magnetic bearings do not require lubrication. Additionally, system performance can be monitored in real time via the signals from the control system. These advantages make magnetic bearings suitable for many applications.

Because there is no physical contact between the rotating shaft and the support structure the lifespan is set by the electrical components such as sensors, amplifiers, and magnetic coils. These items are electrical in nature rather then mechanical, resulting in a longer life span and higher reliability. This makes magnetic bearings ideal for industrial use on critical systems where reliability is paramount. Due to the respective costs of conventional bearings and magnetic bearings, it is currently not cost effective to implement magnetic bearings on all the systems, but it is cost effective to implement magnetic bearings on the critical systems.

Another class of applications is directly due to the high rotational speeds of magnetic bearing. This makes magnetic bearings ideal for certain applications such as milling

spindles and turbocompressors. Some examples of commercially available systems are the electrospindle produced by S2M which is capable of operating up to 45,000 rpm, shown in Fig. 1.1, and the high speed grinding machine capable of operating up to 60,000 rpm, shown in Fig. 1.2. Another example is the textile spindle by Mecos-Traxler that operates at 80,000 rpm at under 200 Watts, shown in Fig. 1.3.

Figure 1.1: S2M Electrospindle [S2M, 2001]

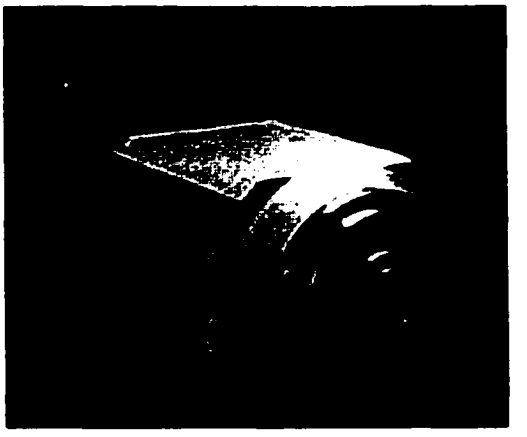

Figure 1.2: S2M High Speed Grinding Machine [S2M, 2001]

Figure 1.3: Mecos-Traxler Textile Spindle [Mecos, 2001]

The fact that magnetic bearings do not require lubrication makes them ideal for many specialized applications. Lubricants can cause contamination problems, they can impose minimum and maximum operational temperatures, and they can cause debris problems when used in space. Because of this, many companies are using magnetic bearings in natural gas pipelines and petrochemical compressors to avoid oil contamination. Magnetic bearings are being used in systems such as hydraulic, gas, and steam turbines because of the high temperatures and speeds at which they must operate. Additionally, many cryogenic pumps are also being manufactured using magnetic bearings due to lubrication problems at such low temperatures. One commercial example is the turbo expander produced by S2M for the production of oxygen, where oil contamination would prove catastrophic, shown in Fig. 1.4.

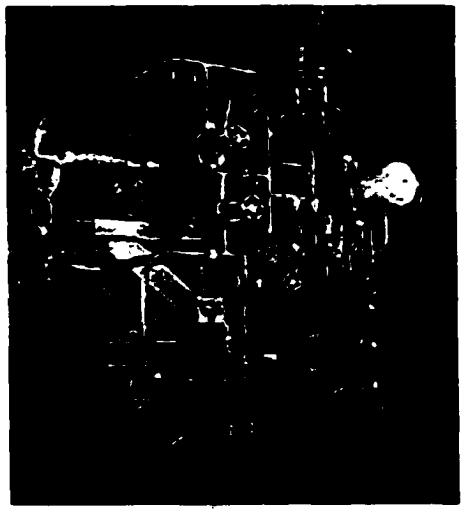

Figure 1.4: S2M Turbo Expander used for Oxygen Production [S2M, 2001]

Another application which holds a lot of promise is the magnetically suspended ventricular assist device. Several devices are now being developed and tested to aid in the circulation of blood though the heart. The centrifugal blood pumps are suspended magnetically ensuring that no contact points exist to damage blood cells. This is another example of a situation where contamination from lubrication is unacceptable. Research in this area currently is progressing at the University of Virginia, the University of Pittsburgh, and ETH Zurich, as well as in industry.

Specific applications for magnetic bearings in the aerospace industry include magnetically suspended momentum wheels for energy storage, magnetic bearings capable of withstanding high temperatures for gas generator rotors of turboshaft engines, and vibration attenuating systems for airborne measuring and observation equipment [Downer, 1994].

The discussions of this section have been limited to active magnetic bearings. Other classes of magnetic bearings exist such as repulsive eddy-current bearings and systems using superconducting flux pinning and flux excluding technologies. Additionally, there are other classes of systems such as maglev trains and vibration isolation systems which use small-gap technology that have not been discussed. These areas have been subject to a considerable amount of research over the last few decades but do not directly apply to the aim of this research and have therefore not been included here.

1.2. Large-Gap Systems

The number of commercial applications associated with large-gap magnetic suspension systems is not as high as those associated with magnetic bearings. The small amount of research and development, or commercial activity, devoted to this area makes this point evident. However, there are three main areas where large-gap technologies are continuously being developed. These areas are electrodynamic levitation, magnetic suspension and balance systems for wind tunnel testing, and interference-free control of systems in multi-degrees-of-freedom.

The majority of research in large-gap magnetic suspension has been in the development of Magnetic Suspension and Balance Systems (MSBS). MSBSs are used to magnetically support a model in a wind tunnel in order to eliminate the aerodynamic interference from physical supports. The system not only supports the model, but the suspension currents can be used to determine the aerodynamic loads applied to the model, such the lift, drag, and moments. In the early 1990's, tests conducted using a MSBS showed that drag correction for support interference could be as high as 200% of the actual drag [Britcher, 1990; Britcher, 1991]. MSBSs also allow for dynamic testing which is very difficult with conventional wind tunnel support systems.

Initial research in this area began in the late 1950s in France, Britain, and the US. Japan, Russia, China, and Taiwan began developing MSBSs in the 1970's and 1980's [Britcher, 1997]. Significant amounts of research have been focused on this topic, but unlike magnetic bearings the majority of research has been on the development and

improvement of MSBS technology rather than in aerodynamic testing. As a result of the minimal productivity, many MSBS systems have been decommissioned. The decommissioned systems include the low speed MSBS at Southampton University, the MAI/TsAGI and MAI-CAHI/TsAGI in Moscow, and the 13 inch at NASA Langley Research Center. At NAL in Japan the research is still continuing with the commissioning of a 100 mm × 100mm system in 1987, and a 600 mm × 600 mm system in 1993.

Currently the US Office of Naval Research (ONR) is funding the design and construction of a high Reynolds number MSBS test facility at Princeton University which will be used for aerodynamic and hydrodynamic testing. The facility will be able to operate at length Reynolds numbers ranging from 5000 to 10^8 and at test pressures as high as 240 atmospheres [Smits, 1997]. The magnetic suspension and balance system is mounted outside of a stainless steel pressure vessel with a wall thickness of approximately 2.5 inches. The primary concern with this system is the effects of eddy-currents. This issue is still being addressed [Britcher, 2000].

Another form of large-gap system that is still receiving a significant amount of research is Electro-Dynamic Levitation (EDL) of maglev vehicles. EDL uses induced eddy-currents to create a repulsive force to levitate a vehicle. An eddy current is produced when a time varying flux passes through an electrically conducting medium. This eddy-current in turn produces an electrical current which opposes the change in flux. This opposition of flux change creates a net repulsive force. The variation in flux can be produced by moving a

field source relative to a conductive body or it can be produced by alternating the field source in the presence of a stationary conductive body.

The first experiments of EDL occurred in the laboratory in 1912 by the French engineer Emile Bachelet. He levitated an aluminum plate over a row of electromagnets. The idea was to construct a full-scale railway of electromagnets to support a vehicle. This was never practical due to the prohibitive costs of the guideway. In 1963, a British engineer Eric Laithwaite inverted Bachelet's design and placed the linear induction motors on the vehicle, which operated over an aluminum guideway. This configuration dramatically reduced the guide-way cost but at the same time significantly increased the weight of the vehicle.

Variations of this configuration were studied at MIT, Princeton, and Cornell University in the early 1970's as part of the US Maglev Initiative. At MIT, Kolm and Thornton used a channel-shaped aluminum sheet as the conductive track, which allowed the vehicle to roll naturally as it banked on turns [Kolm, 1972]. This configuration became known as the Magneplane. The design suffered from lateral instabilities and high electromagnetic drag. A similar design was studied at Princeton and Cornell Universities using a "V" shaped track by Moon and Chu [Moon, 1994]. Research eventually shifted from continuous tracks to discrete conducting loops. This change led to the null-flux design used in the JR test track in the Yamanashi prefecture of Japan [Tanaka, 1992]. The Japanese MLX-01, operating on the null-flux design, set the world's speed record of 550 kph (340 mph) for a train in December 1997 [KWJ, 1998].

To date, Japan is the only country operating an EDL vehicle, and it is still in the testing and development phase. An EDL system was proposed for use at Old Dominion University in Norfolk, Virginia, as a student transportation system in 2000. The system was proposed primarily as a technology demonstration in order increase the acceptance of this technology in the United States. The test track was a little less than a mile long, which made the EDL system impractical; the design was subsequently changed to the more suitable electro-magnetic system. In the electro-magnetic system the vehicle is supported by attraction forces between the guidway and electro-magnets on the vehicle and is thus not dependent upon velocity. The system is currently under construction.

A significant amount of large-gap research dealing with multi-degree-of-freedom control has been going on at NASA Langley Research Center over the past 30 years. A Large Angle Magnetic Suspension Test Fixture (LAMSTF) was constructed to suspend a cylindrical, axially magnetized body with 5 degrees-of-freedom control at a suspension height of 100 mm [Britcher, 1993]. The system was used to investigate control aspects and eddy-current effects. The 6DOF-8C/2L system was designed as a scaled down version of the Large-Gap Magnetic Suspension System (LGMSS) to aid in the development of the control law. These two laboratory test fixtures are discussed in detail in Section 6. The LGMSS is being designed to suspend a cylindrical, transversely magnetized body in 6 degrees-of-freedom at a suspension height of approximately 1 meter.

1.3. Need for Improved Modeling Techniques

Two specific issues with magnetic bearings are the cost and the weight. The cost of a magnetic bearing and the required components is considerably higher than that of a standard contact bearing. A working magnetic bearing requires accurate sensors, a control system, power amplifiers, power supply, the bearing itself, and redundant backup systems. Each of these components increases the cost and weight of the bearing. In most industrial applications the weight is not a critical factor, but for aerospace systems it is often a deciding factor. These problems must be improved before magnetic bearings can reach their full potential in industry and in space based applications.

An additional factor which has been receiving significant attention in recent years is the effect of eddy-currents. Eddy-currents induce drag forces on rotating shafts and cause power losses due to rotor heating. In energy storage flywheel systems, where the flywheel is typically suspended in a vacuum, the cumulative effects of even slight rotor heating can prove catastrophic. The effects of eddy-current drag can also lower the efficiency to the point that magnetic bearings are impractical. In the case of the large-gap systems discussed in the previous section, eddy-currents again show a negative effect. The field canceling effect changes the frequency response characteristics of the suspended element. The lift and drag ratio of an EDL maglev vehicle is completely dependent upon eddy-current characteristics.

In order to improve upon these issues it is necessary to develop a full understanding of the systems. This requires accurate modeling techniques that truly describe the physical

systems. The common techniques which are generally used to model these systems are discussed in detail in Sections 2, 3, and 5, along with the imbedded assumptions and limitations. The research discussed in this dissertation is motivated by the need for more accurate models of both small-gap and large-gap systems. Section 4 deals with the modification of static design considerations in magnetic bearings.

Sections 5 and 6 discuss fundamental issues involving eddy-currents that have been, for the most part, omitted in classical theory. Inclusion of these phenomena have a significant effect on the physical understanding of eddy-currents. The combination of improved static design of small-gap systems and the dynamic effects of eddy-currents in both small-gap and large-gap systems discussed in this dissertation culminate in a useful and practical addition to the understanding of magnetic suspension technology.

2 MODELING TECHNIQUES

Many different techniques have been developed over the years to model the behavior of magnetic systems. This section will discuss the most commonly used in the area of magnetic suspension. The topics will include Maxwell's Equations, magnetic dipoles, volumetric energy density, magnetic circuit theory, and finite element analysis.

2.1. Maxwell's Equations

The fundamental equations in electromagnetic theory are known as Maxwell's equations. For "low frequency" analysis in conductors, the displacement current is negligible and can be omitted, resulting in the use of only three of Maxwell's four equations. A low frequency system is defined by considering the product of the frequency and a characteristic dimension, if this product is small when compared to the speed of light the system can be considered a low frequency system. Generally, the limiting frequency is on the order of a few MHz [Perry, 1985]. For magnetic suspension systems and magnetic bearings, the maximum frequencies are on the order of a few hundred to a few thousand, well within the low frequency region. The resulting governing equations are,

$$\nabla \cdot \vec{B} = 0 \tag{2.1}$$

$$\nabla \times \vec{E} = -\frac{\partial \vec{B}}{\partial t} \tag{2.2}$$

$$\nabla \times \vec{H} = \vec{J} \tag{2.3}$$

Eq. 2.1 defines the conservation of flux, Eq. 2.2 is commonly referred to as Faraday's law of induction, and Eq. 2.3 is known as Maxwell's generalization of Ampere's law. The

equations are commonly used in both the differential and the integral forms; the integral forms are given in Eqs. 2.4 –2.6.

$$\int_s \vec{B} \cdot d\vec{A} = 0 \tag{2.4}$$

$$\oint_c \vec{E} \cdot d\vec{l} = -\frac{\partial}{\partial t} \int_s \vec{B} \cdot d\vec{a} \tag{2.5}$$

$$\oint_c \vec{H} \cdot d\vec{l} = \int_s \vec{J} \cdot d\vec{a} \tag{2.6}$$

The set of equations given by 2.1 – 2.3 or 2.4 – 2.6 define the fundamental set of governing equations for electromagnetic systems. Both sets of equations are discussed in detail in numerous fundamental electromagnetic texts.

2.2. Constitutive Relations

The governing differential or integral equations given in the previous section do not fully describe an electromagnetic system because there are more unknowns than equations. Analogous to the stress-strain relationship in structural mechanics, the remaining equations relate the magnetic fields to the material properties. The two constitutive relations are,

$$\vec{B} = \mu_0 \mu_r \left(\vec{H} + \vec{M} \right) \tag{2.7}$$

$$\vec{J} = \sigma \vec{E} \tag{2.8}$$

The constant μ_0 is the permeability of free space and is equal to $4\pi \times 10^{-7}$ H/m, μ_r is the relative permeability of the material with respect to free space, and $\vec{M}$ is the magnetization vector of the material which is zero in non-magnetic alloys. The constant σ is the electrical conductivity of the material.

2.3. Maxwell's Stress Tensor and Maxwell's Stresses

Maxwell's stress tensor is defined in terms of the Lorenz force equation,

$$\bar{F} = d\bar{I} \times \bar{B} \tag{2.9}$$

where F is the force and dI is a differential current element. After some manipulation and the introduction of Eq. 2.3, the Lorenz force equation can be written using indicial notation as,

$$\frac{dF_i}{dV} = \frac{dT_{ij}}{dx_j} \qquad T_{ij} = \left(\mu H_i H_j - \frac{\mu}{2} \partial_{ij} H_k^2 \right) \tag{2.10}$$

This equation is valid when the body is immersed in a region of constant permeability and the magnetic field is known at all points on the surface of the control volume. The net force acting on the body is found by integrating over the surface of the volume,

$$F_i = \int T_{ij} \hat{n}_j ds \tag{2.11}$$

Where $\hat{n}$ is the normal unit vector on the surface of the body. Eq. 2.11 is used in most finite element programs to calculate magnetic forces.

One use of Maxwell's stress tensor is in the definition of magnetic stress. Consider a flat surface within a magnetic field defined by its normal and tangential components, $\bar{B} = B_n \hat{n} + B_t \hat{t}$, where the normal and tangential components are defined with respect to the surface. Direct substitution into Eq. 2.11 results in,

$$\frac{\bar{F}}{s} = \frac{B_n^2 - B_t^2}{2\mu_0} \hat{n} + \frac{B_n B_t}{\mu_0} \hat{t} \tag{2.12}$$

When $B_n \neq 0, B_t = 0$ a tensile normal force is produced, the magnetic stress. When $B_n = 0, B_t \neq 0$ a compressive normal force is produced, the magnetic pressure. When

both components are non-zero, a shear force is induced. These three cases define the magnetic stress, magnetic pressure, and magnetic shear stress,

$$\sigma_m = \frac{B_n^2}{2\mu_0} \quad P_m = \frac{B_t^2}{2\mu_0} \quad \tau_m = \frac{B_n B_t}{\mu_0} \tag{2.13}$$

The stresses have units of N/m^2.

2.4. Magnetic Monopoles and Dipoles

The analogies between magnetic fields and electric fields can be used to introduce the concept of magnetic monopoles. While magnetic monopoles do not exist in nature they are analogous to electric charges in terms of force. The force between two magnetic monopoles, p_1 and p_2, can be written using the same relation as that of two electric charges separated by a distance r.

$$F = \frac{p_1 p_2}{r^2} \tag{2.14}$$

The magnetic dipole consists of two monopoles of equal strength but of opposite sign, $p_1 = -p_2$, separated by a distance l. As a result, a magnetic dipole has a magnitude and a direction and is defined as,

$$\bar{m} = p\bar{l} \tag{2.15}$$

For the idealized case, the magnitude of p goes to ∞ as l goes to zero such that pl remains constant. In the case of a magnetized body, the magnetic dipole strength is defined in terms of the magnetization vector $\bar{M}$ and the volume of the body v, $\bar{m} = \bar{M}v$. In the same way that a force is induced on an electric charge by an electric field, a force is also induced on a magnetic monopole from a magnetic field. Thus, the force acting on a magnetic dipole due to a magnetic field can be given by,

$$\vec{F} = p_1\vec{B}_1 + p_2\vec{B}_2$$

$$\vec{F} = p\left(\vec{B}_1 - \vec{B}_2\right)$$

$$\vec{F} = p\left(\vec{B}_1 - \left\{\vec{B}_1 + \nabla\vec{B}_1 \cdot d\vec{l}\right\}\right) \tag{2.16}$$

$$\vec{F} = p\left(\nabla\vec{B}_1 \cdot d\vec{l}\right)$$

$$\vec{F} = \left(\vec{m} \cdot \nabla\vec{B}_1\right)$$

When considering a physical body instead of a magnetic dipole, the magnetic dipole can be replaced by $\vec{m} = \vec{M}v$ to yield the net force acting on a magnetized body.

$$\vec{F} = \int_v \vec{M} \cdot \nabla\vec{B}dv \tag{2.17}$$

If moments of each dipole were summed about the center of the dipole the net torque that results is given by,

$$\vec{T}_q = \vec{m} \times \vec{B} = \int_v \vec{M} \times \vec{B}dv \tag{2.18}$$

The force and torque acting on a magnetized body could be calculated using either Eqs. 2.17 and 2.18 or by Maxwell's stress tensor. However, consider the case where the field is relatively uniform over the volume of the magnetized body. In this case, Eqs. 2.17 and 2.18 simplify greatly and become much more useful than Maxwell's stress tensor.

$$\vec{F} \approx \left(\vec{M} \cdot \nabla\vec{B}\right)v$$

$$\vec{T}_q \approx \left(\vec{M} \times \vec{B}\right)v \tag{2.19}$$

Quite often in the case of large-gap magnetic suspension systems, the magnetic field gradient is relatively uniform over the volume of the suspended element. As a result, the

forces induced by a large-gap system are generally calculated using the dipole formulations.

2.5. Magnetic Circuit Theory

The analogy between electric circuits and magnetic circuits has been used to aid in the design of magnetic bearings and other small-gap systems since the early days of magnetic suspension research. This has resulted in magnetic circuit theory being one of the primary tools in the design of small–gap magnetic suspension systems. The details of this theory will be discussed in detail to give adequate background for the analysis presented in Section 4.

2.5.1. Development of Theory

Consider the actuator shown in Fig. 2.1. The actuator is biased by two permanent magnets placed on the poles of the stator. The force acting on the armature from the permanent magnets and the windings can be determined using Maxwell's stress tensor. This requires that the orientation of the flux crossing the air gap be known. Since flux entering or exiting a region of high permeability does so approximately perpendicular to the surface, it is assumed that flux crosses the air gap at exactly 90°. From Eq. 2.12, the force acting on the armature is,

$$F = \frac{B_n^2 (2A_g)}{2\mu_0} \tag{2.20}$$

where the $2A_g$ is the area of the two pole faces.

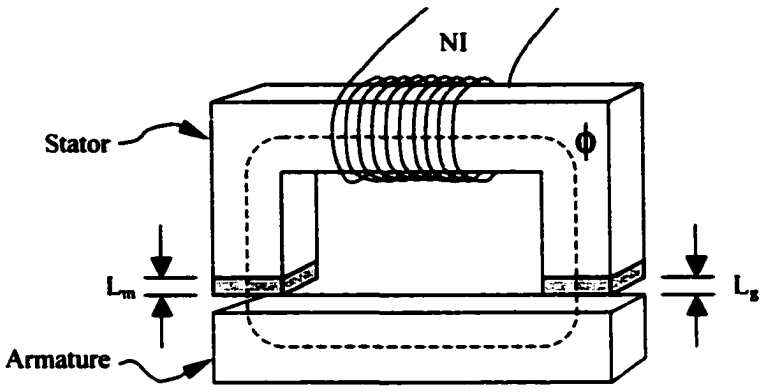

Figure 2.1: Magnetic Actuator with Biasing Permanent Magnets

The flux crossing the air gap can be determined using Eq. 2.6.

$$\int_c \bar{H} \cdot d\bar{l} = \int_s \bar{J} \cdot \bar{n} dA \tag{2.21}$$

The line integral of the field intensity around the closed loop is approximated by the sum of the individual components.

$$\int_c \bar{H} \cdot d\bar{l} \approx 2H_g L_g + 2H_m L_m + H_{Fe} L_{Fe} \tag{2.22}$$

Substituting Eq. 2.22 for the left side of Eq. 2.21 and *NI* for the right side, along with the constitutive relation given in Eq. 2.7, results in,

$$2\frac{B_g L_g}{\mu_g} + 2\left(\frac{B_m}{\mu_m} - \mu_0 M\right)L_m + \frac{B_{Fe} L_{Fe}}{\mu_{Fe}} = \mu_0 NI \tag{2.23}$$

Eq. 2.1 states that flux is conservative, it then follows that $B_m A_m = B_{Fe} A_{Fe} = B_g A_g$. Substituting and rearranging results in,

$$B_g = \frac{\mu_0 (NI + ML_m)}{\left(2\frac{L_g}{\mu_g} + 2\frac{L_m}{\mu_m}\frac{A_g}{A_m} + \frac{L_{Fe}}{\mu_{Fe}}\frac{A_g}{A_{Fe}}\right)} \tag{2.24}$$

Substituting into Eq. 2.20 results in,

$$F = \frac{\mu_0 A_g (NI + 2ML_m)^2}{\left(2\frac{L_g}{\mu_g} + 2\frac{L_m}{\mu_m}\frac{A_g}{A_m} + \frac{L_{Fe}}{\mu_{Fe}}\frac{A_g}{A_{Fe}}\right)^2} \tag{2.25}$$

The conventional practice at this point is to neglect the iron-loss term in the denominator due to the relative magnitudes of the relative permeabilities. The relative permeability of the air gap and permanent magnet are approximately equal to 1, whereas the relative permeability of the iron is on the order of 1000. This typically makes the iron loss term very small when compared to the other terms in the denominator. Many authors arrive at the same result by assuming the permeability of the iron is infinite.

2.5.2. Electrical Circuit Analogy

The same results can be obtained by comparing the magnetic circuit shown in Fig. 2.1 to an equivalent electrical circuit shown in Figure 2.2. The magnetomotive force, *NI*, and the magnetization of the permanent magnets, *M*, are analogous to voltage sources. The magnetic flux, φ, which passes through the ferrous path, is equivalent to current in an electrical circuit. The air gaps in the circuit cause an equivalent resistance known as reluctance, R_g. Additionally, just as copper wires induce a slight resistance in an electrical circuit, the ferrous material causes a slight reluctance, R_{Fe}. The permanent magnets also have a reluctance associated with them, R_m.

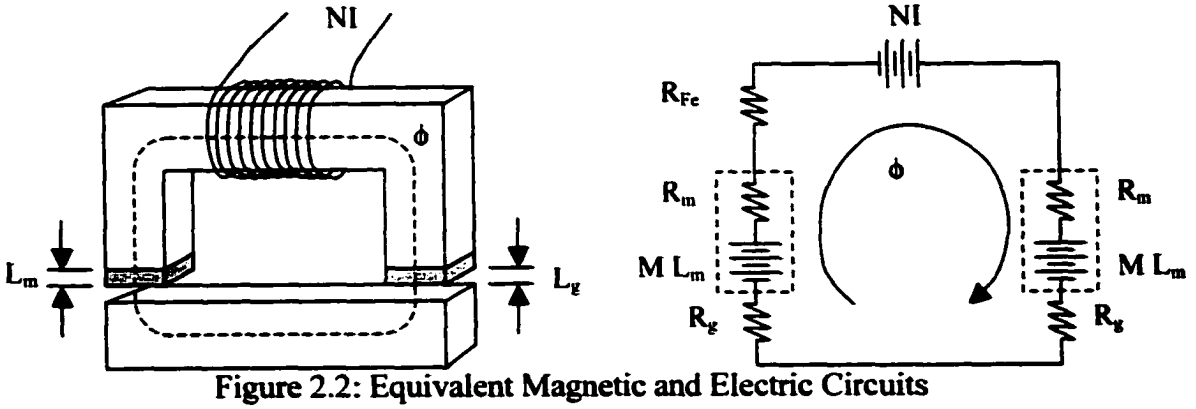

Figure 2.2: Equivalent Magnetic and Electric Circuits

The reluctance is defined as,

$$R_i = \frac{1}{\mu_i \mu_0} \frac{L_i}{A_i} \tag{2.26}$$

The circuit equation for the system can be found using the equivalent of Kirchoff's Voltage Law. Summing the magneto-motive forces around the loop yields,

$$NI + 2L_m M = 2\phi_g R_g + 2\phi_m R_m + \phi_{Fe} R_{Fe} \tag{2.27}$$

Using conservation of flux and rearranging terms results in an expression for the magnetic flux passing through the air gap. If the flux is assumed to pass directly across the poles and remain within the area defined by the pole boundaries, then the flux can be divided by A_g to give the flux density in the gap.

$$B_g = \frac{\mu_0 (NI + ML_m)}{\left(2\frac{L_g}{\mu_g} + 2\frac{L_m}{\mu_m}\frac{A_g}{A_m} + \frac{L_{Fe}}{\mu_{Fe}}\frac{A_g}{A_{Fe}} \right)} \tag{2.28}$$

This is the same result as Eq. 2.24, and it makes clear why this method has been termed Magnetic Circuit Theory.

To develop the force relation in Eq. 2.25, it was assumed that the flux density crossed the air gap in the area defined by A_g in order to allow B_g from Eq. 2.28 to be used in Maxwell's stress tensor. Likewise, in order to develop Eq. 2.23, an area was defined to convert the magnetic flux into a flux density. So the same assumptions about flux behavior at the air gap are inherent to both derivations. The statement that all the flux passes within the area defined by the pole face simply means that no flux leakage occurs at the gap, which is generally not the case. There will be a certain amount of leakage in any system and the accuracy of the model is highly dependant on the amount of flux that actually leaks around the air gap.

2.5.3. Iron Losses

Inherent in both derivations is the assumption that the flux does not saturate anywhere within the iron circuit. This is embedded in the formulation due to the use of the constitutive equation, Eq. 2.7, which implies that the flux density varies linearly with the field intensity. This is only true when the flux density is within the linear range. This is illustrated in the *B-H* curve for a mild steel shown in Fig. 2.3 [Vector Fields, 1999]. If the field intensity within the iron exceeds the linear range limit, then the linear model is no longer valid. The linear range shown in Fig. 2.3 has a relative permeability of 1000 while the initial relative permeability of the saturation region is only 12. As the magnitude of H is increased further the relative permeability asymptotically approaches unity. Not only does this case invalidate the constitutive relation, but it also increases the reluctance of the iron to the point where the iron loss term can no longer be neglected.

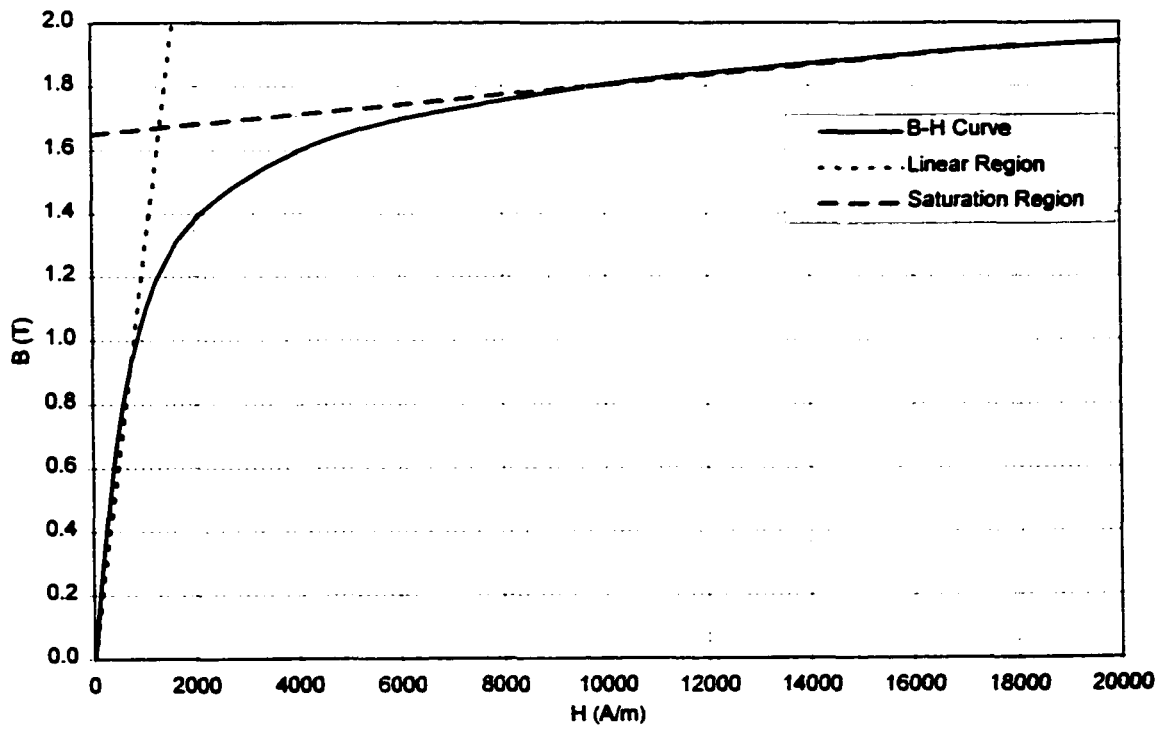

Figure 2.3: B-H Curve for Mild Steel

The effect of neglecting the iron-loss term can be seen by examining the ratio of Eq. 2.25 with and without the iron loss term. Dividing the two equations makes it possible to write the components in terms of the reluctances. The ratio of the exact force over the force calculated with the iron losses neglected is,

$$\frac{F_{Exact}}{F_{Approx}} = \frac{\left(R_g + R_m\right)^2}{\left(R_g + R_m + \frac{1}{2}R_{Fe}\right)^2} \tag{2.29}$$

The equation can be written as,

$$\frac{F_{Exact}}{F_{Approx}} = \left(\frac{R_g + R_m}{R_{Fe}}\right)^2 \frac{1}{\left(\frac{R_g + R_m}{R_{Fe}}\right)^2 + \left(\frac{R_g + R_m}{R_{Fe}}\right) + \frac{1}{4}} = \frac{\kappa^2}{\kappa^2 + \kappa + 1/4} \tag{2.30}$$

where κ is defined as the ratio of reluctance of the air gap and permanent magnet path to the reluctance of the iron path. The percentage error due to neglecting the iron term is plotted in Fig. 2.4 for the range of κ between 0 and 50.

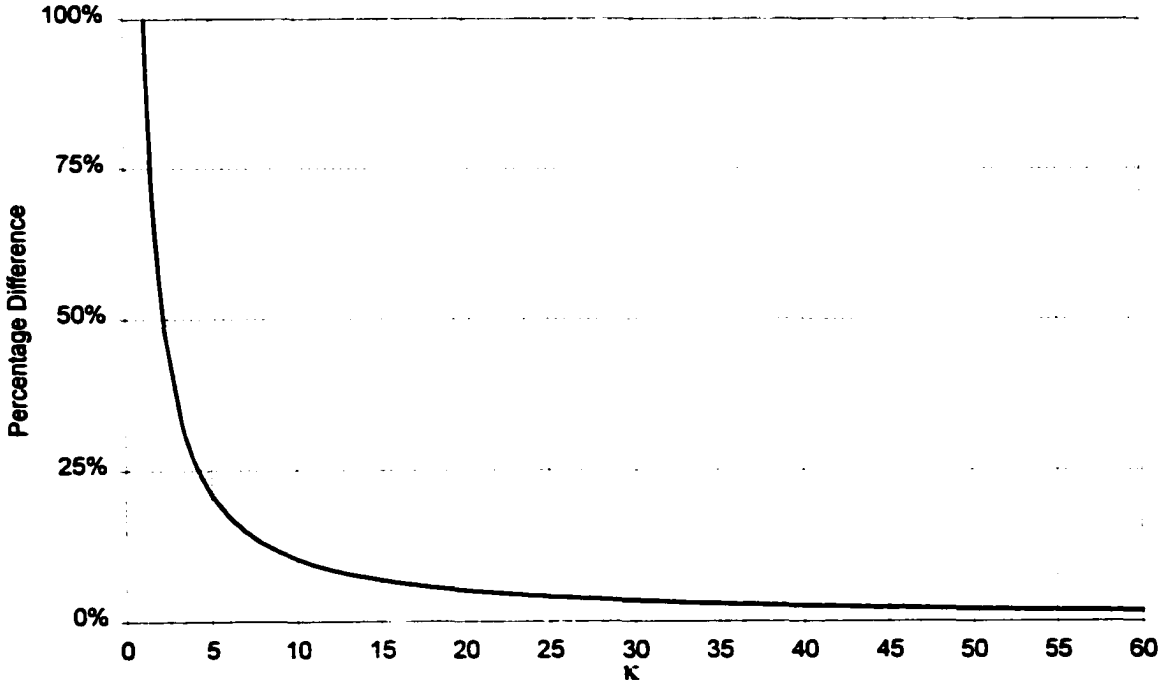

Figure 2.4: Percentage Error in Computed Force when Neglecting Iron Losses

For example, consider the actuator shown in Fig. 2.3 with a permanent magnet thickness of 0.05", an air gap of 0.05", $\mu_{Fe} = 5000$, $\mu_m = 1.05$, $\mu_g = 1$, all the areas equal, and an equivalent iron length of 8.5". The value of κ for this configuration is 57. The percent age difference between the exact formulation and the simplified formulation is 1.7%.

For most bearing-like configurations the value of κ will be larger then 50, so the error induced by neglecting the iron losses will be small, less then 2%. However, if less permeable steel is used, then the value of κ can be reduced to around 10, which results in an error of around 10%. Thus, the determination of whether or not to ignore the iron losses is dependent upon the geometric design and the materials used.

2.5.4. Leakage Factor

One method that has been used in the past to increase the accuracy of circuit theory is the addition of leakage factors. The leakage factor, K, represents the ratio of the amount of flux that passes between the pole piece and the total amount of flux passing through the circuit. Eq. 2.20 can be modified to include the leakage factor by replacing B_g with $K \cdot B_g$. The loss factor is calculated by estimating the permeance of the leakage path, where the permeance is defined as the inverse of the reluctance. Using the circuit model, the amount of flux passing within the area of the pole can be related to the total flux using the magnetic equivalent to the law of current division.

$$B_g = \frac{R_L}{R_g + R_L} B_{Total} \tag{2.31}$$

Where R_L is the reluctance of the leakage path and R_g is the reluctance of the air gap. Using this definition, the loss factor is defined as,

$$K = \frac{B_g}{B_{Total}} = \frac{P_g}{P_g + P_L} \tag{2.32}$$

When the permeance of the leakage path is zero, equivalent of $R_L = \infty$, the value of K becomes 1 and the force relation remains identical to Eq. 2.20.

Several possible leakage paths for the geometry in Fig. 2.1, with the permanent magnets removed, are shown in Fig. 2.5. Part A of the figure shows one corner of the actuator and Part B illustrates the approximated leakage path geometries.

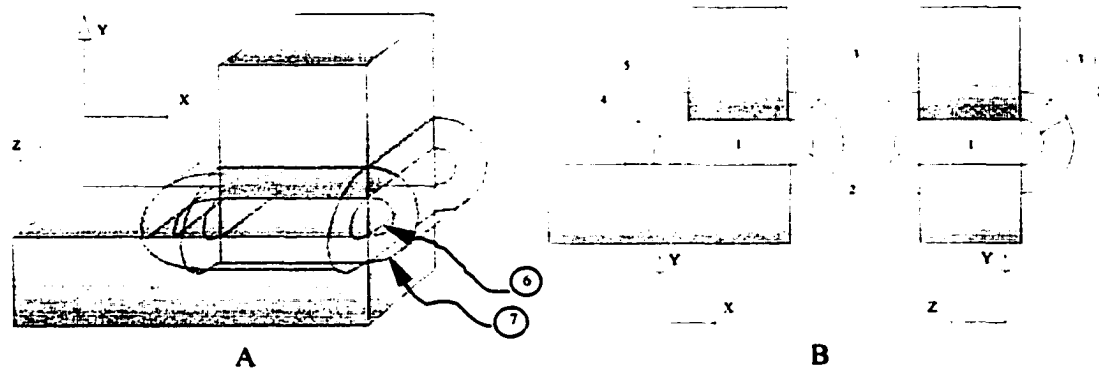

Figure 2.5: Possible Flux Leakage Paths at Air Gap

There are additional flux paths at each of the four corners. The inner piece, #6, is shaped like a quarter of a sphere. The outer piece, #7, is about the same but larger with the volume of #6 subtracted from its center. The permeance estimations for the individual flux paths for the seven volumes are defined in [Rotors, 1941]. The permeance estimations for a geometry with a square pole area of width w_g and a leakage height t, are given in Eq. 2.33.

$$
\begin{aligned}
P_1 &= \frac{\mu_0 A_g}{L_g} = \frac{\mu_0 w_g^2}{L_g} \\
P_2 &= 2.6\mu_0 w_g \\
P_3 &= \begin{cases} 0.64\mu_0 w_g \left(\dfrac{t}{t+L_g}\right) & g \geq 3t \\ \dfrac{\mu_0 w_g}{\pi} \ln\left(1+\dfrac{2t}{L_g}\right) & g < 3t \end{cases} \\
P_4 &= 0.52\mu_0 w_g \\
P_5 &= \begin{cases} 1.28\mu_0 w_g \left(\dfrac{t}{t+2L_g}\right) & g \geq 3t \\ \dfrac{2\mu_0 w_g}{\pi} \ln\left(1+\dfrac{t}{L_g}\right) & g < 3t \end{cases} \\
P_6 &= 0.077\mu_0 L_g \\
P_7 &= 0.25\mu_0 t
\end{aligned}
\tag{2.33}
$$

For each pole, the net permeance is found by summing up the individual permeances,

$$P_g = P_1 \qquad P_L = 3(P_2 + P_3) + P_4 + P_5 + 4(P_6 + P_7) \tag{2.34}$$

The leakage factor is then,

$$K = \frac{P_1}{P_1 + 3(P_2 + P_3) + P_4 + P_5 + 4(P_6 + P_7)} \tag{2.35}$$

Two non-dimensional ratios, $\alpha = L_g/w_g$ and $\beta = t/L_g$, can be substituted into Eq. 2.35 to yield,

$$
K = \begin{cases} \dfrac{1}{1+\alpha\left(1.3+1.92\left(\dfrac{\beta}{1+\beta}\right)+1.28\left(\dfrac{\beta}{2+\beta}\right)\right)+\alpha^2(0.308+\beta)} & \beta \leq \dfrac{1}{3} \\ \dfrac{1}{1+\alpha\left(1.3+\dfrac{1}{\pi}\ln(1+2\beta)^3+\dfrac{1}{\pi}(1+\beta)^2\right)+\alpha^2(0.308+\beta)} & \beta > \dfrac{1}{3} \end{cases}
\tag{2.36}
$$

The results are plotted in Fig. 2.6 for the range of $0 < \alpha, \beta < 1$. The results show that the smaller the value of α the less flux that leaks outside of the flux path. This can be interpreted in two ways. First this ratio is representative of the reluctance of the air gap.

The lower the reluctance the lower the leakage. Secondly, the situation can also be seen intuitively. If the pole face is wide then there is a large area for the flux to cross the air gap, and since the flux only leaks from the edges of the gap, having a large pole face should result in a larger percentage of flux passing through the air gap.

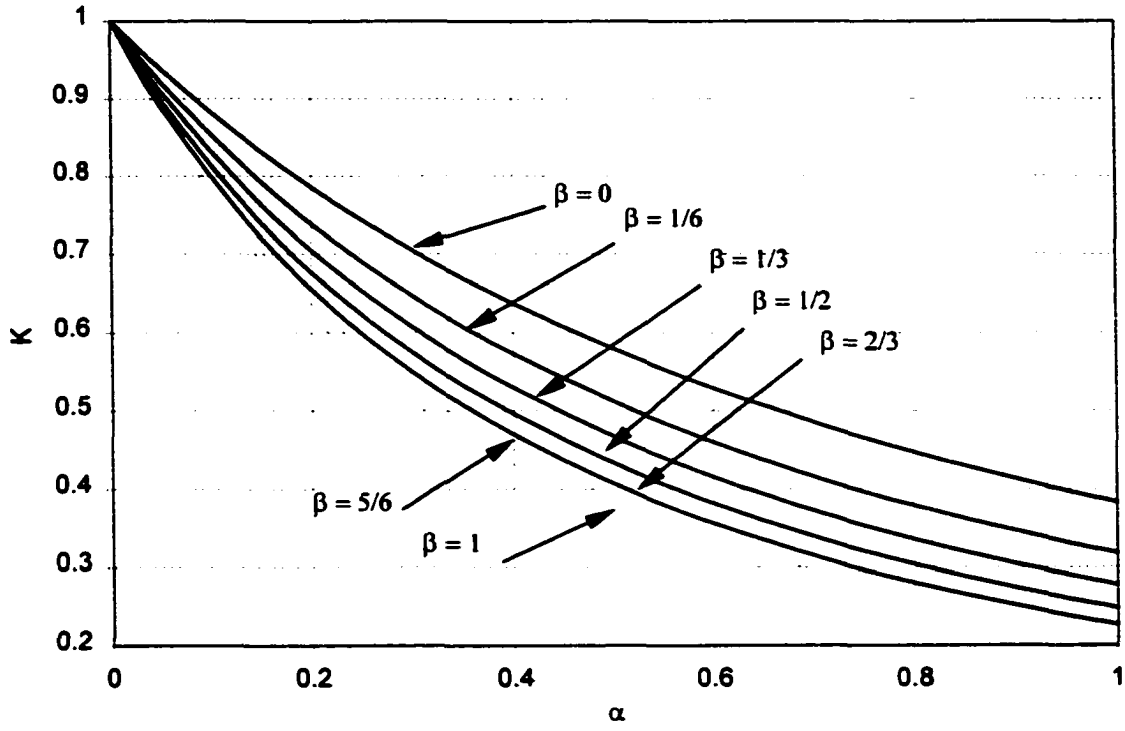

Figure 2.6: Variation of loss factor with $\alpha = L_g/w_g$ and $\beta = t/L_g$

The problem in using this technique is that β is essentially arbitrary. It is dependent upon the value of *t* which can only be estimated.

2.6. Dynamic Analysis of Eddy Currents

The analysis methods discussed thus far have been, for the most part, static systems described by Eqs. 2.1 and 2.3, or 2.4 and 2.5. Maxwell's second equation and Faradays law introduce the time variation of magnetic fields. Substituting the constitutive relation

between $\bar{J}$ and $\bar{E}$, Eq. 2.8, into Eq. 2.2 defines the fundamental relationship between an induced current and a time varying field.

$$\frac{1}{\sigma}\left(\bar{\nabla}\times\bar{J}\right)=-\frac{\partial\bar{B}}{\partial t} \tag{2.37}$$

It is clear from Eq. 2.37 that whenever a conducting material is in the presence of a time varying magnetic field an electrical current will be produced. These currents are referred to as eddy currents. These induced currents can be either desirable or undesirable, depending on the specific situation.

With the proper substitutions of the remaining Maxwell's equations, it can be shown that the magnetic field behaves as a diffuse system. The complete derivation is given in Section 5.

$$\nabla^2\bar{H}=\mu_0\mu_r\sigma\frac{\partial\bar{H}}{\partial t} \tag{2.38}$$

The effects of the diffusive behavior on the magnetic fields is covered in detail in Section 5. For now it is sufficient to note that the inherent complexity of the vector diffusion equation limits the existence of analytical solutions to a small number of simple geometries. As a result, the solution to the eddy current problem is generally found using finite element analysis.

2.7. Fundamental Issues

The modeling of magnetic bearings involves both the static modeling methods discussed in Section 2.2 and the dynamic methods discussed later in Section 5.1. The overall performance of a magnetic bearing is determined by the combined effects of the two

cases. Configuration trade-offs must usually be made between the ideal static design model and the ideal dynamic design model. Fortunately, in the analysis stages the two can be uncoupled and analyzed separately.

Static modeling techniques are typically used to dictate the basic operating point of the bearing, and to design for general bearing performance. Issues such as the geometric design, load capacity, and nominal power usage are addressed in the static design stage. For a system performing at low rotational speeds these considerations may dominate. Dynamic modeling dictates the dynamic response of the bearing, including considerations such as stiffness, gain and phase margins. In addition, rotational power losses and rotor heating are examined using dynamic analysis techniques. As the required stiffness of the bearing, and/or as the rotational speed of the bearing increase, the dynamic effects of induced eddy currents must be addressed more carefully.

Historically, both the static and dynamic design models have suffered from shortcomings embedded within the fundamental theory. For the case of static modeling techniques, when the underlying assumptions are closely met the models provide sufficiently accurate information. The drawback is that when the assumptions are not closely met the model can error significantly; errors above 80% serve as example in Section 3. Additionally, geometric considerations which affect flux leakage and flux fringing are not considered in classical circuit models.

Similar problems are present in the dynamic modeling of eddy currents. The fundamental theory is developed for specific cases, such as very low frequencies or very high frequencies. The formulations for the two cases are very different and for most situations the truth lies somewhere in between.

The remainder of this dissertation is focused on improving the existing modeling techniques. An improved version of magnetic circuit theory is developed which accounts for geometric considerations and relaxes many of the embedded assumptions. Experimental data is collected from a set of magnetic actuators and the results are used to discern the origin of the errors in the classical circuit model in order to develop an improved, or extended, model. The experimental data sets are analyzed in Section 3 and the extended circuit model is developed in Section 4. The behavior of eddy currents is examined over the entire range of conductor thickness in order to blend the existing models into a single, complete model. The model is developed using Maxwell's equations, experimental data, and finite element results. The analysis is discussed in Sections 5 and 6.

3. EXPERIMENTAL PERFORMANCE OF A MAGNETIC ACTUATOR

A set of magnetic actuators were designed, built, and tested to develop a reference data set which was used to compare analytical circuit theory models to actual actuator performance. The results were used to develop and validate the extended circuit theory model discussed in Section 4 as well as to verify the finite element results used in Sections 4 and 5. Additionally, the data set was used to determine performance trends with respect to magnet locations, winding locations, and actuator geometry.

3.1. Description of Experiment

A simple horseshoe design was chosen which represents a large class of magnetic actuators and magnetic bearings, as shown in Fig. 3.1. The stator and the armature are 0.5 inch wide and 0.5 inch deep. Two stators were built, one with a 2.0 inch pole separation distance and one with a 4.5 inch pole separation distance. The pole height was set at 1 inch to allow ample room for the windings to be wound around the back of the stator. The nominal

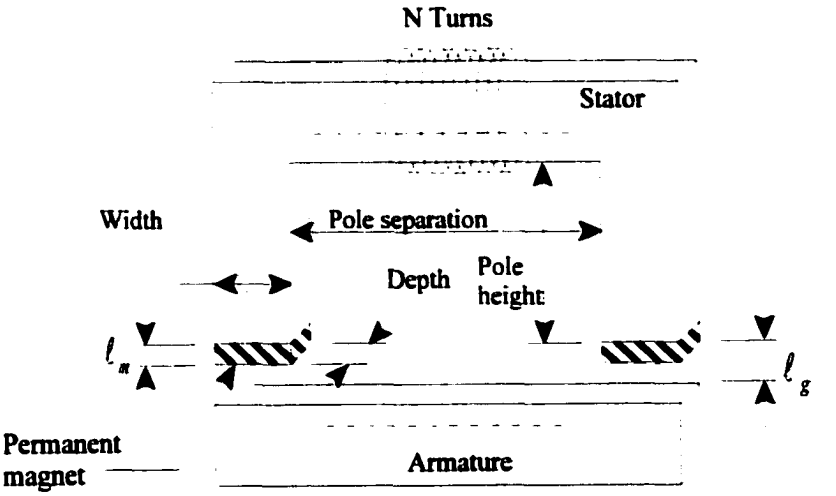

Figure 3.1: Geometry of Actuator

operating air gap was chosen to be 0.05 inch, and force data were recorded around the operating point at 0.02, 0.04, 0.06, and 0.07 inch. The complete design of the 2 inch actuator is shown in Fig. 3.2. The 4.5 inch stator is identical in design in every way except in the pole separation distance. Attachment points were added to the back of the stators and the armatures to allow for mounting to the test fixture.

The actuators were biased with permanent magnets 0.05 in thick. The location of the magnets were varied between being placed on the pole faces, within the armature, or at both locations. The actuator was controlled by a set of windings wound around the stator. The windings were wound around the pole pieces or around the back of the stator, with a total of 2000 turns for both cases. The possible permutations due to variations in the winding locations, magnet locations, and pole separation distance lead to 22 possible configurations. The configurations are listed in Tables 3.1 and 3.2 for the 2 inch actuator and the 4.5 inch actuator, respectively, along with the designation test numbers. The experimental results for each test are listed in Appendix A.

The actuators were constructed from Connecticut Metal's CMI-C cold drawn steel, a material manufactured for solenoid and relay cores, magnetic control devices, and magnetic plungers, with a very low carbon content (0.01%). The material has a saturation level of 1.5 T and shows weak hysteresis behavior. The stator and armature were milled from a single piece of 2 inch diameter rod. The B-H curve for the material is shown in Fig. 2.3 in section 2.5.3.. The relative permeability of the material is approximately 8000 at low values of induction. Neodymium-Iron-Boron (NdFeB) permanent magnets were chosen for the magnet material.

The permanent magnet properties were determined experimentally and were found to have a residual induction $B_r = 1.24$ T. The experimental techniques used to determine B_r, and results, are discussed in detail in Appendix B.

		Magnet Locations			
		None	Pole	Armature	Both
Winding Locations	None		16	21	25
	Poles	14	17	20	19
	Back Iron	23	22	26	24

Table 3.1: Experimental Test Numbers for 2 inch Actuator

		Magnet Locations			
		None	Pole	Armature	Both
Winding Locations	None		3	8	12
	Poles	1	4	7	6
	Back Iron	10	9	13	11

Table 3.2: Experimental Test Numbers for 4.5 inch Actuator

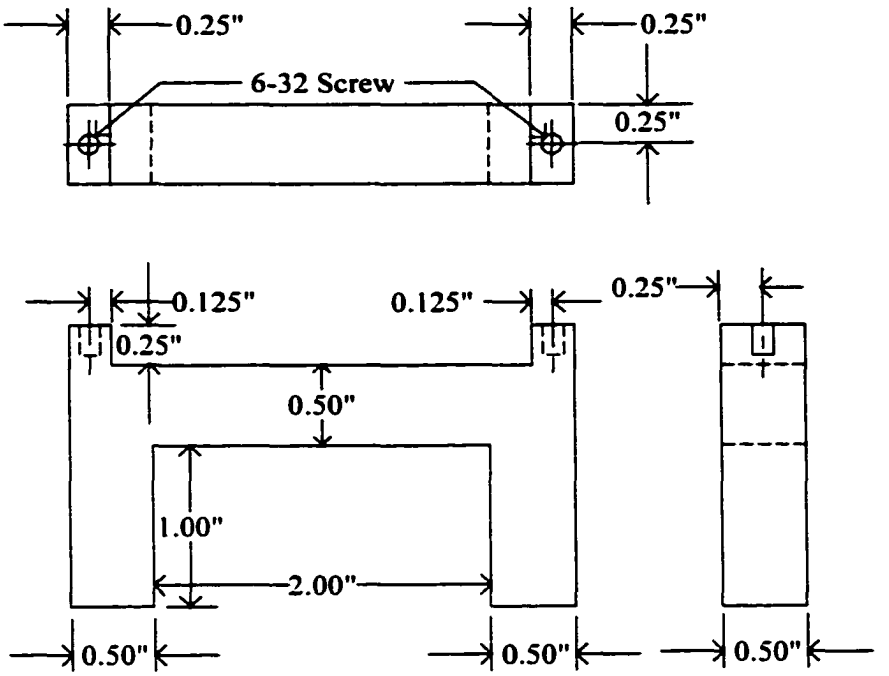

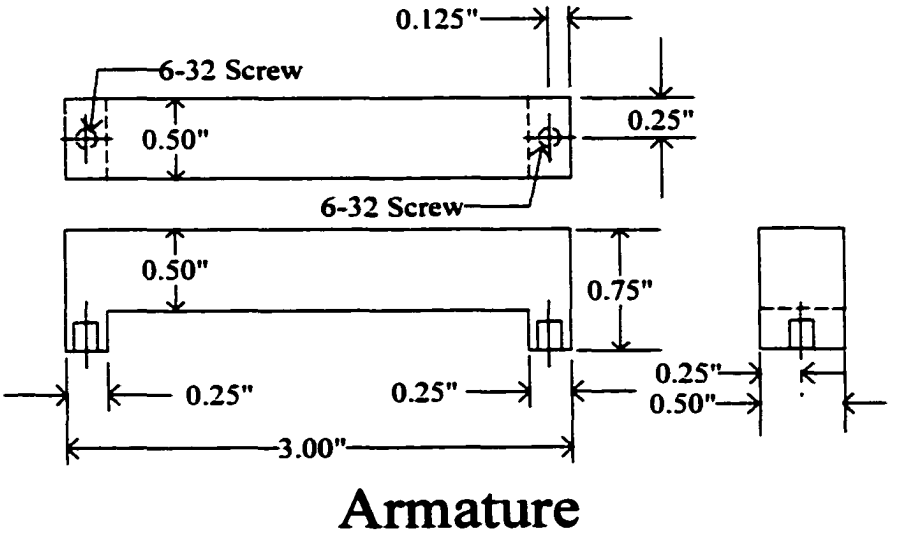

Figure 3.2: Detailed Design of Magnetic Actuator

3.2. Experimental Set Up and Procedure

The experimental set up is shown schematically in Fig. 3.3. The relative position of the stator and armature were controlled using a DAEDAL Precision Positioner, Model 506241S. The positioner was controlled by a DAEDAL MS 2000 controller. The controller received the commanded signal from a PC running Labview 4.1, which also controlled the coil current. The digital signal was converted to an analog signal using a Instrunet 100B D/A Converter. The current was supplied by a 5A, 28 Volt current amplifier. The amplifier and the power supply were both constructed in house at NASA Langley Research Center. A photograph of the complete setup is shown in Fig. 3.4.

The force between the stator and the armature was measured using a load cell rated for 50 lbs. The load cell was connected to the actuator using an aluminum rod which was supported by a linear bearing to ensure that no lateral forces were transmitted to the load cell. The armature was allowed to rotate freely so that no torques would be transmitted to the load cell. The armature and stator were attached to the positioner by aluminum mounting brackets. The mounting brackets are shown in Fig. 3.5 along with the 4.5 inch actuator configuration. The maximum number of ampere-turns was set by the 1.25 Amp driving current, the 2000 turn coils resulted in a range of ± 2500 ampere-turns.

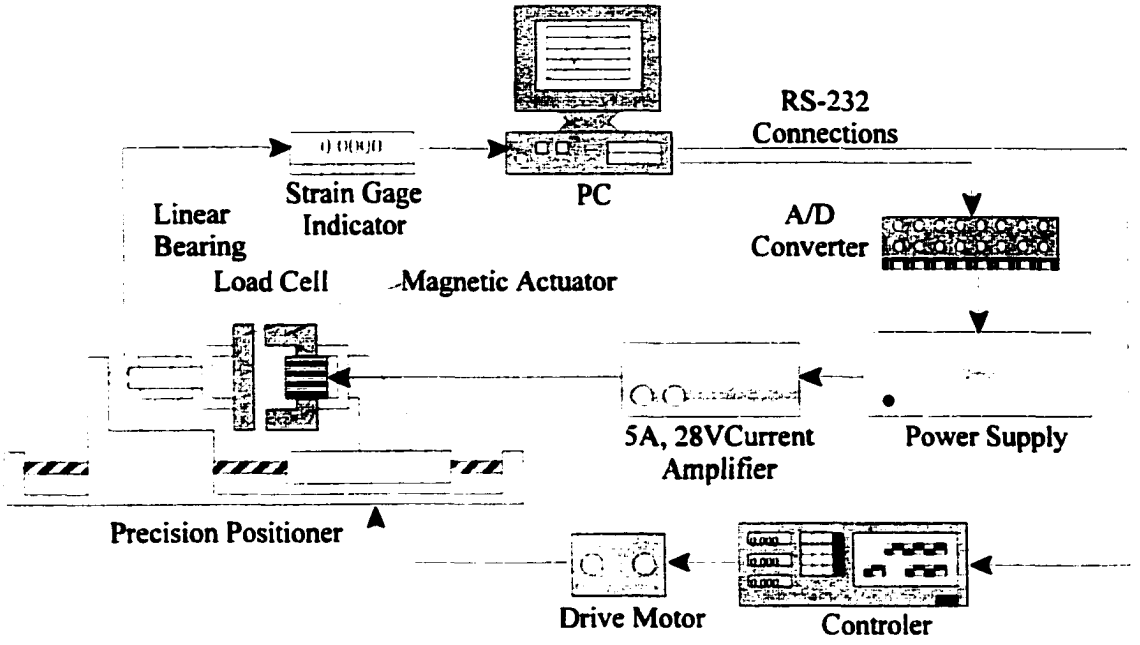

Figure 3.3: Experimental Setup

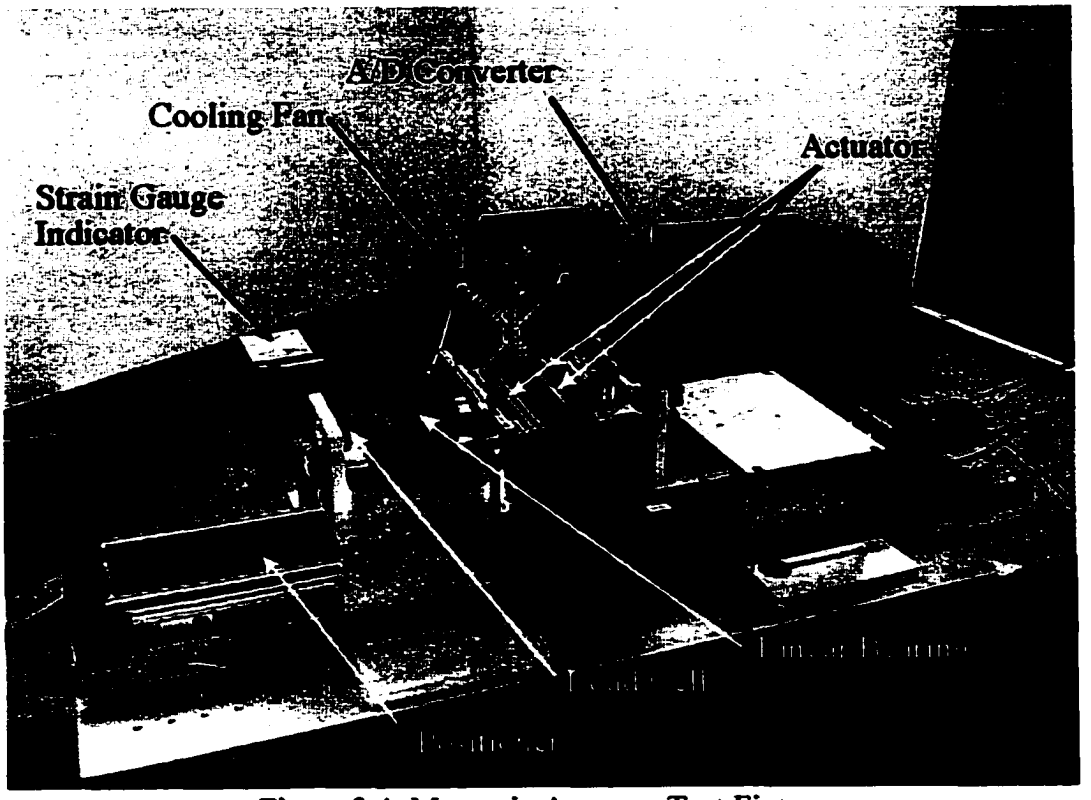

Figure 3.4: Magnetic Actuator Test Fixture

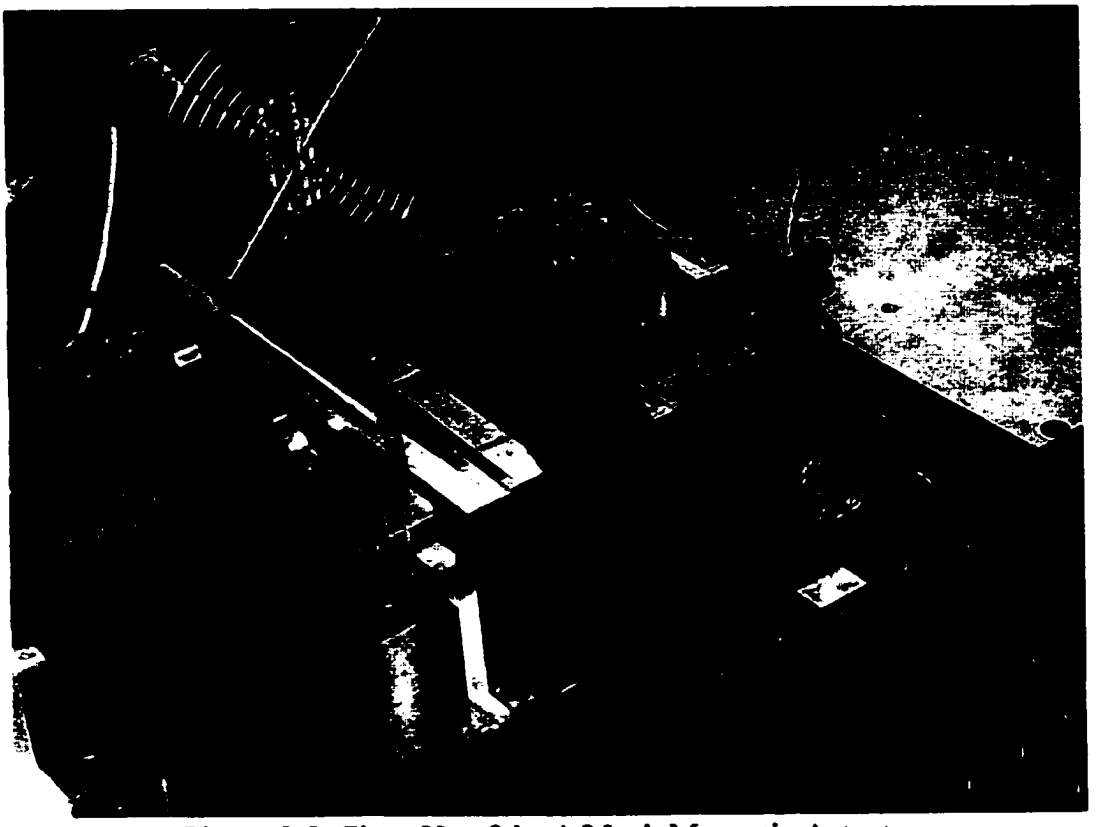

Figure 3.5: Close Up of the 4.5 Inch Magnetic Actuator

3.2.1. Calibration Procedure

The load cell was calibrated immediately before and after each actuator configuration was tested. The average of the two tests was used to reduce the experimental data. The calibration setup is shown in Fig. 3.6. The load cell was tested using three different weights: 5lb, 15lb, and 20lb. Each weight was measured five times with the average recorded. The ranges of the five measurements were recorded for each of the three weights for each calibration test, and were then used to determine the 3σ (3 standard deviations) distribution for each of the three weights. The final margin of error was determined to be 0.18 lb. The range data for the three weights is shown in Figs. 3.7, 3.8, and 3.9.

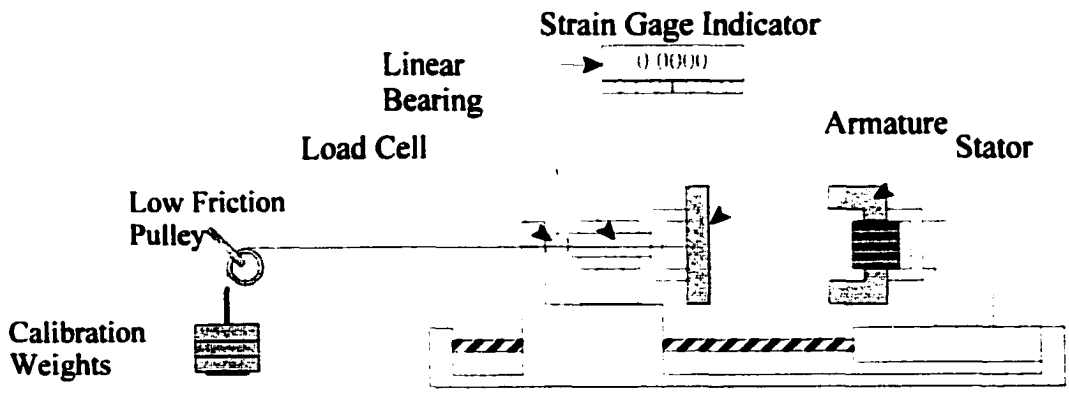

Figure 3.6: Calibration Setup for Magnetic Actuator Test Fixture

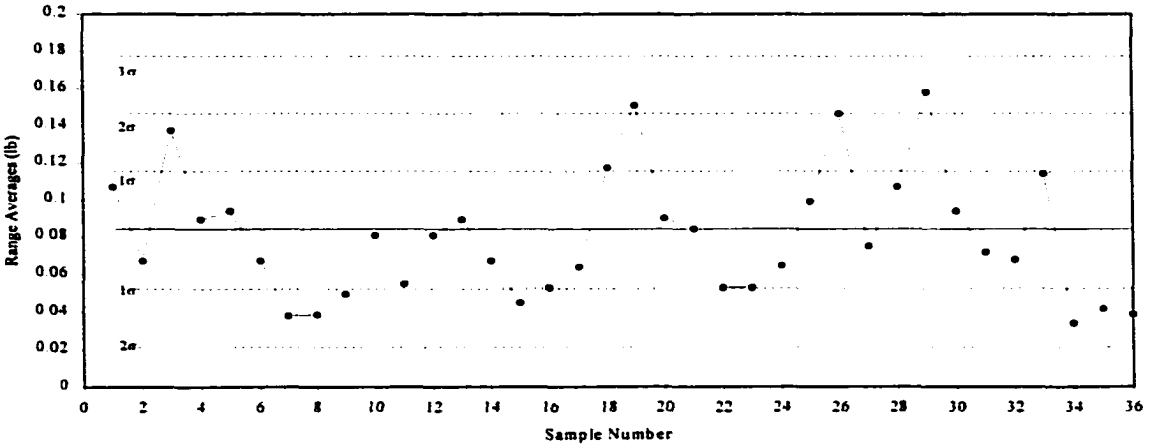

Figure 3.7: 5 lb Calibration Data

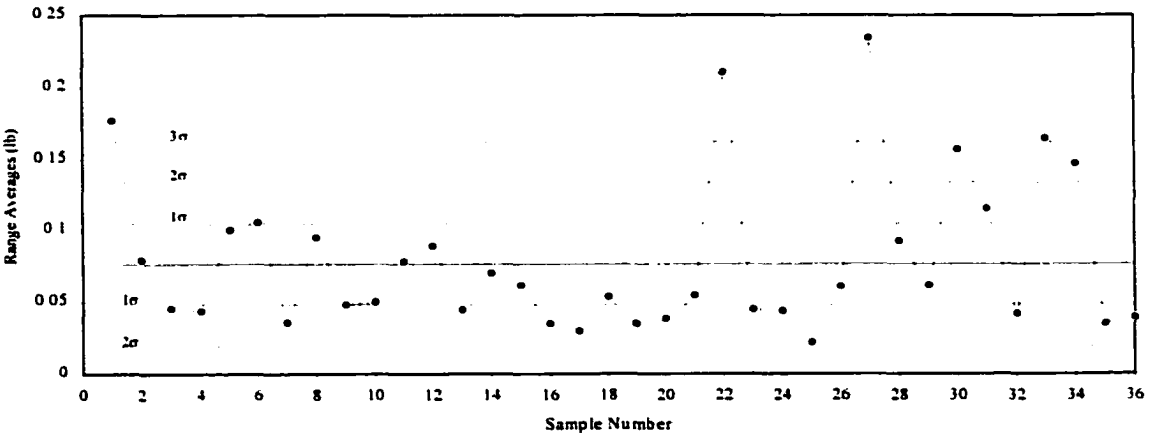

Figure 3.8: 15 lb Calibration Data

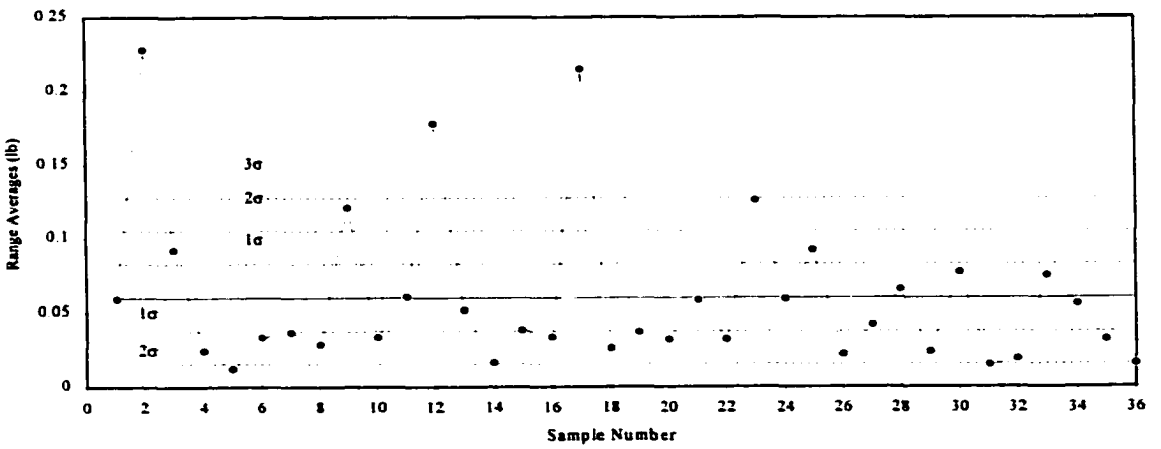

Figure 3.9: 20 lb Calibration Data

3.3. Experimental Comparison of Permanent Magnet Locations

Three different permanent magnet configurations were tested. For the first configuration the magnets were placed on the pole faces. The second configuration had a single magnet twice the thickness of the magnets of the poles (so L_m would be the same for each case) placed in the armature. The third configuration had magnets placed in both locations. The test numbers corresponding to these cases are 3, 8, 12, 16, 21, and 25. The experimental data is tabulated in Table A1 in Appendix A.

The performance of the actuators versus gap distance is shown in Fig. 3.10 with zero ampere-turns. There are four important trends present in these results. First, moving the permanent magnets from the armature to the pole faces significantly increased the actuator performance. Second, increasing the pole separation distance from 2 in to 4.5 in slightly decreased the actuator performance for all three cases. Third, doubling the permanent magnet thickness did not significantly increase the force produced by the actuator. Fourth, the difference between magnetic circuit theory and the experimental results is significant for all three actuator configurations. These points become clearer by examining the percentage difference between the experimental data (F_{exp}) and the analytical models (F_{Ideal}). The percentage difference is shown Fig. 3.11 and is defined by Eq. 3.1.

$$\%Diff = \frac{F_{Ideal} - F_{Exp}}{F_{Ideal}} \tag{3.1}$$

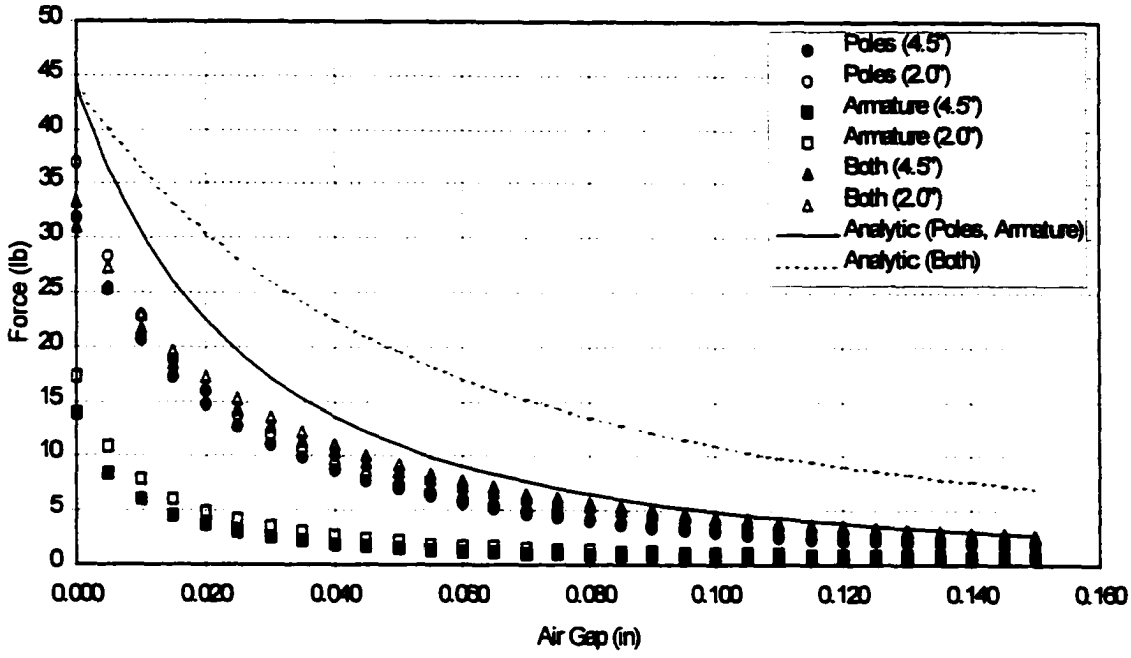

Figure 3.10: Experimental Comparison of Magnet Locations

The difference between the predicted force and the force produced with the magnets on the

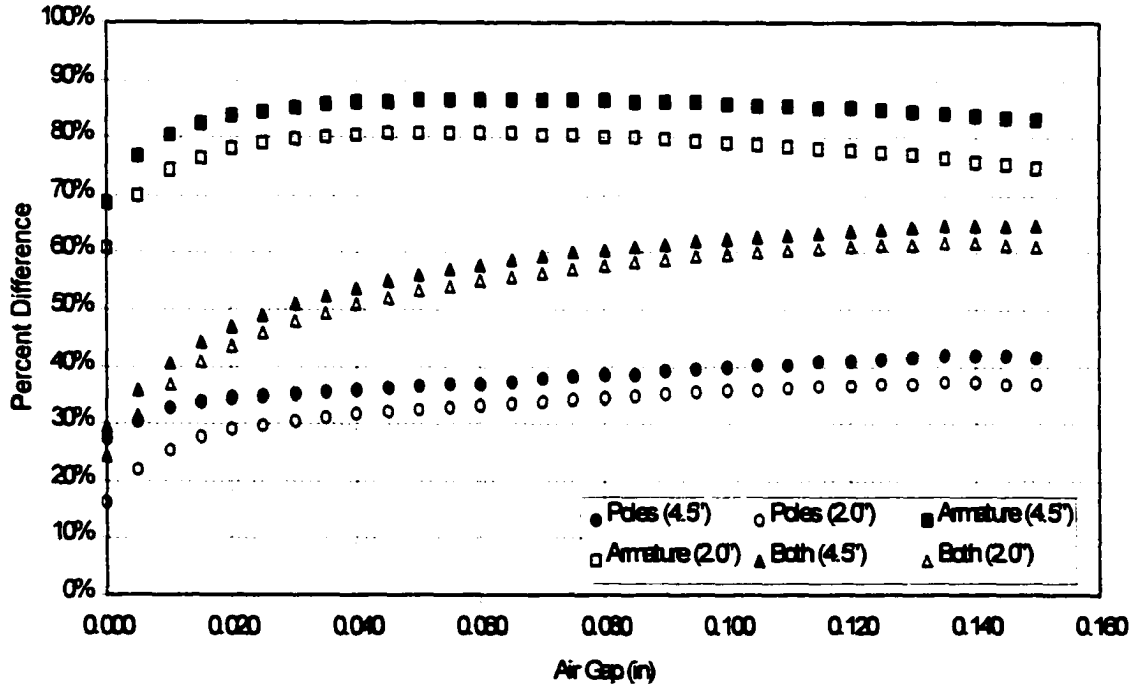

Figure 3.11: Percentage Difference Between Analytical Model and Experimental Results

pole faces averages about 35%. The difference between the predicted force and the force produced with the magnet in the armature averages around 85%. These differences are due to violations in the assumptions involved in magnetic circuit theory concerning flux leakage mechanisms and the relative reluctances of the flux paths.

When magnetic flux enters or exits a volume of high permeability, it does so practically normal to the surface. When the air gap is on the permanent magnet surface, the normal plane is aligned with the desired flux path, resulting in low leakage levels. When the permanent magnet is placed between two pieces of ferrous material the dipole behavior tends to "re-direct" the flux inside the material. As a result, the flux near the outer surface of the iron is directed perpendicular to the desired flux path. This creates a leakage path for the flux to follow which does not contribute to the generation of force. These trends can be seen in the Vector Fields PC-OPERA finite element model shown in Fig. 3.12 where the lines represent magnetic potential.

The model is a 2-D model, so flux leakage into and out of the page is not considered. Full details on the finite element analysis are given in Section 4.5. The figure illustrates the flux leakage around the permanent magnet and between the stator and the armature. Closer inspection of Fig. 3.13 reveals the redirection mechanism. The ferrous material surrounding the biasing magnet allows the natural dipole shape of the field to redirect the flux lines out of the iron flux path and bypass the air gap.

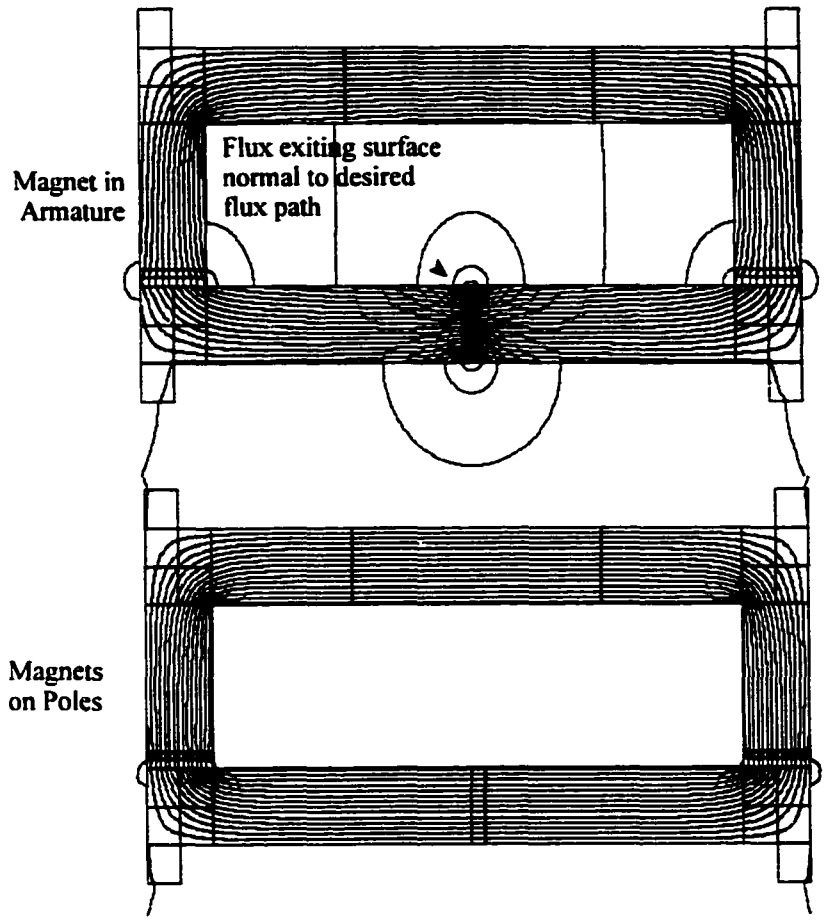

Figure 3.12: PC-OPERA Analysis of Permanent Magnet Location

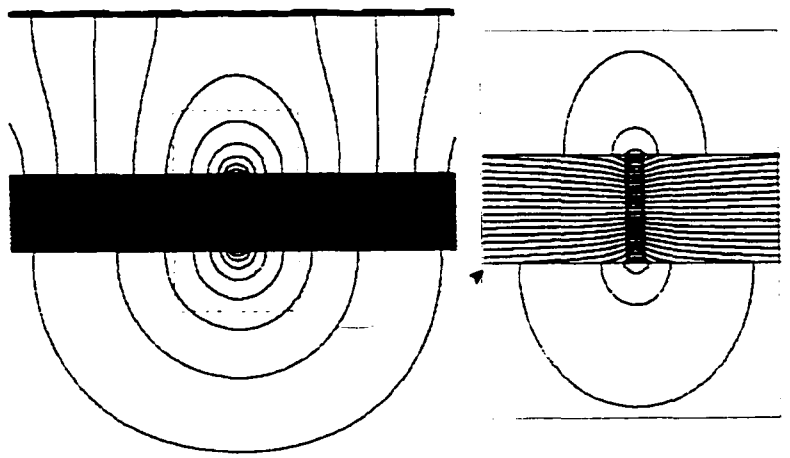

Figure 3.13: PC-OPERA Analysis of Permanent Magnet in Center of Armature

Locating the permanent magnets on the poles decreases the flux leakage between the stator and the armature. It also appears to decrease the flux leakage at the air gap. This can be seen in Fig. 3.14. The flux leakage shown in Fig. 3.14a can be considered typical flux leakage for this type of configuration regardless of the field source. Thus, locating the biasing magnets on the pole face not only decreased the permanent magnet flux loss and eliminated the stator-armature flux leakage, it also decreased the flux fringing at the air gap.

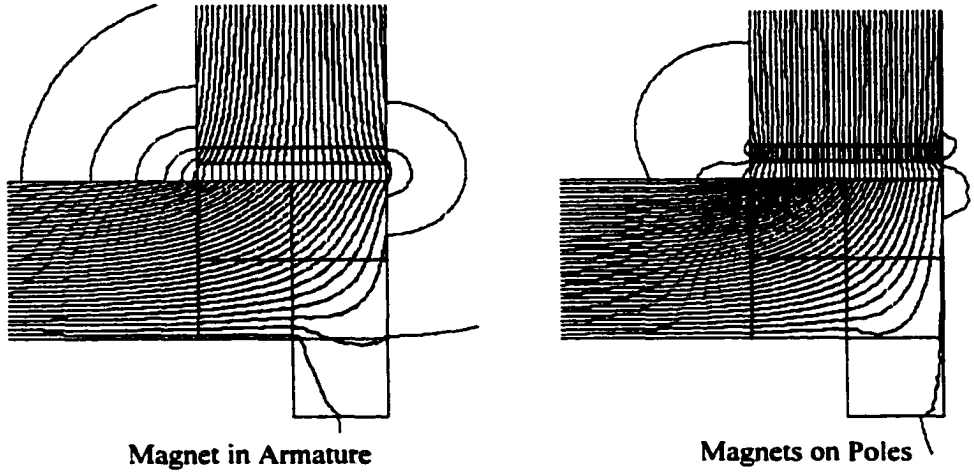

Figure 3.14: PC-OPERA Analysis of Flux Leakage at Air Gap

The decrease in flux fringing at the gap can be attributed to the field shaping effects of the permanent magnet. From visual inspection it appears that the biasing magnet is drawing the flux down the pole piece and driving it across the air gap. Indeed, this is what is happening and can be seen by considering the field shaping effects of the permanent magnet. Additionally, consider the equivalent magnetic circuit at the air gap shown in Fig. 3.15. The reluctance of the designed flux path is R_1 and the reluctance of the leakage path is R_2. From the equivalent to the law of current division, the amount of flux passing through path 1 relative to the total flux passing through the circuit is defined in Eq. 3.2.

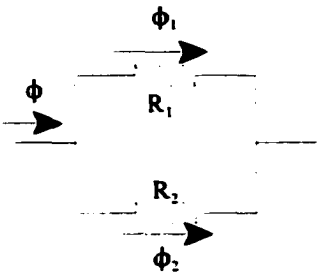

Figure 3.15: Equivalent Current Division Circuit for Magnetic Flux

$$\phi_1 = \frac{R_2}{R_1 + R_2}\phi \qquad R_i = \frac{1}{\mu_0 \mu_{r_i}} \frac{L_i}{A_i} \tag{3.2}$$

Consider the case when the flux is not in proximity to the air gap. When the flux is within the iron circuit the reluctance is very low (μ_r is on the order of 1000). According to Eq. 3.2, as R_1 tends towards zero, ϕ_1 tends toward ϕ, i.e., all the flux passes within the iron path. In the region of the air gap, R_1 has increased in magnitude (μ_r is on the order of 1) resulting in a decrease of ϕ_1. Thus, ϕ_2, or the flux fringing, increases. It is clear that as long as R_1 is larger then zero some flux leakage will occur.

The longer actuator does not perform as well as the shorter one. This behavior is observed in all three configurations. The primary cause of this difference can be attributed to the iron losses in the circuit. Examining Eq. 2.6, the iron loss term in the denominator increases with increased pole separation distance. However, the difference between the two designs can not all be attributed to iron losses. From Eq. 3.2, increasing the length of the stator and armature increased the reluctance of the circuit. The larger the reluctance of the circuit, the larger the potential for flux leakage to occur. The largest difference occurred for the case with the magnet in the armature. This is due to flux leakage between the stator and the armature as

seen in Fig. 3.12. The larger the separation distance between the poles, the more surface area there is for flux leakage to occur.

Placing magnets on the poles and in the armature resulted in a performance level between that of the two individual cases. This can be attributed to the previous flux leakage discussions. The flux produced by the permanent magnet in the armature is subject to significant losses due to the flux leaking around the magnet. However, the flux that does pass the circuit crosses the air-gaps in a more uniform manner due to the flux shaping effects of the magnets on the poles.

The differences in the experimental results and the analytical circuit model are due to several factors, the main one being the flux leakage and loss. The model assumes that all the flux will travel through the magnetic circuit with no leakage or fringing. This assumption is clearly violated when compared to the magnetic potential lines in Figs. 3.12, 3.13, and 3.14. For the circuit model to accurately predict the behavior of the three systems, modifications must be added to account for the effects of magnet placement. The effects of the iron losses are clearly present in the experimental results. However, the exact magnitude of the error introduced due to neglecting the loss terms cannot be determined due to the coupling with flux leakage and loss behavior.

3.4. Comparison of Winding Locations

The actuators were controlled by a set of windings wrapped around the stator. The windings were wrapped around each pole face, or around the back iron of the stator, as shown in Fig. 3.16.

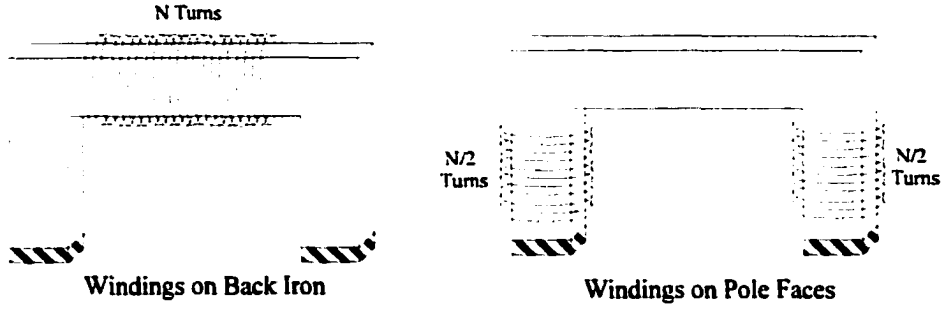

Figure 3.16: Winding Locations

Each stator has a total of 2000 turns of 24 gauge wire. Each of the two sets of windings on the pole faces had a resistance of 9.33 Ω. The windings on the short stator had a resistance of 20.5 Ω. The windings on the long stator had a resistance of 15.3 Ω. The difference in the resistance between the windings on the back iron is due to the total length of the wire; the longer stator allows the winding to be spread across a longer distance, thus decreasing the radius of each turn.

3.4.1. Comparison of Winding Locations with No Permanent Magnets

There are four different configurations examined for the case of no biasing magnets; the windings are wound around the pole faces or wound around the rear of the stator with the pole separation distance at both 2.0 inch and 4.5 inch. The experimental results are shown in Fig. 3.17 and the corresponding test numbers are 1, 10, 14, and 23. The percentage differences between the experimental results and the analytical model are shown in Fig. 3.18.

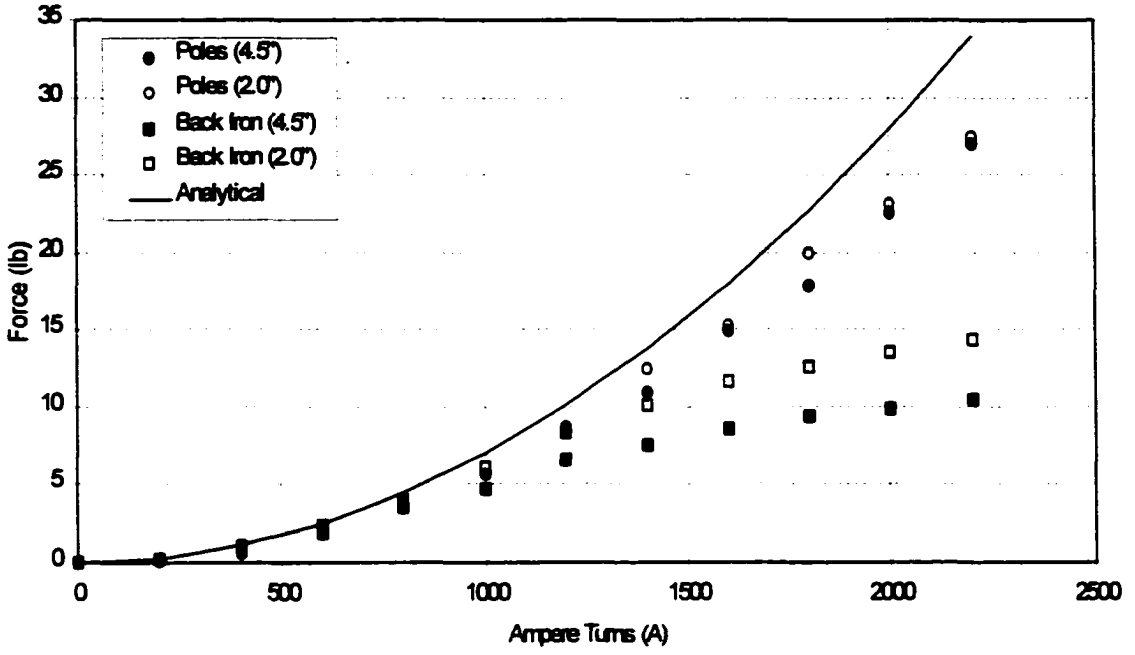

Figure 3.17: Experimental Comparison of Winding Locations with No Biasing Magnets

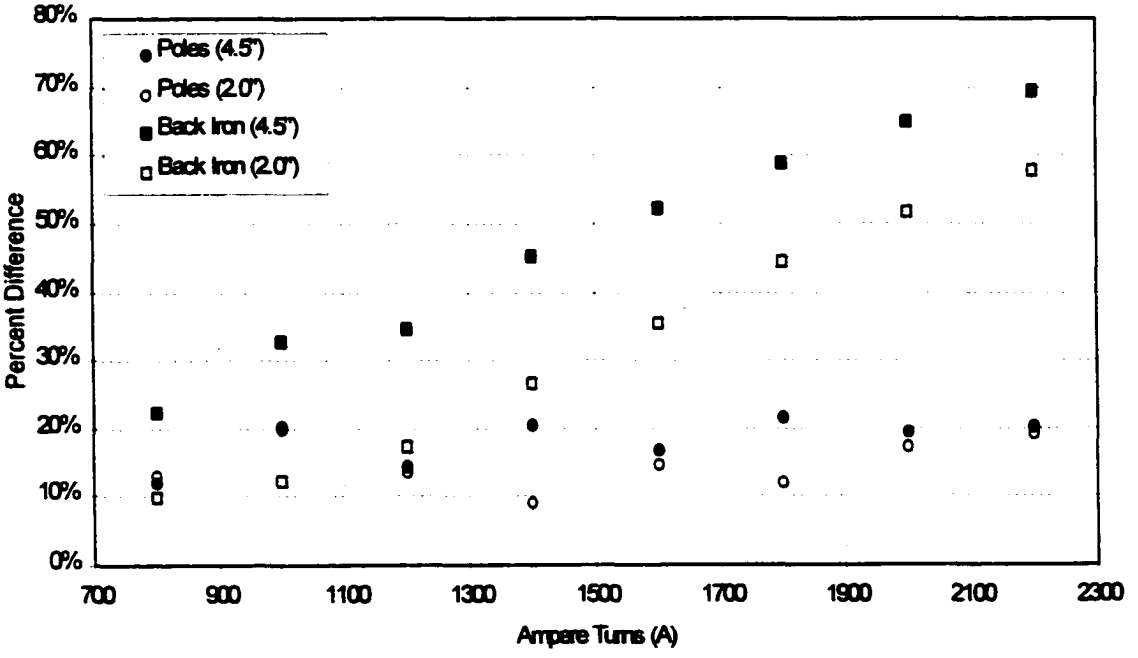

Figure 3.18: Percentage Difference Between Experimental and Analytical Models

The percentage differences with the driving currents below 700 ampere-turns were not shown because the forces were very close to zero which distorted the error comparison. The experimental data is tabulated in Tables A2-A5 in Appendix A. As was the case in Section 3.3, the analytical model over-predicted the performance of the actuator for all cases. At driving currents below 1000 ampere-turns, there does not appear to be much difference between the four configurations. When the driving current exceeds 1000 ampere-turns, there is a distinct drop in the force production of the actuator with the windings on the back iron while the actuators with the windings on the poles continue to follow the general trend of the analytical model.

Increasing the pole separation distance had little effect with the windings on the poles, but when the windings were placed on the back iron there was a significant difference between the 2.0 inch and the 4.5 inch designs. Thus, the difference is not solely due to iron losses because both stators have the same iron path lengths. The difference is due to the amount of leakage between the stator and the armature. The longer the pole separation distance the more area there is for the flux leakage to occur.

Part of this increased flux leakage is illustrated in Fig. 3.19 which shows several possible mmf leakage paths for the two designs. Consider the case where the windings have been placed on the rear of the stator. Two mechanisms are present that will cause the mmf to leak between the stator and the armature. First, as the flux leaves the region surrounded by the windings the flux is allowed to turn within the iron path, aiding the flux in exiting the surface of the stator and jumping to the armature.

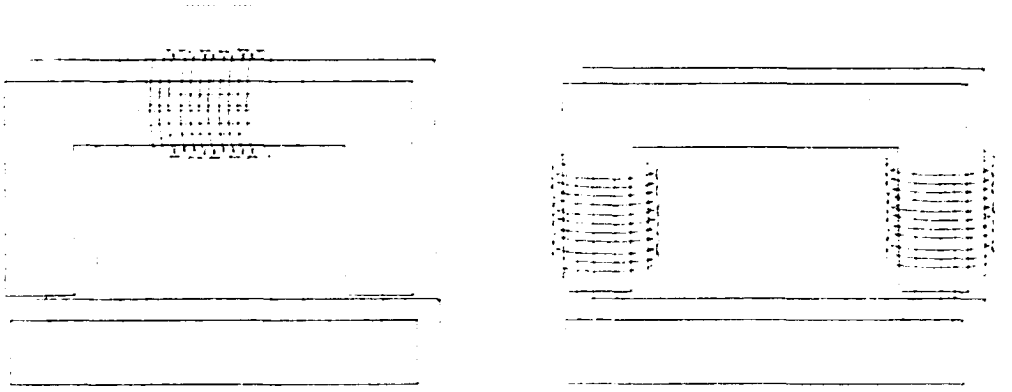

Figure 3.19: Possible MMF Leakage Paths

As was the case with the magnets placed on the pole faces, when the windings are placed on the poles this mechanism is somewhat weakened, resulting in more flux crossing the air gap. When the windings are placed on the poles, the mmf is generated in the pole pieces make it nearly impossible for the pole pieces to be bypassed. As a result, the flux leakage between the stator and the armature is reduced.

This effect can be seen in the finite element analysis of the two cases, Fig. 3.20. The figure shows the y-component of the flux density on the surface of the armature with NI = 2000 ampere-turns. In the ideal case, the flux density would be zero everywhere except in the vicinity of the pole face. When the windings are placed on the poles, significant flux leakage is present over 37% of the armature surface (excluding the pole areas). However, when the windings are located on the back iron, the flux leakage occurs over 100% of the armature surface, reaching zero at the center of the armature.

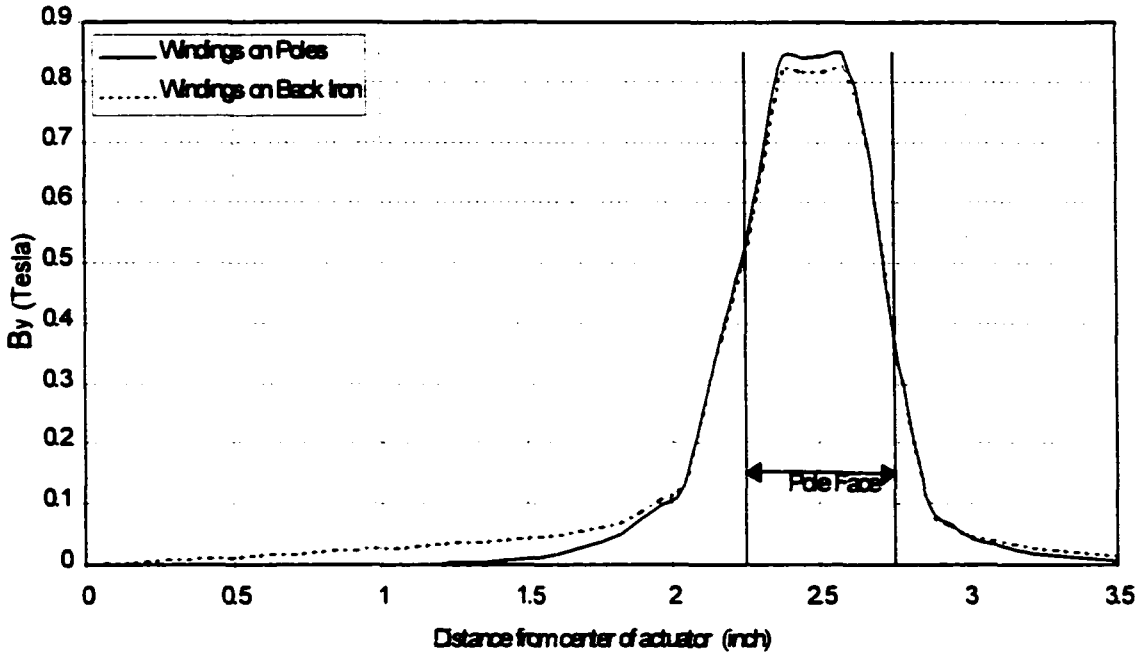

Figure 3.20: PC-OPERA Analysis of Flux Across Armature Surface with NI = 2000 A

3.4.2. Comparison of Winding Locations with Permanent Magnets on Pole Faces

There are four different configurations examined for this case, test numbers 4, 9, 17, and 21. The windings are wrapped around the pole faces or the back iron with the pole separation distance at both 2.0 inch and 4.5 inch. The experimental results are shown in Fig. 3.21 and the percentage differences between the experimental results and the analytical model are shown in Fig. 3.22. The percentage differences below -1600 ampere-turns were not shown because the forces were very close to zero which distorted the error comparison. The data is tabulated in Tables A6-A9 in Appendix A.

The experimental results show the same trends as the case with no permanent magnets. The model over-predicts the performance for all four designs. The actuator with the windings

placed on the poles outperformed the actuator with the windings placed on the back iron. There was essentially no variation with pole separation distance when the windings were placed on the poles while there was significant variation with pole separation distance when the windings were placed on the back iron.

All four actuators performed similarly when operating at low ampere-turns, the variation in performance becomes clear at currents above 1000 ampere-turns. Placing the permanent magnets on the poles of the actuator with the windings on the back iron increased the performance. With no magnets, the percentage difference from the analytical model reached 60% and 70% for the 2.0" and 4.5" actuators, respectively. With the magnets on the poles, the percentage differences decreased to 50% and 60%, respectively. However, in the case with the windings on the poles there was a slight decrease in agreement. For the 2.0" and 4.5" cases, without the magnets, the percentage difference was around 20%. With the magnets on the poles, the percentage difference increased slightly to 25%. The additional 5% difference is probably due to permanent magnet mmf losses that were not present for the cases in Section 3.4.1.

The percentage difference between the experimental results and the analytical model began to decrease as the current dropped below -1200 ampere-turns. This is not due to an increase in accuracy of the model; rather, the model is under-estimating the force produced by the coils. The model would eventually cross the experimental results yielding a zero percentage difference. The error in the larger negative ranges of ampere-turns is due to a limitation of the model.

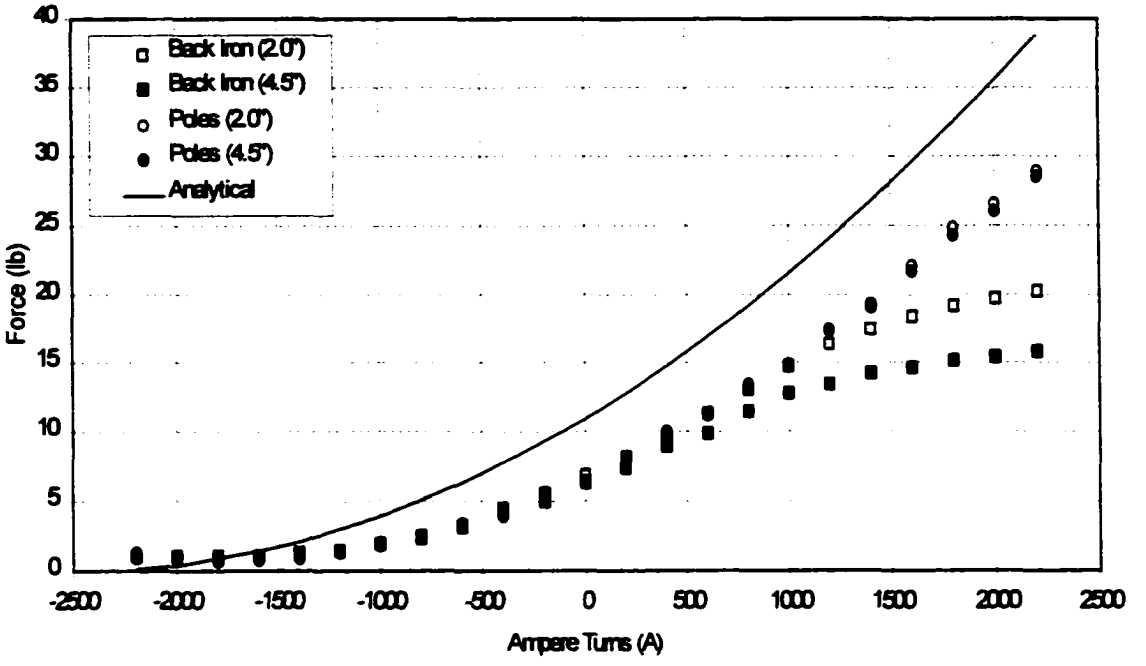

Figure 3.21: Experimental Comparison of Winding Locations with Permanent Magnets on Poles

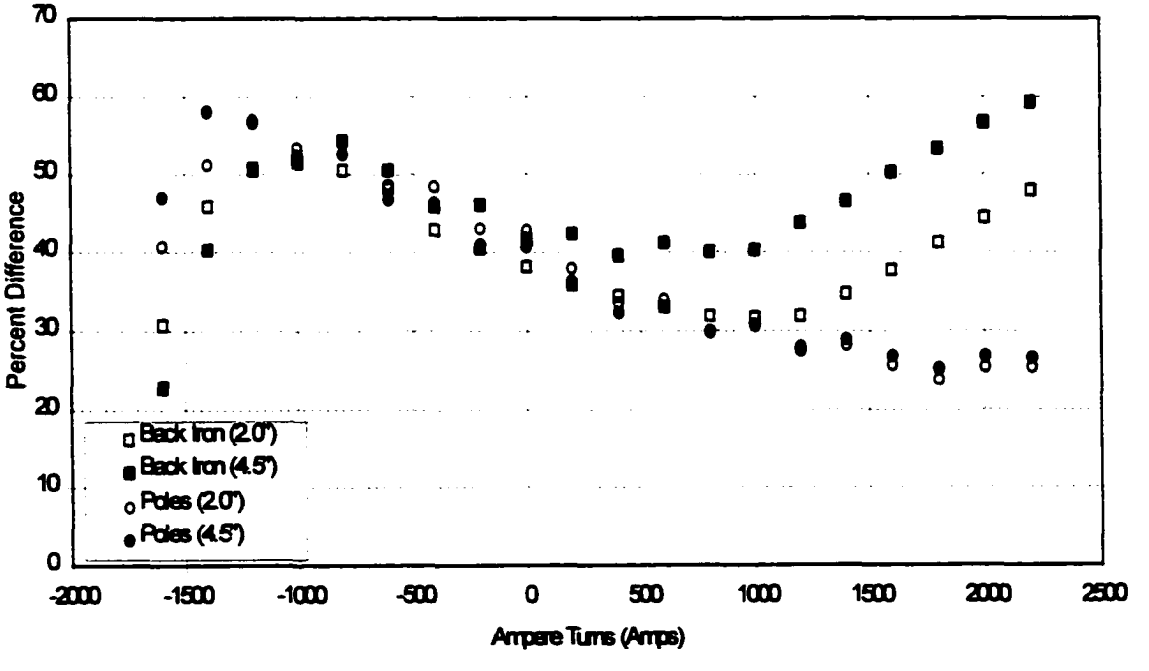

Figure 3.22: Percentage Difference Between Experimental and Analytical Model

Consider again the force model for the biased actuator given in Eq. 2.6. According to the formulation the force should equal zero when,

$$\left(NI + 2ML_m\right) = 0 \tag{3.3}$$

This statement implies that the two mmfs will cancel in the air gap driving the net force to zero. However, this is an over-simplified statement of what is actually occurring in the air gaps. In fact, the force will never equal zero when the permanent magnets are located on the pole faces.

As the negative mmf from the coils reach the magnet locations, the permanent magnet flux forces the coil mmf flux to bypass the air gap by leaking around the sides. The minimum force location occurs when an equal and opposite amount of flux leaks around the air gap as is present across the air gap. As the driving mmf is further increased, the flux in the air gap continues to decrease and the leakage flux continues to increase, resulting in a net increase in force. This is why the force never equals zero. Eventually, the net flux will overpower the permanent magnet and the flux direction in the air gap will be reversed, traversing the point when the net flux in the air gap is zero. This is not the point where $-NI = 2ML_m$ but rather when $-NI > 2ML_m$. This has the effect of moving the minimum force location to a higher ampere-turn value than suggested in Eq. 3.3. This is illustrated in Fig. 3.23. At 0 ampere-turns the typical behavior is seen. As the ampere-turns are decreased the fringing flux increases in magnitude and starts to creep towards the center of the armature. The actuator reaches its minimum force condition around -1800 ampere-turns. At this point, there is still a significant amount of flux in the air gap due to the permanent magnet.

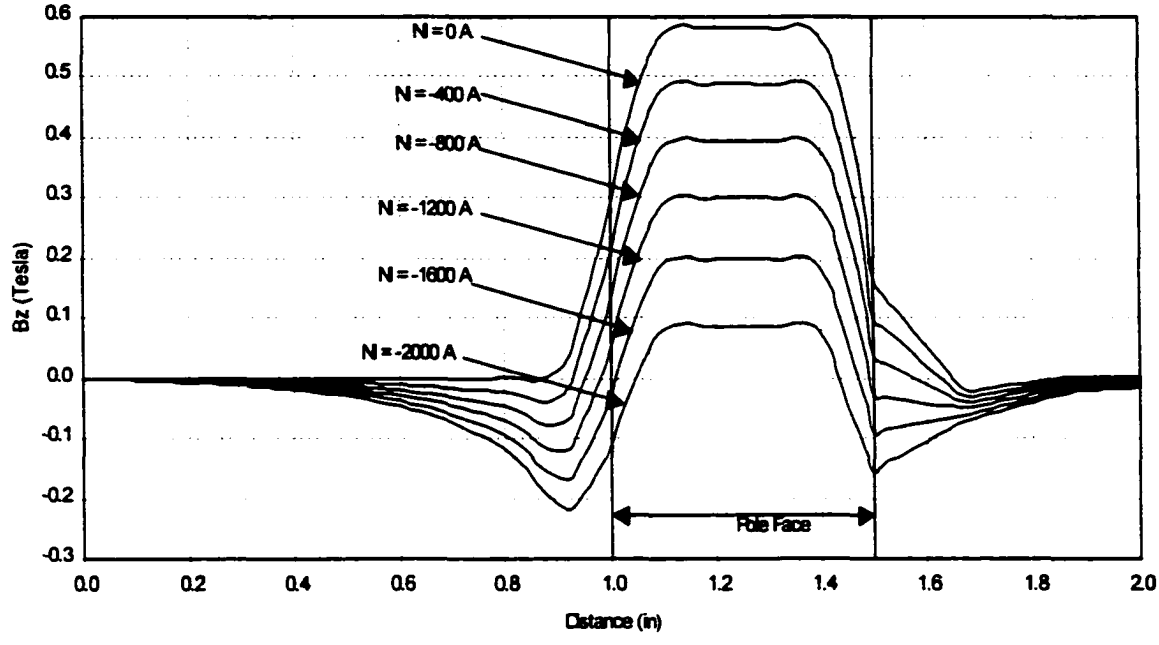

Figure 3.23: OPERA-3D Analysis of 2 Inch Stator With Windings and Magnets on Poles

This behavior is better demonstrated in Fig. 3.24 which shows the entire 3-D effect of the fringing flux. The figure shows B_y on the surface of the armature, over an area extending 0.25 inches beyond the pole face in the x and y directions. The side listed as 2 - 3 is the side that faces the center of the armature. If there was no fringing the plot would be rectangular in shape with no sloping surfaces. At zero ampere-turns, the sloping sides indicate the nominal flux fringing effects. As the ampere turns are decreased, the flux leakage begins to become apparent on the inside of pole face. The flux leakage on the interior of the armature increases with increased current. As the ampere-turns reach -1600 amps the flux leakage on the front and back of the stator begins to show. Finally, as the current reaches -2000 ampere-turns there is significant flux leakage on all sides of the pole.

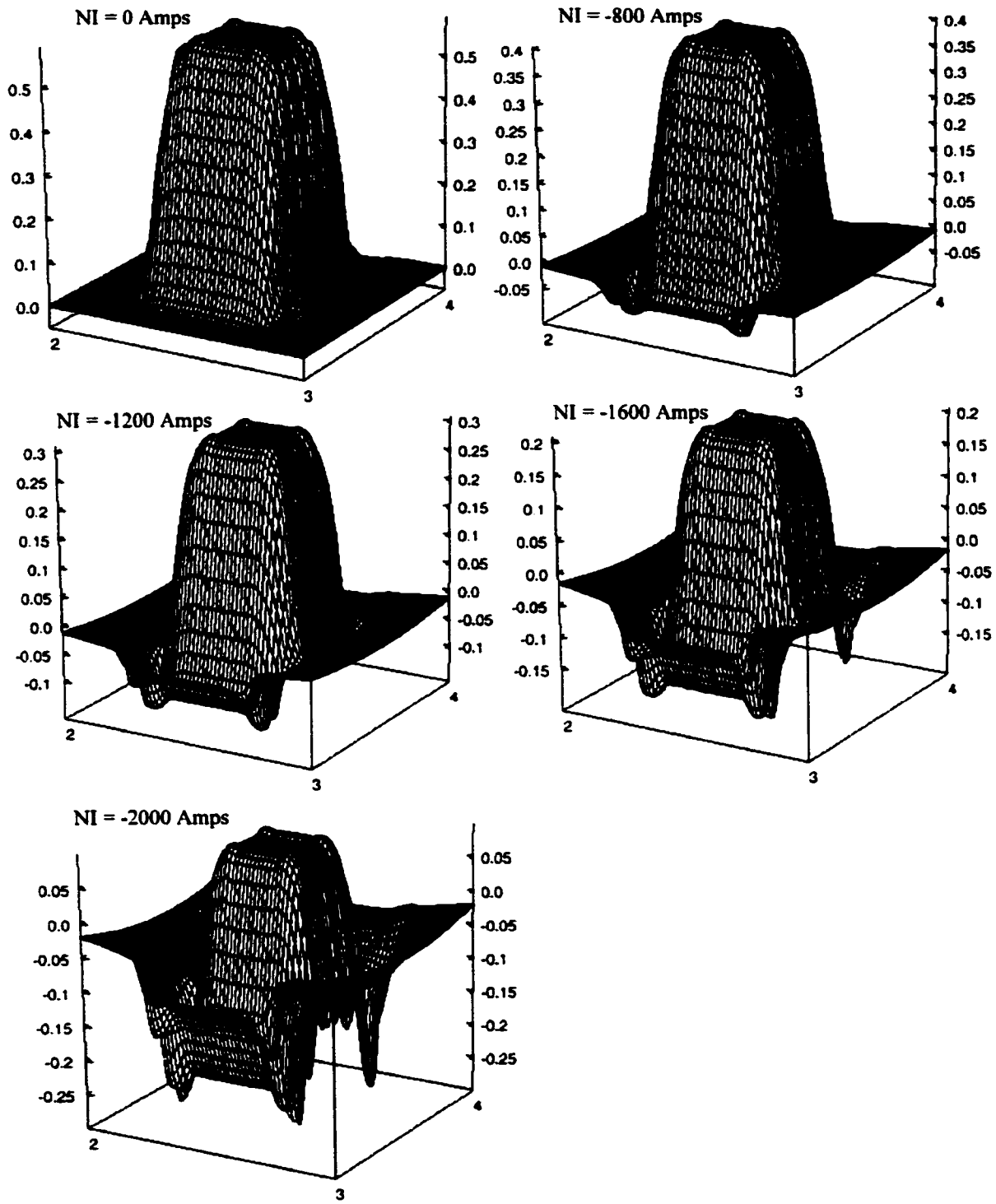

Figure 3.24: OPERA-3D Analysis of 2 Inch Stator with Magnets and Windings on Poles

The significance of this modeling error must be weighted according to the operating conditions of the magnetic bearing. Magnetic bearings are made up of sets of actuators, generally oriented in pull-pull configurations. As one actuator is working at 1000 ampere-turns the other is operating at -1000 ampere-turns. So if the minimum force condition were to be reached, it would mean that the magnetic bearing was operating at its maximum limit which is generally outside the design range of the application.

3.4.3. Comparison of Winding Locations with Permanent Magnets in Armature

There are four different configurations examined for this case, test numbers 7, 13, 20, and 26. The windings are wrapped around the back of the stator with the pole separation distance at both 2.0 inch and 4.5 inch. The experimental results are shown in Fig. 3.25. The percentage differences between the experimental results and the analytical model are shown in Fig. 3.26. The percentage differences below -1600 ampere-turns were not shown because the forces were very close to zero which made the error comparison meaningless. The data is tabulated in Tables A10-A13 in Appendix A.

The results show the same type of behavior as that with the magnets on the pole faces. The important point to notice is the percentage difference as compared with the magnets on the pole faces. The performance of all four actuator configurations deteriorated when the magnets were moved from the pole faces to the armature. It was shown in Section 3.3 that placing the permanent magnet on the pole faces is more efficient than placing them on the back of the stator when no coils were involved. In Section 3.4.1, it was shown that placing the windings on the poles is more efficient than placing them on the back

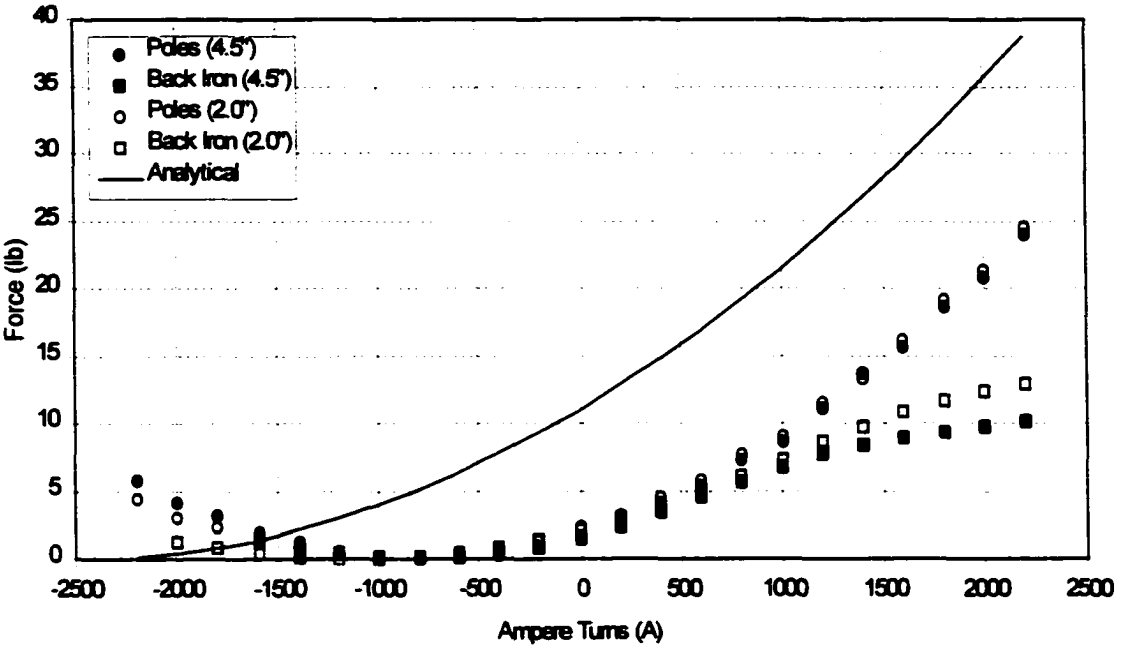

Figure 3.25: Experimental Comparison of Winding Location with the Magnet in the Armature

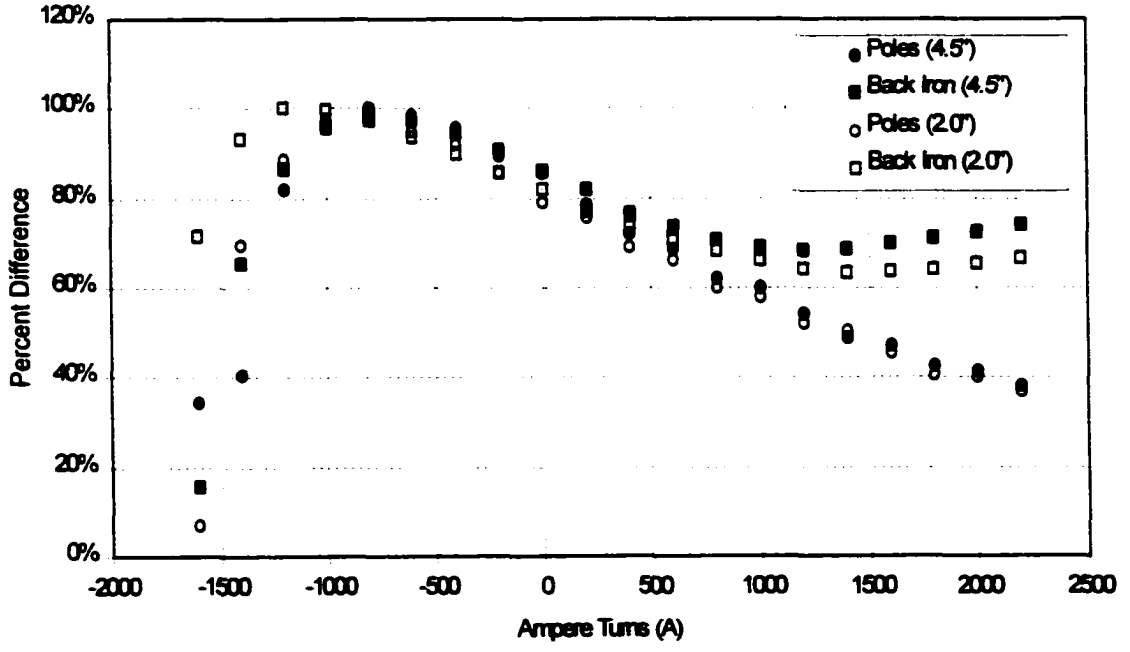

Figure 3.26: Percentage Difference Between Analytical Model and Experimental Results

iron when no permanent magnets were present. Thus, it should be no surprise that the performance of the actuator with the windings on the back iron and the permanent magnet in the armature shows the worst performance of all the cases discussed.

When the ampere-turns become negative, the force produced by the actuator does in fact go to zero. However, the minimum force location occurs at a lower ampere-turn value than expected. This is because of mmf leakage around the permanent magnet. The y-component of the flux density on the upper surface of the armature, with the magnet in the center of the armature, is shown in Fig. 3.27.

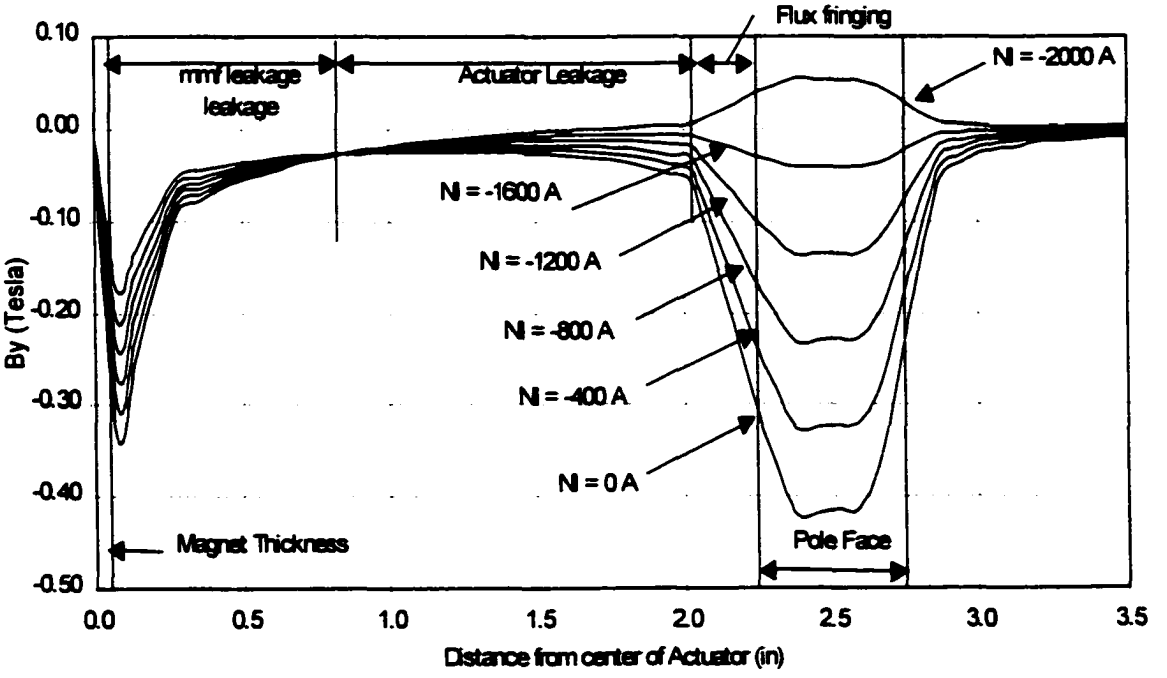

Figure 3.27: PC-OPERA Analysis of 4.5 Inch Stator with Windings on Back Iron and Magnet in Armature

When $NI = 0$ ampere-turns, the flux behaves similarly to that shown in Fig. 3.20 with the addition of the mmf leakage at the location of the permanent magnet. This mmf leakage is

the flux that is exiting the surface of the armature, looping around the permanent magnet, and returning to the magnet (as discussed in section 3.3.) The flux leaking around the permanent magnet does not contribute to the force between the armature and the stator.

As the ampere-turns are increased, the amount of mmf leakage increases while the amount of flux fringing at the air gap decreases. For this case, the analytical model accurately predicts the flux density in the air gap as being proportional to the difference between the two mmf sources. However, it does not account for the increased mmf leakage around the permanent magnet. This increased mmf loss can be explained by considering interaction between the magnet flux and the flux produced by the windings. The flux produced by the permanent magnet has the tendancy to leak out of the armature and create a loss to the system, as discussed in Section 3.3. As the ampere-turns are increased, the new flux is opposing the permanent magnet flux. As a result, the tendancy for the permanent magnet flux to cause an mmf loss is increased. The increase in mmf leakage results in the zero force location of the actuator being slightly shifted in the direction of positive ampere-turns.

3.4.4. Comparison of Winding Locations with Permanent Magnets in Armature And Pole Faces

There are four different configurations examined for this case, test numbers 6, 11, 19, and 24. The windings are wrapped around the poles or the back of the stator with the pole separation distance at both 2.0 inch and 4.5 inch. The experimental results are shown in Fig. 3.28. The percentage difference between the experimental results and the analytical model are shown in Fig. 3.29.

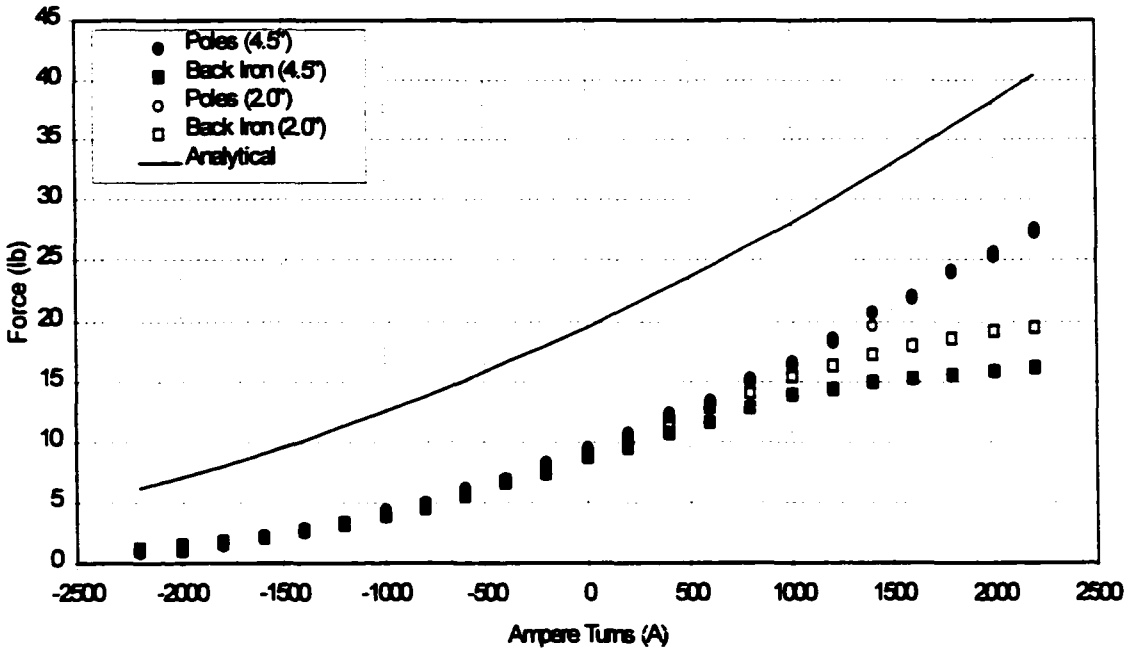

Figure 3.28: Experimental Comparison of Winding Locations with Magnets in the Armature and on the Pole Faces

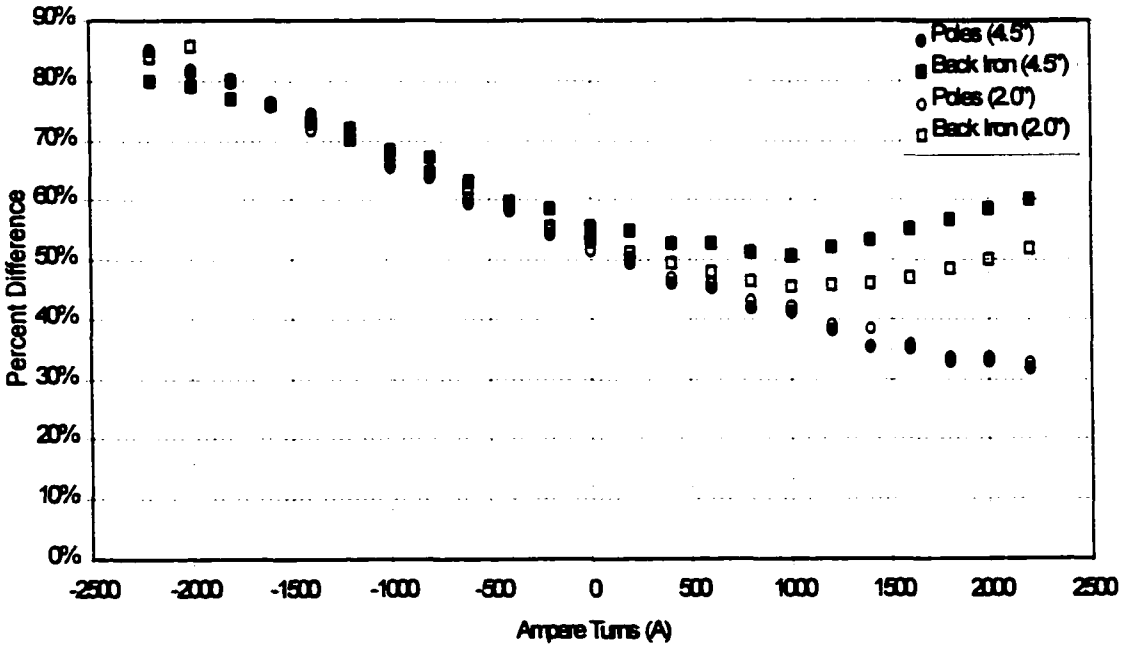

Figure 3.29: Percentage Difference Between Analytical Model and Experimental Results

The actuators with the magnets placed in both positions behaved similarly to those discussed in previous sections. These test results do not shed light on any new information about the actuator performance but reinforce previous results. The overall system performed better than that with the biasing magnet placed in the armature but not as well as with the magnets on the pole faces. This agrees with the result seen in Section 3.3. The actuator with the windings on the poles again outperformed the actuator with the windings on the back iron for all cases. These results could have been predicted based on the information discussed in Sections 3.3 and 3.4.1 - 4.

3.5. Discussion of Results

The overall performance of each of the 22 actuators discussed in this section are compared in Tables 3.3 and 3.4. The tables show the percentage difference in actuator performance and predicted performance at 2000 ampere-turns at an air gap of 0.05 inches. The percentage difference in force production is related to the field behavior and how well the assumptions discussed in Section 2 were met.

When comparing winding locations, placing the windings on the pole faces results in a higher performance actuator as compared to placing them on the back iron for all cases. When comparing magnet locations, placing the magnets on the poles results in a better performing actuator then when the magnets are placed in the armature or in both locations, for all cases. When comparing stator lengths, the shorter stator had lower losses than the longer one for all the cases other than with the windings on the pole faces, for which the results agreed to within ± 1%.

Winding Locations	Magnet Locations: None	Pole	Armature	Both
None		32%*	81%*	53%*
Poles	20%	25%	38%	32%
Back Iron	58%	48%	67%	52%

Table 3.3: Percentage Difference in 2" Actuator at NI = 2000 A and L_g = 0.05 inch. * 0 Ampere-turns

Winding Locations	Magnet Locations: None	Pole	Armature	Both
None		36%*	86%*	56%*
Poles	19%	26%	37%	33%
Back Iron	69%	59%	74%	60%

Table 3.4: Percentage Difference in 4.5" Actuator at NI = 2000 A and L_g = 0.05 inch. * 0 Ampere-turns

Another performance indicator for a magnetic bearing is the current stiffness. The experimental data can be used to determine how the magnetic actuators would behave if they were placed in a pull-pull configuration on a single armature. In this configuration, the force-current relationship is linear so the current stiffness measured at zero ampere-turns is representative of the entire operating range. The current stiffness for each of the actuators

is listed in Table 3.5. The results mirror those shown in Tables 3.3 and 3.4. The optimum magnet location is on the pole faces and the optimum winding location is on the poles, for this set of variations.

			Magnet Locations		
			Poles	Armature	Both
Winding Location	2.0"	Poles	13.7	9.2	12.3
		Back Iron	13.1	7.6	11.8
	4.5"	Poles	13.7	8.9	12.6
		Back Iron	11.4	7.3	10.2

Table 3.5: Current Stiffness at 0 Ampere-Turns(10^{-3} Lb/A)

While the overall performance of an actuator is dependent upon many factors, the magnet location and winding locations can be analyzed separately. Placing the magnets on the pole faces aids the actuator performance in several ways. The magnetization of the magnets directs the flux across the air gaps at an optimum angle, normal to the pole face. The flux leakage between the armature and the stator is minimized because the flux travels down the pole faces instead of jumping between the stator and armature. The redirection mechanism that causes the mmf losses with the magnet placed in the armature is removed by removing the iron from one side of the magnets.

When the magnets are placed in the armature, the mmf loss can be considerable. Additionally, the flux leakage between the stator and armature can now affect the performance of the actuator. In all cases, the experimental performance with the permanent magnets in the armature was much less than that with the magnets on the poles.

When the permanent magnets were placed on the pole faces and in the armature, the performance increased from that with just the magnets in the armature, but decreased as compared with having the magnets on the pole faces. The performance of the composite actuator took on the average of the two individual performance levels.

The placement of the windings plays an important role in the overall performance of the system. Placing the windings on the poles reduced the flux leakage between the armature and the stator. It also helped to focus the flux in the pole pieces which aided the flux density when crossing the air gap. For these tests the pole height was set to 1 inch so that windings could be placed on both the pole pieces and on the back iron. Generally, when the windings are placed on the back iron, the pole height is set by the outer radius of the windings. For this case, that would have reduced the pole height to about 0.5 inches, which would cause the flux leakage between the armature and the stator to increase.

The length of the stator can play an important role depending on the actuator configuration. When the windings were placed on the back iron the stator length became very important. The longer the stator the more surface area there was for flux leakage to occur between the stator and the armature. When the windings were placed on the pole pieces there was little to no difference due to the stator length.

3.6. Design Guidelines

Several important design guidelines can be drawn from the experimental testing discussed in this section. The guidelines concern the location of the biasing permanent magnet, the location of the control windings, and the length of the iron path. These design considerations can have a significant effect on the performance of the system.

The permanent magnets should be placed on the pole faces of the stator rather than other locations within the iron circuit. This is due to two primary effects. First, having a region of low permeability on one side of the permanent magnet decreases mmf losses. Second, the field shaping effects of the permanent magnet help to reduce flux leakage at the air gap. The actuator geometries that were tested had a pole height of 1 inch, larger then typical pole heights in similar commercial designs. Thus, the effects of mmf leakage would most likely be more significant then illustrated in this set of tests.

The location of the permanent magnets lead to additional considerations concerning the protection of the soft magnet material. When a permanent magnet is placed on a pole face it is at risk of being damaged from accidental contact with the rotor. A common technique used to prevent this is to place a thin ferrous cap on the surface of the permanent magnet. This cap can reduce the field shaping benefits of the permanent magnet and increase mmf losses. To avoid this, the cap should be very thin and possibly have a low permeability. Further testing is needed in order to determine the optimal configuration.

The windings should be located on the pole pieces. In many commercial magnetic bearing designs the windings are placed on the rear of the stator due to space limitations. Prior to this research, little was published on the effect of winding locations so there was no motivation to increase the geometric complexities by placing the windings on the poles. This experimental analysis shows how important winding location can be to the performance of a magnetic actuator or magnetic bearing.

It is also recommended to keep the flux path through the iron as short as possible. If the permanent magnets are located on the pole faces and the windings are wrapped around the poles, there is only a slight decrease in performance due to increases in the flux path length. However, if the system is not designed as previously indicated, the losses due to the iron flux path can have noticeable affects of the performance of the system.

It should be noted again that the considerations discussed in this section are due to experimental analysis and are not discernable from classical modeling techniques. It might be tempting to ignore these suggestions due to other considerations, but that would most certainly reduce the performance level and the efficiency of the system. The lack of "robustness" in the classical modeling methods is discussed in the following sections.

4. EXTENDED CIRCUIT THEORY

The fundamental behavior of magnetic bearings and magnetic actuators is captured in classical magnetic circuit theory. There are, however, several assumptions associated with the theory that can cause large differences between theoretical performance and actual performance. The four basic assumptions previously discussed in Section 2.5. are:

1. There is no fringing or leakage flux
2. There are no actuator mmf losses
3. The reluctance losses in the iron flux path are negligible
4. There is no flux saturation anywhere within the circuit

This research extends classical magnetic circuit theory by taking into account the factors which violate the above assumptions, increasing the accuracy of the model. The additional loss terms introduced by relaxing the above assumptions are included as new variables in the extended circuit model [Groom, 2000].

4.1. Theoretical Development

The classical magnetic circuit model was discussed in Section 2.5 and shown in Fig. 2.2. A more realistic system model is introduced in Fig. 4.1, with three new flux paths illustrated. There is a flux loss around the coil, a flux loss around the permanent magnets, and a leakage flux path at the air gaps. The losses at the coil and at the biasing magnets represent a mmf loss, equivalent to a voltage loss in an electric circuit. The flux produced by the source leaks around the source via a flux path in the air and does not cross the air gaps. As a result, there appears to be less mmf acting within the system. At the air gaps a new flux path has been introduced that accounts for the fringing flux. There is a finite amount of flux passing through the circuit so any flux which follows the fringing path results in a loss from the flux

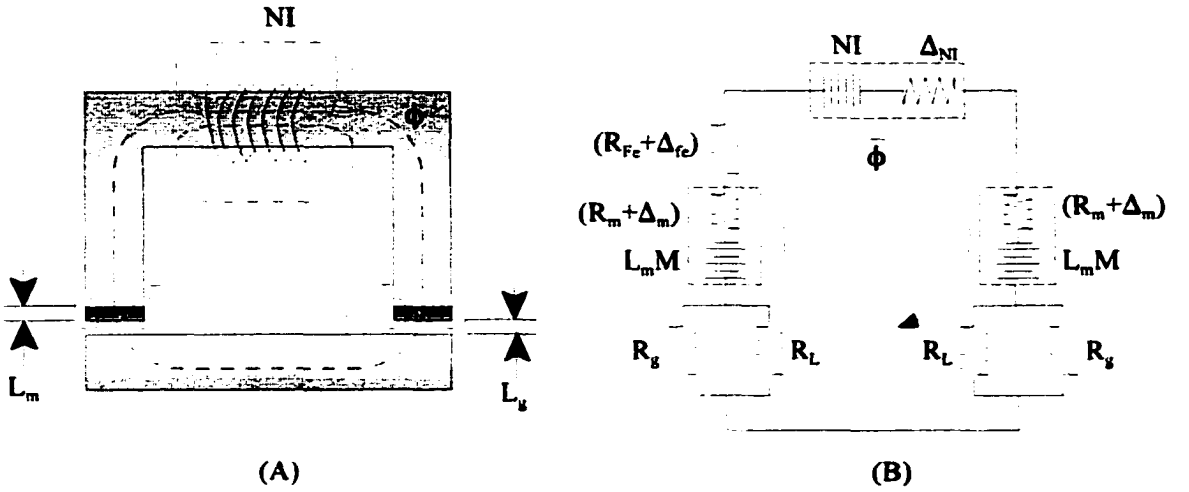

(A) (B)

Figure 4.1: Model of Actuator and Extended Magnetic Circuit

crossing between the pole faces. The apparent length of the air gap of the leakage path is significantly larger than that between the pole faces, resulting in a reduction of force.

The changes in the magnetic actuator in Fig. 4.1a are modeled in the magnetic circuit shown in Fig. 4.1b. The mmf losses are modeled by an increase in reluctance at the mmf source. The net reluctance of the permanent magnets is increased by the amount Δ_m and a reluctance associated with the ampere-turns is given by Δ_{NI}. The introduction of the leakage path at the air gaps decreases the reluctance, modeled as a reluctance being added in parallel.

In order for the linear model to be valid the flux must not saturate within the circuit. However, there are generally small regions where the flux density comes close to saturating. As discussed in section 2.2.6, saturation has the result of increasing the reluctance of the iron path. To account for this slight increase in reluctance due to concentrations of flux saturation, the reluctance of the iron has also been increased by the amount Δ_{fe}.

Summing the mmf sources around the loop yields,

$$NI + 2ML_m = 2\phi \frac{R_L R_g}{R_g + R_L} + 2\phi(R_m + \Delta_m) + \phi(R_{fe} + \Delta_{fe}) + \phi\Delta_{NI} \tag{4.1}$$

The value of reluctance, defined in Eq. 2.7, is dependent upon the geometry of the region. For the cases of Δ_m, Δ_{fe}, Δ_{NI}, and R_L there are no geometries to consider. However, it is reasonable to assume that these changes in reluctance can be linearly related to the overall reluctance as in Eq. 4.2.

$$\Delta_j = k_j R_j \qquad j = NI, m, Fe \tag{4.2}$$

According to this definition, k_i represent the relative proportion of R_i that makes up Δ_i. Thus, when k_i equals zero, there are no additional losses. The reluctance of the leakage path is expressed using the equivalent to current division in an electrical circuit. For the flux leakage to vanish the reluctance R_L must increase to infinity. In this case $R_L = k_g R_g$ where k_g is very large. Substituting these changes into Eq. 4.1 and rearranging terms results in,

$$\phi = \frac{NI(1 - k_i) + 2ML_m}{\frac{2k_g}{1 + k_g} R_g + 2(k_m + 1)R_m + (k_{fe} + 1)R_{fe}} \tag{4.3}$$

At this point, several changes should be examined. First, ϕ is the flux crossing between the poles at the air gap, where the fringing flux has been taken into account separately. Second, the iron loss term has now been increased to a point where it is not possible to simply neglect the term on the basis of relative magnitudes. To account for these changes the equation can be divided through by the constant (k_{fe} +1), resulting in Eq. 4.4.

$$B_g = \frac{\mu_0\left(K_i NI + \frac{2B_r L_m}{\mu_0}\right)}{K_a \frac{2}{\mu_g} L_g + K_F \frac{2}{\mu_m}\frac{A_g}{A_m} L_m + \frac{1}{\mu_{fe}}\frac{A_g}{A_{fe}}} \tag{4.4}$$

Where,

$$K_i = \frac{1-k_i}{1+k_{fe}} \quad K_a = \frac{k_g}{(1+k_g)(1+k_{fe})} \quad K_F = \frac{1+k_m}{1+k_{fe}} \tag{4.5}$$

An additional coefficient could have been placed in front of the permanent magnet term in the numerator. It would have simply been $(1 + k_{fe})^{-1}$. However, since the bulk of the circuit must remain linear for this formulation to be valid, this term will remain very close to one. So, it has been neglected in order to limit the number of unknowns. This assumption is validated in Section 4.2.1.

Eq. 4.4 is identical to Eq. 2.10 when K_a, K_i, and $K_F = 1$. Thus, when the coefficients are one the system behaves according to classical circuit theory. The magnitude in variation from one is a measure of how much the assumptions in classical circuit theory have been violated. Substituting Eq. 4.4 into Maxwell's stress tensor results in the force formulation for the extended circuit model.

$$F = \frac{\mu_0 A_g\left(K_i NI + \frac{2B_r}{\mu_0} L_m\right)^2}{\left(\frac{2K_a}{\mu_g} L_g + \frac{2K_F}{\mu_m}\frac{A_g}{A_m} L_m + \frac{1}{\mu_{Fe}}\frac{A_g}{A_{Fe}} L_{Fe}\right)^2} \tag{4.6}$$

The extended model for the case of a non-biased magnetic actuator can be determined directly from Eq. 4.6 by setting L_m to zero.

$$F = \frac{\mu_0 A_g (K_i NI)^2}{\left(\frac{2K_a L_g}{\mu_g} + \frac{1}{\mu_g} \frac{A_g}{A_{fe}} L_g \right)^2} \tag{4.7}$$

It should be noted that if the iron loss term is neglected then K_i is no longer independent of K_a and they must be combined into a new loss coefficient, $K_L = K_i / K_a$.

4.2. Determination of Loss Coefficients

The loss coefficients in Eq. 4.6 cannot be calculated analytically; they must be determined using finite element computations or empirically by experimental measurements. The first step is to determine the variation of force with displacement. This is done by setting the ampere-turns in Eq. 4.6 to zero. The equation can then be arranged in the form,

$$\underbrace{\begin{bmatrix} \frac{2L_g}{\mu_g} & \frac{2L_m}{\mu_m} \frac{A_g}{A_m} \end{bmatrix}}_{[L]} \underbrace{\begin{Bmatrix} K_a \\ K_F \end{Bmatrix}}_{\{K\}} = \underbrace{\left(\sqrt{\frac{\mu_0 A_g}{F}} \frac{2B_r L_m}{\mu_0} - \frac{1}{\mu_{fe}} \frac{A_g}{A_{fe}} L_{fe} \right)}_{\{r\}} \tag{4.8}$$

Using the information collected from finite element analysis or experimental data, the results can be inserted into Eq. 4.8 to form a set of n equations. The more reference points that are used the more accurate the model. Using this set of n reference points, Eq. 4.8 can be written in matrix form.

$$\begin{bmatrix} \lfloor t_1 \rfloor \\ \vdots \\ \lfloor t_n \rfloor \end{bmatrix} \begin{Bmatrix} K_a \\ K_F \end{Bmatrix} = \begin{Bmatrix} r_1 \\ \vdots \\ r_n \end{Bmatrix} \tag{4.9}$$

or,

$$\underbrace{[T]}_{n\times 2}\underbrace{\{K\}}_{2\times 1} = \underbrace{\{R\}}_{1\times n} \tag{4.10}$$

The matrix $[T]$ is a generally a non-square matrix, which means the vector $\{K\}$ cannot be solved for directly by inverting $[T]$. Instead, the generalized inverse, or pseudo-inverse can be used [Penrose, 1955]. When the matrix is over-determined, as in this case, the generalized inverse has the properties of minimizing the error between all n reference points in a least squares sense. The solution for $\{K\}$ then becomes,

$$\{K\} = [T]^{\#}\{R\} \tag{4.11}$$

Where the generalized inverse (for an over-determined system) is defined as,

$$[T]^{\#} = \left([T]^T[T]\right)^{-1}[T]^T \tag{4.12}$$

Having calculated K_a and K_F, the variation of force with ampere-turns can now be used to determine K_r. Eq. 4.6 can be written in the form of Eq. 4.13.

$$NIK_r = \sqrt{\frac{F}{\mu_0 A_g}}\left(\frac{2K_a L_g}{\mu_g} + \frac{2K_F}{\mu_m}\frac{A_g}{A_m}L_m + \frac{1}{\mu_{fe}}\frac{A_g}{A_{fe}}L_{fe}\right) - \frac{2B_r L_m}{\mu_0} \tag{4.13}$$

Using finite element results or experimental data, a set of force vs ampere-turns results can be inserted into Eq. 4.13 to develop a set of *m* equations.

$$\begin{Bmatrix} NI_1 \\ \vdots \\ NI_m \end{Bmatrix} K_I = \begin{Bmatrix} \sqrt{\frac{F_1}{\mu_0 A_g}} \\ \vdots \\ \sqrt{\frac{F_m}{\mu_0 A_g}} \end{Bmatrix} \left(\frac{2K_a L_g}{\mu_g} + \frac{2K_F A_g}{\mu_m A_m} L_m + \frac{A_g}{\mu_{fe} A_{fe}} L_{fe} \right) - \frac{2B_r L_m}{\mu_0} \begin{Bmatrix} 1 \\ \vdots \\ 1 \end{Bmatrix} \tag{4.14}$$

The coefficient K_I is found using the generalized inverse following the same procedures discussed in the determination of K_a and K_F. The coefficient could be found using a single reference point, but the more points that are used the more representative the solution is of the actual system. Care should be taken in choosing the points used to calculate K_I. At low ampere-turns, the value of K_I will not have much effect on the system because it is multiplied by $NI \approx 0$. If too high a value of NI is chosen the flux density may have saturated, which will corrupt the solution.

If there is no permanent magnet biasing then Eq. 4.8 and 4.13 cannot be solved independently. The loss factors must be determined from Eq. 4.7, which is written in matrix form as,

$$\begin{bmatrix} \frac{2L_g}{\mu_g} & -NI\sqrt{\frac{\mu_0 A_g}{F}} \end{bmatrix} \begin{Bmatrix} K_a \\ K_I \end{Bmatrix} = \begin{Bmatrix} L_{fe} & A_g \\ \mu_{fe} & A_{fe} \end{Bmatrix} \tag{4.15}$$

The right hand side of Eq. 4.15 is very close to zero. This will cause the loss factors K_a and K_I to go to zero, a trivial solution. As a result, when no permanent magnet biasing is used the iron loss term must be neglected. This results in K_a and K_I being combined into $K_L = K_I/K_a$.

$$\left[\frac{NI\mu_g}{2L_g}\right]\{K_L\} = \left\{\sqrt{\frac{F}{\mu_0 A_g}}\right\} \tag{4.16}$$

A consequence of combining the two loss factors is that the variation with air gap distance and the variation with ampere-turns is no longer independent. The value of K_L must be determined for each air gap distance.

4.2.1. Iron Losses

The determination of whether or not to include the iron loss term when using classical circuit theory was discussed in Section 2.5.3 using the parameter κ. The same formulation can be used for extended circuit theory, where the definition of κ is found to be,

$$\kappa = K_a\left(\frac{\mu_{fe}}{\mu_g}\frac{L_g}{L_{fe}}\frac{A_{fe}}{A_g}\right) + K_F\left(\frac{\mu_{fe}}{\mu_m}\frac{L_m}{L_{fe}}\frac{A_{fe}}{A_m}\right) \tag{4.17}$$

The definition of κ for a non biased actuator is found by setting L_m equal to zero in Eq. 4.17. Using Eq. 2.14 or Fig. 4.2, the percentage difference in neglecting iron losses can be determined. It turns out, however, that when the generalized inverse is introduced into the system the iron loss term can always be neglected without introducing any error. This can be seen by examining Eq. 4.8. If the iron loss term is neglected then the denominator changes. If the denominator with the iron loss term neglected were to remain equal to the denominator with the iron loss term present, then no error would be introduced by neglecting the iron losses. The loss factors calculated from Eq. 4.8 are defined as,

$$\begin{aligned} \{K\} &= \left([T]^T[T]\right)^{-1}[T]^T\left(\{R\} - \{R_{fe}\}\right) \quad L_{fe} > 0 \\ \{\bar{K}\} &= \left([T]^T[T]\right)^{-1}[T]^T\{R\} \qquad\qquad L_{fe} = 0 \end{aligned} \tag{4.18}$$

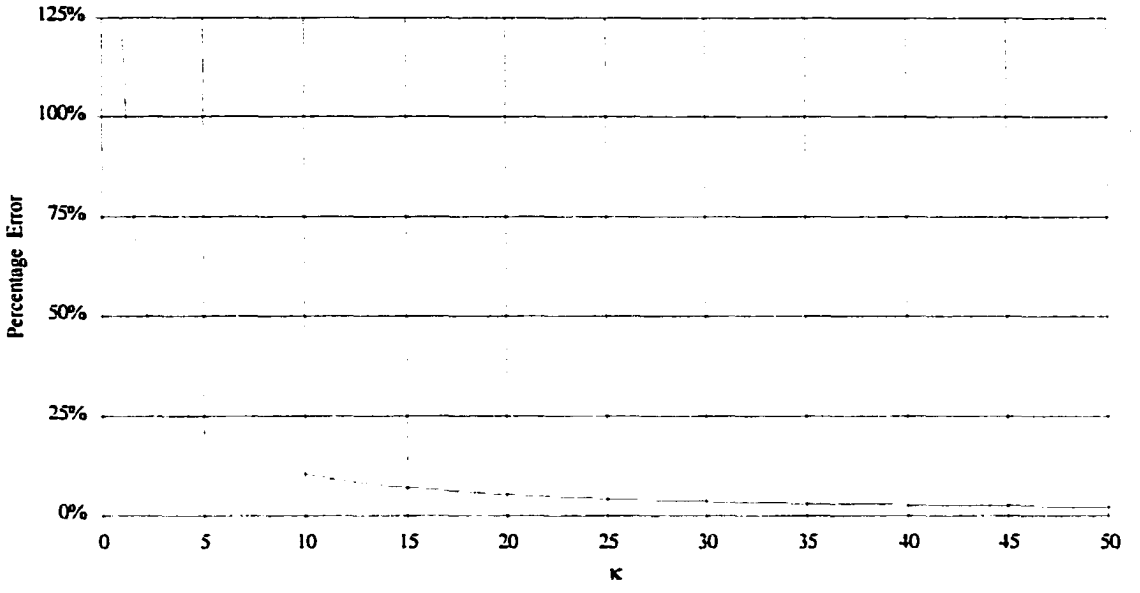

Figure 4.2: Percentage Error in Computed Force Due to Neglecting Iron Losses

Where $\{R\}$ is defined in Eq. 4.10 with the iron loss term set to zero, and $\{R_{fe}\}$ is the vector representing the iron loss term, $L_{fe}A_g/\mu_f A_{fe}$. Substituting Eq. 4.18 into Eq. 4.6 where $\lfloor T_i \rfloor$ is defined in Eq. 4.8, and temporarily mixing matrix notation yields,

$$F = \frac{\mu_0 A_g \left(\frac{2B_r L_m}{\mu_0}\right)^2}{\left(\lfloor T_i \rfloor ([T]^T[T])^{-1}[T]^T\{R\} - \lfloor T_i \rfloor ([T]^T[T])^{-1}[T]^T\{R_{fe}\} + R_{fe}\right)^2} \qquad L_{fe} > 0$$

$$F = \frac{\mu_0 A_g \left(\frac{2B_r L_m}{\mu_0}\right)^2}{\left(\lfloor T_i \rfloor ([T]^T[T])^{-1}[T]^T\{R\}\right)^2} \qquad L_{fe} = 0 \tag{4.19}$$

Examining the terms in the denominators show that the two systems will be identical at the i^{th} data point if,

$$\lfloor T_i \rfloor ([T]^T[T])^{-1}[T]^T\{1\}R_{fe} = R_{fe} \tag{4.20}$$

where the vector $\{1\}$ is a vector of ones with the same number of rows as $[T]$. Applying this condition to every data point results in,

$$[T]\left([T]^T[T]\right)^{-1}[T]^T\{1\} = \{1\} \tag{4.21}$$

Pre-multiplying both sides by $[T]^T$ results in,

$$\begin{gathered}\left([T]^T[T]\right)\left([T]^T[T]\right)^{-1}[T]^T\{1\} = [T]^T\{1\} \\ [T]^T\{1\} = [T]^T\{1\}\end{gathered} \tag{4.22}$$

Thus, the least-squares behavior of the generalized inverse will modify the loss factors when the iron loss term is neglected to make the two formulations equal. Additionally, examination of Eq. 4.6 shows that K_i will be independent of including or excluding the iron loss term. Hence, in extended circuit theory the iron losses can be accounted for in K_a and K_F.

4.3. Quality Factor

It is useful to develop a quantity that can be used to relate the overall quality of one actuator design to that of another. A quality factor can be developed to relate the three loss coefficients to actuator performance. Here, the quality factor will be based on the current stiffness of an actuator pair. In an actual magnetic bearing the magnetic actuators typically act in a pull-pull configuration [Groom, 1979]. In this configuration, the force acting on the suspended element is linearized with respect to current. The ratio of the force output to the current input is the current stiffness. This can be seen by taking the actuator in Section 3.4 and summing the $+NI$ and $-NI$ force results, emulating a pull-pull configuration with

identical actuators. The predicted net force acting on the suspended element is that shown in Fig. 4.3.

The extended circuit model results in designs that are predictably not as stiff as indicated by classical magnetic circuit theory. If the actuator performed perfectly with no losses then the two results would overlay. Thus, the ratio between the slope of the extended circuit model to the classical circuit model can be used to indicate the overall quality of the actuator performance. A well designed actuator will have a quality factor close to 1 while a poorly designed actuator will be closer to 0.

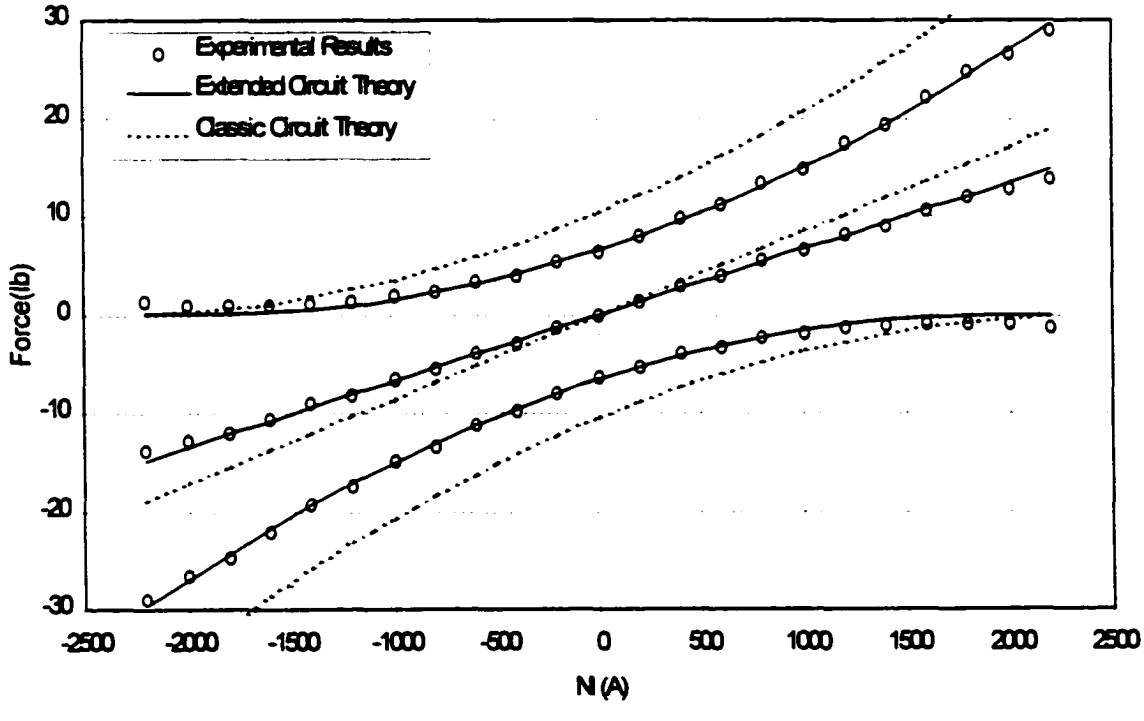

Figure 4.3: Prediction Based on Experimental Results of Test-17 in a Pull-Pull Configuration

The force for this configuration is derived from Eq. 4.6 placed in a pull-pull configuration. Where,

$$\begin{aligned} L_{g1} &= (x_0 - x) \\ L_{g2} &= (x_0 + x) \\ I_1 &= i \\ I_2 &= -i \end{aligned} \qquad (4.23)$$

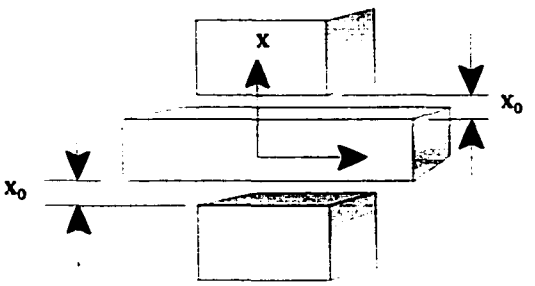

Figure 4.4: Geometry of Pull-Pull Configuration

This results in,

$$F = F_1 - F_2 = \frac{\mu_0 A_g}{4} \frac{\left(K_i N I_1 + \frac{2 B_r L_m}{\mu_0} \right)^2}{\left(K_a L_{g1} + K_F L_m \right)^2} - \frac{\mu_0 A_g}{4} \frac{\left(K_i N I_2 + \frac{2 B_r L_m}{\mu_0} \right)^2}{\left(K_a L_{g2} + K_F L_m \right)^2} \qquad (4.24)$$

Substituting Eqs. 4.23 into 4.24 and rearranging results in,

$$F = \frac{A_g \mu_0}{4} \left[\left(\frac{\left(K_i N i + 2 B_r L_m / \mu_0 \right)}{K_a (x_0 - x) + K_F L_m} \right)^2 - \left(\frac{\left(2 B_r L_m / \mu_0 - K_i N i \right)}{K_a (x_0 + x) + K_F L_m} \right)^2 \right] \qquad (4.25)$$

The stiffness of the magnetic bearing with respect to current can be found by taking the derivative of Eq. 4.25 with respect to *Ni*. This is referred to as the electromagnetic gain.

$$K_B = \frac{\partial F}{\partial N i} = \frac{A_g \mu_0 K_i}{2} \left(\frac{K_i N i + 2 B_r L_m / \mu_0}{\left(K_a (x_0 - x) + K_F L_m \right)^2} + \frac{2 B_r L_m / \mu_0 - K_i N i}{\left(K_a (x_0 + x) + K_F L_m \right)^2} \right) \qquad (4.26)$$

The current stiffness is linear, so any ampere-turn value can be chosen to determine K_B. Choosing $Ni = 0$ ampere-turns at the operating air gap distance, $x = 0$, results in Eq. 4.27.

$$K_B \big|_{x=0} = \frac{2 K_i A_g B_r L_m}{\left(K_a x_0 + K_F L_m \right)^2} \qquad (4.27)$$

The current stiffness for the classical magnetic circuit model is found by setting the loss coefficients in Eq. 4.27 to 1. Taking the ratio of the classical model current stiffness and the extended model current stiffness results in the actuator performance quality factor.

$$Q = \frac{K_{B.Classical}}{K_{B.Extended}} = K_i \frac{(x_0 + L_m)^2}{(K_a x_0 + K_F L_m)^2} \tag{4.28}$$

This quality factor represents the percentage difference between the current stiffness of the classically predicted model and the enhanced model. This can be used to relate one bearing configuration to another with respect to the permanent magnet thickness. If the permanent magnet thickness is different from one configuration to another, this comparison will not be useful. When no biasing magnets are used, the quality factor is found by setting $L_m = 0$ in Eq. 4.23, which results in $Q = K_i / K_a = K_L$.

4.4. Comparison of Experimental Results with Theory

The formulations developed in Sections 4.1 - 4.3 can be verified by comparing the experimental data in Section 3 to the extended circuit model. Three sets of configurations exist that require three different sets of loss coefficients. They are the non-biased actuators, passive actuators with no control windings, and the complete actuator with both permanent magnet biasing and control windings. The three cases will be discussed in Sections 4.4.1. - 4.4.3.

4.4.1. Passive Actuators

This section compares the experimental results of the passive magnetic actuator of Section 3.3 (tests 3, 8, 12, 16, 21, and 25, i.e., no control windings) to extended circuit theory. The

loss factors K_a and K_f are calculated from Eq. 4.8 using the experimental data points from L_g = 0.005 inch to 0.07 inch. The loss factors for the six tests along with the quality factors are given in Table 4.1.

Test Number	Magnet(s) Location	Stator Length	Loss Coefficients K_a	K_f	K_i	Q
3	Poles	4.5"	1.362	1.228	-	0.596
8	Armature	4.5"	3.258	2.249	-	0.132
12	Both	4.5"	2.083	1.293	-	0.351
16	Poles	2.0"	1.311	1.191	-	0.639
21	Armature	2.0"	2.623	2.009	-	0.186
25	Both	2.0"	2.013	1.255	-	0.375

Table 4.1: Loss Factors of Passive Actuators

The results of the 4.5 inch actuators with the magnets on the poles and in the armature are shown in Fig. 4.5 and the results with the magnets in both locations are shown in Fig. 4.7. The error between the experimental data and the classical and extended models is given in Figs. 4.6 and 4.8. It is clear from the figures that extended circuit theory models capture the behavior of the magnetic actuators much better than classical circuit theory. The addition of the two loss coefficients allows the model to capture the mmf leakage and flux fringing, along with the iron losses. The quality factors indicate that the best performing actuators are with the magnets on the poles, next best is with the magnets on the poles and in the armature, and the worst performance is with the magnets in the armature. Also, the 2.0 inch actuator outperforms the 4.5 inch for all cases. These conclusions agree with the results presented earlier in Tables 3.3 and 3.4. Thus, the quality factor does qualitatively rate the performance of the passive actuator.

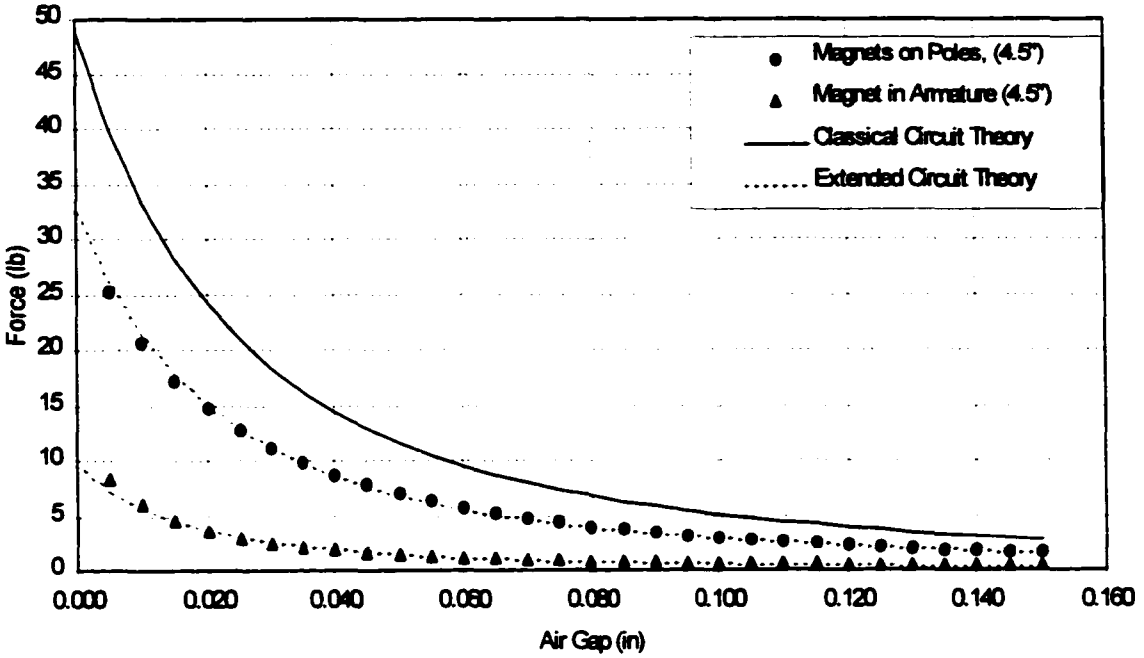

Figure 4.5: Comparison of Extended Circuit Theory to Experimental Data (Test 3 & 8)

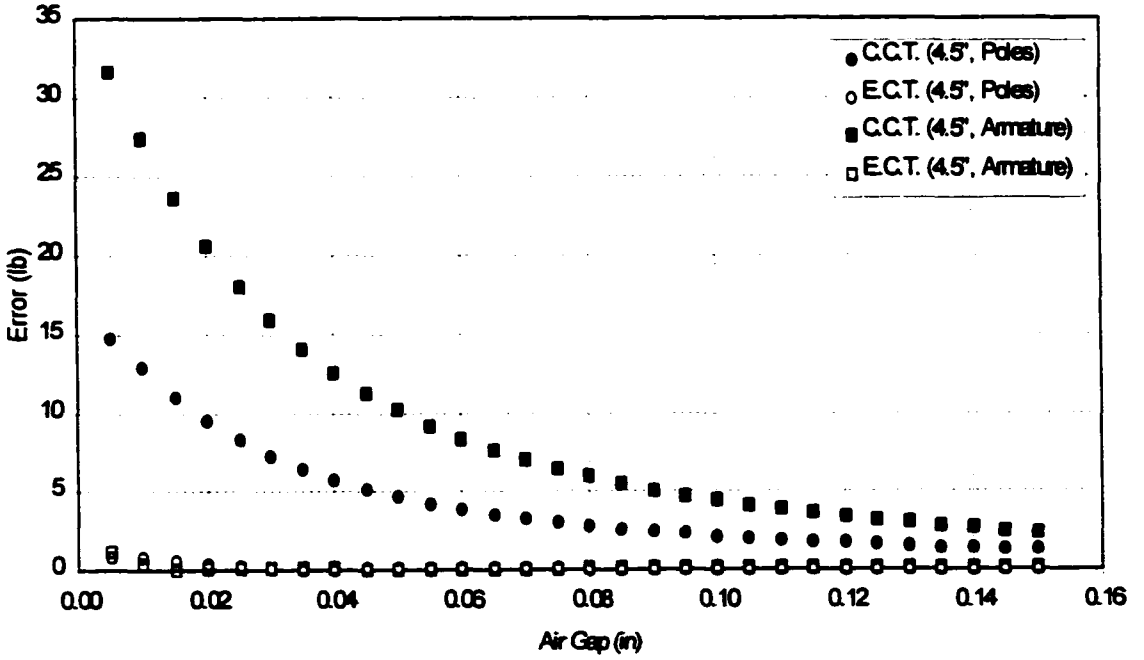

4.6: Error Comparison Between Classical and Extended Circuit Theory (Tests 3 & 8)

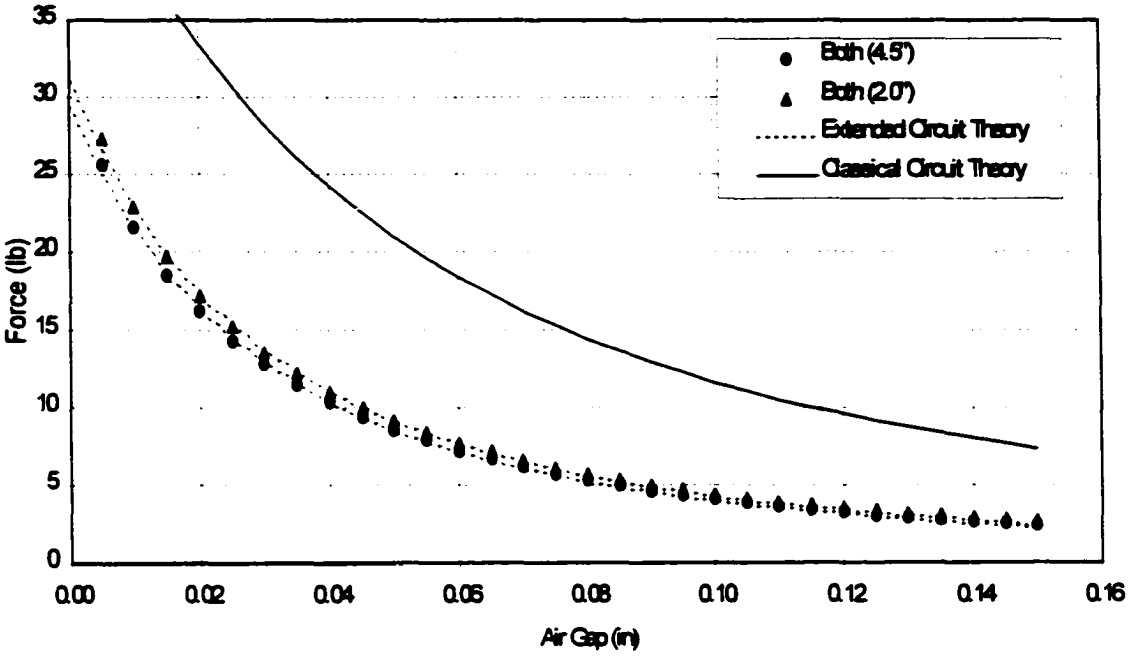

Figure 4.7: Comparison of Extended Circuit Theory to Experimental Results (Tests 12 & 25)

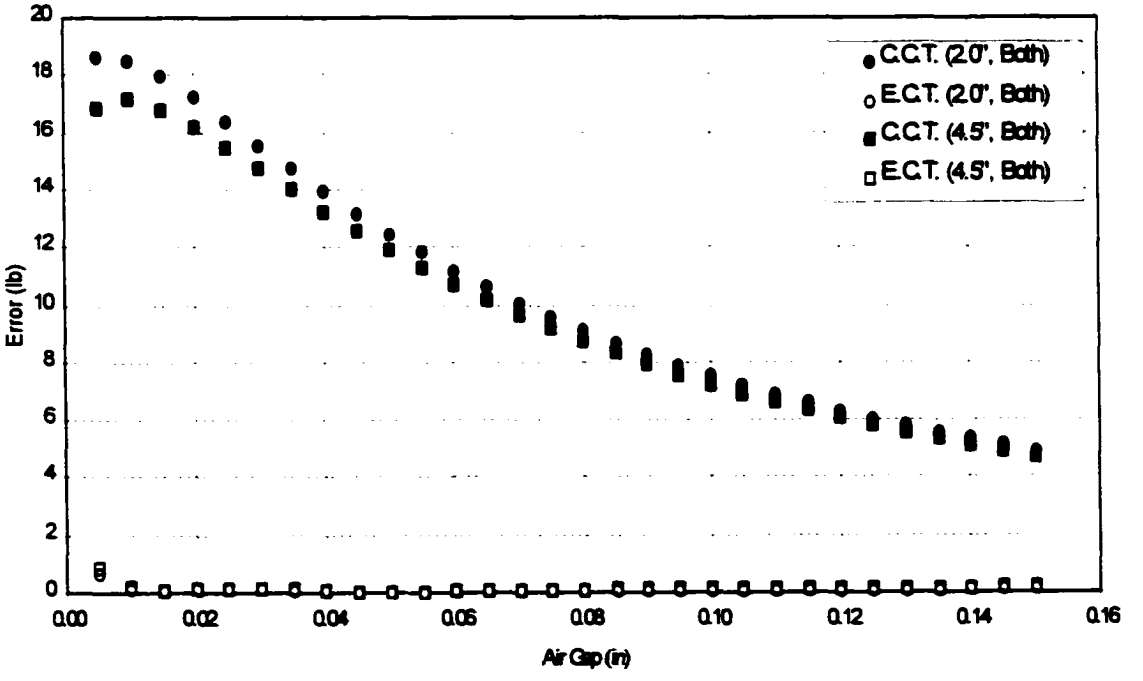

Figure 4.8: Error Comparison of Classical and Extended Circuit Theory (Tests 12 & 25)

4.4.2. Active Actuators with Biasing Permanent Magnets

This section compares the experimental results of the active magnetic actuators biased with permanent magnets in Sections 3.4.2 - 3.4.4 to extended circuit theory. The loss factors K_a, K_f, and K_i are calculated from Eqs. 4.8 and 4.14. The test numbers, loss factors, and quality factors for the twelve tests are given in Table 4.2.

Test Number	Magnet(s) Location	Winding Location	Stator Length	Loss Coefficients K_a	K_f	K_i	Q
4	Poles	Poles	4.5"	1.368	1.235	1.212	0.715
7	Armature	Poles	4.5"	2.577	2.989	3.512	0.454
6	Both	Poles	4.5"	2.102	1.206	1.738	0.768
9	Poles	Back Iron	4.5"	1.591	1.118	1.092	0.595
13	Armature	Back Iron	4.5"	2.449	2.934	2.735	0.378
11	Both	Back Iron	4.5"	2.143	1.246	1.325	0.555
17	Poles	Poles	2.0"	1.311	1.194	1.117	0.710
20	Armature	Poles	2.0"	1.770	2.777	2.562	0.496
19	Both	Poles	2.0"	1.932	1.251	1.592	0.729
22	Poles	Back Iron	2.0"	1.549	1.108	1.286	0.729
26	Armature	Back Iron	2.0"	2.171	2.529	2.170	0.393
24	Both	Back Iron	2.0"	1.955	1.285	1.500	0.659

Table 4.2: Loss Factors of Active Biased Actuators

The results of test 4 are shown in Fig. 4.9, which compares the extended model accuracy with the windings on the pole face and the permanent magnet on the pole face of a 4.5 inch actuator. The results show that the extended circuit model accurately predicts the performance of the actuator of the entire operating range. The results also show that with the addition of the third loss coefficient, K_i, the model not only models the variation with gap distance but also accurately predicts the variation with ampere-turns. The extended circuit

model falls short when the ampere-turns reach the maximum negative values. This is due to the flux in the air gap from the permanent magnets not going to zero.

The roll off of the data at the 0.2 inch air gap in Fig. 4.9 is due to flux saturation in the iron. This can be seen by calculating the flux density in the iron using the extended circuit model, Eq. 4.4. The results show that the flux density for 1600, 2000, and 2200 ampere-turns should ideally be 1.3, 1.4, and 1.5 Tesla. The B-H curve for the CMI-C Cold Drawn Steel is given in Section 4.5.1, Fig. 4.15 and shows that the flux density in the steel begins to saturate at 1 - 1.2 Tesla. Even if the flux has not reached the saturation level, at such a high nominal value of flux a significant amount of saturation is likely occurring in corners and other high concentration areas.

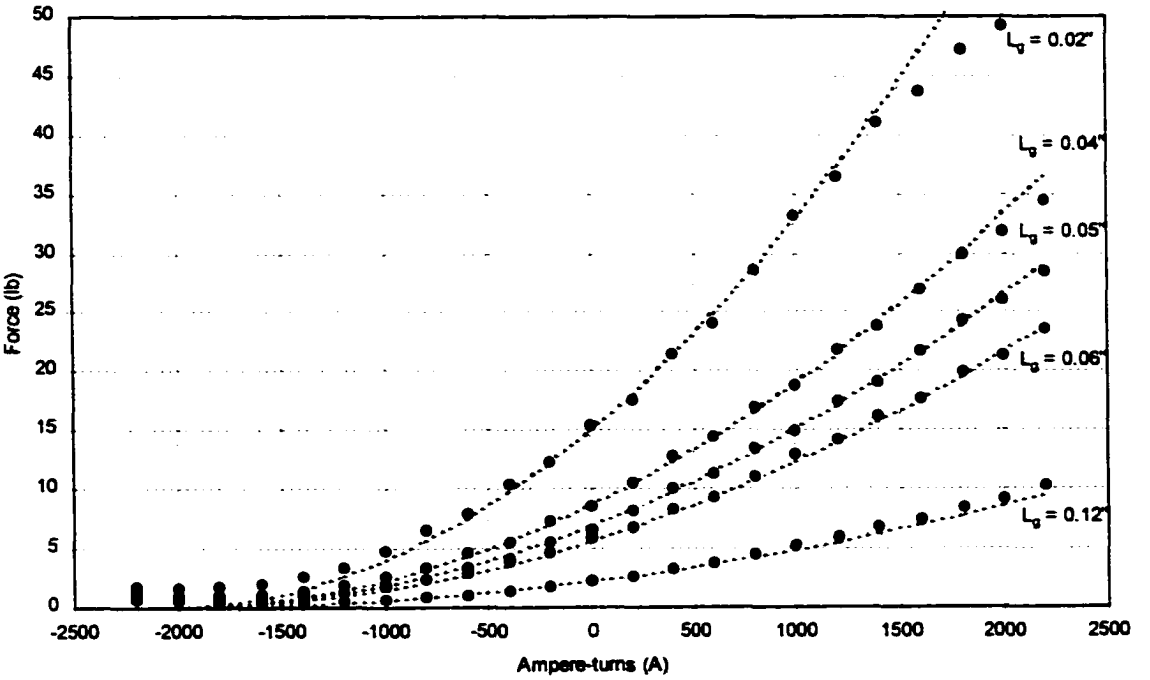

Figure 4.9: Comparison of Extended Circuit Theory to Experimental Results (Test 4)

At the point of flux saturation, the model fails to accurately predict the performance of the actuator. This is expected because the model is linear. Once the flux starts to saturate the actuator becomes nonlinear and the underlying assumptions are violated. As a result, the roll-off of the 0.02inch force data indicates the limitations of the model and is not a failure in the theory.

Fig. 4.10 compares the extended model to the actuator with the windings on the back iron and the magnets on the pole faces of a 2.0 inch actuator. The results shows a distinct roll-off for all five air gap distances. The roll-off occurs at a much lower value of ampere-turns where the flux has not yet saturated. The roll-off in this case is due to coil mmf losses which are present over the entire operating range of the actuator. However, as the ampere-turns are increased the flux density increases which increases the amount of mmf leakage.

The extended circuit model can account for small values of mmf leakage, but as the leakage increases the model becomes inaccurate. The failure of the model is due to the quadratic variation with NI. Both classical and extended circuit theory formulations show that the force varies as NI^2. As a result, the F vs. NI curve will always be concave-up. When the ampere-turns increase and the coil mmf leakage increases, the experimental data curve becomes concave-down. The classical and extended circuit models cannot account for this behavior.

There is a small error for both configurations when the actuator approaches the zero force region. The classical and extended circuit models predict a distinct zero force point.

However, due to the behavior of the flux at the air gap discussed in Section 3, the force never goes to zero when the magnets are placed on the pole faces. This error is not considered significant because these errors would only be of consequence when a bearing was operating at or beyond its normal operating limits.

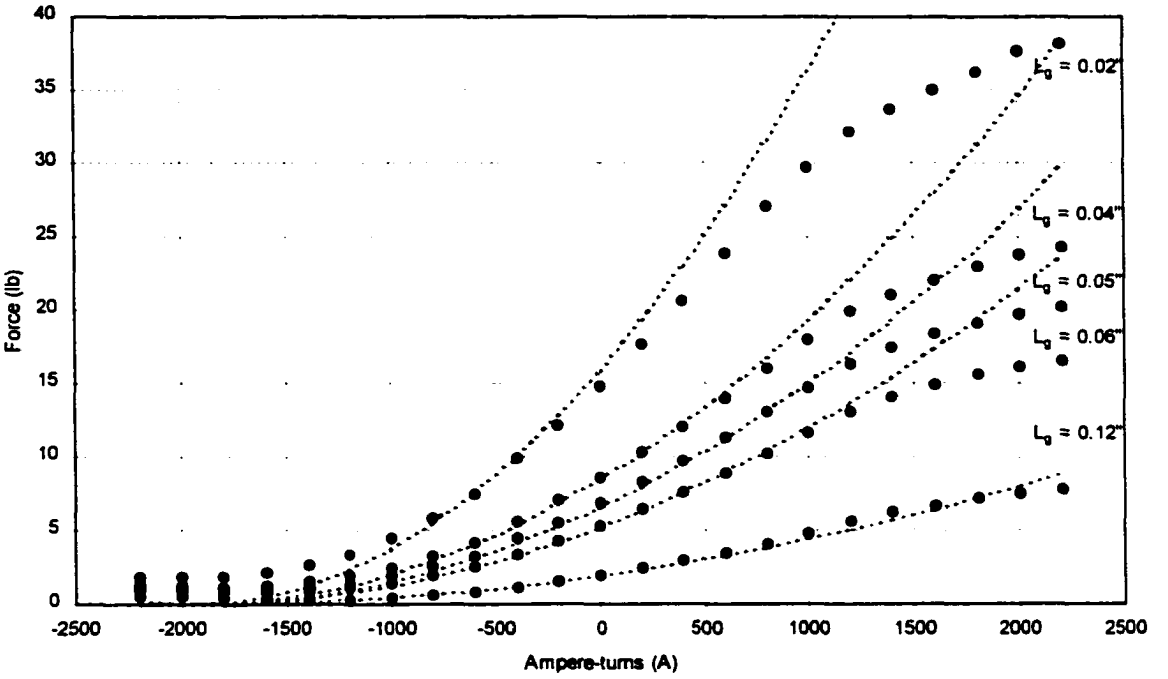

Figure 4.10: Comparison of Extended Circuit Theory with Experimental Results (Test 22)

The results of test 20 with the windings on the poles and the magnet in the armature are shown in Fig. 4.11. The model accurately predicts the zero force point for the actuator at all five air gap distances. It is more critical for this case than for tests 4 and 22 because the permanent magnet mmf leakage has shifted the zero point into the nominal operating range of the actuator. The extended circuit model shows good agreement with the experimental

data points at all regions except the maximum negative ampere-turns. The 0.02 inch data shows the effects of saturation at 1800 ampere-turns.

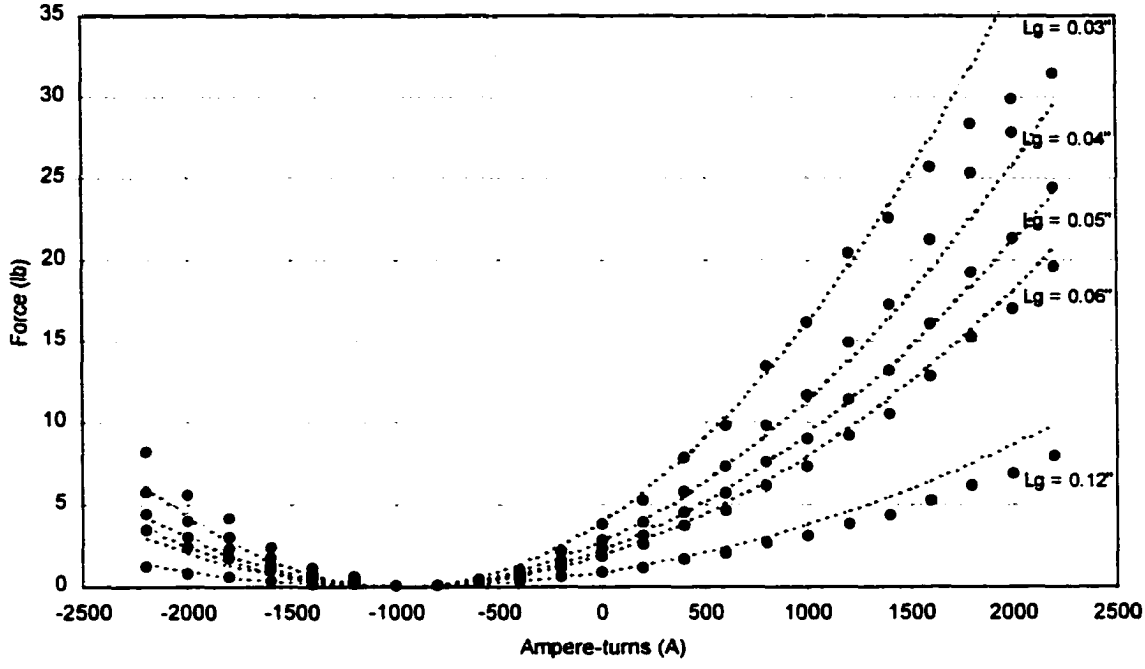

Figure 4.11: Comparison of Extended Circuit Theory and Experimental Results (Test 20)

The quality factor is based on the force vs. ampere-turn slope of a pair of magnetic actuators. However, since the extended circuit model does not account for winding mmf loses at high levels of ampere-turns, the quality factor does not include the roll off due to winding mmf losses. Regardless of this, the quality factors calculated for this set of data show the same trends found in Tables 3.3, 3.4, and 3.5.

4.4.3. Active Actuators with No Biasing Magnets

The non-biased actuators have control windings placed either on the poles or on the back iron with no permanent magnets. The experimental data for this case comes from tests 1, 10, 14,

and 23. The values of K_L where solved from Eq. 4.16. The data points used to calculate K_L with the windings on the pole were NI = 200 - 2000 ampere-turns and NI = 200 -1000 with the windings on the back iron. The loss factors for the four cases are given in Table 4.3.

Test Number	Winding Location	Stator Length	K_L 0.02"	0.04"	0.05"	0.06"	0.07"
1	Poles	4.5"	-	0.851	0.894	0.920	0.940
10	Back of Stator	4.5"	0.710	0.817	0.851	0.880	0.580
14	Poles	2.0"	-	0.873	0.919	0.941	0.962
23	Back of Stator	2.0"	0.803	0.906	0.944	0.946	0.612

Table 4.3: Loss Factors of Active, Non-Biased Actuators

The results with the windings on the poles of the 4.5 inch actuator are shown in Fig. 4.12. The extended circuit model characterizes the actuator much better than the classical circuit model and accurately predicts the performance of the actuator over the entire range of ampere-turns. The effects of saturation begin to show in the 0.04 inch air gap data when NI = 2200 ampere-turns.

The results with the windings on the back iron of the 2.0 inch actuator are shown in Fig. 4.13. The extended circuit model still characterizes the actuator better the classical circuit model but only accurately predicts the performance of the actuator when the coil mmf losses are low. As the ampere-turns are increased the mmf leakage increases to the point where the model can no longer account for the losses. As was the case in Section 4.4.2, the quadratic nature of the circuit model cannot account for the concavity of the true behavior.

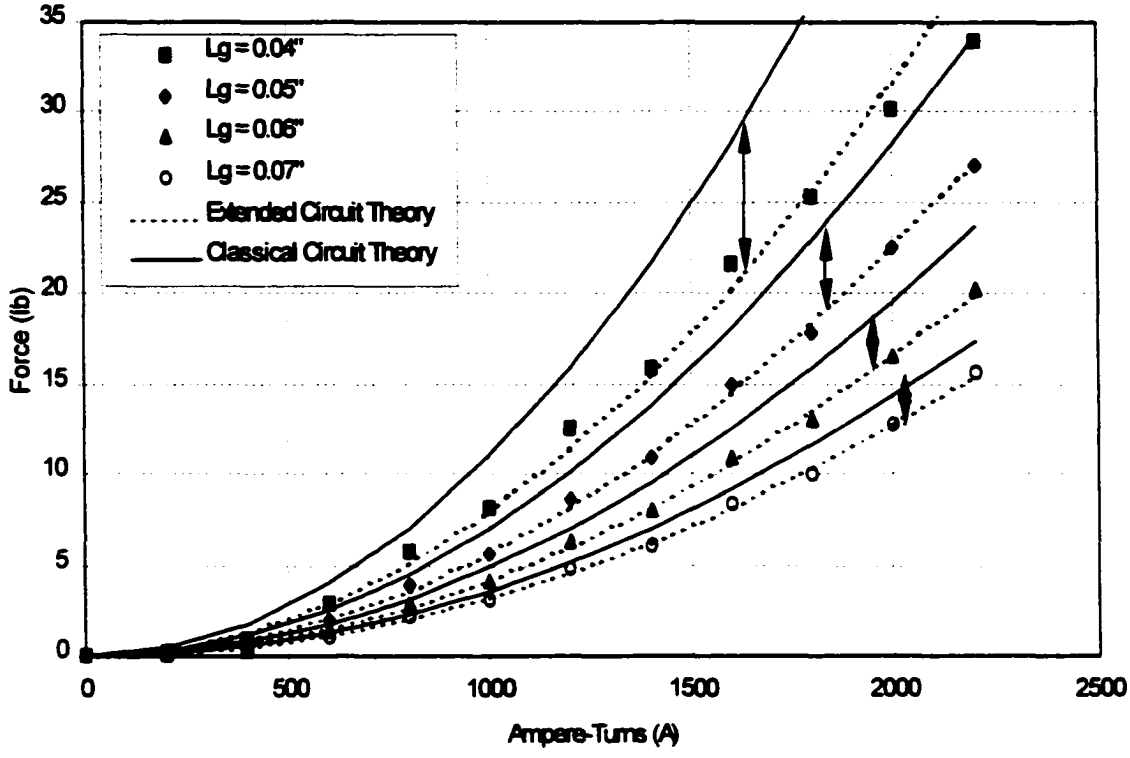

Figure 4.12: Comparison of Extended Circuit Theory with Experimental Data (Test 1)

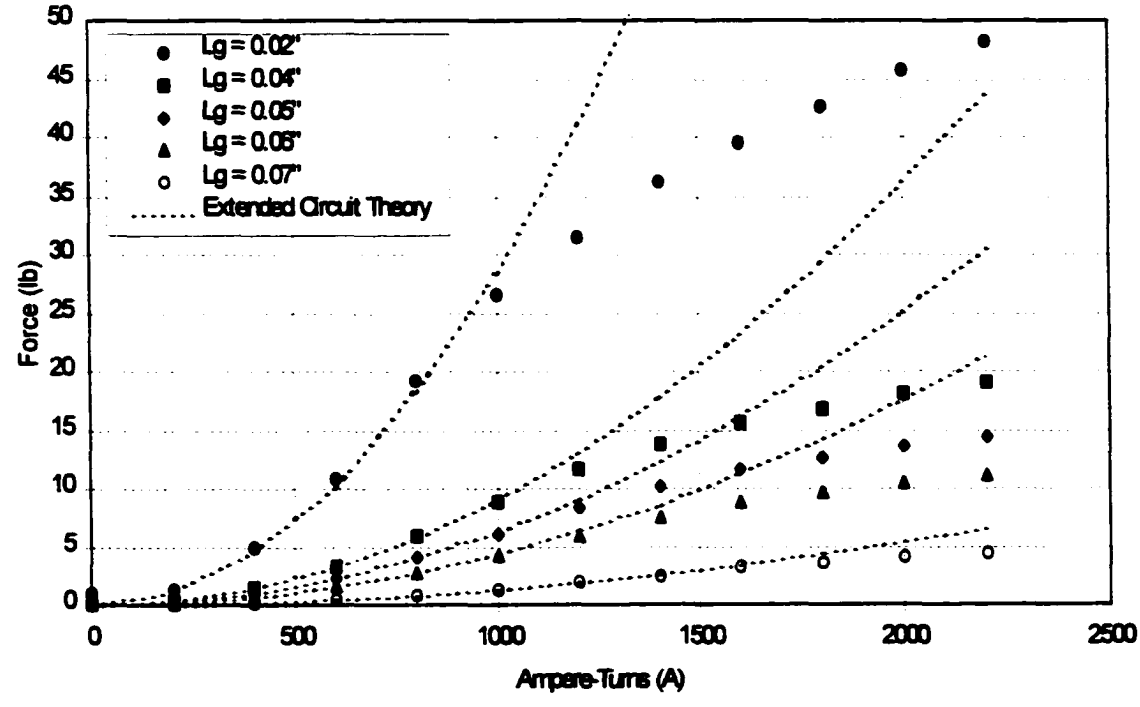

Figure 4.13: Comparison of Extended Circuit Theory to Experimental Data (Test 23)

The quality factors given in Table 4.3 (equivalent to K_L for the case of no permanent magnets) mirror the percentage difference results given in Tables 3.3 and 3.4. Even though the loss factors do not account for coil mmf losses, the quality factors still accurately relate the relative performances of the actuators.

4.5. Comparison of Extended Circuit Theory with Finite Element Analysis

Combining extended circuit theory with experimental data provides a useful tool in modeling existing magnetic bearings. However, there remains a need for an improved modeling technique that can be used prior to manufacturing. Combining extended circuit theory with finite element analysis has the ability to accurately characterize a system prior to its construction.

4.5.1. Finite Element Analysis

The finite element modeling was performed using Vector Fields OPERA-3D [Vector Fields, 1999]. Linear elements were used to model the steel and permanent magnet material. The air surrounding the actuators was also modeled using linear elements. The air gap was modeled using quadratic elements because this is the region where the Maxwell stress integration was performed. Non-linear material properties were used for the steel and magnet material to capture the effects of saturation and demagnetization. The finite element model is shown in Fig. 4.14. Details regarding Vector Fields finite element method are discussed in Section 6.

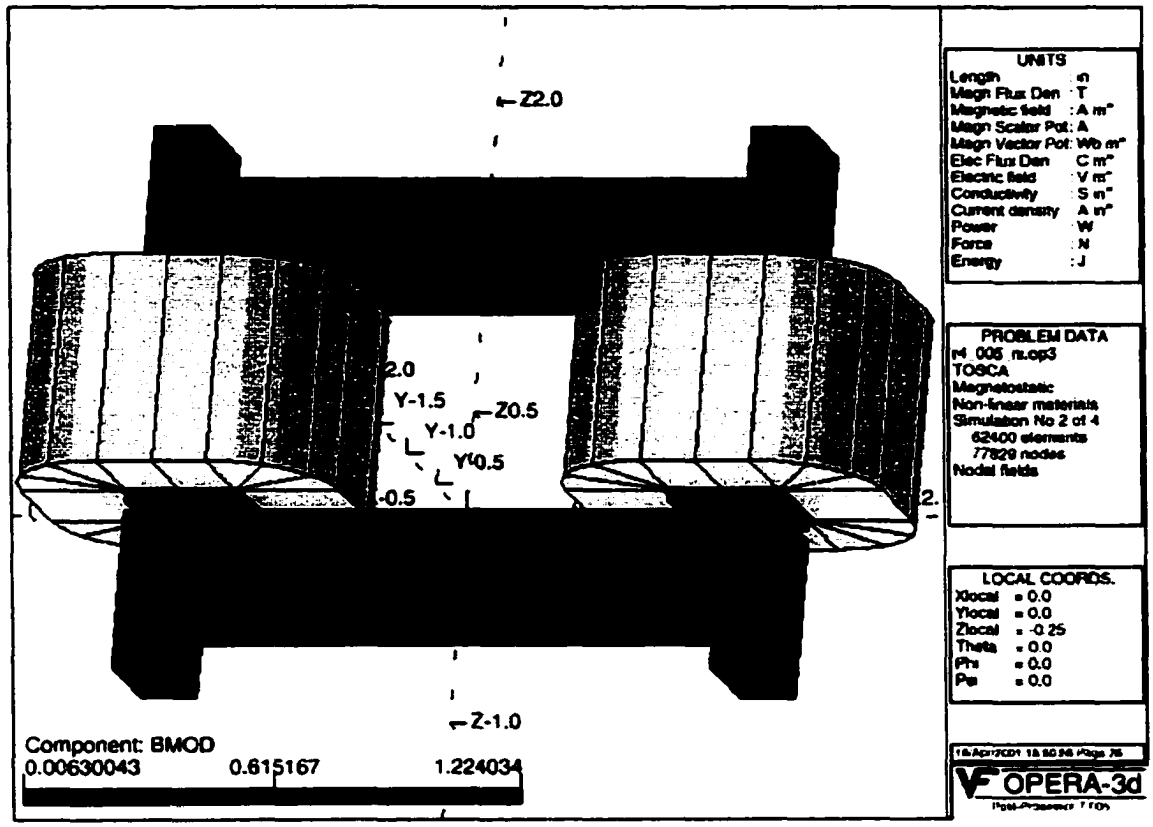

Figure 4.14: OPERA-3D Finite Element Model of 2 inch Actuator with Magnets and Windings on Poles

The data sheet provided by the manufacturer indicated that the relative permeability of the material is approximately 1000. As a result, the iron was modeled using the "mild-high" BH curve supplied by Vector Fields which is for mild steel with a high saturation level. The BH-curve is shown in Fig. 4.15. The permanent magnet used to bias the actuators was neodymium-iron-boron (NdFeB). The NdFeB was experimentally tested and was found to have a residual induction of 1.24 Tesla (See Appendix B). The BH-curve for the permanent magnet is shown in Fig. 4.16.

4.5.2. Comparison of Finite Element Results to Experimental Data

OPERA-3D was used to model the 2 inch actuator with the magnets on the pole faces and the windings wrapped around the poles. The force between the stator and the armature was determined by integrating the Maxwell's stresses over the surface of the armature. Nine points were recorded vs. ampere-turns at the operating gap distance and six points were recorded vs. air gap distance with $NI = 0$. The results are given in Table 4.4.

The loss coefficients K_a and K_f were calculated using all the gap distance data and K_i was calculated using the data corresponding to 400, 800, 1200, and 1600 ampere-turns. The results for the three loss coefficients are given in Table 4.5 and compared to the coefficients determined using the experimental data.

NI (Amps)	Force (lb)	Air Gap (in)	Force (lb)
-1600	1.00	0.02	16.95
-1200	1.72	0.03	12.41
-800	3.02	0.04	9.52
-400	4.95	0.05	7.48
0	7.48	0.06	6
400	10.63	0.07	4.88
800	14.36		
1200	18.31		
1600	22.27		
2000	25.84		

Table 4.4: OPERA-3D finite element results

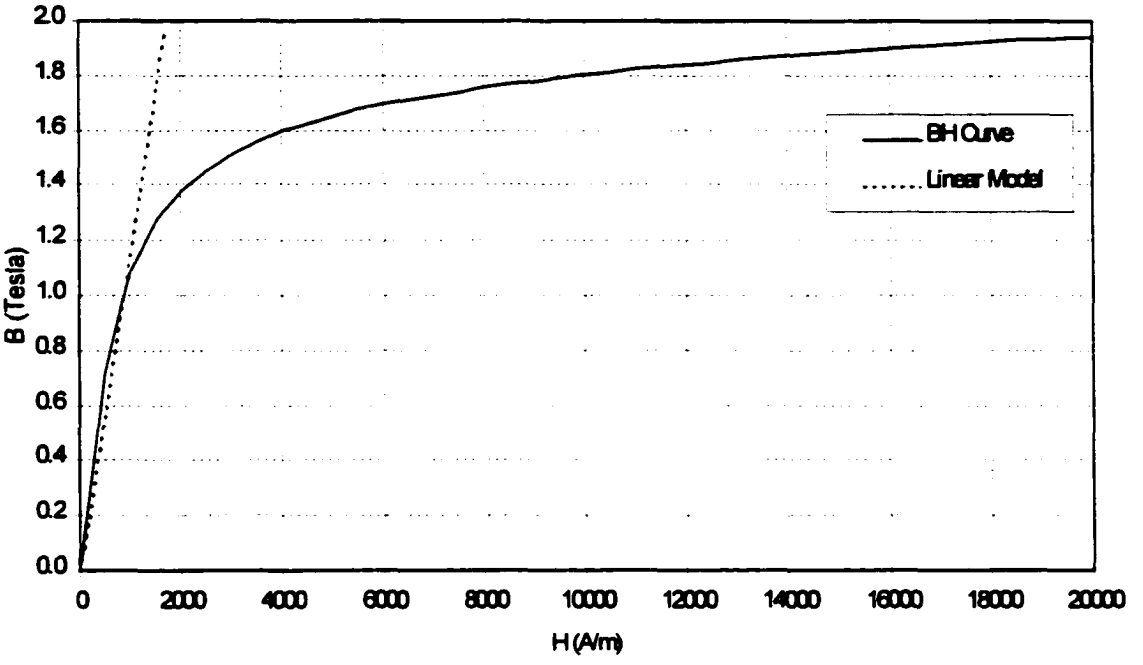

Figure 4.15: "Mild-high" BH-Curve Used to Model Actuator Steel in OPERA-3D

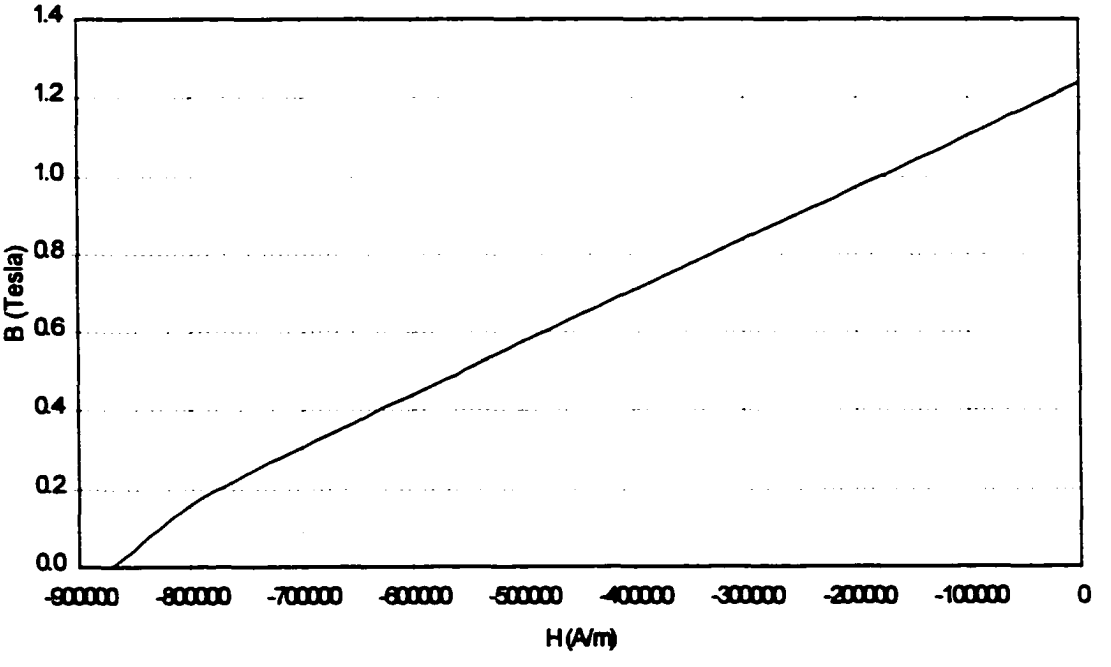

Figure 4.16: BH-Curve for NdFeB Material in OPERA-3D

	Experimental Data	Finite Element Data	Percentage Difference
K_a	1.311	1.392	6%
K_f	1.194	1.105	7%
K_i	1.117	1.174	5%
Q	0.710	0.753	6%

Table 4.5: Comparison of Loss Coefficients

The loss coefficients varied slightly from those calculated using experimental data, but the variation remained below 10% including the quality factor. The finite element results and the resulting extended model are shown in Figs. 4.17 and 4.18. The results show that the extended circuit model overlays the finite element data points. The extended model is compared to the experimental for all air gaps and ampere-turns in Fig. 4.19.

The results show that the extended circuit model based on the finite element loss coefficients very accurately predicts the performance of the actuator. As a result, using the combination of extended circuit theory and finite element analysis, a very accurate model can be developed. The conclusion can be drawn that the accuracy of the extended circuit model is dependent upon the accuracy of the finite element analysis. If the finite element data accurately predicts the performance of the actuator, then the extended circuit model will accurately model the actuator within the circumstances discussed in Section 4.4.

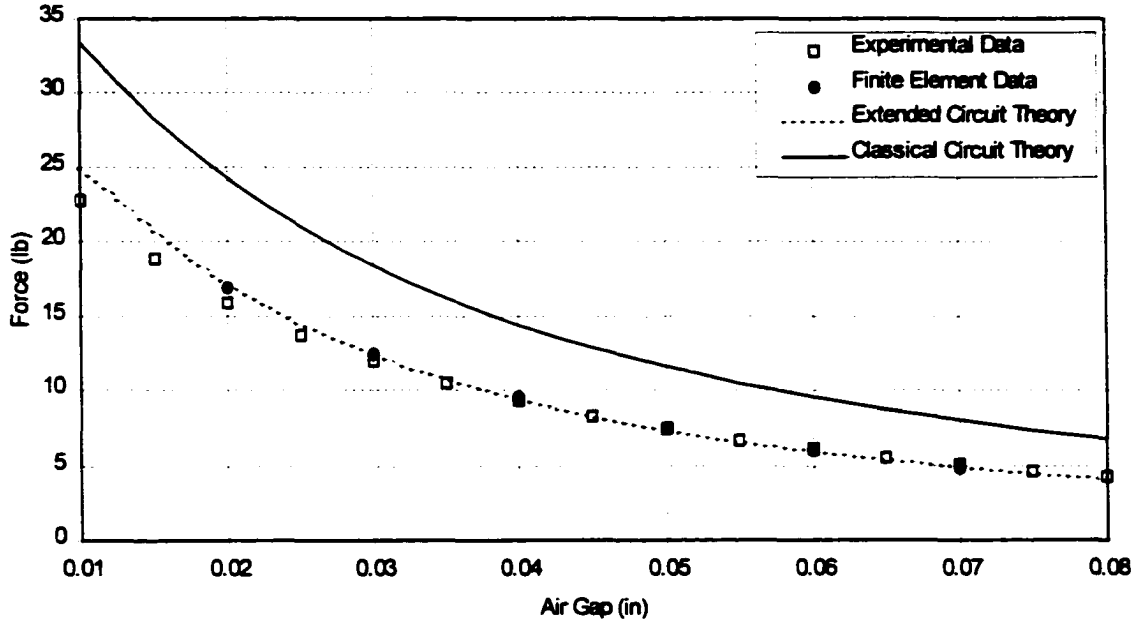

Figure 4.17: Extended Circuit Model Based on FEA Loss Coefficients, Force vs. Gap Distance (Test 16)

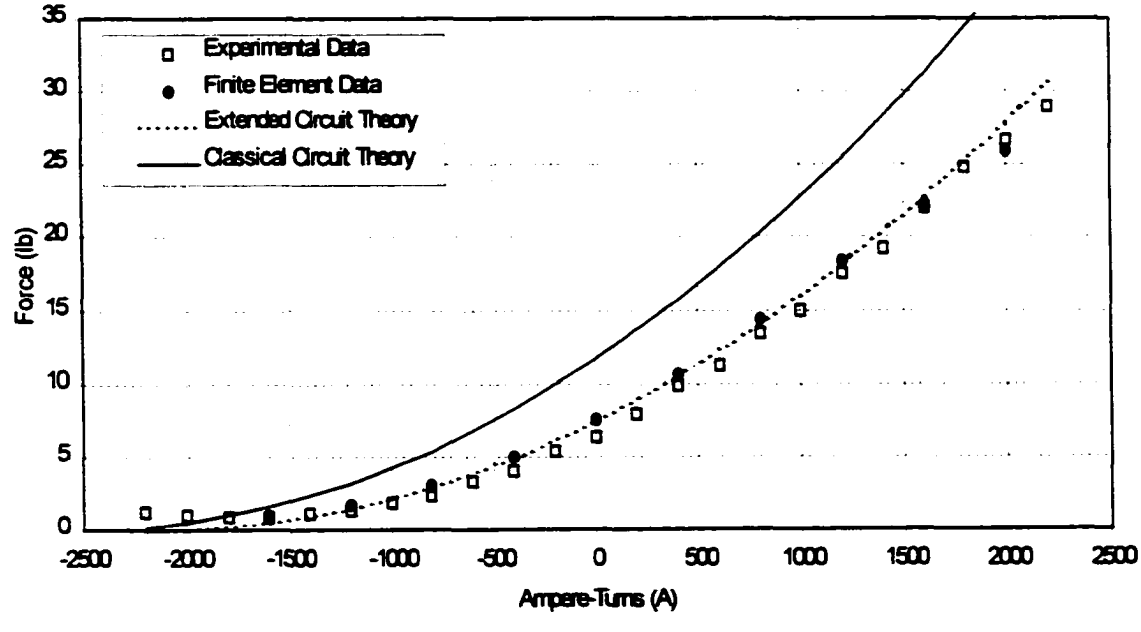

Figure 4.18: Extended Circuit Model Based On FEA Loss Coefficients, Force vs Ampere-Turns (Test 17)

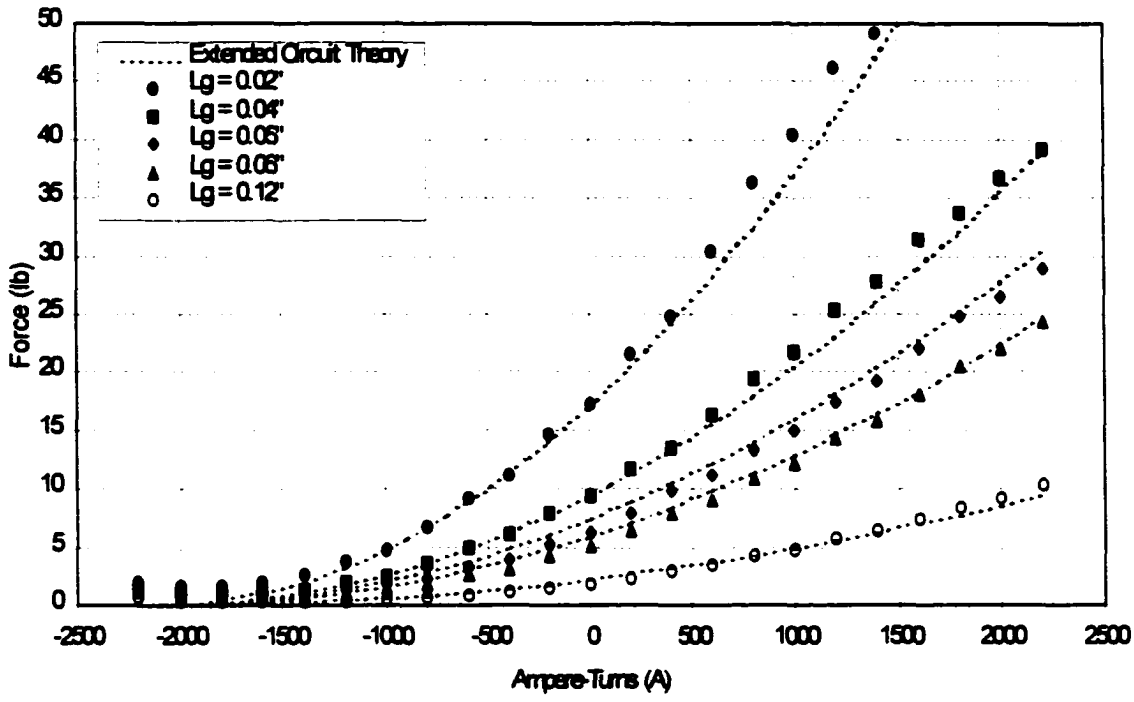

Figure 4.19: Extended Circuit Model Based on FEA Loss Factors, Force vs Ampere-Turns For All Gap Distances (Test 17)

4.6. Loss Coefficient Prediction

There are many situations where it is desirable to know how altering the geometry of a magnetic bearing will effect the performance. In order to do so using extended circuit theory the loss coefficients must vary with actuator geometry. Calculating the loss coefficients from finite element data for every possible configuration is not feasible. The loss coefficients must be analytically known over the entire design space. This can be done using a small number of finite element runs along with multi-dimensional linear and quadratic interpolations.

4.6.1. Prediction Method

The loss coefficients will be analytically modeled using a linear interpolation function based on the design space of the actuator. For an actuator that varies with n degrees-of-freedom ($d_1, d_2, \ldots, d_n$), a set of linear interpolation equations can be written for the loss coefficients K_a, K_F, and K_t, where $\hat{K}$ is the estimated loss coefficient.

$$\begin{aligned}
\hat{K}_a &= C_{11}d_1 + C_{12}d_2 + \cdots + C_{1n}d_n + C_{1,n+1} \\
\hat{K}_F &= C_{21}d_1 + C_{22}d_2 + \cdots + C_{2n}d_n + C_{2,n+1} \\
\hat{K}_t &= C_{31}d_1 + C_{32}d_2 + \cdots + C_{3n}d_n + C_{3,n+1}
\end{aligned} \tag{4.29}$$

In matrix form,

$$\begin{Bmatrix} \hat{K}_a \\ \hat{K}_F \\ \hat{K}_t \end{Bmatrix} = \begin{bmatrix} C_{11} & C_{12} & \cdots & C_{1,n+1} \\ C_{21} & C_{22} & \cdots & C_{2,n+1} \\ C_{31} & C_{32} & \cdots & C_{3,n+1} \end{bmatrix} \begin{Bmatrix} d_1 \\ d_2 \\ \vdots \\ d_n \\ 1 \end{Bmatrix} \tag{4.30}$$

For a linear variation with each degree-of-freedom a minimum of 2^n finite element models need to be run. Including the baseline design, this results in a total of $m = 2^n + 1$ finite element runs. For each of the m runs, the loss factors should be calculated using the procedures outlined in Section 4.2. The limiting values of each degree-of-freedom, $d_i = d_{i,\text{nominal}} \pm \Delta d_i$, should be used to calculate the loss coefficients. More points can be used to increase the accuracy of the formulation.

Once the m sets of coefficients have been determined, Eq. 4.30 can be written in the form,

$$\underbrace{\begin{bmatrix} \begin{Bmatrix} K_a \\ K_F \\ K_t \end{Bmatrix}_1 & \cdots & \begin{Bmatrix} K_a \\ K_F \\ K_t \end{Bmatrix}_m \end{bmatrix}}_{3\times m} = \underbrace{\begin{bmatrix} C_{11} & C_{12} & \cdots & C_{1,n+1} \\ C_{21} & C_{22} & \cdots & C_{2,n+1} \\ C_{31} & C_{32} & \cdots & C_{3,n+1} \end{bmatrix}}_{3\times n+1} \underbrace{\begin{bmatrix} \begin{Bmatrix} d_1 \\ d_2 \\ \vdots \\ d_n \\ 1 \end{Bmatrix}_1 & \cdots & \begin{Bmatrix} d_1 \\ d_2 \\ \vdots \\ d_n \\ 1 \end{Bmatrix}_m \end{bmatrix}}_{n+1\times m} \tag{4.31}$$

In compact form,

$$[K] = [C][D] \tag{4.32}$$

It can be seen from Eq. 4.31 that the first n columns of the coefficient matrix $[C]$ is a sensitivity matrix of the loss factors with respect to the individual degrees-of-freedom.

The design matrix $[D]$ is a non-square matrix so the coefficient matrix can not be solved using the direct inverse. To solve for the coefficient matrix in a least squares best fit sense, the generalized inverse can be used, defined in Eq. 4.12. Using the generalized inverse, the loss factors over the design space can now be estimated using Eq. 4.33.

$$[C] = [K][D]^{\#} = [K]\left([D]^T[D]\right)^{-1}[D]^T \tag{4.33}$$

To mathematically satisfy the linear formulation for the n+1 coefficients there must be n+1 equations. Because there are $2^n + 1$ equations the system is over-determined. This makes it possible to increase the order of the approximation by raising the order of the interpolation equation to quadratic, assuming that an interior data point is known.

$$K = c_{11}d_1^2 + c_{12}d_1 + \cdots + c_{1,2i-1}d_i^2 + c_{1,2i}d_i + \cdots + c_{1,2n+1} \tag{4.34}$$

The sensitivity of the loss factors to the n linear, or quadratic, degrees-of-freedom can be seen by examining the magnitude of the first n columns in $[C]$. Because the magnitude of each variable varies, the contribution from each $c_{i,j}$ term can be better interpreted by normalizing it with respect to d_i by multiplying each row of the matrix by $\max(|d_i|)$, or $\max(|d_i|^2)$ for quadratic interpolations.

4.6.2 Experimental Verification of Loss Coefficient Prediction

In this section the magnetic actuator in Section 4.5 is examined using the techniques covered in the previous section. The method is examined with the variation in 1, 2, and 3 degrees-of-freedom.

The first case involves the variation of 1 degree of freedom, the permanent magnet length L_m, with the pole separation distance of 2 inches and a pole thickness of 0.5 inches. The single degree of freedom required $2^1+1 = 3$ permutations, the magnet length will be allowed to vary from 0.03 inches to 0.07 inches, with the nominal design at 0.05 inch. Six finite element runs were performed for each design, leading to a total of 18 runs. The prediction method is tested against a design with a permanent magnet thickness of 0.04 inches. The loss coefficients are formulated using a linear and quadratic interpolation function, the results are given in Table 4.6.

Magnet Thickness (in)	Interpolation Method	Direct Calculation			Predicted			Percent Difference		
		K_a	K_F	K_i	K_a	K_F	K_i	K_a	K_F	K_i
0.03	Linear	1.324	1.145	1.207	1.286	1.148	1.201	2.9%	0.3%	0.5%
0.05	Linear	1.403	1.129	1.217	1.362	1.143	1.213	2.9%	1.2%	0.3%
0.07	Linear	1.479	1.123	1.23	1.438	1.137	1.226	2.8%	1.2%	0.3%
0.03	Quadratic	1.324	1.145	1.207	1.324	1.146	1.208	0.05%	0.05%	0.05%
0.05	Quadratic	1.403	1.129	1.217	1.403	1.129	1.218	0.05%	0.05%	0.05%
0.07	Quadratic	1.479	1.123	1.23	1.480	1.124	1.230	0.04%	0.05%	0.05%
0.04	Linear	1.361	1.139	1.211	1.324	1.145	1.207	2.70%	0.55%	0.27%
0.04	Quadratic	1.361	1.139	1.211	1.364	1.136	1.213	0.27%	0.25%	0.17%

Table 4.6: Linear and Quadratic Interpolation Results for Single Degree-of-Freedom

The results show that for this case the linear interpolation can estimate the loss factors to within 3 percent. Quadratic interpolation performs better with a difference of less then 1 percent at the three test points. At the intermediate point of $L_m = 0.04$, inches the linear model was within 3 percent of the exact value and there was less than 1 percent of difference between the quadratic model and the exact value.

The two degree-of-freedom model allows a variation in the magnet thickness and the pole thickness with the pole separation distance set at 3 inches. The magnet thickness will vary between 0.03 inches and 0.07 inches and the pole thickness will vary between 0.3 inches and 0.7 inches. Five models were needed to model the design space, which resulted in 30 finite element runs. The final results are shown in Table 4.7.

Magnet Thickness (in)	Pole Thickness (in)	Interpolation Method	Direct Calculation			Predicted			Percent Difference		
			K_a	K_F	K_i	K_a	K_F	K_i	K_a	K_F	K_i
0.03	0.3	Linear	1.713	1.274	1.148	1.745	1.293	1.148	1.8%	1.5%	0.05%
0.03	0.7	Linear	1.246	1.304	1.116	1.133	1.278	1.117	9.1%	2.0%	0.04%
0.07	0.3	Linear	2.093	1.270	1.159	1.980	1.244	1.160	5.4%	2.0%	0.07%
0.07	0.7	Linear	1.336	1.211	1.128	1.368	1.230	1.128	2.4%	1.5%	0.01%
0.05	0.5	Linear	1.394	1.247	1.140	1.556	1.261	1.138	11.7%	1.1%	0.20%
0.03	0.3	Quadratic	1.713	1.274	1.148	1.785	1.296	1.148	4.2%	1.7%	0.00%
0.03	0.7	Quadratic	1.246	1.304	1.116	1.173	1.282	1.116	5.8%	1.7%	0.00%
0.07	0.3	Quadratic	2.093	1.270	1.159	2.020	1.248	1.159	3.5%	1.7%	0.03%
0.07	0.7	Quadratic	1.336	1.211	1.128	1.408	1.233	1.128	5.4%	1.8%	0.05%
0.05	0.5	Quadratic	1.394	1.247	1.140	1.394	1.247	1.140	0.0%	0.0%	0.05%
0.04	0.4	Linear	1.537	1.339	1.167	1.651	1.277	1.143	7.4%	4.6%	2.0%
0.04	0.4	Quadratic	1.537	1.339	1.167	1.539	1.267	1.144	0.1%	5.4%	1.9%

Table 4.7: Linear and Quadratic Interpolation Results for 2 Degrees-of-Freedom

The linear interpolation model adequately predicts the loss coefficients K_F and K_i to within 2 and 0.5 percent, respectively. However, the prediction of K_a varied as much as 11 percent. The quadratic model performs much better. The accuracy of the loss factors K_F and K_i are improved slightly while the accuracy of K_a is improved from 11 percent to 6 percent. The same trends are present when attempting to predict an intermediate design with $L_m = 0.04$ inches and $T = 0.4$ inches. The linear and quadratic interpolation schemes predict K_F and K_i to within 5 percent, but the linear prediction of K_a is off by 7 percent, whereas the quadratic is off by less than 2 percent.

These differences are due to the nature of the interpolation scheme. The minimum number of permutations based on a linear model is 2^n. The addition of the nominal design point makes it possible to completely model the 1 degree-of-freedom case as quadratic. However,

in order to completely model the 2 degree-of-freedom case as quadratic a total of $3^n = 9$ permutations, plus the nominal design point, are necessary. This is a very undesirable situation because it causes the number of necessary finite element runs to dramatically increase. A single intermediate point can be used because the generalized inverse uses a least squares best fit methodology, which allows for fewer than 3^n permutations to provide the quadratic information to the curve fit. The result is a trade-off between number of computations and accuracy of the solution. Since there were only five permutations used, the accuracy of the model was decreased.

The three degree-of-freedom model allows the magnet thickness, the pole thickness, and the pole separation distance to vary. The results are shown in Table 4.8. Again, the quadratic interpolation scheme does a better job predicting the loss coefficients than the linear interpolation model. Both interpolation schemes were used to estimate the performance of an actuator with $L_m = 0.04$ inches, pole thickness of 0.5 inches, and pole separation distance of 2 inches. The linear model predicts the loss factors to within 10 percent, while the quadratic predicts to within 2 percent.

Magnet Thick. (in)	Pole Thick. (in)	Pole Sep. (in)	Interp. Method	Direct Calculation			Predicted			Percent Difference		
				K_a	K_F	K_i	K_a	K_F	K_i	K_a	K_F	K_i
0.03	0.3	1.0	Lin.	1.583	1.125	1.153	1.662	1.165	1.175	4.9%	3.6%	1.93%
0.03	0.3	3.0	Lin.	1.722	1.297	1.172	1.742	1.268	1.165	1.2%	2.2%	0.58%
0.03	0.7	1.0	Lin.	1.235	1.219	1.126	1.115	1.180	1.132	9.7%	3.3%	0.58%
0.03	0.7	3.0	Lin.	1.246	1.304	1.116	1.195	1.283	1.122	4.1%	1.6%	0.51%
0.07	0.3	1.0	Lin.	1.932	1.155	1.198	1.887	1.131	1.190	2.3%	2.1%	0.73%
0.07	0.3	3.0	Lin.	2.093	1.270	1.159	1.967	1.234	1.179	6.0%	2.9%	1.77%
0.07	0.7	1.0	Lin.	1.325	1.171	1.139	1.340	1.145	1.146	1.1%	2.2%	0.69%
0.07	0.7	3.0	Lin.	1.336	1.211	1.128	1.420	1.248	1.136	6.3%	3.0%	0.70%
0.05	0.5	2.0	Lin.	1.382	1.156	1.225	1.541	1.207	1.156	11.5%	4.4%	5.63%
0.03	0.3	1.0	Quad.	1.583	1.125	1.153	1.680	1.178	1.168	6.1%	4.7%	1.32%
0.03	0.3	3.0	Quad.	1.722	1.297	1.172	1.760	1.281	1.158	2.3%	1.3%	1.18%
0.03	0.7	1.0	Quad.	1.235	1.219	1.126	1.133	1.192	1.125	8.3%	2.2%	0.03%
0.03	0.7	3.0	Quad.	1.246	1.304	1.116	1.213	1.295	1.115	2.6%	0.7%	0.12%
0.07	0.3	1.0	Quad.	1.932	1.155	1.198	1.905	1.143	1.183	1.4%	1.1%	1.31%
0.07	0.3	3.0	Quad.	2.093	1.270	1.159	1.985	1.246	1.172	5.1%	1.9%	1.17%
0.07	0.7	1.0	Quad.	1.325	1.171	1.139	1.358	1.158	1.139	2.5%	1.2%	0.08%
0.07	0.7	3.0	Quad.	1.336	1.211	1.128	1.438	1.261	1.129	7.7%	4.1%	0.08%
0.05	0.5	2.0	Quad.	1.382	1.156	1.225	1.395	1.107	1.211	1.0%	4.2%	1.12%
0.04	0.5	2.0	Lin.	1.361	1.139	1.211	1.485	1.215	1.152	9.1%	6.7%	4.81%
0.04	0.5	2.0	Quad.	1.361	1.139	1.211	1.339	1.116	1.207	1.6%	2.1%	0.25%

Table 4.8: Linear and Quadratic Interpolation Results for 3 Degrees-of-Freedom

Three degree-of-freedom quadratic interpolation was used to predict the performance of the experimental actuator with the windings on the poles and 0.05 inch magnets on the pole faces. The interpolated loss coefficients K_a, K_F, and K_i differed from the directly calculated loss coefficients by 5%, 3%, and 2%, respectively. The force vs ampere-turns results are shown in Fig. 4.20 and show that even though the interpolated loss coefficients differed by as much as 5%, the model still adequately predicted the performance of the magnet actuator. The results from these three tests show that using a quadratic interpolation scheme and a relatively small number of finite element runs, an accurate model can be developed which

accounts for variations in geometry. The linear interpolation proved to predict the loss coefficients to within 10 percent, but the quadratic interpolation provided for a more accurate result. It should be noted that, if the degree-of-freedom is only allowed to vary slightly from the design point, the linear model should be adequate. The interpolated loss coefficients are not as accurate as those calculated directly, but they do introduce a lot of flexibility to the design process.

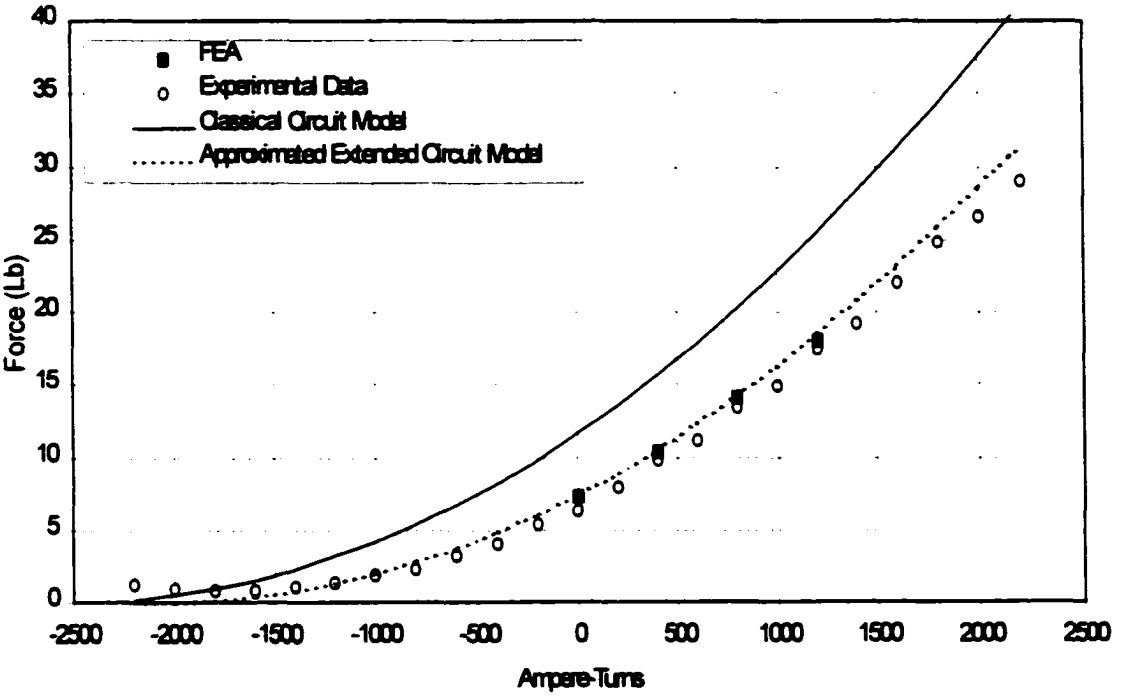

Figure 4.20: Extended Circuit Model Based on Quadratically Interpolated Loss Coefficients (Test 17)

The linear coefficient matrices for the three tests discussed in this section are given in Eq. 4.35a-c. The columns respectively correspond to $\lfloor L_m \;\; T \;\; P_s \rfloor$, where the last column is a constant and all units are in meters. The quadratic coefficient matrices given in Eq. 4.36a-c, where the columns correspond to $\lfloor L_m^2 \;\; L_m \;\; T^2 \;\; T \;\; P_s^2 \;\; P_s \rfloor$ and the last column is a constant.

$$[C_1] = \begin{bmatrix} 149.936 & 1.171 \\ -11.267 & 1.157 \\ 24.342 & 1.183 \end{bmatrix} \tag{4.35a}$$

$$[C_2] = \begin{bmatrix} 231.299 & -60.236 & 2.028 \\ -47.736 & -1.427 & 1.340 \\ 11.319 & -3.100 & 1.163 \end{bmatrix} \tag{4.35b}$$

$$[C_3] = \begin{bmatrix} 221.460 & -53.839 & 1.585 & 1.863 \\ -33.957 & 1.427 & 2.028 & 1.129 \\ 14.026 & -4.257 & -0.202 & 1.202 \end{bmatrix} \tag{4.35c}$$

$$[C_1] = \begin{bmatrix} -5321.321 & 166.152 & 1.201 \\ 21106.902 & -75.600 & 1.191 \\ 4476.746 & 10.696 & 1.197 \end{bmatrix} \tag{4.36a}$$

$$[C_2] = \begin{bmatrix} 79.306 & 231.100 & 7865.300 & -260.020 & 3.134 \\ 6.761 & -47.753 & 687.730 & -18.896 & 1.437 \\ -0.843 & 11.321 & -87.177 & -0.886 & 1.151 \end{bmatrix} \tag{4.36b}$$

$$[C_3] = \begin{bmatrix} 0.665 & 221.460 & 8.886 & -54.064 & 254.070 & -24.226 & 2.374 \\ -0.016 & -33.957 & 7.033 & 1.249 & 173.470 & -15.595 & 1.478 \\ -0.003 & 14.026 & -3.993 & -4.156 & -96.218 & 9.573 & 1.009 \end{bmatrix} \tag{4.36c}$$

4.7. Example: Optimization of a Magnetic Actuator

In order to optimize a magnetic bearing, an accurate mathematical model must be known. The classical circuit model has not been accurate enough to warrant the combination of magnetic theory with optimization theory, other than for systematic studies [Malone, 1993; Bloodgood, 1998; Klesen, 1999]. Extended circuit theory makes it possible to use an accurate mathematical model of a magnetic bearing in an optimization routine. As a result, designers now have the ability to optimally tailor a bearing's performance to specific design criteria.

As an example, an axial magnetic thrust bearing is designed for minimum power. One of the most important factors to consider in the design of an active magnetic bearing is its power efficiency. Reducing the power consumption will reduce not only the operational costs, but also the acquisition costs. If the required power can be reduced, then smaller and therefore cheaper amplifiers and power supplies can be used. Reduction of power also lessens cooling requirements. While applications such as space-based systems and small pumps for medical applications have the most to gain by reducing power requirements, more typical commercial systems can also be significantly improved.

4.7.1. Problem Statement

The bearing geometry that is being optimized is shown in Fig. 4.21. The system is being optimized for minimum power and is designed to support a nominal load of 2025 N at an air gap of 4 mm. It is biased by a pair of neodymium-iron-boron permanent magnets placed on the poles of the stator. The residual inductance of the neodymium-iron-boron is 1.2 Tesla. The clearance for the shaft has a radius of 25 mm. The flux density in the iron is assumed to behave linearly up to a level of 1 Tesla and the maximum allowable current density of the windings is limited to 4 A/mm^2. The windings have a packing factor of 0.85, and the overall volume of the coil is limited to 820 cm^3.

The magnetic actuator will be modeled by three different systems. These include the classical magnetic circuit model, the extended magnetic circuit model with constant loss coefficients, and the extended circuit model with geometry specific loss coefficients. The three models

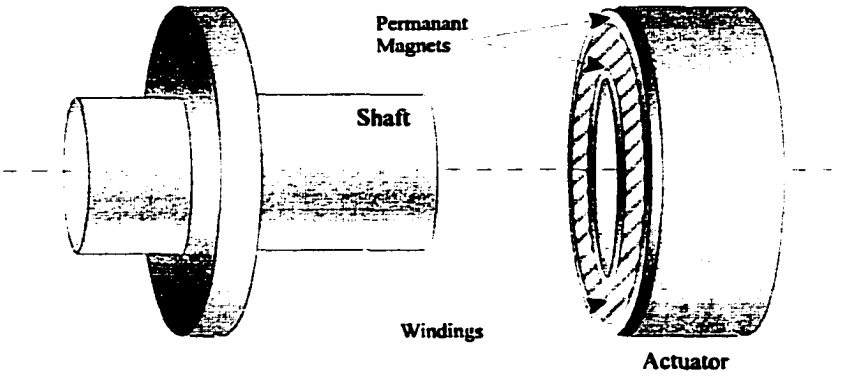

Figure 4.21: Axial Thrust Bearing Geometry

will be optimized independently and the results compared. Preliminary results for this approach are given in [Bloodgood, 2000].

4.7.2. Optimization

The power dissipated by a coil can be determined using the standard power equation [Bloodgood, 1998],

$$P = \rho \eta J^2 V_c \tag{4.37}$$

where ρ is the resistivity of the windings, η is the packing factor, J is the current density, and V_c is the volume of the windings. At the operating point, the permanent magnets should provide a bias flux to carry the nominal load on the bearing. As a result, the power required to suspend the shaft at the equilibrium is ideally zero. The power required by the coil will only be a factor when disturbance forces are present. The disturbance forces acting on the shaft will be assumed to have a frequency of occurrence that follows a Gaussian distribution.

$$\omega(F)=\frac{1}{\sigma\sqrt{2\pi}}e^{-\frac{1}{2}\left(\frac{F-\bar{F}}{\sigma}\right)^2} \qquad \sigma=\sqrt{\frac{\sum_{i=1}^{n}\left(F_i-\bar{F}\right)^2}{n}} \tag{4.38}$$

The magnitude of the disturbance forces are assumed to vary between ± 10% of the operating force. The current density required to provide the designated loads can be written as a function of force. With this, the objective function to be minimized can be written as Eq. 4.39.

$$\begin{aligned} f &= \rho\eta V_c \int_{F_{min}}^{F_{max}} J^2(F)e^{-\frac{1}{2}\left(\frac{F-\bar{F}}{\sigma}\right)^2} dF \\ &\approx \rho\eta V_c \frac{0.2\bar{F}}{n-1}\sum_{i=1}^{n} J^2(F_i)e^{-\frac{1}{2}\left(\frac{F_i-\bar{F}}{\sigma}\right)^2} \end{aligned} \tag{4.39}$$

The performance characteristics of the actuator are controlled through the constraint equations. The bearing is being designed to support a specified load at a specified air gap. This introduces the equality constraint.

$$F=\frac{\mu_0 A_g\left(K_i NI+\frac{2B_r L_m}{\mu_0}\right)^2}{4\left(K_a L_g+K_F L_m\right)^2} \tag{4.40}$$

There are three additional inequality constraints that must be added to the system. The first requires that the current density required to support the load at the high and low end of the design range remain below J_{max}. The equation can be developed by substituting $NI=\eta A_c J$ into Eq. 4.40 and solving for J which results in,

$$J_{max} \geq \left| \sqrt{\frac{4F_{Max,Min}}{\mu_0 A_g}} \left(\frac{K_a L_g + K_F L_m}{\eta A_c} \right) - \frac{2B_r L_m}{\mu_0 \eta A_c} \right| \tag{4.41}$$

The second inequality constraint requires that the flux density within the iron remains below the saturation level, 1 Tesla, at every point within the circuit. To avoid contractions where the flux may saturate, the minimum cross sectional area of the iron was specified to equal the pole area at all points.

$$B_{Sat} \geq \frac{\mu_0 \left(K_i N I_{max} + \frac{2B_r L_m}{\mu_0} \right)}{2\left(K_a L_g + K_F L_m \right)} \tag{4.42}$$

The final constraint requires the volume of the actuator to remain finite. For this case the maximum volume was limited to 820 cm^3.

$$V_{MAX} \geq V \tag{4.43}$$

The coil geometry has been divided as shown in Fig. 4.22. Because the cross sectional area of the circuit was specified to equal the pole area, the outer wall thickness t, and the back wall thickness b, can be written in terms of the other variables. The design vector can therefore be reduced to 5 variables,

$$\bar{x} = \lfloor r \quad w \quad h \quad L_m \quad J \rfloor \tag{4.44}$$

Three separate optimization runs will be performed. First, the classical circuit model will be optimized. Second, the extended circuit model will be optimized with constant loss

coefficients and third, the extended circuit model will be optimized with loss coefficients that vary with the actuator geometry. In the third case, the methods discussed in Section 4.6 are used. For the second case, the model is optimized and a solution is obtained (with the loss factors set to 1 for the first run.) The actuator is then analyzed using finite element analysis and the loss factors are obtained. These loss factors are then introduced into the optimization code and the extended circuit theory model is optimized. Assuming that the geometry does not change significantly, the optimizer should converge to a solution in a few iterations.

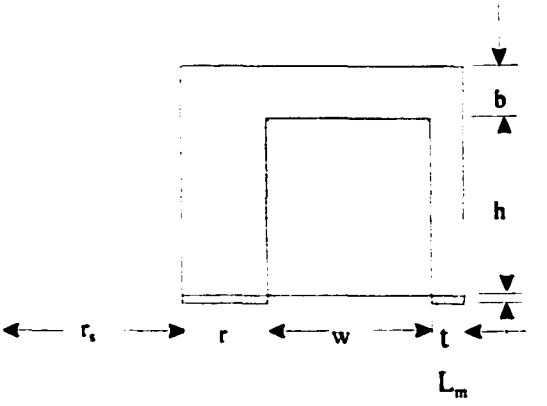

Figure 4.22: Description of Actuator Geometry

4.7.3. Implementation of Equations

MATLAB's optimization toolbox version 5.3. was chosen to optimize the axial thrust bearing. The package uses the Sequential Quadratic Programming Method (SQP), which is ideally suited for nonlinear problems with nonlinear constraints. SQP uses the BFGS quasi-Newton method to approximate the Hessian of the Lagrangian function. The new Hessian is used to solve a Quadratic Programing subproblem in order to determine the best search direction and step length [Coleman, 1999].

The finite element modeling was performed using Vector Fields PC-OPERA 2D. Axial symmetry was used with the modified $r \times a$ potential [Vector Fields, 1997]. The calculations

were performed using quadratic elements with non-linear material properties. The iron was modeled using the standard material BH curve supplied by Vector Fields, and the neodymium-iron-boron had a residual induction of 1.2 Tesla and a coercivity of 9.7×10^5 A/m. K_a and K_F were determined using five air gap lengths about the operating point, L_g = 3.0, 3.5, 4.0, 4.5, and 5.0 mm. K_i was determined by setting $NI = \eta A_c J_{max}$.

Convergence of the optimization was dependent upon the initial conditions. When convergence was achieved, it was always to the same solution. When converge was not achieved, the initial conditions were randomly perturbed by ±10% until a solution was found.

4.7.4. Discussion of Results

The classical circuit model was optimized and a minimum power configuration was found. The model predicted that the actuator would meet the design requirements. However, once the loss coefficients were calculated and included in the model the result no longer met the design specifications. The configuration delivered a zero power force of 1778 N, 12% below the desired value. The resulting configuration and loss factors are given in Table 4.9.

Design	r (mm)	w (mm)	h (mm)	L_m (mm)	t (mm)	b (mm)	K_a	K_F	K_i
Classical Circuit Theory	25.1	17.4	19.8	4.9	12.8	18.8	1.363	0.841	1.072
E.C.T. with constant loss coeffs.	22.2	19.5	23.4	6.5	11.1	17.0	1.508	0.862	1.082
E.C.T. with varying loss coeffs.	26.6	17.4	15.9	5.00	13.5	19.7	1.319	0.840	1.071

Table 4.9: Optimization Results

The loss factors were then used in the optimization loop to develop the extended optimized model with constant loss coefficients. After a single iteration, the addition of the constant

loss coefficients only increased the zero power force to 1800 N, an improvement of less then 2%. The results of both cases are shown in Fig. 4.23.

The loss coefficients were calculated for the new design. They were substituted into the optimization loop and a second iteration was performed. The performance of the actuator deteriorated with each subsequent iteration and the loss coefficients never converged to a final solution. The geometry of the actuator was changing significantly with each optimization solution. As a result, the optimizer was working with an inaccurate model. The third optimization run used the loss coefficient interpolation method discussed in Section 4.6. This allowed the loss coefficients to vary with the coil geometry. As a result,

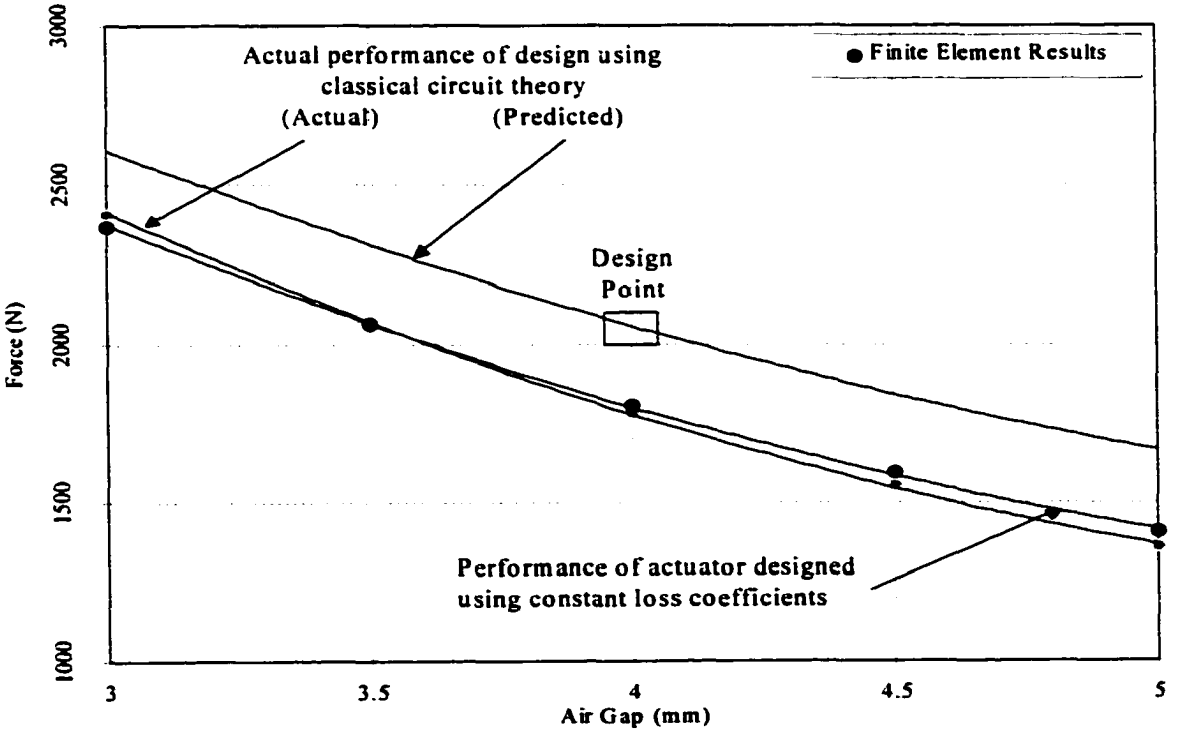

Figure 4.23: Actuator Performance for Designs Using Classical Circuit Theory and Extended Circuit Theory Using Constant Loss Coefficients

the leakage and loss characteristics of each design iteration were included in the optimization run and the optimizer converged to the appropriate design. The results are shown in Figs. 4.24 and 4.25. The differences between the optimization algorithm for the constant loss factors and the interpolated loss factors are shown in Fig. 4.26. The final design is shown in Fig. 4.27.

The classical design could not meet the performance requirements because of losses in the system not accounted for in classical circuit theory. Including the loss factors took into account the flux leakage and losses. The actuator design changed by increasing the permanent magnet volume while keeping the thickness the same. This increased the bias force produced by the actuator while reducing the reluctance of the magnet. Also, the height of the conductor was reduced which lessened the volume of the copper windings and reduced the reluctance of the iron path.

Inclusion of the varying loss factors in the optimization loop resulted in a zero current force of 2046 N, only 1% from the desired value. With the interpolated loss factors in the optimization loop, the actuator performance improved by 268 N at the zero current condition for the same size actuator. The estimated loss factors K_a, K_F, and K_i varied from the exact values by 1.4%, 1.4%, and 3% respectively. Improvements to these values would slightly modify the optimum results but should not produce any significant changes.

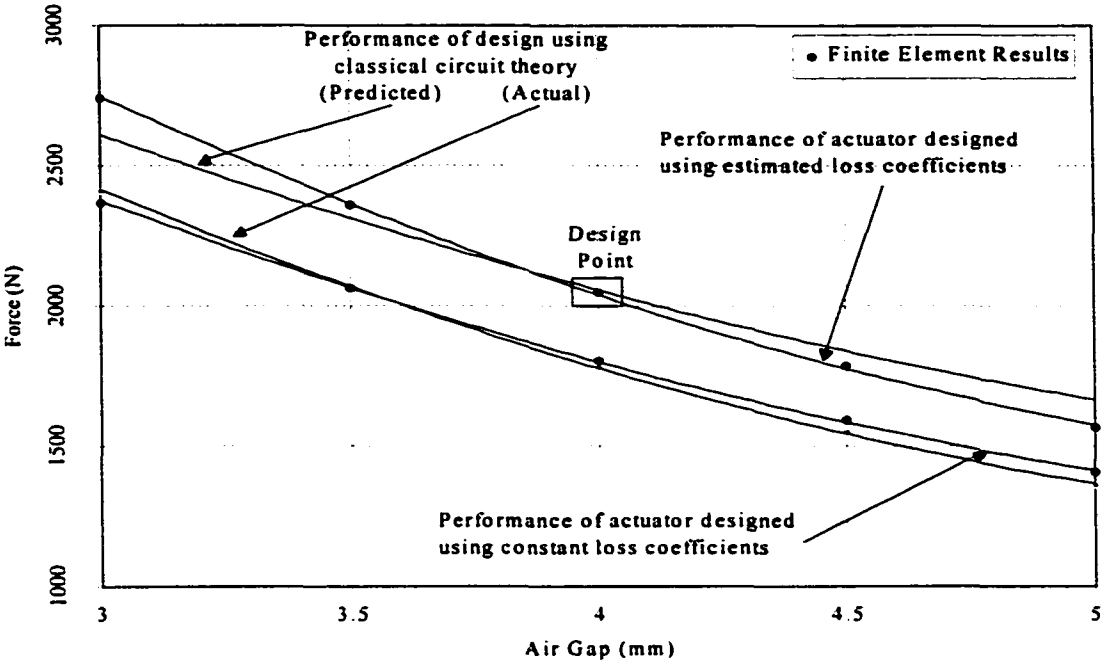

Figure 4.24: Actuator Performance for Designs Using Classical Circuit Theory and Extended Circuit Theory with Constant and Variable Loss Coefficients

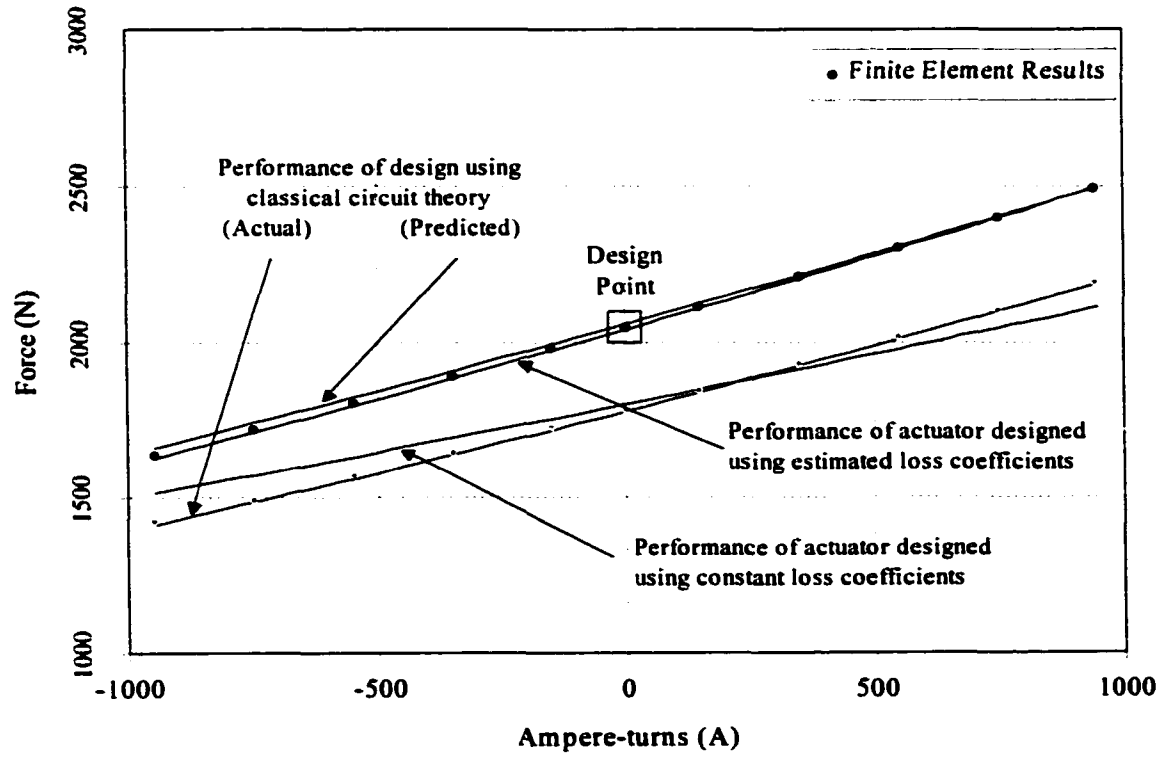

Figure 4.25: Actuator Performance of Designs Using Classical Circuit Theory and Extended Circuit Theory with Constant and Variable Loss Coefficients

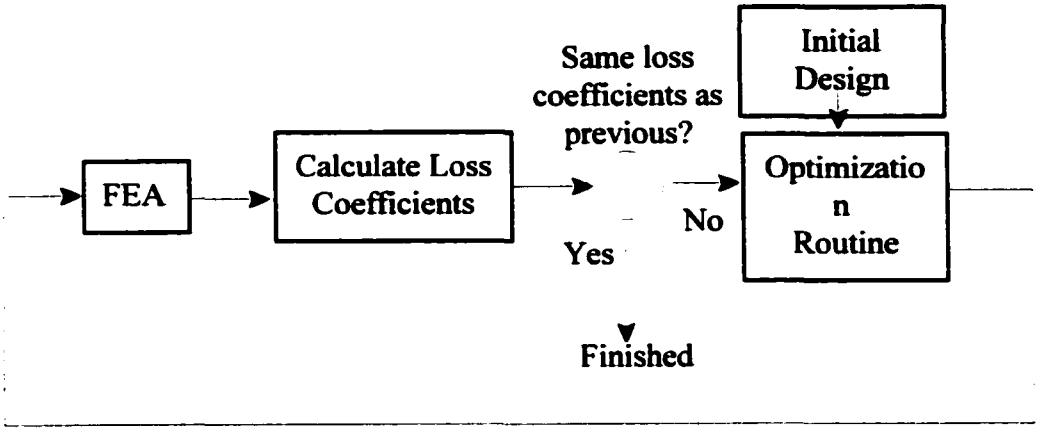

Iterative Approach

Figure 4.26: Optimization Techniques

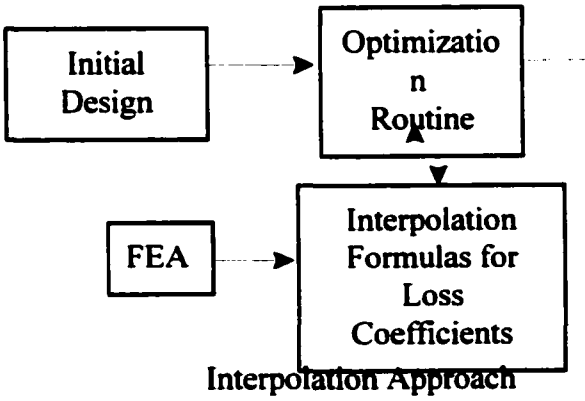

Interpolation Approach

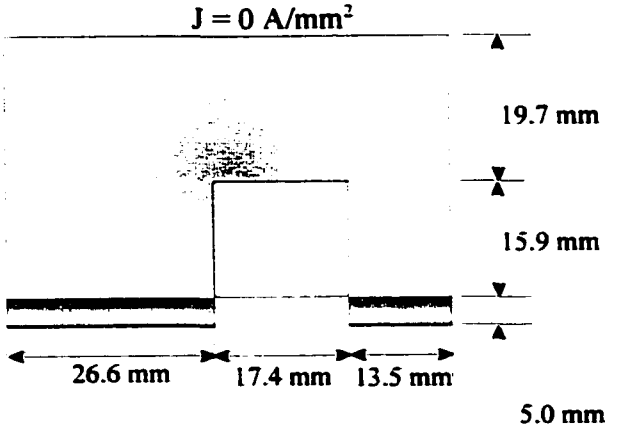

Figure 4.27: Optimized Actuator Configuration

This design method provides a unique approach for the design of magnetic bearings. Not only is the final design optimally suited to the specifications of the designer, but it also results in a very accurate model if the finite element results are correct. The method allows design constraints to be easily incorporated. In this case, the bearing was optimized for minimum power but the objective statement could be easily modified to maximize or minimize force, stiffness, weight, and volume, as well as many other possibilities.

5. FRACTIONAL ORDER BEHAVIOR OF EDDY CURRENTS

Eddy currents are electrical currents induced in conductive materials due to time-varying magnetic fields. These currents can produce desirable effects such as electro-dynamic levitation used by maglev vehicles, or undesirable effects such as power loss, rotor heating, and electromagnetic drag. In either case, the effects of the eddy currents must be accurately modeled.

In recent years the observed "half order behavior" of eddy currents has been a topic of discussion by experts in the field of magnetic suspension. These discussions arose due to the recurrence of an odd behavior in the frequency response of electromagnetic systems. Specifically, roll-offs of 10 dB per decade (instead of 20 dB) and phase responses that asymptote to 45° (instead of 90°) were observed in experimental data and can also be seen in some of the classical analytical solutions.

This section discusses the fractional order behavior of eddy currents as described by Maxwell's equations and introduces the concept of fractional order calculus along with a brief historical survey. The research effort discussed in the next two sections is focused on combining the various eddy current models into a single, complete model using a fractional calculus approach.

5.1. Description of Eddy Currents

The governing equations describing eddy current behavior are developed from Maxwell's Equations discussed in Section 2.1 and Section 2.6. The governing equations are repeated here for thoroughness.

$$\nabla \times \vec{E} = -\frac{\partial \vec{B}}{\partial t} \tag{5.1}$$

$$\nabla \cdot \vec{B} = 0 \tag{5.2}$$

$$\nabla \times \vec{H} = \vec{J} \tag{5.3}$$

In addition, there are two constitutive relations that need to be included. The relation between the current in a conductor and the electric field is given in Eq. 5.4, and the relation between the flux density and the magnetic field strength in a conductor is given in Eq. 5.5.

$$\vec{J} = \sigma \vec{E} \tag{5.4}$$

$$\vec{B} = \mu_0 \mu_r \vec{H} \tag{5.5}$$

The following derivation can be found in most fundamental electromagnetic texts; it is presented here for thoroughness. The first order differential equations in terms of E and H can be combined into a second order equation in terms of H only. Substituting Eq. 5.4 into Eq. 5.3 and taking the curl of both sides results in,

$$\nabla \times \left(\nabla \times \vec{H}\right) = \nabla \times \left(\sigma \vec{E}\right) \tag{5.6}$$

This equation can be modified with the use of two identities [Beyer, 1991]:

$$\begin{aligned} \nabla \times \left(\nabla \times \vec{H}\right) &= \nabla \cdot \left(\nabla \cdot \vec{H}\right) - \nabla^2 \vec{H} \\ \nabla \times \left(c\vec{H}\right) &= (\nabla c) \times \vec{H} + c\left(\nabla \times \vec{H}\right) \end{aligned} \tag{5.7}$$

Applying the first identity to the left side of Eq. 5.6 and the second to the right side of Eq. 5.6 results in Eq. 5.8.

$$\nabla\times(\nabla\cdot\bar{H})-\nabla^2\bar{H}=\nabla\sigma\times\bar{E}+\sigma(\nabla\times\bar{E}) \tag{5.8}$$

Substituting Eq. 5.5 into Eq. 5.2 yields,

$$\nabla\cdot(\mu\bar{H})=\bar{H}\cdot\nabla\mu+\mu(\nabla\cdot\bar{H})=0 \tag{5.9}$$

This can be rearranged into the form of Eq. 5.10 and substituted into the left side of Eq. 5.8.

$$\nabla\cdot\bar{H}=-\frac{1}{\mu}(\bar{H}\cdot\nabla\mu) \tag{5.10}$$

The dependence on E in the first term on the right of Eq. 5.8 can be removed with the aid of Eqs. 5.2 and 5.4.

$$\nabla\sigma\times\bar{E}=\frac{1}{\sigma}(\nabla\sigma\times\bar{H})=\frac{1}{\sigma}(\nabla\sigma\times(\bar{\nabla}\times\bar{H})) \tag{5.11}$$

The last term on the left side of Eq. 5.8 can be replaced by Eq. 5.1 where,

$$(\nabla\times\bar{E})=-\frac{\partial\bar{B}}{\partial t}=-\frac{\partial\bar{B}}{\partial\bar{H}}\frac{\partial\bar{H}}{\partial t} \tag{5.12}$$

With the use of Eqs. 5.10, 5.11, and 5.12, Eq. 5.8 can now be written as,

$$\nabla^2\bar{H}+\frac{1}{\mu}\nabla(\bar{H}\cdot\nabla\mu)+\frac{1}{\sigma}\nabla\sigma\times(\nabla\times\bar{H})=\sigma\frac{\partial\bar{B}}{\partial\bar{H}}\frac{\partial\bar{H}}{\partial t} \tag{5.13}$$

Eq. 5.13 describes the magnetic field strength inside a conducting medium with non-uniform permeability and conductivity. The classical formulations are developed for materials of constant permeability and conductivity. Applying these assumptions, the governing differential equation for field inside a conducting medium becomes,

$$\nabla^2\bar{H}=\mu_0\mu_r\sigma\frac{\partial\bar{H}}{\partial t} \tag{5.14}$$

This is the vector form of the diffusion equation. In rectangular Cartesian coordinates this equation expands to,

$$\begin{aligned}
\frac{\partial^2 H_x}{\partial x^2}+\frac{\partial^2 H_x}{\partial y^2}+\frac{\partial^2 H_x}{\partial z^2} &= \mu_0\mu_r\sigma\frac{\partial H_x}{\partial t} \\
\frac{\partial^2 H_y}{\partial x^2}+\frac{\partial^2 H_y}{\partial y^2}+\frac{\partial^2 H_y}{\partial z^2} &= \mu_0\mu_r\sigma\frac{\partial H_y}{\partial t} \\
\frac{\partial^2 H_z}{\partial x^2}+\frac{\partial^2 H_z}{\partial y^2}+\frac{\partial^2 H_z}{\partial z^2} &= \mu_0\mu_r\sigma\frac{\partial H_z}{\partial t}
\end{aligned} \tag{5.15}$$

5.2. One Degree-of-Freedom Systems

The general behavior of eddy currents can be illustrated by examining the simple 1-DOF system of a semi-infinite flat plate. The behavior of the eddy currents in the flat plate can be used to define the eddy current skin depth along with the categorization of inductance limited and resistance limited systems.

5.2.1. Semi-Infinite Plate

One of the most fundamental eddy current problems is that of a semi-infinite flat plate of thickness *b*, as shown in Fig. 5.1.

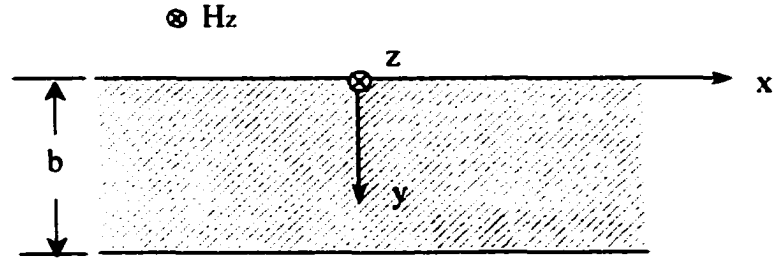

Figure 5.1: Semi-Infinite Flat Plate

The only non-zero field component is H_z and it is only a function of y and t, where H_z is specified to vary sinusoidally. For this situation Eq. 5.14 reduces to,

$$\frac{\partial^2 H_z}{\partial y^2} = \mu_0 \mu_r \sigma \frac{\partial H_z}{\partial t} \tag{5.16}$$

This second order partial differential equation can be solved using separation of variables with the substitution $H_z(y,t) = H(y)G(t)$. Substituting $H_z(y,t)$ into Eq. 5.17 results in,

$$\frac{1}{\mu_0 \mu_r \sigma} \frac{1}{H} \frac{d^2 H}{dy^2} = \frac{1}{G} \frac{dG}{dt} \tag{5.17}$$

H_z varies sinusoidally with time, so $G(t)$ can be defined as $G(t)=e^{j\omega t}$ where ω is the frequency of oscillation. $H(y)$ can be written as an ordinary differential equation with constant coefficients. Solving for $H(y)$ yields,

$$H(y) = C_1 e^{\alpha y} + C_2 e^{-\alpha y}$$
$$\alpha = \frac{1+j}{\partial} \qquad \delta = \sqrt{\frac{2}{\mu_0 \mu_r \sigma \omega}} \tag{5.18}$$

where C_1 and C_2 are constants to be determined by the boundary conditions. The variable δ is known as the skin depth and will be discussed in more detail in Section 5.2.2. Consider a thick plate where b is very large, the field intensity at $y = b$ is zero and the field intensity on the surface is specified by H_s. Applying the boundary conditions results in,

$$H(y) = H_s e^{-\alpha y} \tag{5.19}$$

The current density induced in the conducting plate can be found using Eq. 5.2 and Eq. 5.19, where J_S is the current density on the surface of the plate.

$$\bar{J} = \nabla \times \bar{H} = \frac{dH(y)}{dy} \hat{i} = -\alpha H_s e^{-\alpha y} \hat{i} = -J_s e^{-\alpha y} \hat{i} \tag{5.20}$$

The eddy current per unit width flowing in the x direction is found by integrating the current density from $-\infty$ to 0.

$$I_{eddy} = -J_s \int_{-\infty}^{0} e^{-\alpha y} dy = \frac{J_s}{\alpha} = \frac{J_s \delta}{2}(1-j) \tag{5.21}$$

The magnitude and phase of the integrated eddy current is given by,

$$\left|I_{eddy}\right| = \frac{J_s}{\sqrt{\mu_0 \mu_r \sigma}} \omega^{-1/2} \qquad \phi = -45° \tag{5.22}$$

The normalized magnitude and phase of the current density as a function of penetration depth are shown in Fig. 5.2. The diffusing wave behavior of the induced eddy current is clear in the magnitude plot as well as the depth dependant phase lag.

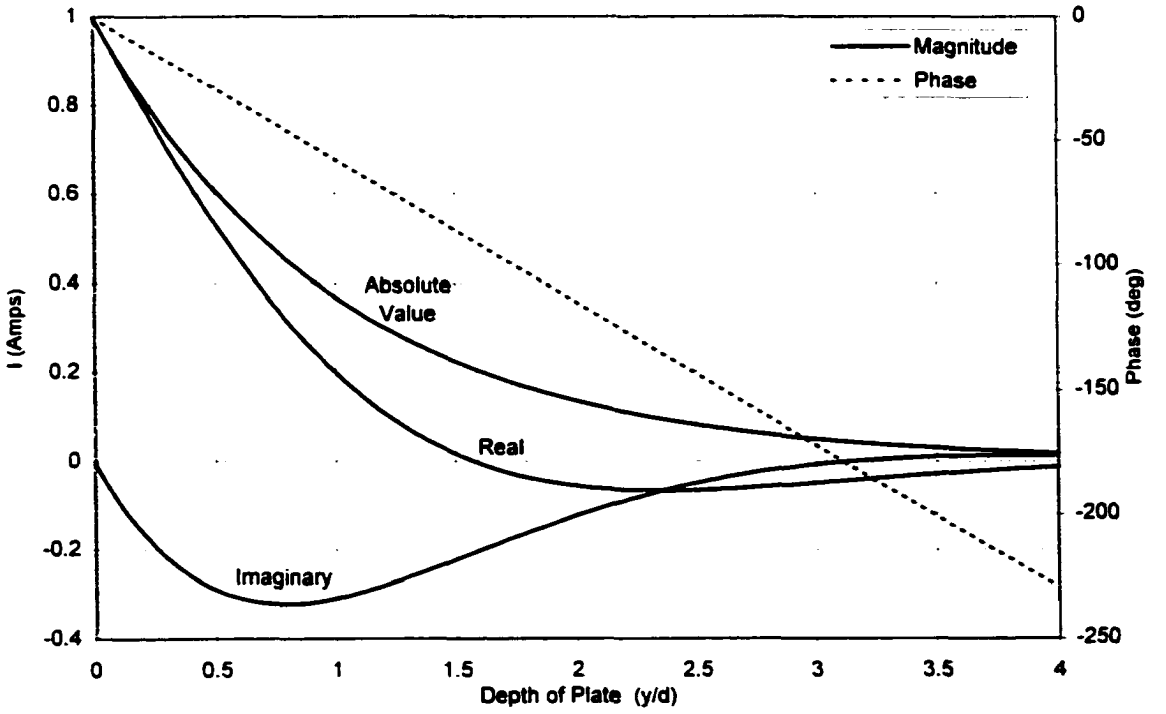

Figure 5.2: Magnitude and Phase of J vs Depth of Plate, ω = 100 Hz

Thus, the magnitude of the integrated eddy current varies as $\omega^{-1/2}$ with a 45° phase lag. If this were analyzed using a Bode plot, the slope of the magnitude in dB/decade would be,

$$\frac{d|I_{eddy}|}{d\{\log_{10}(\omega)\}} = \frac{d}{d\{\log_{10}(\omega)\}} 20\log_{10}\left(c\omega^{-1/2}\right)$$
$$\frac{d|I_{eddy}|}{d\{\log_{10}(\omega)\}} = \frac{d}{d\{\log_{10}(\omega)\}} \left(20\log_{10}(c) + 20\log_{10}\left(\omega^{-1/2}\right)\right) \tag{5.23}$$
$$\frac{d|I_{eddy}|}{d\{\log_{10}(\omega)\}} = -10\frac{d}{d\{\log_{10}(\omega)\}}\log_{10}(\omega) = -10$$

It is clear from Eqs. 5.22 and 5.23 that the magnitude and phase of the Bode plot behave as if it were a "half-order" system, i.e., half the roll-off and half the phase of a simple pole. The magnetic field produced by this eddy current would oppose the driving field that produced H_S on the surface of the plate. Thus, the magnetic field in the vicinity of the flat plate would contain a contribution from the half-order pole.

5.2.2. Eddy Current Skin Depth

The skin depth as derived in Eq. 5.18 is a defined as,

$$\delta = \sqrt{\frac{2}{\mu_0 \mu_r \sigma \omega}} \tag{5.24}$$

It is a relationship between the material properties of the conducting material and the frequency of excitation and has units of length. The meaning of the skin depth can be seen by examining the eddy currents induced in the semi-infinite plate. The integrated eddy current for the plate was given in Eq. 5.21 and can be re-written as,

$$I_{eddy} = \frac{J_s \delta}{\sqrt{2}} e^{-j\pi/4} \tag{5.25}$$

This eddy current is equivalent to the r.m.s. of J_S flowing in the conductor with a depth of δ. Thus, the skin depth is representative of the depth of penetration from the magnetic field and

the resulting eddy currents. Further insight can be gained by examining the instantaneous part of the magnetic field in the plate given by Eq. 5.20.

$$\mathrm{Re}\{H(y)\} = \mathrm{Re}\{H_s e^{\alpha y} e^{j\omega t}\} = H_s e^{y/\delta} \cos\left(\omega t + \frac{y}{\delta}\right) \tag{5.26}$$

The magnitude of the field strength decays exponentially with depth into the conducting material. It should be clear that the field strength and the eddy currents extend beyond the depth of y = δ. The exact percentage of field excluded is a function of y/δ according to the equation, $\% = (1-e^{-n}) \times 100$, where $n = y/\delta$. Thus, when $y = \delta$, 63% of the field intensity has been excluded. At $y = 2\delta$ the percentage increases to 86% and when $y = 4\delta$ the majority of the field, 98%, has been excluded.

5.2.3. Inductance Limited and Resistance Limited Systems

The power loss of a system can be categorized according to its skin depth. Consider the semi-infinite plate of thickness $2b$ where the field intensity is defined to be H_S on the upper and lower surfaces. The field strength inside the conducting material is given by Eq. 5.19. Stoll showed that the power loss due to eddy currents is given by [Stoll, 1974],

$$P = \frac{H_s^2}{\sigma\delta}\left(\frac{\sinh(2b/\delta) - \sin(2b/\delta)}{\cosh(2b/\delta) + \cos(2b/\delta)}\right) \tag{5.27}$$

Two distinct cases can now be considered. The first case to consider is when the plate thickness is much larger than the skin depth. In this case $\sinh(2b/\delta) \approx \cosh(2b/\delta)$ and the magnitude is much larger than $\sin(2b/\delta)$ and $\cos(2b/\delta)$. This allows the fraction in Eq. 5.27 to be approximated by 1. Thus, when the current is excluded from the majority of the material by the shielding effects of the eddy currents the power loss is,

$$P \approx \frac{H_x^2}{\sigma\delta} \qquad 2b >> \delta \tag{5.28}$$

When 2b is much less than δ, the terms in the second fraction can be approximated using the truncated series expansions, $cosh(2b/\delta)+cos(2b/\delta) \approx 2$ and $sinh(2b/\delta)-sin(2b/\delta) \approx (2b/\delta)^3/3$ when $2b/\delta << 1$. Thus, when the eddy currents are fully distributed across the depth of the plate the power loss is,

$$P \approx \frac{1}{3}\omega^2\sigma\mu_0^2\mu_r^2 H_x^2 b^3 \qquad 2b << \delta \tag{5.29}$$

It is clear that the losses produced by the eddy currents vary significantly with plate thickness. In the case of the thick plate, $2b>>\delta$, the current distribution into the plate is limited by the exclusionary effects of the eddy currents themselves. This type of system is referred to as an inductance-limited system. In the case of the thin plate, $2b<<\delta$, the currents are limited by the small amount of space available for the currents to flow. This type of system is known as a resistance-limited case.

5.3. Lumped Parameter Analysis of Eddy Currents

It is common in many fields of engineering to model systems as a series of lumped parameters instead of as a continuous system. The same approach can be applied to the analysis of eddy currents and is commonly referred to as the transformer model, or the single time constant model. The model can be used to show the first order pole-zero behavior of a system at low frequencies and can be enhanced to show a fractional half-order behavior at higher frequencies.

5.3.1. Transformer Model

Consider the pair of current loops shown in Fig. 5.3. The driving loop is the flux producing coil and the shorted secondary supports the eddy currents. The first expression in Eq. 5.30 represents conditions in the driving current loop, the second represents the shorted secondary loop where I_e, L_e, and R_e are the current, inductance, and resistance of the eddy current circuit, respectively. L_m is the mutual inductance between the driving current loop and the eddy current loop.

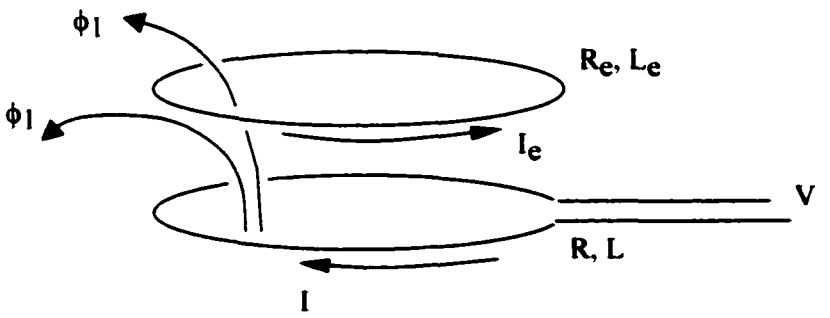

Figure 5.3: Primary and Secondary Current Loops

$$V = IR + L\frac{dI}{dt} + L_m\frac{dI_e}{dt} + L_m\frac{dI_e}{dt} + \cdots$$
$$0 = I_eR_e + L_e\frac{dI_e}{dt} + L_m\frac{dI}{dt} \qquad (5.30)$$

The assumption imposed on this model is that the eddy currents must be independent of frequency. This is the case when the skin depth is much greater than the thickness of the material. In other words, the current distribution across the thickness of the plate is relatively uniform. Under these circumstances, the resulting field source and eddy current region can be modeled as a single time constant model.

The model is derived by defining the magnetic field as proportional to the driving current, $\{B\}=[K]\{I\}$. In the near presence of a conducting media, the total field also has a component from the induced eddy currents, $\{B\}=[K]\{I\}+[K_e]\{I_e\}$. Taking the Laplace transform of the second part of Eq. 5.30 allows the eddy current, $\{I_e\}$, to be written in terms of the driving current, $\{I\}$.

$$\frac{I_e(s)}{I(s)}=-\frac{sL_m}{(R_e+sL_e)} \tag{5.31}$$

For simplicity, consider the magnetic field along the line that passes through the center of the two loops, $B(r,z) = B_z(0,z)$. The field at a point on this line can be written as,

$$B_z = kI + k_e I_e \tag{5.32}$$

where k and k_e are proportionality constants. Substituting Eq. 5.32 in for I_e results in [Britcher, 1994],

$$G(s)=\frac{B_z}{I}=k\left(1-\frac{k_{el}L_{ml}s}{k(R_{el}+L_{el}s)}\right)=k\frac{1+as}{1+bs} \tag{5.33}$$

Thus, the transfer function between the flux density and the driving current can be modeled as a simple pole-zero pair. The coefficients k, a and b can be determined from the system parameters L_e, L_m, and R_e, or from finite element data or from experimental data using a curve fitting algorithm.

5.3.2. Development of a Fractional Order Transformer Model

Consider again the semi-infinite plate of thickness 2b discussed in Section 5.2. The eddy current induced in the plate was given in Eq. 5.22. This can be rewritten as,

$$I=\frac{J_s\delta}{2}(1-j)=\frac{J_s\delta}{\sqrt{2}}e^{-j\pi/4} \tag{5.34}$$

It was shown in Section 5.2.2. that this current is equivalent to the r.m.s. of the surface

current density flowing uniformly in a layer of thickness δ with a phase lag of 45°. Now consider how this will affect the resistance of the plate. The relationship between the resistance and the cross sectional area containing the eddy currents is found directly from the definition of resistance.

$$R = \frac{1}{\sigma}\frac{L}{A} \tag{5.35}$$

Where L is the length of the material, A is the cross sectional area of the plate, and σ is the electrical conductivity of the material. Thus, the resistance per unit length and width of a plate of thickness b is,

$$R = \frac{1}{\sigma b} \tag{5.36}$$

If $b << \delta$ then the resistance given by Eq. 5.36 is valid for the plate. However, if the skin depth decreases (or the plate thickness increases) to a point where this is no longer true then the depth of the eddy currents no longer cover the entire cross sectional area of the plate. It might be tempting to replace the depth b with δ using the r.m.s. value of the current as was previously shown when $b >> \delta$. However, when $b \approx \delta$ this is no longer true because some of the field passes through the thickness of the plate to the other side. Thus, the r.m.s. value cannot be used when $b \approx \delta$. Instead of using the r.m.s. value of the current flowing with a depth δ, the true current can be used, penetrating a specified depth, say $n\delta$, where n is a constant. If n is set equal to 4, then 98% of the magnetic field will be contained in the conductive material.

At the point where $\delta = b/4$, the effective resistance will no longer be constant but will start to vary by $1/\delta$, or as $\omega^{1/2}$. This idea of a frequency dependant resistance was discussed by Stoll in 1974 when calculating the power dissipation in the semi-infinite plate, $P = I^2R$, where I

was the r.m.s. current and R was defined in terms of δ. He briefly discussed the relationship between the DC resistance and the AC resistance but only for the extreme cases, when $b >> \delta$ or $\delta << b$ [Stoll, 1974].

To model the resistance over the entire frequency range it must be defined in terms of a critical frequency, the frequency at which the current density is not fully distributed across the cross section of the material. The critical frequency will be defined in terms of the skin depth ratio, $b/\delta = n$, where n should be greater than or equal to 4.

$$\omega_{cr} = \frac{n^2}{b^2}\frac{2}{\sigma\mu_0\mu_r} \tag{5.37}$$

Since the r.m.s. current is no longer being used, the effective depth of the resistance must be defined in terms of the active depth of the instantaneous eddy currents. Subsequently, the frequency dependant resistance must also contain the phase information. From Eq. 5.28 the averaged phase lag of the eddy current is 45°, resulting in the complex form of the AC resistance,

$$R_{AC} = \begin{cases} \dfrac{1}{\sigma b} & \delta \geq \dfrac{b}{n} \rightarrow \omega < \omega_{crit} \\ \dfrac{1}{n\delta\sigma}(1+j) & \delta < \dfrac{b}{n} \rightarrow \omega \geq \omega_{crit} \end{cases} \tag{5.38}$$

or using the unit step function U,

$$\frac{R_{AC}}{R_{DC}} = 1 + \left(\frac{b}{n\delta}(1+j) - 1\right)U(1-\omega_{crit}) \tag{5.39}$$

The AC resistance can also be written in terms of frequency by expanding the definition of δ. The real part of the effective resistance can be written as,

$$R_{AC} = \frac{bR_{DC}}{n\delta} = R_{DC}\frac{b}{n}\sqrt{\frac{\sigma\mu_0\mu_r}{2}}\omega^{1/2} = R_{DC}\left(\frac{\omega}{\omega_{cr}}\right)^{1/2} \tag{5.40}$$

The complex component can be rewritten using the identity,

$$(1+j)=\sqrt{2}j^{1/2} \tag{5.41}$$

The frequency dependent resistance can then be written in terms of the complex frequency $s=j\omega$.

$$R_{AC}=\sqrt{2}R_{DC}\left(\frac{s}{\omega_{cr}}\right)^{1/2} \tag{5.42}$$

This allows the resistance to be written as,

$$R_{AC}(s)=R_{DC}+\left(\sqrt{\frac{2}{\omega_{cr}}}R_{DC}s^{1/2}-R_{DC}\right)U(1-s_{cr}) \tag{5.43}$$

Substituting R_{AC} into Eqs. 5.32 and 5.33 and limiting consideration to the higher frequencies results in,

$$G(s)=k\frac{1+as^{1/2}}{1+bs^{1/2}} \qquad \omega>\omega_{cr} \tag{5.44}$$

Thus, the half-order power appears in both the diffusion model and in the augmented lumped parameter model. These two examples show the tendency of the half-order systems to appear from the most fundamental eddy current models. The transition between Eqs. 5.33 and 5.44 is discussed in detail in Section 6.

5.4. Fractional Calculus

5.4.1. A Brief History of Fractional Calculus

The idea of fractional order calculus is not on the forefront of modern mathematical theory and is rarely discussed in common calculus texts. This does not, however, mean that it is a new or unexplored concept. The examination of fractional order derivatives and integrals first arose in 1695 when Leibniz introduced the now common derivative operator notation

d^n/dx^n. This notation sparked L'Hôpital to ask Leibniz the question "What if n be 1/2?" With this simple inquiry, the field of fractional calculus was born. The historical development of fractional calculus was aided by the likes of Euler, Laplace, Fourier, Abel, Liouville, Riemann, and Laurent.

Despite the inquiry in the late 1600s and some early investigations by Euler in 1730 and indirectly by Lagrange in 1772, the first systematic investigation into the field occurred in the early 1800s. In 1812, P. S. Laplace defined a fractional derivative in terms of an integral. The first book containing information about fractional derivatives appeared in 1837 by S. F. Lacroix, though it only slightly mentioned arbitrary order systems. In 1822 Joseph B. Fourier developed a definition for an arbitrary order derivative based on an integral representation of $f(x)$. Fractional calculus was first credited as a tool in solving a problem in 1823 when N. H. Abel used it to solve the tautochrone problem[1].

The first major study of fractional calculus was performed by Liouville in 1832 which consisted of a set of three memoirs. He developed what has now become known as Liouville's first and second formulas, which defined the arbitrary derivative of the functions $f(x) = e^{ax}$ and $f(x) = e^{-ax}$. Liouville is also credited with being the first to introduce the idea of the complementary function associated with fractional derivatives. His argument was simply that if the solution of $d^n y/dx^n = 0$ had a complementary solution of $y(x) = c_0 x + c_1 x + c_2 x^2 + \ldots + c_{n-1} x^{n-1}$, then the solution of $d^u y/dx^u = 0$, where u is arbitrary, should also have a complementary solution. Around 1833, Peacock and Greatheed examined the complementary function and published concerns about its indeterminate nature.

---

[1] The tautochrone problem determines the shape of the curve for which the time of descent of a frictionless point mass under the effects of gravity is independent of its initial starting location.

The presently accepted form of the fractional derivative was developed by Bernhard Riemann as a student and published posthumously in 1847. He was trying to develop a generalized Taylor series,

$$\frac{d^{-v}}{dt^{-v}} f(x) = \frac{1}{\Gamma(v)} \int_a^t (x-\tau)^{v-1} f(\tau) d\tau + \psi(x) \tag{5.45}$$

The complementary function $\psi(x)$ was introduced because of the ambiguity of the lower limit *a*. Riemann saw the need for the complementary solution in order to have a measure of the deviation from the law of indices, which holds true for integer values of m and n. The modern definition of the fractional derivative is known as the Riemann-Liouville definition. It was developed from Cauchy's integral equation from a combination of work done by N. Ya. Sonin, A. V. Letnikov, and H. Laurent. The modern formulation is discussed in Section 5.4.2.

The first text book entirely dedicated to the study of fractional calculus was written in 1974 by Oldham and Spanier. The first international conference was sponsored by the National Science Foundation and held at the University of New Haven, Connecticut, in 1974. Between the years of 1975 and 1993, more than 400 papers were published on the subject.

Many texts cover the history of fractional calculus, but the historical surveys by Oldham and Spanier [Oldham, 1974] and Miller and Ross [Miller, 1993] provide the most thorough discussions. Additionally, Oldham and Spanier have assembled a chronological reference list discussing the history and relevance of the publications between 1695 and 1974.

5.4.2. Introduction to Fractional Calculus

Fractional calculus can be viewed as the unification and generalization of integer order differentiation and integration. Several forms of a common operator capable of describing both differentiation and integration have been suggested by different authors, but the most commonly accepted is that originated by [Davis, 1936].

$$ {}_aD_t^{\alpha} f(t) \tag{5.46} $$

The subscripts a and t indicate the limits of differentiation or integration, referred to as terminals in fractional calculus. The superscript α represents the order of differentiation or the number of integrals.

There are two commonly used basis definitions for integration of arbitrary order, the Riemann-Liouville definition and the Grünwald-Letnikov definition [Pudlubny, 1999]. The Riemann-Liouville defininition is given in Eq. 5.47.

$$ {}_aD_t^{-\alpha} f(t) = \frac{1}{\Gamma(\alpha)} \int_a^t (t-\tau)^{\alpha-1} f(\tau) d\tau \tag{5.47} $$

The value of a is between $-\infty$ and t, the value of α represents the order of integration where $\alpha \geq 0$ and real, and $\Gamma(\alpha)$ is the Gamma function. The Grünwald-Letnikov definition is given in Eq. 5.48.

$$ {}_aD_t^{-\alpha} f(t) = \lim_{n \to \infty} \frac{\left(\frac{t-a}{n}\right)^{-q}}{\Gamma(-\alpha)} \sum_{j=0}^{n-1} \frac{\Gamma(j-\alpha)}{\Gamma(j+1)} f\left(t - j\frac{t-a}{n}\right) \tag{5.48} $$

Early texts on the subject were split between these two forms but most modern authors prefer to use the Riemann-Liouville definition due to its more convenient form.

The derivative of arbitrary order is readily derived using the Riemann-Liouville form by taking the k[th] derivative of Eq. 5.48. Here, k is an integer greater than α and the value of α is between 0 and 1.

$$ {}_aD_t^{k-\alpha} f(t) = \frac{1}{\Gamma(\alpha)} \frac{d^k}{dt^k} \int_a^t (t-\tau)^{\alpha-1} f(\tau) d\tau \tag{5.49} $$

One of the largest problems in dealing with fractional differintegrals is that under general circumstances they do not commute, i.e., the law of indices in Eq. 5.50 is not satisfied.

$$ {}_aD_t^{\mu}\,{}_aD_t^{\nu} f(t) = {}_aD_t^{\nu}\,{}_aD_t^{\mu} f(t) = {}_aD_t^{\mu+\nu} f(t) \tag{5.50} $$

To get around this problem, contemporary fractional calculus has been limited to systems where $f(t)$ and its derivatives are all zero at the time of initialization, $t = a$. This is one of the reasons that fractional calculus has remained under-utilized in the field of engineering.

This point was illustrated by Oldham and Spanier using the following example [Oldham, 1974]. Consider the system defined by,

$$ \frac{d^Q f(x)}{dx^Q} = F \tag{5.51} $$

where F is a known forcing function, Q is an arbitrary value, and $f(x)$ is the unknown function. The apparent solution is found by "inverting" the system by taking the Q^{th} integral of both sides.

$$ f(x) = \frac{d^{-Q} F}{dx^{-Q}} \tag{5.52} $$

This assumes that

$$ f(x) - \frac{d^{-Q}}{dx^{-Q}} \left(\frac{d^Q f(x)}{dx^Q} \right) = 0 \tag{5.53} $$

However, Oldham and Spanier showed that when Q is not an integer the most general form of Eq. 5.53 is,

$$f(x)-\frac{d^{-Q}}{dx^{-Q}}\left(\frac{d^{Q}f(x)}{dx^{Q}}\right)=C_1x^{Q-1}+C_2x^{Q-2}+\cdots+C_mx^{Q-m} \tag{5.54}$$

Thus, the most general form of the solution of Eq. 5.52 is,

$$f(x)=\frac{d^{-Q}F}{dx^{-Q}}+C_1x^{Q-1}+C_2x^{Q-2}+\cdots+C_mx^{Q-m} \tag{5.55}$$

where $0 < Q \leq m < Q + 1$ or $m = 0$ for $Q \leq 0$.

Lorenzo and Hartley describe this inadequacy of the composition law as a problem with the fundamental basis definition of fractional calculus [Lorenzo, 1998]. They have written a series of technical papers on this topic and have offered the following definitions for the fractional integrand. The modified definition will be valid for any time $a \leq c < t$ and $f(t) = 0$ for all $t \leq a$,

$${}_cD_t^{-\alpha}f(t)=\frac{1}{\Gamma(\alpha)}\int_c^t(t-\tau)^{\alpha-1}f(\tau)d\tau+\Psi(f,-\alpha,a,c,t) \tag{5.56}$$

It should be noted that this is the same formulation derived by Bernhard Riemann in 1847. Riemann referred to the additional term as a complementary solution while Lorenzo and Hartley defined it as an initialization function. Riemann's introduction of the complementary function stirred up quite a bit of controversy over whether or not the complementary function actually exists. Others who investigated the existence of the complementary function included Cayley, Liouville, Davis, and Peacock [Miller, 1993]. Lorenzo and Hartley introduced the formalized initialization function in the hope of generalizing fractional calculus for scientist and engineers.

The initialization functions are subcategorized into two groups. The first is defined as *terminal initialization*, for this case the differintegral is initialized by differintegrating prior

to the start time at $t = c$. The second type is called *side initialization;* this is a fully arbitrary initialization. The initialization function for the terminal case is defined such that ${}_aD_t^{-q} f(t) = {}_cD_t^{-q} f(t)$ for all $t > c$. Substituting Eq. 5.47 and 5.56 into this expression yields,

$$\frac{1}{\Gamma(\alpha)}\int_a^t (t-\tau)^{\alpha-1} f(\tau)d\tau = \frac{1}{\Gamma(\alpha)}\int_c^t (t-\tau)^{\alpha-1} f(\tau)d\tau + \Psi(f,-\alpha,a,c,t) \qquad (5.57)$$

Since,

$$\int_a^t f(\tau)d\tau = \int_a^c f(\tau)d\tau + \int_c^t f(\tau)d\tau \qquad (5.58)$$

The initialization term for the case of terminal initialization is,

$$\Psi(f,-\alpha,a,c,t) = {}_aD_c^{-\alpha} f(t) = \frac{1}{\Gamma(\alpha)}\int_a^c (t-\tau)^{\alpha-1} f(\tau)d\tau \qquad (5.59)$$

The terminal initialization term has the effect of fractionally integrating the past history of $f(t)$ from $t = a$ to c. Consider the case when α is an integer value n. Substituting into Eq. 5.59 results in,

$$\Psi(f,-n,a,c,t) = \sum_{i=0}^{n} c_i t^i, i = 1,2,3... \qquad (5.60)$$

Eq. 5.60 is the standard solution consisting of the constants of integration. When α is a non-integer, the initialization function is a function of time, not just a constant at $t = a$.

The generalized definition of integer order differentiation is defined as,

$${}_cD_c^m f(t) = \frac{d^m}{dt^m} f(t) + \Psi(f,m,a,c,t) \qquad (5.61)$$

This is the generalized form, where the initialization function is zero in the case of integer order differentiation [Lorenzo, 1998]. The initialization function can be determined using the relationship ${}_aD_t^{-q} f(t) = {}_cD_t^{-q} f(t)$ for all $t > c$. It therefore follows that ${}_aD_t^m {}_aD_t^{-q} f(t) = {}_cD_t^m {}_cD_t^{-q} f(t)$. Restricting the order of differentiation to integers results in,

$$\frac{d^m}{dt^m}\left\{\frac{1}{\Gamma(\alpha)}\int_c^t (t-\tau)^{\alpha-1} f(\tau)d\tau + \Psi(f,-\alpha,a,c,t)\right\} + \Psi\left({}_a D_t^{-\alpha} f(t), m, a, c, t\right) = \frac{d^m}{dt^m}\left\{\frac{1}{\Gamma(\alpha)}\int_a^t (t-\tau)^{\alpha-1} f(\tau)d\tau + \Psi(f,-\alpha,a,a,t)\right\} + \Psi\left({}_a D_t^{-\alpha} f(t), m, a, a, t\right) \quad (5.62)$$

It is clear that the functions $\Psi(f,-\alpha,a,a,t)$ and $\Psi({}_aD_t^{-\alpha} f(t),-\alpha,a,a,t)$ are equal to zero. Combining the two integrals results in the expression for $\Psi({}_aD_t^{-\alpha} f(t),$m $,a,c,t)$.

$$\Psi\left({}_a D_t^{-\alpha} f(t), m, a, c, t\right) = \frac{d^m}{dt^m}\left\{\frac{1}{\Gamma(\alpha)}\int_a^c (t-\tau)^{\alpha-1} f(\tau)d\tau + \Psi(f,-\alpha,a,c,t)\right\} \quad (5.63)$$

Thus, the generalized fractional derivative as defined by Lorenzo and Hartley is,

$${}_c D_t^{(m-\alpha)} f(t) = \frac{d^m}{dt^m}\frac{1}{\Gamma(\alpha)}\int_c^t (t-\tau)^{\alpha-1} f(\tau)d\tau + \frac{d^m}{dt^m}\Psi(f,-\alpha,a,c,t) + \Psi\left({}_a D_t^{-\alpha} f(t), m, a, c, t\right) \quad (5.64)$$

The value of $m-\alpha > 0$ where m is the least positive integer greater than α, $t > c$, and the term $\Psi(f(t),-\alpha,a,c,t)$ is defined by Eq. 5.63. The differintegral equations defined by Lorenzo and Hartley are identical to the Riemann-Liouville definitions with the exception of the initialization functions.

Applications associated with fractional calculus are increasing with number due to the increased awareness of fractional systems by scientists and engineers. It is impractical to attempt to fully discuss these applications due to the inherent complexities. Instead, a list of applications offered by the authors of the primary texts is given in Table 5.1. The source of the summaries are listed with respect to the application.

Topic/Application	Reference
Acoustics, boundary layer, and turbulence	[Lorenzo, 1998]
Controls and dynamics	[Lorenzo, 1998], [Podlubny, 1999]
Diffusion	[Podlubny, 1999], [Lorenzo, 1998]
Electrical	[Podlubny, 1999], [Lorenzo, 1998]
Electrochemistry	[Lorenzo, 1998]
Fractal	[Lorenzo, 1998]
Rheology, viscoelasticity, and creep	[Podlubny, 1999], [Lorenzo, 1998]
Abel's integral equation	[Podlubny, 1999], [Miller, 1993]
Fractance	[Podlubny, 1999]
Electrode-electrolyte interface	[Podlubny, 1999]
Fractional multipoles	[Podlubny, 1999]
Electric conductance of biological systems	[Podlubny, 1999]
Reliability of steel wires	[Podlubny, 1999]
Potential theory	[Miller, 1993]
Weir notch	[Miller, 1993]

Table 5.1: Applications Modeled by Fractional Calculus

5.4.3. Control Theory of Fractional Order Systems

The purpose of this section is to expose the reader to the existence of fractional order control theory and to show the benefits of fractional order modeling, not to develop control theory for fractional order system. Along with a brief discussion of fractional order control methodologies two important points will be discussed. First, even though a fractional order system can often be approximated using an integer order formulation, that does not ensure that the control system based on the approximated model will be sufficient to control the process. This will be illustrated in a simple example. Second, the standard pole-zero analysis procedures used in integer order systems can be performed on fractional order systems via simple conformal transformations.

The first study of fractional order controllers was done by A. Oustaloup, a French engineer who developed the CRONE controller, CRONE is an acronym for *Commande Robuste d'Ordre Non Entier*, which roughly translates to non-integer order robust control. Details of this control method are given by Oustaloup [Oustaloup, 1995].

Another method used for fractional order systems is referred to as the $PI^{\lambda}D^{\mu}$ method. This method is a generalization of PID control where superscripts λ and μ are of arbitrary order. Thus, when λ and $\mu = 1$, it is the same as PID control, and when $\lambda = 0$ and $\mu = 1$, it is PD control, etc. It should be noted that the symbol μ is being used to be consistent with published notation and does not describe magnetic permeability. For more detailed information about this control method, see Podlubny [Podlubny, 1999].

Podlubny demonstrates an important point concerning the approximation of a fractional order system with an integer order system. His example uses the transfer function given in Eq. 5.66 with $\alpha = 0.9$, $\beta = 2.2$, $a_2 = 0.8$, $a_1 = 0.5$, and $a_0 = 1$.

$$G(s) = \frac{1}{a_2 s^{\beta} + a_1 s^{\alpha} + a_0} \tag{5.65}$$

This model is compared to the integer order model with $\alpha = 1$ and $\beta = 2$. The coefficients in Eq. 5.66 were determined using a least squares best fit method, similar to that discussed in Section 6. The results of the unit step response for both systems are shown in Fig. 5.4a and shows that the integer order transfer function does a good job at approximating the fractional order transfer function.

Next, a PD controller is designed for the system to yield a settling time of 2 sec, and a damping ratio of $\xi = 0.4$, the transfer function of the controller is given in Eq. 5.66 with $\mu = 1$.

$$G_c(s) = K_p + K_D s^{\mu} \tag{5.66}$$

The controller is applied to both the approximated integer order and fractional order systems; the results are shown in Fig. 5.4b. The integer order approximation demonstrates the desired results, but when the controller is applied to the actual system the controller does not meet the initial requirements. Podlubny also showed that the approximated system is much more sensitive to changes. Fig. 5.4c shows the same controller but this time with K_D changed from 2.7343 to 1. The change slightly decreased the settling time of the integer order approximation, but it made the actual fractional system go unstable.

Finally, Fig. 5.4d shows the results of the PD and PD$^{\mu}$ controller with $K_D = 3.7343$ and $\mu = 1.15$ applied to the fractional order controller. It is clear that the fractional order controller performs much better than the integer order controller. This example illustrates how important it can be to identify a fractional order system and implement the best suited control algorithm.

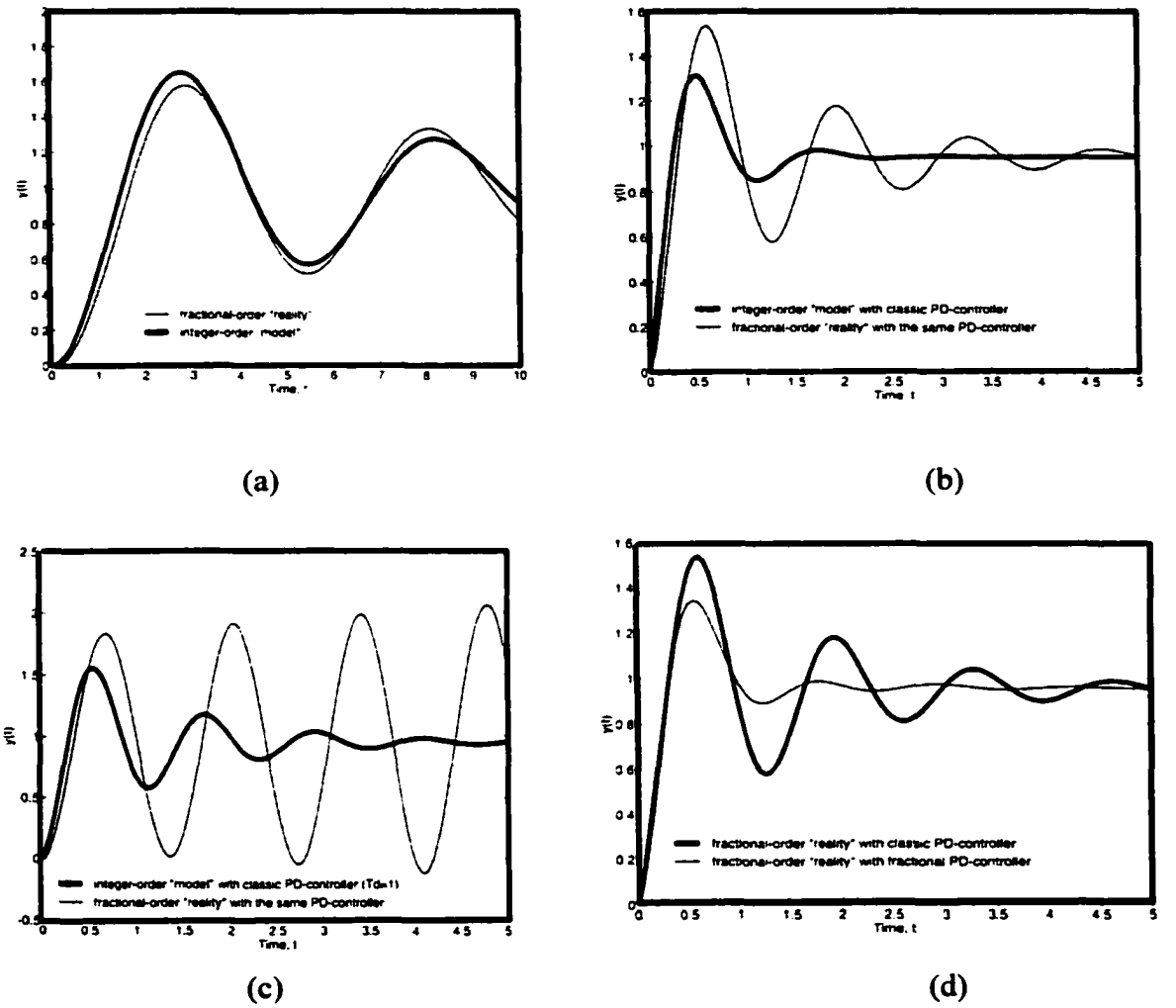

Figure 5.4: Unit Step Response of $G(s)$ and $\tilde{G}(s)$ [Podlubny, 1999]

Another way to design a control system for a fractional order system is using pole-zero placement. The standard pole-zero placement methods are limited to integer powers of s. For fractional powers of s the system must be transformed using conformal mapping. This can be illustrated by considering the linear fractional order differential equation,

$$ {}_0d_t^q x(t) = -ax(t) + bu(t) \tag{5.67}$$

For this example, $t = c = 0$, and all the initial conditions and initialization functions are equal to zero. Hartley and Lorenzo showed that the impulse response of this system was given by the F function, or the Robotnov-Hartley function [Hartley, 1998]. The function is very similar to the Mittag-Leffler function, E. These functions are defined in Eq. 5.68.

$$F_q[-at] = t^{q-1}\sum_{n=0}^{\infty}\frac{(-a)^n t^{qn}}{\Gamma(nq+1)} \quad q>0$$
$$E_q[at^q] = \sum_{n=0}^{\infty}\frac{a^n t^{nq}}{\Gamma(nq+1)} \quad q>0 \tag{5.68}$$

The Laplace transforms of these equations are given by,

$$L\{F_q[-at]\} = \frac{1}{s^q - a} \quad q>0$$
$$L\{E_q[at^q]\} = \frac{s^q}{s(s^q-1)} \quad q>0 \tag{5.69}$$

For a broader class of solutions, Lorenzo and Hartley introduce the R function, defined in Eq. 5.70 [Lorenzo, 1999].

$$R_{q,v}[a,c,t] = \sum_{n=0}^{\infty}\frac{(a)^n (t-c)^{(n+1)q-1-v}}{\Gamma((n+1)q-v)}$$
$$L\{R_{q,v}[a,c,t]\} = \frac{s^v e^{-cs}}{s^q - a} \tag{5.70}$$

Considering the solution to Eq. 5.68, the Laplace transform will be of the form $(s^q + a)^{-1}$. Analysis of this solution in the s-plane with $q<1$ shows that there are no poles on the primary Reimann sheet. There are, however, poles on the secondary Reimann sheet. Rather then working with multiple Reimann sheets, Lorenzo and Hartley map s^q into the w complex plane.

$$w = s^q = \left(re^{j\theta}\right)^q = r^q e^{jq\theta} \tag{5.71}$$

The lines of constant r or constant θ can be mapped from the s-plane to the w-plane using this equation. Analysis of Eq. 5.71 shows that the stable region in the s-plane is transformed into a wedge between the imaginary axis and the angle $\pm q\pi/2$, $0 < q \leq 1$. Consider the case when q = 0.5, the resulting pole-zero stability plot is shown in Fig. 5.5. With careful analysis, the pole and zero locations can be analyzed using the w-plane and then implemented in a controller.

The discussions in this section have been limited and brief, with the intent being to expose fractional order control as a useful technology. For more detailed information, the text by Podlubny and the technical papers by Hartley and Lorenzo, previously referenced in this section, are recommended.

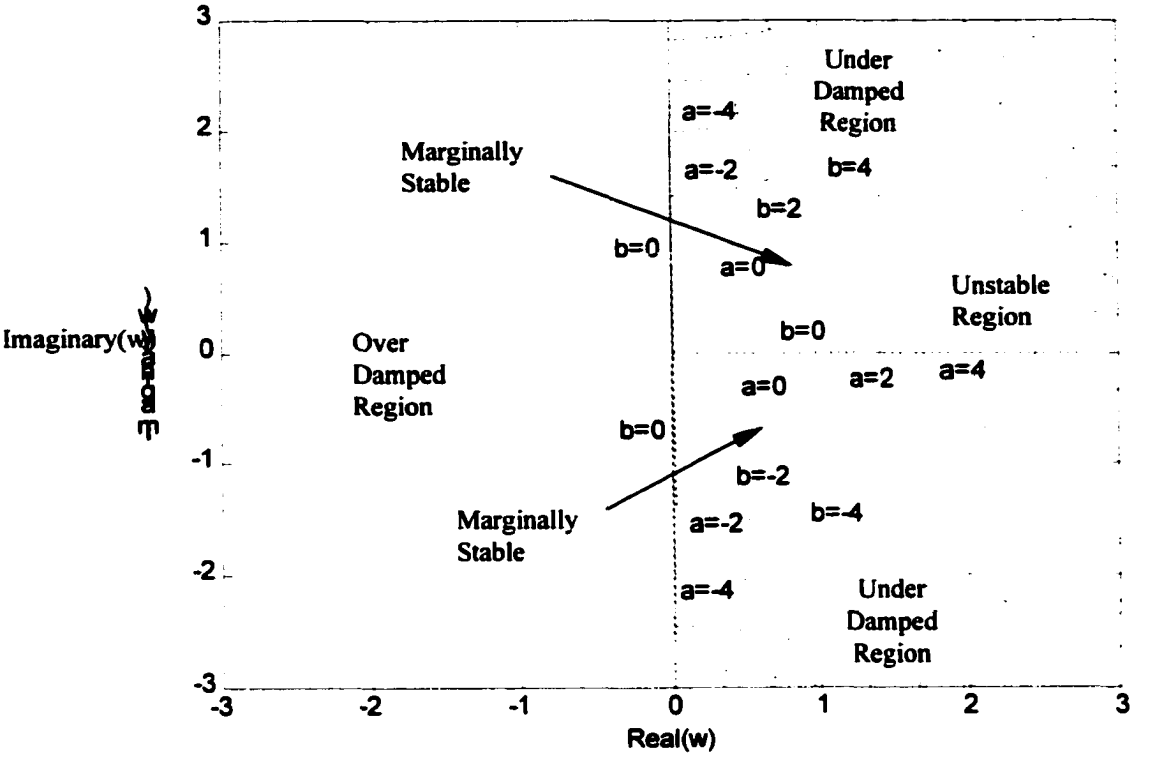

Figure 5.5: w-Plane Stability Regions with $q = 0.5$

6. ANALYSIS OF FRACTIONAL EDDY CURRENT MODELS

6.1. Development of Fractional Order Transformer Model

The fundamental ideas behind the fractional order transformer model were discussed in Section 5 along with the development of a frequency dependent resistance. These concepts are combined in Sections 6.1.1. and 6.1.2. to develop the fractional order eddy current model.

6.1.1. Frequency Dependent Resistance

The concept of the frequency dependent resistance was discussed by Stoll in 1974, as previously mentioned. Stoll only considered the two most extreme cases, that when the skin depth was much less than, or much greater than, the thickness of the plate. In order to usefully model eddy current behavior the entire frequency range must be considered.

The frequency dependent resistance developed in Section 5 is defined in Eq. 6.1.

$$R_{AC} = R_{DC} + R_{DC}\left(\left(\frac{\omega}{\omega_{cr}}\right)^{1/2}(1+j)-1\right)U(1-\omega_{cr})$$
$$\omega_{cr} = \frac{n^2}{b^2}\frac{2}{\sigma\mu_0\mu_r} \tag{6.1}$$

This variation in effective resistance with frequency can be verified by examining the finite element model of the semi-infinite plate. PC-OPERA allows the boundary conditions to be set such that the 1-DOF conditions of the semi-infinite plate are exactly met. The model consists of an aluminum plate with a thickness $b = 150$ mm with a conductivity of 2.79×10^6 $\Omega^{-1}m^{-1}$ and a relative permeability of 1.

The finite element plate section being considered has a width of 50 mm and is meshed with 240 triangular elements, keeping the aspect ratios of the elements between 1.06 and 2.18. The boundary conditions were set to tangential-magnetic and quadratic elements were used for all calculations. The magnetic field is created by a current source equivalent to 1000 Ampere-turns. The finite element model is shown in Fig. 6.1.

Using PC-OPERA, the power dissipation and total current can be determined by integrating over the elements [Vector Fields, 1997].

$$I_{eddy} = \int J ds \tag{6.2}$$

$$P = \int \frac{J^2}{\sigma} ds \tag{6.3}$$

If the current distribution was constant over the thickness of the plate then the resistance at each frequency could be determined using the circuital power equation.

$$R = \frac{P}{I^2} \tag{6.4}$$

The current in the semi-infinite plate is not uniform with plate depth. However, the distribution of current in the upper regions of the plate is known with respect to the skin depth ratio, y/δ. This means that a linear relationship can be made between the net current and the actual current distribution as long as the integration depth of $y = -n\delta$ remains constant.

$$\left(\int_{-n\delta}^{0} I dy \right)^2 = c \int_{-n\delta}^{0} I^2 dy \tag{6.5}$$

Thus, if the current is uniform c will have a value of 1. The value of c must be defined relative to the penetration depth of the field. For this analysis c is defined relative to $y/\delta = -4$, or 98% of the current. The area is $A = w4\delta$ and the length L is unity.

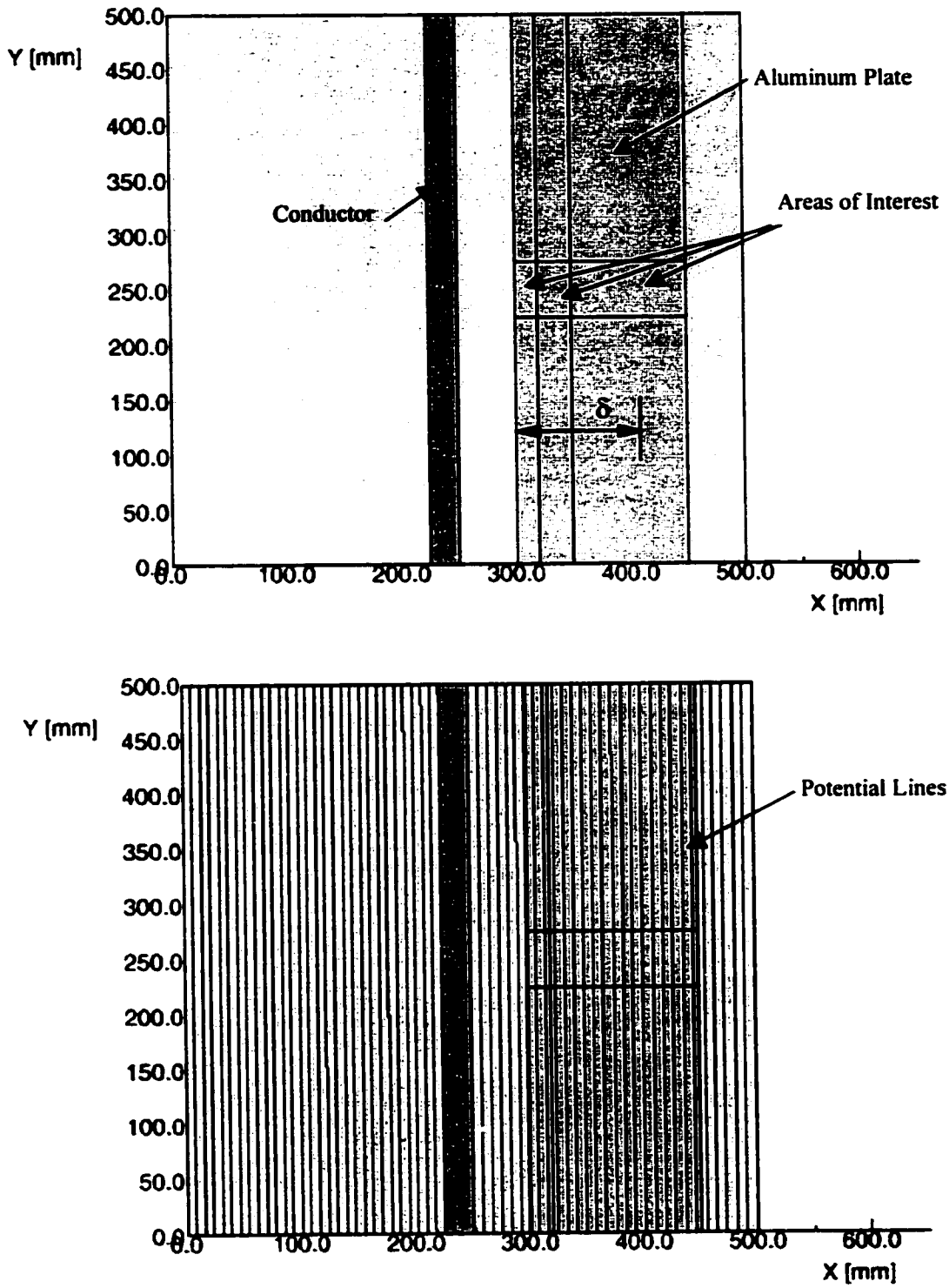

Figure 6.1: PC-OPERA Layout of Finite Element Model

Combining Eqs. 6.3, 6.4 and 6.5 results in,

$$c^2 = \frac{4w^2\delta}{I^2}\int_{4\delta}^{0} J^2 dy \tag{6.6}$$

When the skin depth is greater then the thickness of the plate, this relation will not hold, i.e., the relative depth 4δ cannot be reached and the value of c will vary with frequency. The values of c^2 determined from the finite element analysis are listed in Table 6.1.

f (Hz)	Relative Depth	c^2
1	b	1.048
3.1623	b	1.052
10	b	1.102
31.623	b	1.752
100	4δ	2.339
316.23	4δ	2.354
1000	4δ	2.367
3162.3	4δ	2.377
10000	4δ	2.369

Table 6.1: Values of c^2

The average value of c, with n = 4, for the semi-infinite aluminum plate was determined to be $c = \sqrt{2.361}$. Thus, the AC resistance is related to the power and current calculated using PC-OPERA by,

$$R_{AC}(\omega) = \frac{P}{c^2 I^2} \tag{6.7}$$

The power P and current I were calculated in PC-OPERA by integrating over the entire plate depth. The AC resistance was determined with respect to frequency by integrating P and I over a range of frequencies. The results of the finite element analysis are compared to the analytical model in the Fig. 6.2.

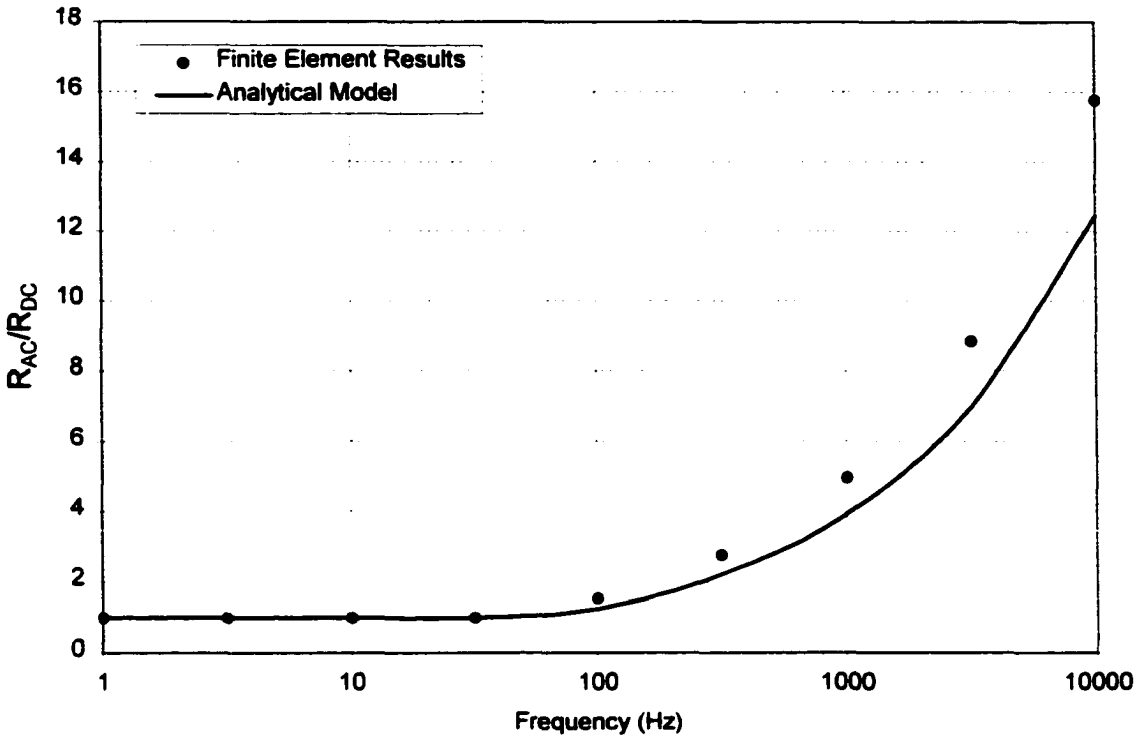

Figure 6.2: Comparison of R_{AC} Analytical and Finite Element Models

The results show that there is indeed a variation in resistance with frequency and that the trend follows the analytical model. In fact, the difference between the finite element results and the analytical model is consistently around 15% for each data point after the critical frequency.

This consistent error is attributed to the choice of integration depth, $y = -4\delta$, because of the small amount of current flowing below the critical depth that is not accounted for, approximately 2% of the total. The power is calculated on the elemental level; thus, the infinitesimal current in each element is squared leading to a negligible contribution in the power term. The current value is summed in each element leading to a non-negligible value and then squared. This can be verified by changing the integration depth of the current from

$y = -b$ to -4δ. This results in the analytical model matching the finite element data with less than 0.9% error. This error can be explained mathematically by considering the expression $\left(I^2 + \Delta^2\right)/(I + \Delta)^2 \neq 1$, where I is the net current between $y = 0$ and -4δ and Δ is the current below $y = -4\delta$. The end result is that the error in Fig. 6.2 is due to the calculation method and not the formulation for the variable resistance.

Eq. 6.1 has now been verified to accurately predict the variation of resistance with frequency. However, the form of Eq. 6.1 is not very useful because it contains the unit step function. In order to design a control system using a single transfer function, the function must be continuous. Thus, the frequency dependent resistance must be transformed into a continuous form.

R_{AC} can be transformed into a continuous form using any variety of methods. Two basic approaches stand out, but they are by no means the only practical solutions. The two approaches are the filtered approach and the direct summation approach. The filtered approach uses high and low pass filters as scaling functions that are multiplied by the respective resistance term. The time constant for the filters can be based on the critical frequency given in Eq. 6.1, $\tau = 1/s_{crit}$.

$$\begin{aligned} &\frac{1}{\tau s + 1} && s \leq s_{crit} \\ &\frac{\tau s}{\tau s + 1} && s \geq s_{crit} \end{aligned} \tag{6.8}$$

Multiplying the two parts of Eq. 6.1 by the respective filters results in,

$$R_{AC}(s) = R_{DC}\,\frac{\tau\gamma s^{3/2} + 1}{\tau s + 1} \qquad \gamma = \sqrt{\frac{2}{\omega_{cr}}} \tag{6.9}$$

The direct summation approach arises due to the relative magnitude of R_{AC} at low

frequencies, $R_{AC}(0) = 0$. Thus, a somewhat crude estimation can be made by simply adding the two terms and neglecting the unit step function.

$$R_{AC}(s) = R_{DC}\left(1 + \gamma s^{1/2}\right) \qquad \gamma = \sqrt{\frac{2}{\omega_{cr}}} \tag{6.10}$$

The two methods are compared against the analytical function containing the unit step function in Fig. 6.3. The results for the summation approach are not as good as the filtered approach, but the overall trend is consistent with R_{AC}.

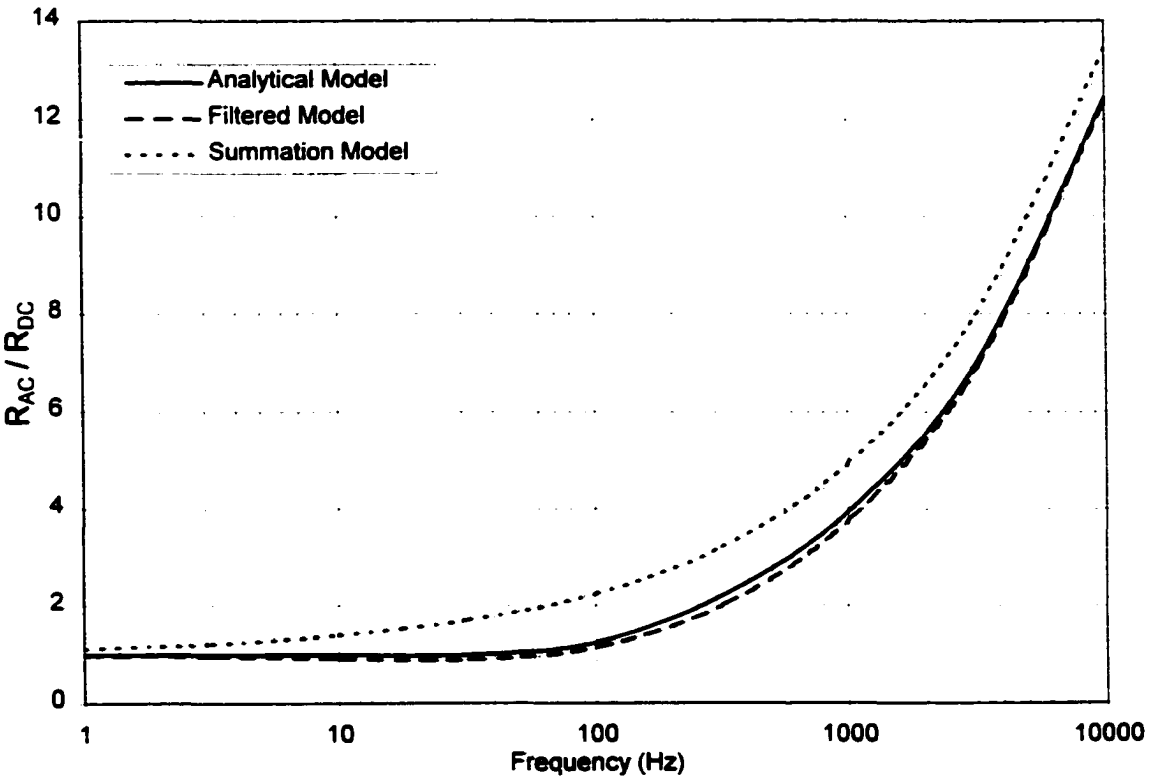

Figure 6.3: Comparison of Analytic R_{AC} vs. Approximate Models

6.1.2. Fractional Order Transformer Model

The single time constant model, or transformer model, developed in Section 5.3.1. is valid when the skin depth is much larger than the thickness of the plate. The single time constant model when the skin depth was the same order as, or less than, the thickness of the plate was derived in Section 5.3.2. The two models are essentially identical with the exception of the order of the polynomial in s. This section will combine the two models to develop a single fractional order transformer model that will cover the entire frequency range.

The models for the integer and fractional order single time constant models were given in Eqs. 5.34 and 5.45, they are repeated here in terms of the electrical time constant of the plate, τ_e, and what has been denoted as the relative mutual time constant of the plate, τ_m.

$$\begin{aligned} \frac{B}{I} &= k\frac{(\tau_e-\tau_m)s+1}{\tau_e s+1} \qquad \omega < \omega_{crit} \\ \frac{B}{I} &= k\frac{(\tau_e-\tau_m)s^{1/2}+\gamma}{\tau_e s^{1/2}+\gamma} \qquad \omega \geq \omega_{crit} \end{aligned} \tag{6.11}$$

where,

$$\tau_e = \frac{L_e}{R_{DC}} \quad \tau_m = \frac{k_e}{k}\frac{L_m}{R_{DC}} \quad \gamma = \sqrt{\frac{2}{\omega_{cr}}} \quad \omega_{cr} = \frac{n^2}{b^2}\frac{2}{\sigma\mu_0\mu_r} \tag{6.12}$$

The only differences between the two equations are the variations in $s \rightarrow s^{1/2}$ and $1 \rightarrow \gamma$. The two formulations could be united into a single form using a variety of methods. The truest form would consist of Eqs. 6.11 combined using a unit step function. This, however, would not yield a very useful form due to the step at the critical frequency. It should be noted, however, that if the step function formulation were to be used, a constant would have to be added to the higher frequency term to ensure that the two formulations would be continuous at the critical frequency. This constant is given in Eq. 6.13.

$$C = k\frac{\tau_m\left(\tau - \gamma\tau^{1/2}\right)}{\left(\tau_e + \tau\right)\left(\tau_e + \gamma\tau^{1/2}\right)} \tag{6.13}$$

Three different approaches that can be used to unite the two forms of Eq. 6.11 are discussed in this section. The first approach is to substitute the frequency dependent resistance defined in terms of the high and low frequency filters, Eq. 6.9, for R into the single time constant model. This results in,

$$\frac{B}{I} = G_1(s) = k\frac{(\tau\tau_e - \tau\tau_m)s^2 + (\tau\gamma)s^{3/2} + (\tau_e - \tau_m)s + 1}{\tau\tau_e s^2 + \tau\gamma s^{3/2} + \tau_e s + 1} \tag{6.14}$$

Eq. 6.14 is a transfer function of second order polynomials with the addition of an $s^{3/2}$ term. Thus, direct substitution of R_{AC} increases the order of the polynomial by 1 and introduces a non-integer power of s into the polynomial. Consider the case when the critical frequency is very high, i.e., the plate is very thin. This causes γ to be very small. If γ is assumed to be zero, Eq. 6.13 becomes a ratio of second order polynomials. In other words, the behavior of the system would revert back to a polynomial of integer order as the thickness of the plate becomes very thin.

The low and high frequency filters could be multiplied by the transfer functions given in Eq. 6.11 directly, including the constant given in Eq. 6.13. This results in,

$$\begin{aligned} G_2(s) = k\frac{\tau\tau_e\left(\tau_e - \tau_m + \tau_e C\right)s^{5/2} + \gamma\tau_e\tau(1+C)s^2 + \left((\tau_e - \tau_m)(\tau_e + \tau) + \tau_e\tau C\right)s^{3/2}}{(\tau_e s + 1)\left(\tau_e s^{1/2} + \gamma\right)(\tau s + 1)} \\ + k\frac{\gamma(\tau + \tau_e - \tau_m + \tau C)s + (\tau_e)s^{1/2} + \gamma}{(\tau_e s + 1)\left(\tau_e s^{1/2} + \gamma\right)(\tau s + 1)} \end{aligned} \tag{6.15}$$

This formulation results in a ratio of polynomials of fractional order, where the highest order on s is 5/2. Interestingly, if γ is again assumed to be zero Eq. 6.15 becomes a ratio of second order integer polynomials.

The model can also be based on the summation model of R_{AC} by substituting Eq. 6.10 for R_{AC} into the single time constant model. The result is given in Eq. 6.16.

$$G_3(s) = k\frac{(\tau_e - \tau_m)s + \gamma s^{1/2} + 1}{\tau_e s + \gamma s^{1/2} + 1} \tag{6.16}$$

Eq. 6.16 is a transfer function of first order polynomials with the addition of an $s^{1/2}$ term. As was the case for $G_1(s)$ and $G_2(s)$, $G_3(s)$ becomes an integer order polynomial when γ is assumed to be zero.

Models $G_1(s)$ and $G_2(s)$ tend toward ratios of second order polynomials when γ becomes very small. This is not consistent with the single time constant model that consisted of a ratio of single order polynomials. This is because the single time constant model was developed using a single shorted turn. When two shorted turns are used instead of one the governing equations become,

$$\begin{aligned} V &= IR + LIs + L_{m_1} I_{e_1} s + L_{m_2} I_{e_2} s \\ 0 &= I_{e_1} R_{e_1} + L_{e_1} I_{e_1} s + L_{m_1} Is + L_{m_{12}} I_{e_2} s \\ 0 &= I_{e_2} R_{e_2} + L_{e_2} I_{e_2} s + L_{m_2} Is + L_{m_{12}} I_{e_1} s \end{aligned} \tag{6.17}$$

From this, I_{e1} and I_{e2} can be written in terms of I. The magnetic field produced from these three current sources can be written as $\{B\} = [K]\{I\} + [K_{e1}]\{I_{e_1}\} + [K_{e2}]\{I_{e_2}\}$. Substituting for I_{e1} and I_{e2} in terms of I results in an equation of the form,

$$\frac{B}{I} = k\left(1 + \frac{k_{e_1}}{k} g_1(s) + \frac{k_{e_2}}{k} g_2(s)\right) = k\frac{1 + a_1 s + a_2 s^2}{1 + b_1 s + b_2 s^2} \tag{6.18}$$

where $g_1(s)$ and $g_2(s)$ are functions of the resistances and inductances in Eq. 6.17. Thus, Eq. 6.18 can be considered a double time constant model. In fact, if n shorted turns were used then the system would consist of the ratio of two n^{th} order polynomials.

6.2. Comparison of Fractional Transformer Model with Finite Element Data

The accuracy of the formulations developed in the previous section can be established by comparison to finite element results. The model chosen simulates the original shorted turn of the transformer model. The shorted turn is incrementally increased in width and height until it forms a thin solid plate. The thin plate is then increased in thickness to form a thick plate. These transformations of the original shorted turn aid in the understanding of the eddy current behavior.

The form of the equations will be written in a generic form and the coefficients will be determined from the finite element data using a least squares best-fit algorithm. Eqs. 6.14 – 6.16 are written in terms of unknown coefficients in Eq. 6.19.

$$G_1(s)=\frac{a_3 s^2+a_2 s^{3/2}+a_1 s+a_0}{s^2+b_2 s^{3/2}+b_1 s+b_0}$$

$$G_2(s)=\frac{a_5 s^{5/2}+a_4 s^2+a_3 s^{3/2}+a_2 s+a_1 s^{1/2}+a_0}{s^{5/2}+b_4 s^2+b_3 s^{3/2}+b_2 s+b_1 s^{1/2}+b_0} \tag{6.19}$$

$$G_3(s)=\frac{a_2 s+a_1 s^{1/2}+a_0}{s+b_1 s^{1/2}+b_0}$$

Two coefficients can be found directly by examining the limiting conditions when $\omega = 0$ and ∞. These are given in Eq. 6.20.

$$G(0)=G^0_{1,2,3}=\frac{a_0}{b_0} \qquad G(\infty)=\begin{cases} G_1^\infty = a_3 \\ G_2^\infty = a_5 \\ G_3^\infty = a_2 \end{cases} \tag{6.20}$$

The remaining coefficients will be determined by minimizing the least squares error between the finite element data points and the analytical function. The error function is defined as,

$$e_i=(Num)-G_i(Den) \tag{6.21}$$

The quadratic error function is the square of the error, $J_i = \bar{e}_i e_i$, where the overbar represents the complex conjugate. Taking the derivatives of J with respect to the coefficients and setting them equal to zero minimizes the error with respect to the coefficients. The minimized set of equations can be written in matrix form for each data point, $[M]\{x\}=\{r\}$, where $\{x\}$ is the vector of coefficients. The value of $\{x\}$ that minimizes all the data points can be found by taking the pseudo-inverse of the non-square matrix. For the case of $G_1(s)$ with q data points this becomes,

$$\underbrace{\begin{Bmatrix} a_2 \\ a_1 \\ b_2 \\ b_1 \\ b_0 \end{Bmatrix}}_{5\times 1} = \underbrace{\begin{bmatrix} M_1 \\ M_2 \\ \vdots \\ M_q \end{bmatrix}^{\#}}_{5\times 5q} \underbrace{\begin{Bmatrix} r_1 \\ r_2 \\ \vdots \\ r_q \end{Bmatrix}}_{5q\times 1} \tag{6.22}$$

The results of the three cases are discussed in Sections 6.2.1. and 6.2.2.

6.2.1. Ring-Plate Transformation

The finite element model consists of a thin conducting loop to simulate a shorted turn. The loop is increased in thickness and in width until it forms a thin solid plate 5 mm thick with a radius of 150 mm. The loop of conducting material has a resistance of $2.25\times10^{-4}\ \Omega$, with a square cross section of 1mm × 1mm and a mean radius of 125mm, and it is placed 100 mm below a coil. The coil has 493 turns, an inner radius of 44.5mm, an outer radius of 79.5mm, and a height of 105mm. A two dimensional model was developed using the radial symmetry of the problem. The model is illustrated in Fig. 6.4.

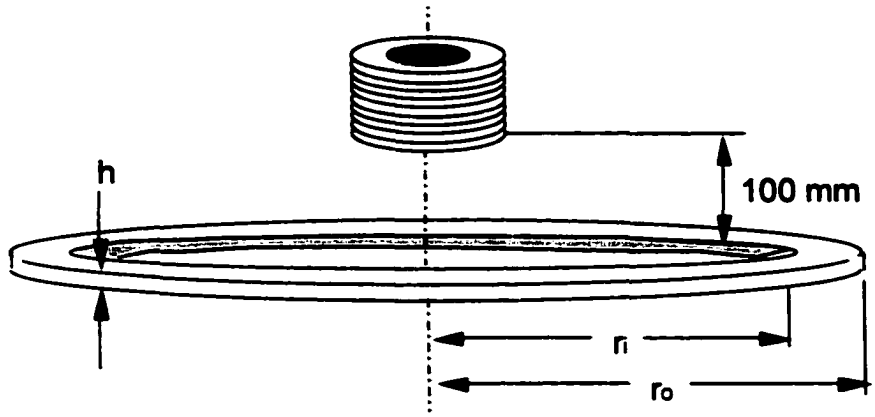

Figure 6.4: Finite Element Ring-Plate Model

The analysis is performed for five configurations of varying thickness and width, listed in Table 6.1. The inner radius is given by r_i, the outer radius r_O, and the height is h as illustrated in Fig. 6.4.

Case	r_i (mm)	r_o (mm)	h (mm)
A	124.5	125.5	1
B	122	128	5
C	100	150	5
D	75	175	5
E	0	250	5

Table 6.2: Dimensions of Ring/Plate Models

Before discussing the fractional order models it is important to see the effectiveness of the original single time constant model. The generalized form of the model is given by,

$$G_0(s) = k\frac{as+1}{bs+1} \tag{6.23}$$

The three unknown coefficients can be solved for without using the least squares algorithm. Examining the system at $\omega = 0$, $\omega = \infty$, and at the point of minimum phase, ω_{mp}, yields,

$$k = G_0(0) \quad a = \frac{1}{\omega_{mp}} \sqrt{\frac{G_0(\infty)}{G_0(0)}} \quad b = \frac{1}{\omega_{mp}} \sqrt{\frac{G_0(0)}{G_0(\infty)}} \tag{6.24}$$

The frequency responses of the finite element data and the single time constant model are shown in Fig. 6.5. The single time constant model does a good job of modeling the thin loop, as in Cases A and B. As the structure takes on the form of a plate, as in Cases C, D and E, differences begin to appear. The model under-predicts the magnitude and over-predicts the phase lag. The overall performance of the model is perhaps still satisfactory, but the weaknesses begin to show as the thin plate takes form. These weaknesses become significant as the plate thickness is increased, as discussed in Section 6.2.2.. It should be noted when examining Fig. 6.5 that the end points of the analytical model are specified, so the variations in model performance will appear in the interior frequency ranges.

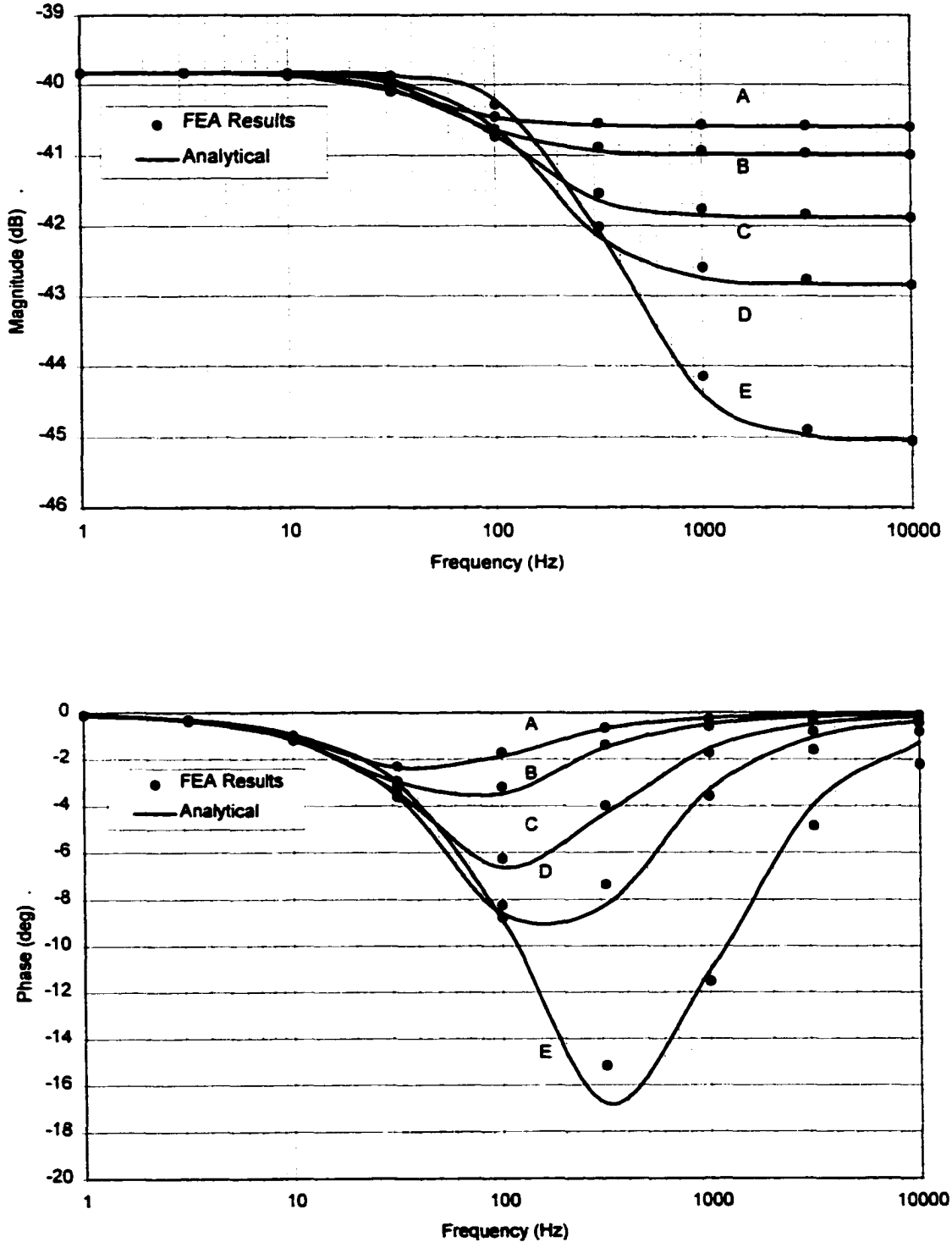

Figure 6.5: Comparison of Single Time Constant Model and Finite Element Ring-Plate

The fractional eddy current models $G_1(s)$, $G_2(s)$ and $G_3(s)$ are compared against the results of the finite element analysis in Figs. 6.6, 6.7, and 6.8, respectively. The details of the least-squares solution technique for these three formulations are given in Appendix D.

The results show that all three formulations do a good job of modeling the frequency response of the eddy currents. The results are essentially the same for the three models for Cases A-D. Models $G_1(s)$ and $G_2(s)$ do the best job for the most difficult of the five cases, Case E. This could be attributed to the somewhat crude approximation of R_{AC} used to derive $G_3(s)$, but it is more likely due to the order of the polynomials. The higher the order of the polynomials in the transfer function the more flexibility the model has in matching the data.

It should be noted that for the simple case of the flat plate, the single time constant model does a satisfactory job of modeling the eddy current behavior. This is because this is the specific case for which the single time constant model was developed. Additionally, in the finite element analysis performed in this section the skin depth never decreases below the thickness of the plate, so the behavior that the fractional terms are supposed to account for is very minimal or non-existent. These circumstances will change as the thickness of the plate is increased. No matter what formulation is used, the inclusion of the fractional order terms increases the accuracy of the model over the single time constant model.

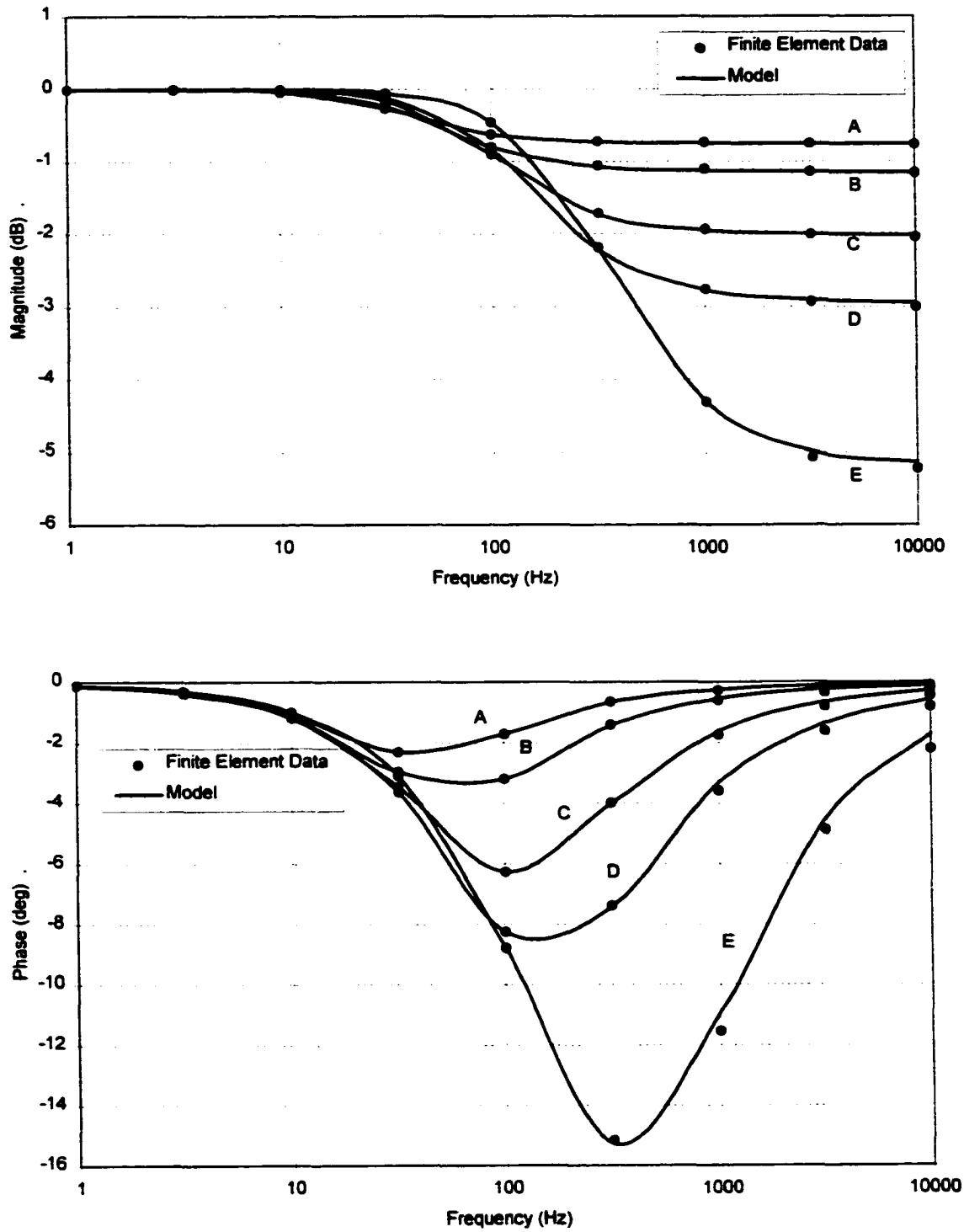

Figure 6.6: Comparison of $G_1(s)$ and Finite Element Ring-Plate Data

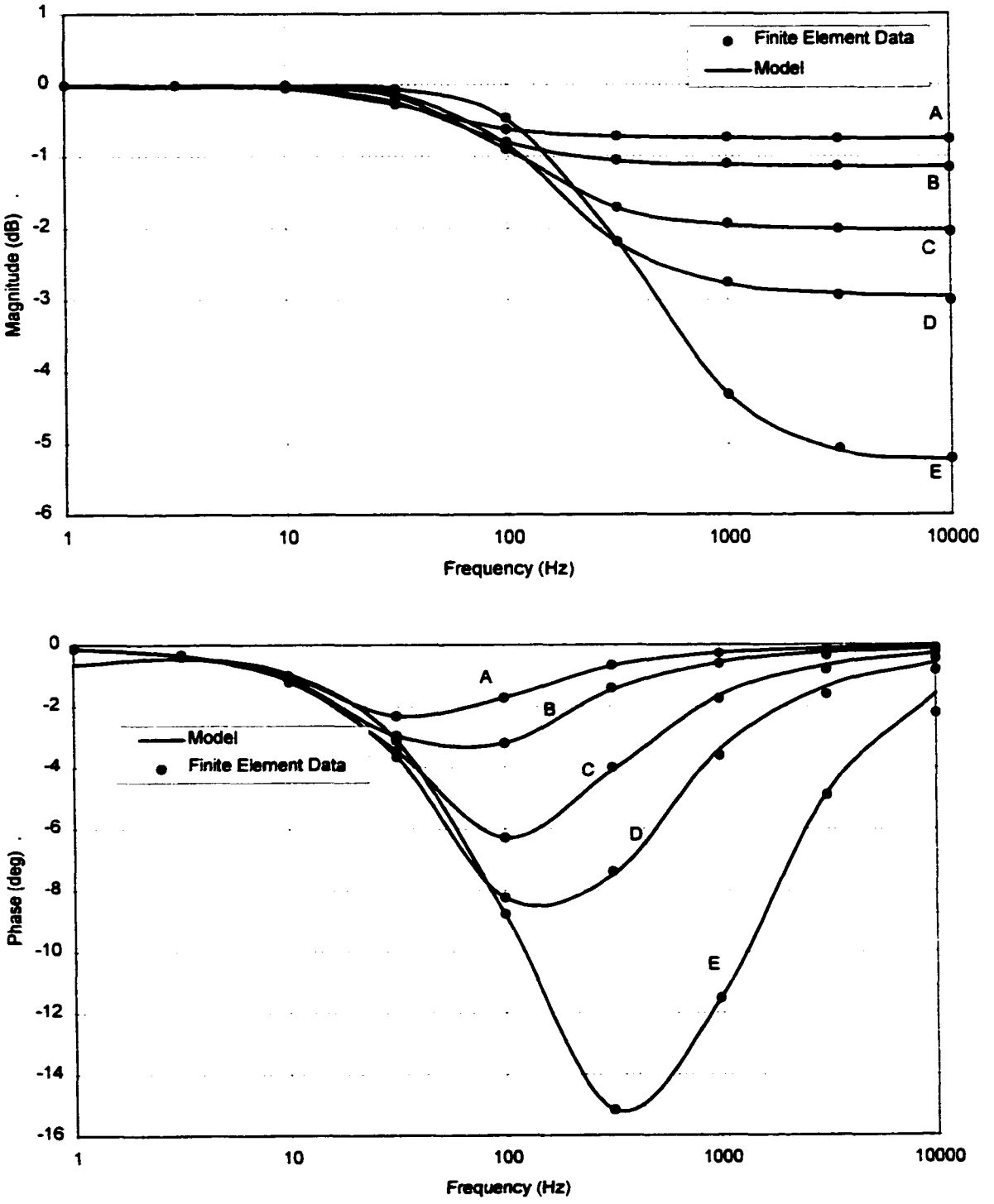

Figure 6.7: Comparison of $G_2(s)$ and Finite Element Ring-Plate Data

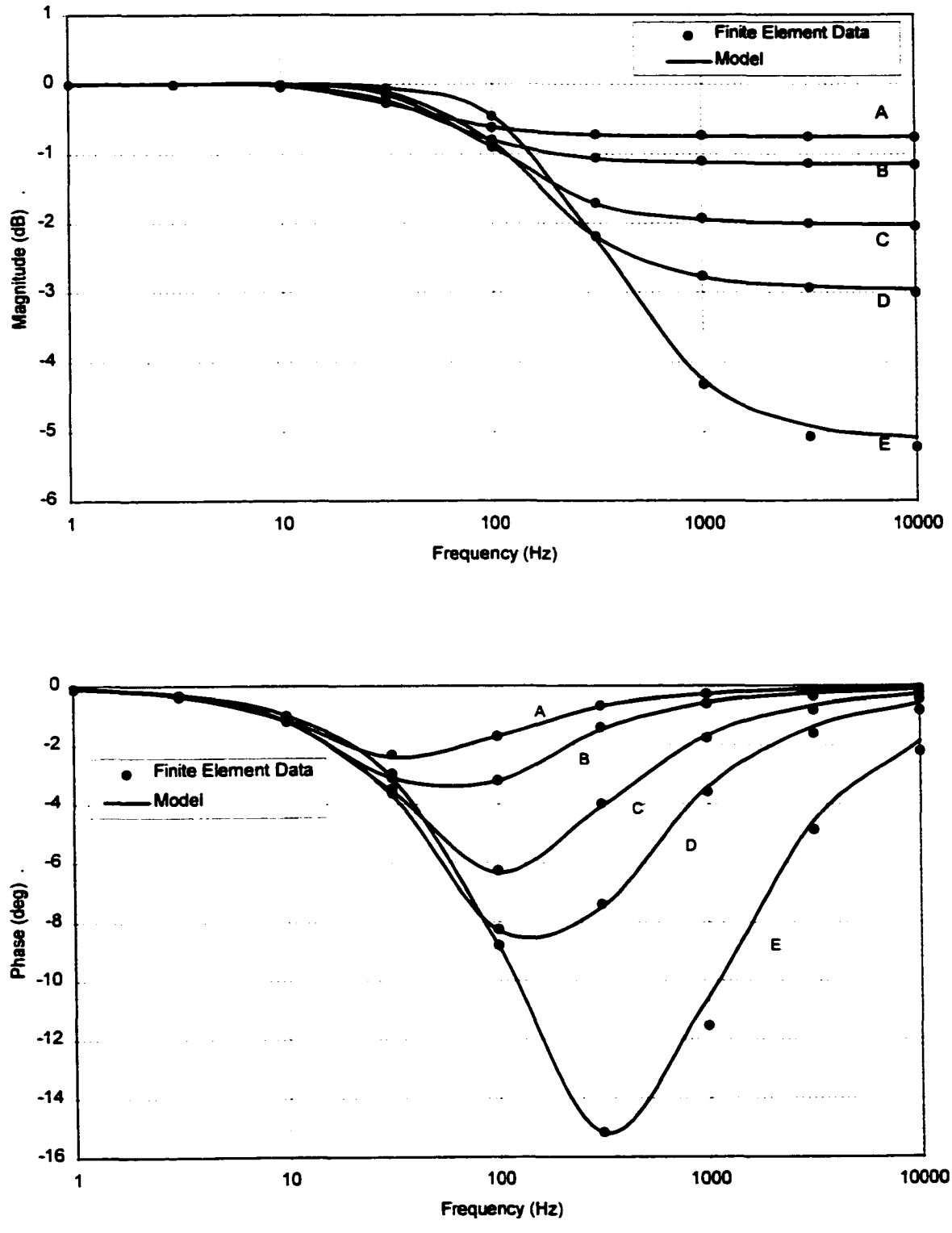

Figure 6.8: Comparison of $G_3(s)$ and Finite Element Ring-Plate Data

6.2.2. Plate of Varying Thickness

The finite element model that is used in this section is the same as the solid plate used in Section 6.2.1. The thin plate that was discussed previously has now increased in thickness from 5 mm to 15 mm and 150 mm. Since the characteristics of the frequency response do not significantly change once the thickness of the plate is increased above 150 mm, it was not increased further. The layout of the model is shown in Fig. 6.9.

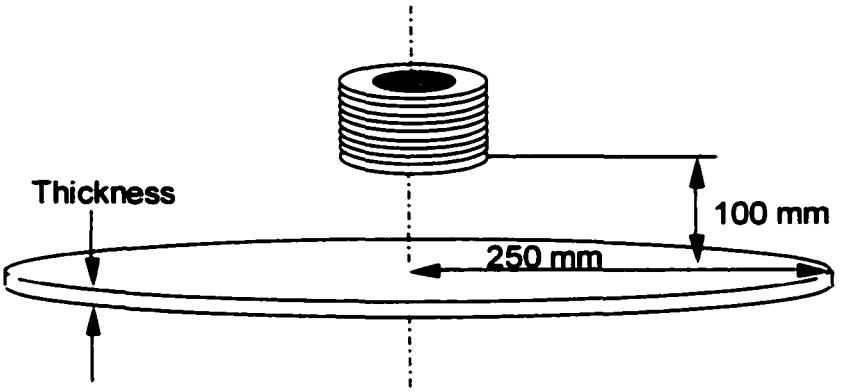

Figure 6.9: Geometry of Finite Element Model

It was shown in the previous section that the single time constant model did a good job at modeling the 5 mm thick plate. The same model is used to model the 250 mm thick plate in Fig. 6.10. It is clear that the model breaks down as the thickness of the plate is increased. This is because at relatively low frequencies the skin depth becomes less than the thickness of the plate and the eddy currents are no longer evenly distributed throughout the cross section of the plate.

The fractional order transformer models are compared against the 5 mm, 15 mm, and 150 mm thick plates in Figs. 6.11, 6.12, and 6.13, respectively.

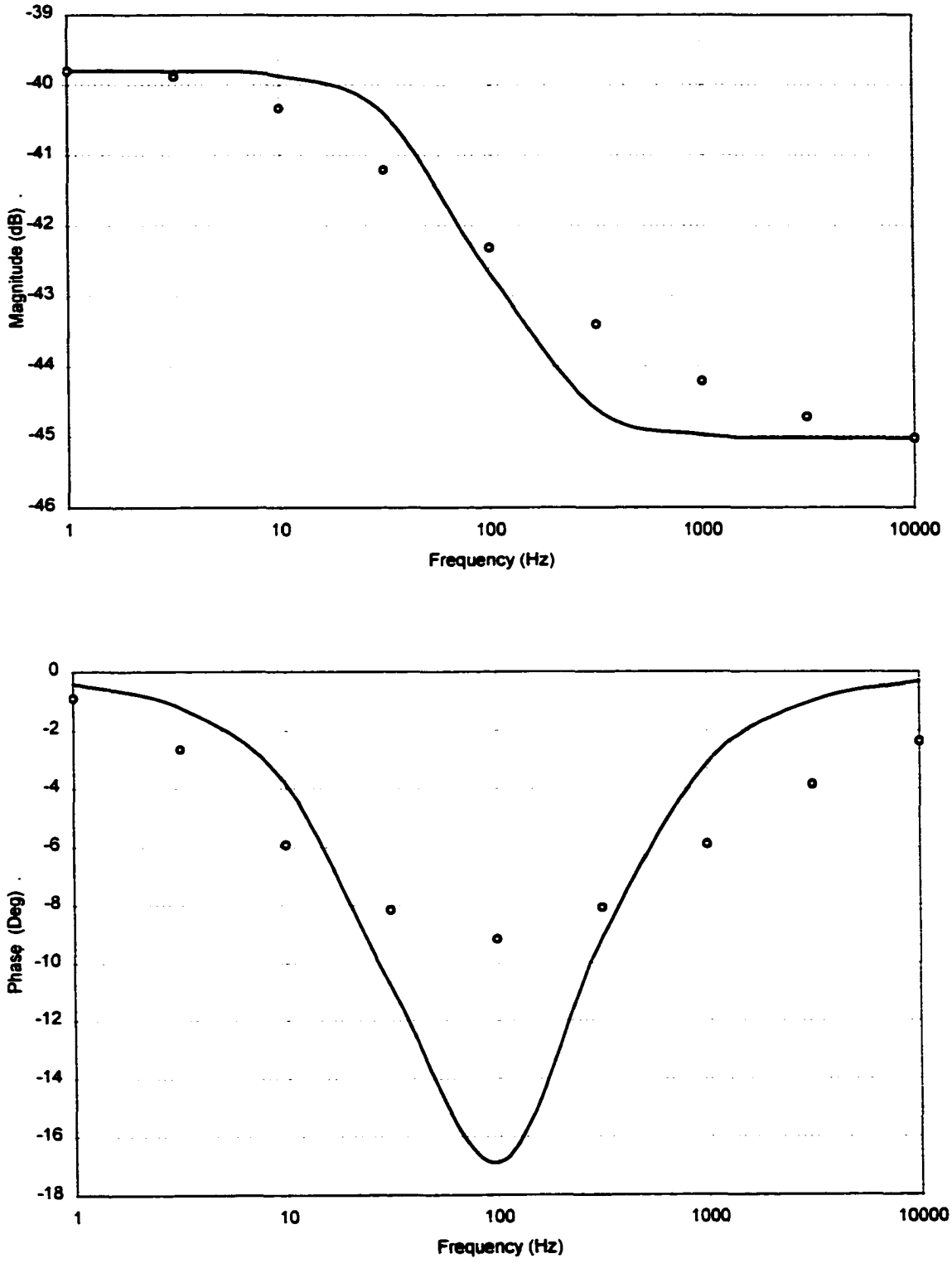

Figure 6.10: Comparison of Single Time Constant Model and Finite Element Thick Plate

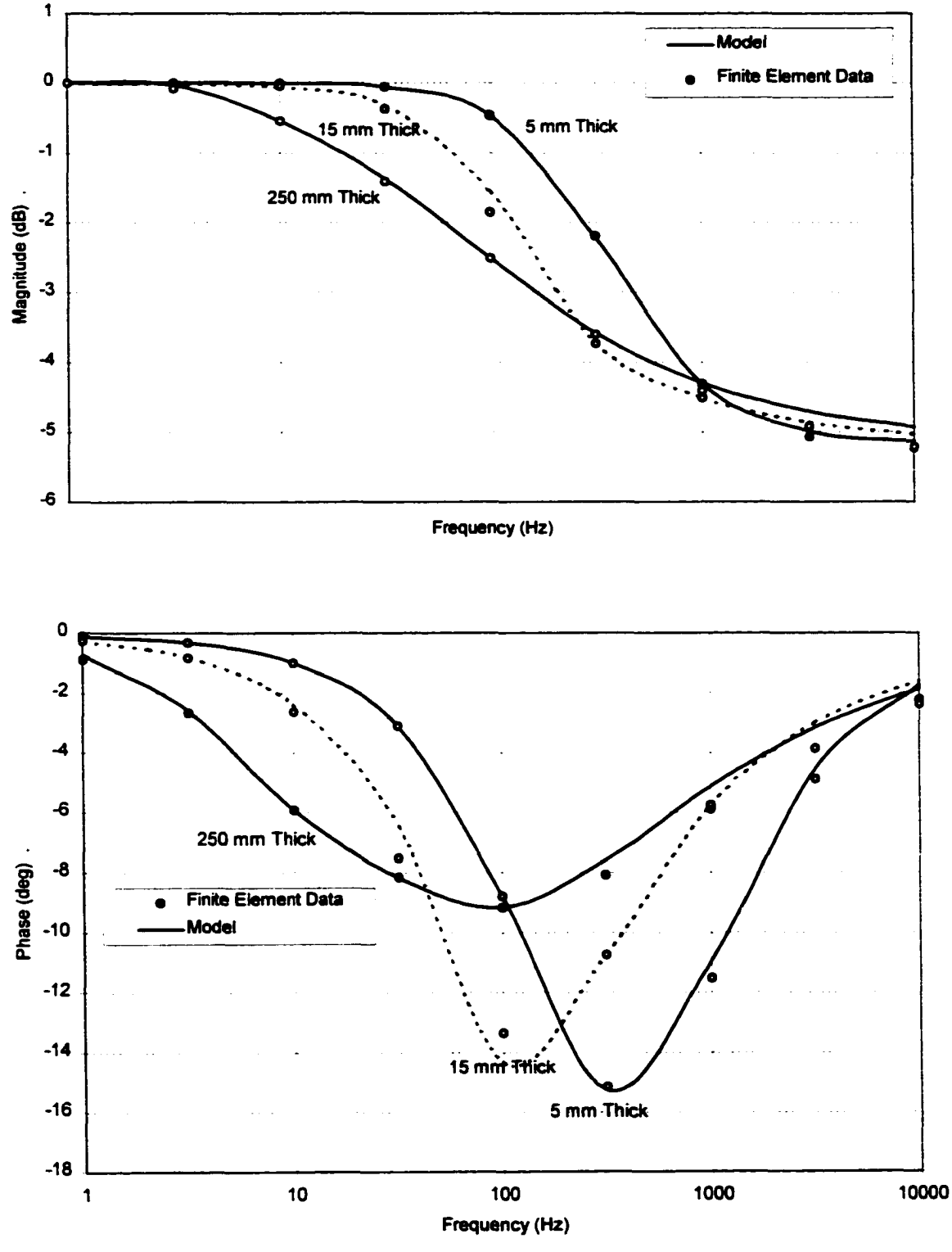

Figure 6.11: Comparison of $G_1(s)$ and Finite Element Thick Plate Data

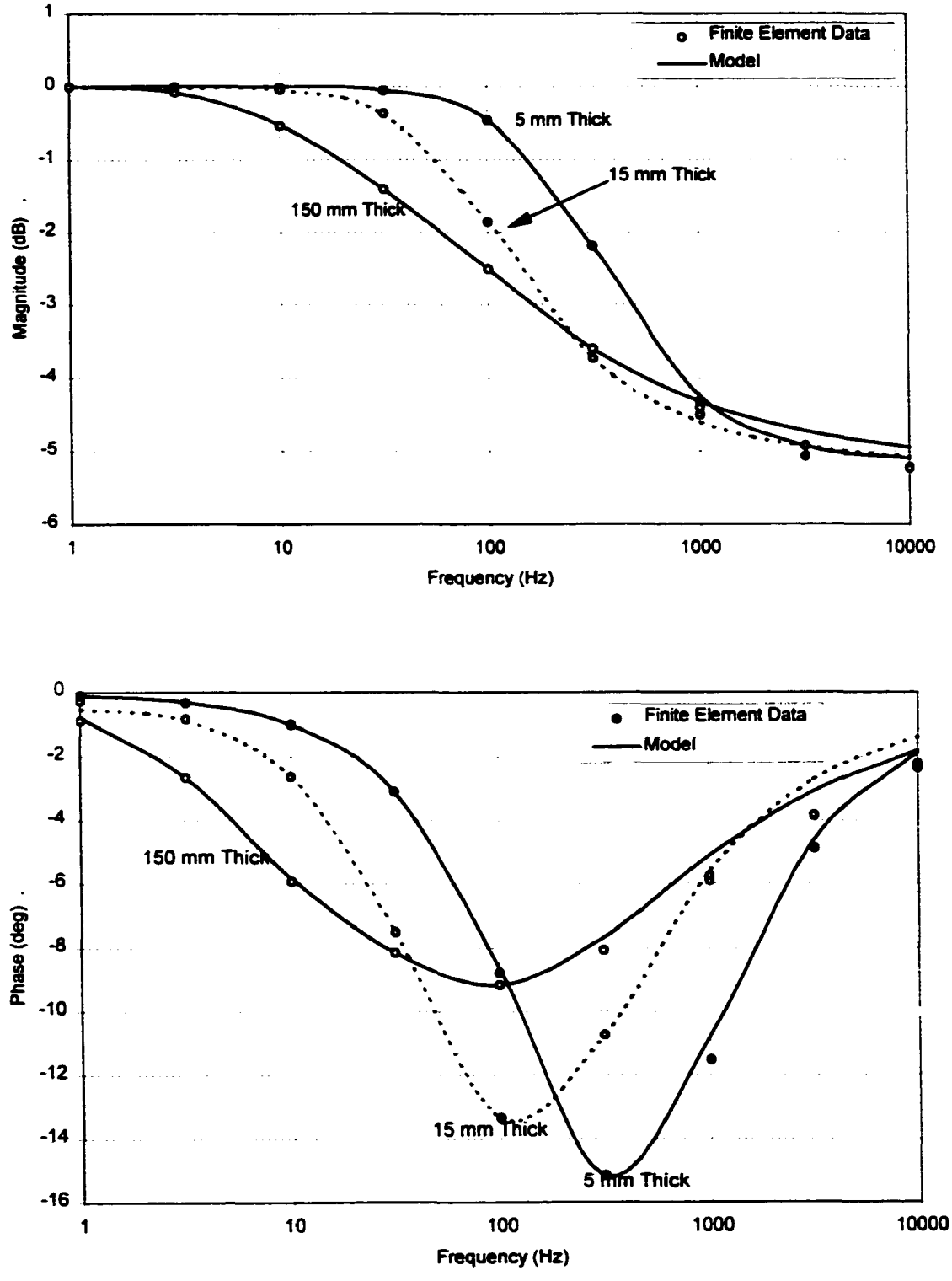

Figure 6.12: Comparison of $G_2(s)$ and Finite Element Thick Plate Data

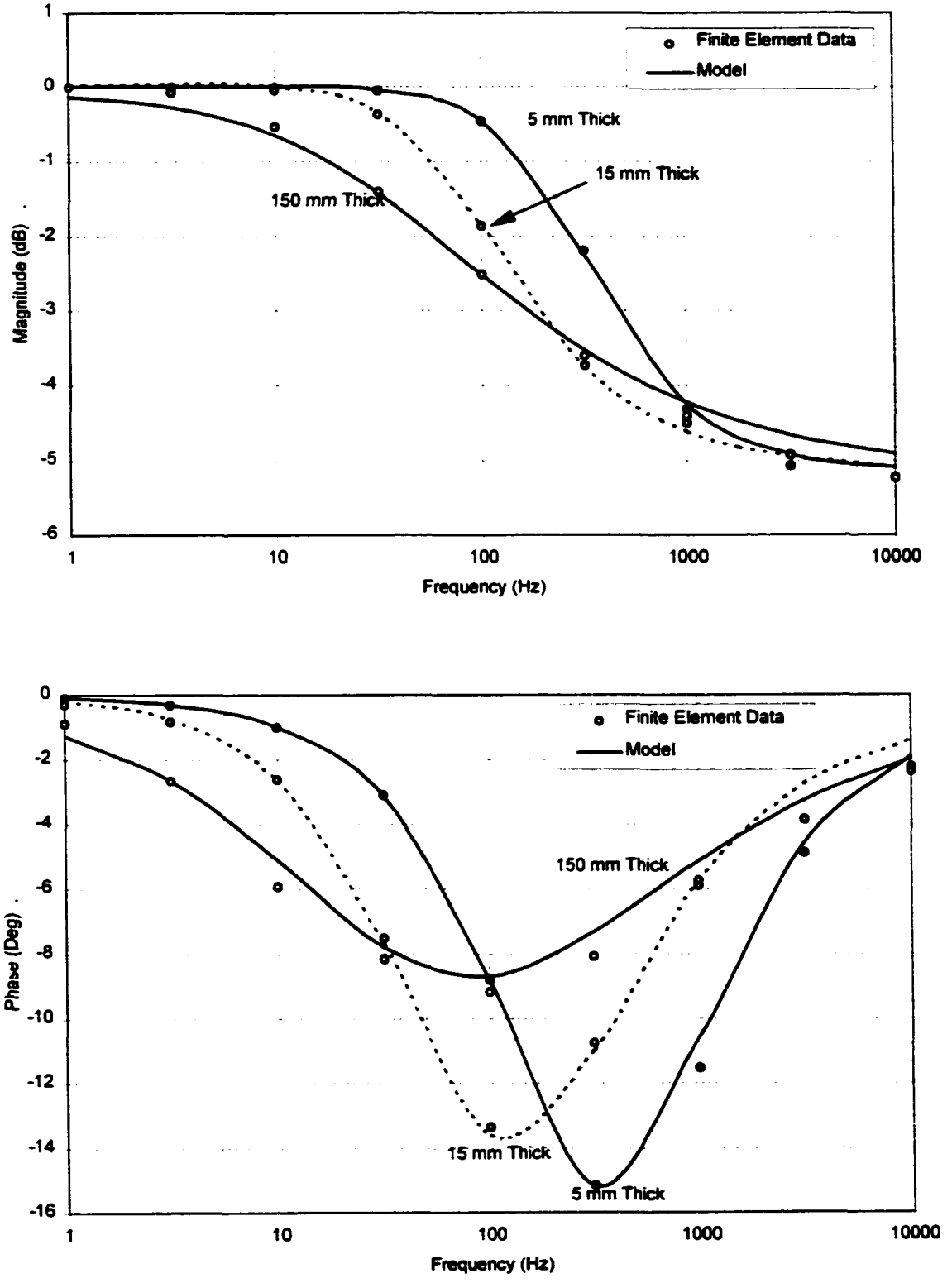

Figure 6.13: Comparison of $G_3(s)$ and Finite Element Thick Plate Data

The three fractional order formulations clearly are able to model the frequency response of the thick plate. The largest variations between the finite element data and the three models occur at frequencies above 1000 Hz. The differences are not very large and are in part due to the formulation of the least squares analysis. The value of $G(\infty)$ was taken from the highest frequency finite element data point, f= 10,000 Hz. If the transfer function asymptotes to a constant value before f= 10,000 Hz then no error is generated since $G(10{,}000\ Hz) = G(\infty)$. This was the case for the thin plate. However, the slope of the frequency response of the thick plate is not constant at f= 10,000 Hz. As a result, the magnitude of the model at the higher frequencies will be larger then the reference data.

The small variations at high frequencies are also in part linked to the finite radius of the plate. The formulation of R_{AC} is defined in terms of the eddy current depth changing with frequency, or the area = $w \cdot n\delta$. Since the radius of the plate is not infinite, there will be an area of flux concentration at the outer corner of the plate leading to a concentrated region of eddy currents. This has the effect of slightly altering the distribution of the eddy currents at high frequencies, although this variation is slight.

6.3. Comparison of Fractional Order Transformer Model with Experimental Data

The experimental data analyzed in this section was collected using two large-gap magnetic suspension test fixtures at NASA Langley Research Center. The first system is the Large Angle Magnetic Suspension Test Fixture (LAMSTF). The system consists of five electromagnets aligned in a circle of radius 137.7 mm. The coils are mounted on an aluminum plate 12.7 mm thick. Due to eddy current effects, the aluminum plate was removed and replaced with a non-conducting material. The electromagnets were made using AWG 10 enameled copper wire wrapped around a bakelite form which surrounded a mild

steel core; the radius of the core is 38.1 mm and the height is 100 mm. The copper windings have an inner radius of 44.5mm, an outer radius of 79.5mm, and a height of 105mm. The test fixture was developed as a small-scale laboratory system to aid in the dynamic modeling of magnetic suspension systems. A photograph of the current system is shown in Fig. 6.14. The original system used an aluminum sensor frame to support the position sensors; it is shown in Fig. 6.15. The system is capable of levitating a magnetized core 100 mm above the electromagnets with control in 5 degrees-of-freedom. More information is available in [Groom, 1991, 1992; Britcher, 1993, 1994].

A second laboratory test fixture was constructed based on information gained from the LAMSTF. This system was designed to suspend a magnetized body in all 6 degrees-of-freedom using two levitation coils and 8 control coils. The system is referred to in literature as the 6DOF-8C/2L system due to its configuration. The eight levitation coils are of similar design as the LAMSTF coils. The two levitation coils carry a DC current and are wrapped around the outside of the control coils. A photograph of the system is shown in Fig. 6.16 without the levitation coils. The levitation coils are illustrated in a schematic of the system shown in Fig. 6.17. More information is available in [Britcher, 1998(a)]

Four eddy current tests were performed on the two test fixtures. The first test was performed on the 6DOF-8C/2L system by placing a 3 mm thick aluminum plate between the control coils and the suspended element. The inner coil was excited and the frequency response of the magnetic field with reference to the exciting current was recorded. The aluminum plate was not centered directly over the coil, so the excitation is not symmetric as was the case of the finite element tests in the previous section. The plate is very thin, so the fractional transformer model and the single time constant model should show good agreement.

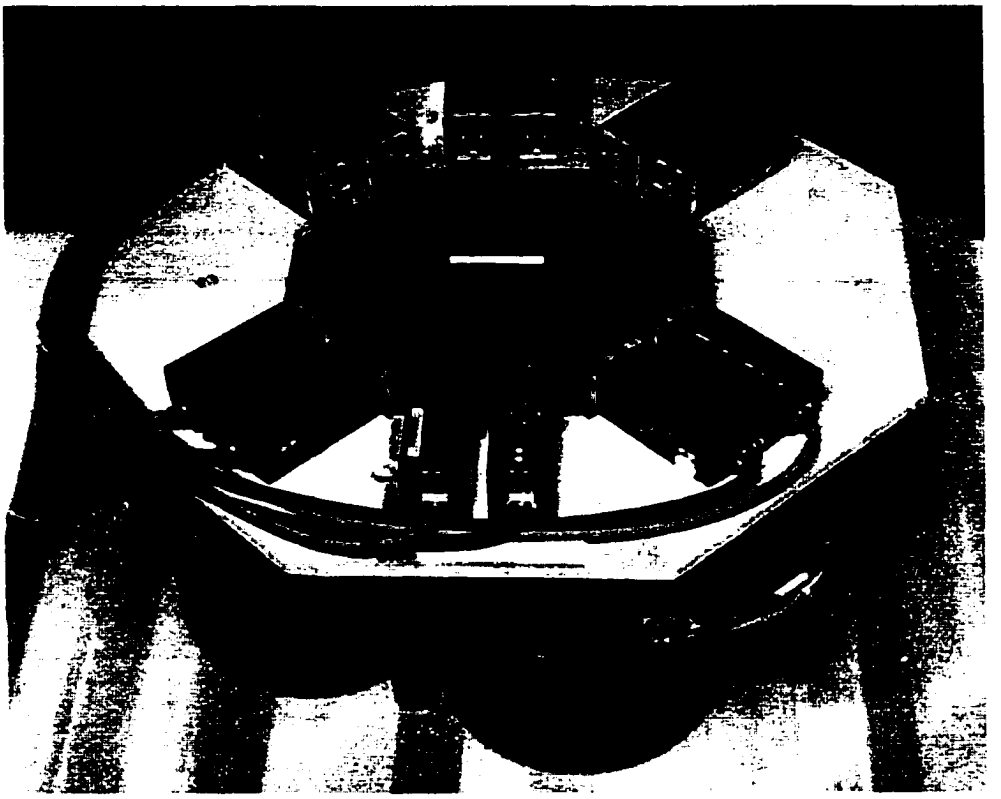

Figure 6.14: Large Angle Magnetic Suspension Test Fixture (LAMSTF)

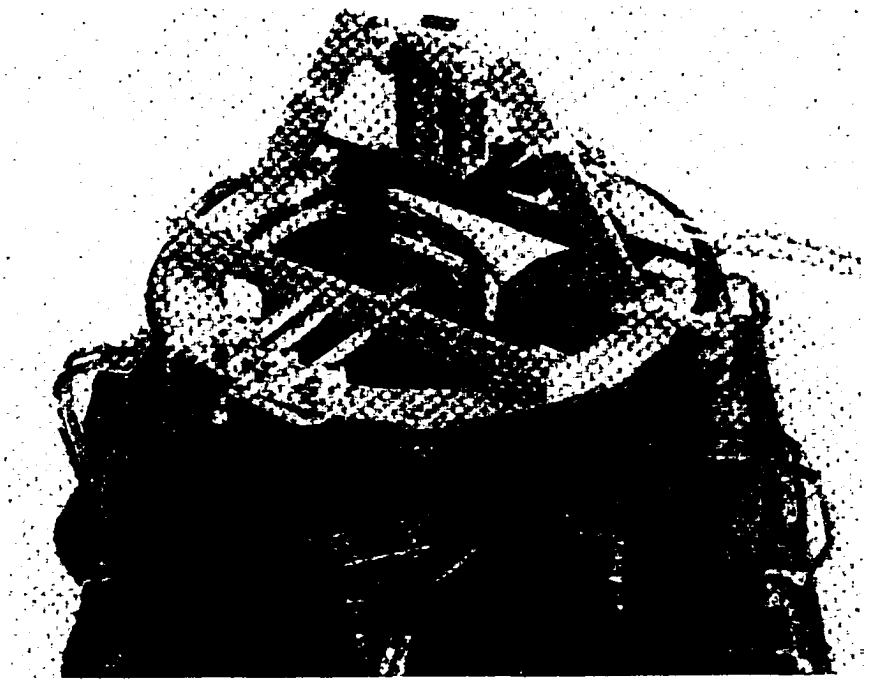

Figure 6.15: LAMSTF with Original Aluminum Sensor Ring

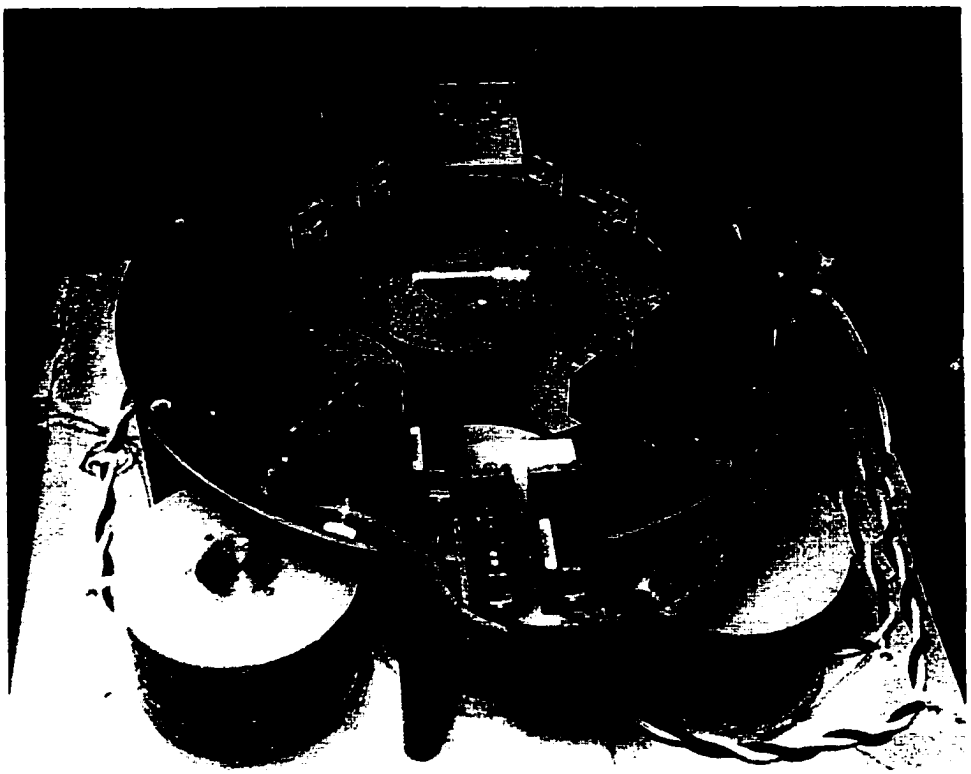

Figure 6.16: Photograph of 6DOF-8C/2L Magnetic Suspension Test Fixture

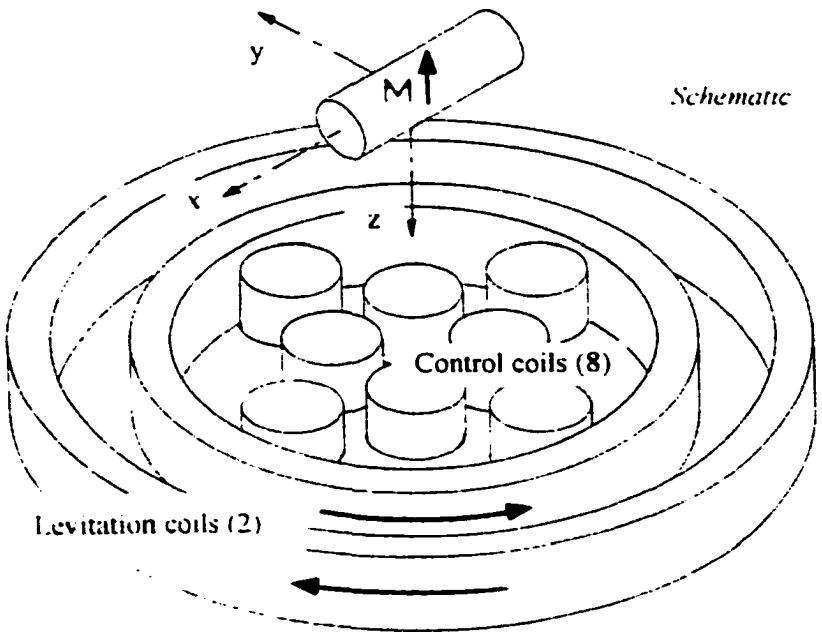

Figure 6.17: Schematic of 6DOF-8C/2L Magnetic Suspension System

The second test was similar to the first except that one of the outer control coils was excited. The outer coils are much closer to the edge of the aluminum plate so the response does include field concentrations at the edge of the plate. The results of the first and second test were published in 1994 [Britcher, 1994(b)].

The third test was performed on the LAMSTF. The electromagnetic coil array was mounted on an aluminum plate and one of the coils was excited. The iron core was removed from the coil to ensure the eddy currents induced were in the aluminum plate. The frequency response between the magnetic field and the driving current was measured.

The fourth test was also performed on the LAMSTF. For this test the iron core was placed in the driving coil and a dummy aluminum sensor ring was placed above the coil array. In the original system, shown in Fig. 6.15, the position sensors were mounted on an aluminum ring. The eddy currents induced in this ring caused problems with the controller so it was replaced by a non-conducting material. The results of the third and fourth tests were published in 1998 [Britcher, 1998(b)].

The experimental setup is shown in Fig. 6.18. The gauss meter for each case was located at the suspension point for the relative test fixtures. The frequency responses of the four tests are shown in Fig. 6.19. The experimental results of the first three tests are all very similar in form. They each have a single break frequency in the magnitude response and a single point of minimum phase in the phase response. This is consistent with the finite element results discussed in the previous section. The roll-off rates and the points of minimum phase is different for all three cases due to the different configurations.

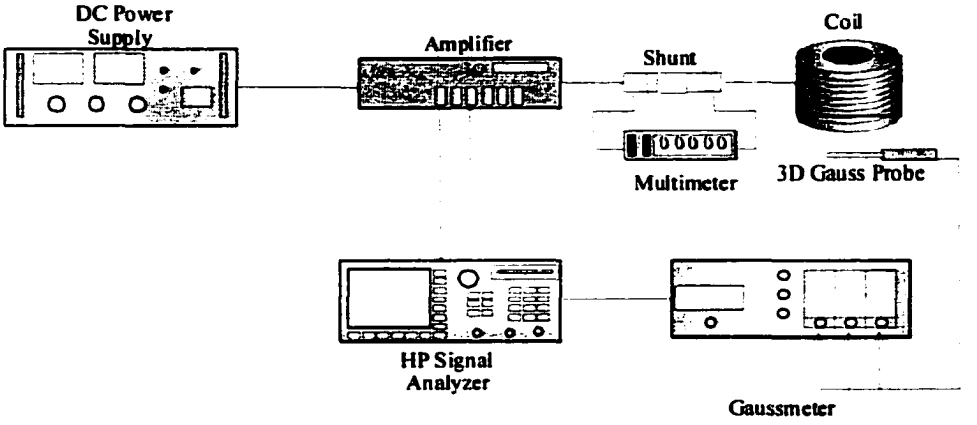

Figure 6.18: Experimental Test Setup for LAMSTF and 6DOF-8C/2L

The fourth response is significantly different from the previous three. This is due to the multiple sources of eddy currents. The first two cases have two sources, the iron core and the aluminum plate. The third case has only one source, the aluminum plate. The fourth case has three sources, the iron core, the aluminum plate, and the aluminum sensor ring.

The iron core does not significantly affect the frequency response of the magnetic field. The eddy currents induced in the iron core are limited to the outer surface of the iron due to the high permeability of the iron. Thus, they shield the majority of the iron from the magnetic field, reducing the eddy current effects. This can be seen by comparing the skin depth thickness of the iron and the aluminum, assuming equal conductivities.

$$\frac{\delta_{Steel}}{\delta_{Alum}} = \sqrt{\frac{\mu_{r,Alum}}{\mu_{r,steel}}} \approx \sqrt{\frac{1}{1000}} \approx 0.03 \qquad (6.25)$$

The penetration depth of the steel is on the order of 3% of the penetration depth of the aluminum. This results in the exclusion of the majority of the flux from the iron core.

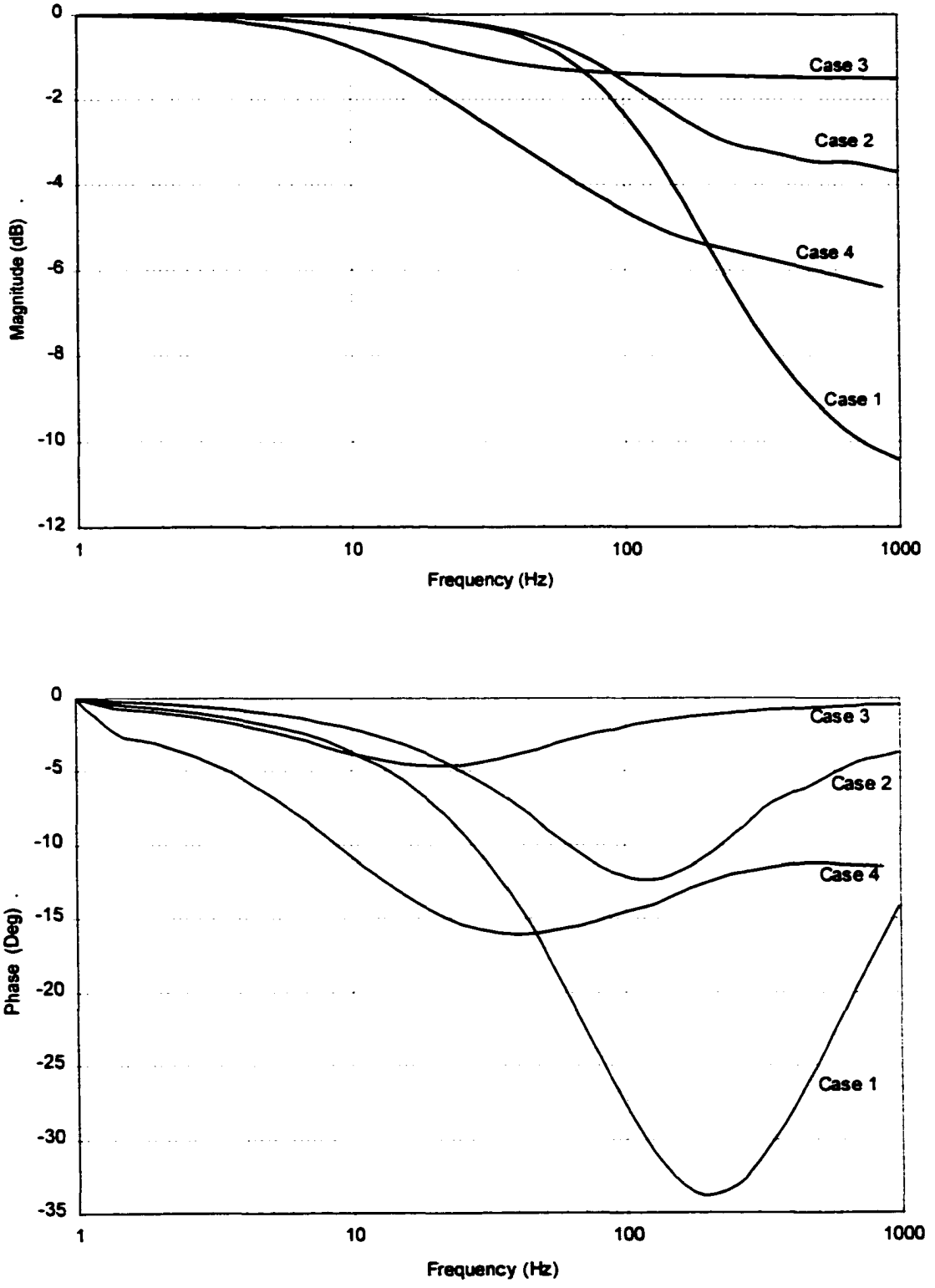

Figure 6.19: Experimental Eddy Current Frequency Response Results

The variations in form of the fourth case are due to the considerably different eddy current characteristics of the aluminum plate and the aluminum sensor ring. The aluminum plate is thinner than the sensor ring and has a stronger field passing through it due to its location with respect to the coil. This means that the magnetic fields produced by the two eddy currents will have different roll-off rates at different frequencies and different points of minimum phase. The composite effect of two different field sources can be seen in the experimental data, Fig. 6.19.

Consider the phase response of the fourth system, as ω increases to ∞ the phase must tend towards zero, thus the apparent asymptote to $-12°$ is actually a second dip in the phase response. It is clear that the phase response can be represented as the sum of two separate phase responses, one with a minimum phase in the region of 30 – 40 Hz and the other at some point greater than 1000 Hz. This can also be seen in the magnitude response. The major roll off of the magnitude response begins around 6 – 10 Hz; however, the slope of the roll off increases at approximately 1000 Hz.

The additive effect can also be seen by examining the phase response at the lower frequencies. At the lower frequencies the behavior of the various systems is known; the phase shift and a rate of change of phase are equal to zero. However, the slope of the fourth test around 1 Hz is about twice that of the other three systems. Additionally, the phase of the response for the first three systems at 10 Hz averages around $-5°$, while the phase of the fourth system is approximately twice that.

The experimental results are compared against the three fractional order transformer models in Figs. 6.20 – 6.24. Each figure compares the results of the three fractional order transformer models discussed in the previous section, repeated here for convenience. In addition, the single time constant model is included as a baseline result, listed as $G_0(s)$.

$$G_1(s) = \frac{a_3 s^2 + a_2 s^{3/2} + a_1 s + a_0}{s^2 + b_2 s^{3/2} + b_1 s + b_0}$$

$$G_2(s) = \frac{a_5 s^{5/2} + a_4 s^2 + a_3 s^{3/2} + a_2 s + a_1 s^{1/2} + a_0}{s^{5/2} + b_4 s^2 + b_3 s^{3/2} + b_2 s + b_1 s^{1/2} + b_0} \tag{6.26}$$

$$G_3(s) = \frac{a_2 s + a_1 s^{1/2} + a_0}{s + b_1 s^{1/2} + b_0}$$

The results show that the single time constant model does an excellent job for the semi-symmetric flat plate and an adequate job for the non-symmetric flat plate. It is not as accurate for the thick plate, and is not capable of modeling the sensor ring and flat plate combination. These results are as expected and serve to verify the single time constant model for simple systems such as the flat plate and discount it for more complex systems, such as the thick plate and the combination plate, sensor ring, and iron core.

The results show that $G_1(s)$ and $G_2(s)$ match the experimental data very well over the entire frequency range for all four sets of experimental data. The transfer functions of either $G_1(s)$ or $G_2(s)$ would provide sufficient accuracy in the design of a control system for these systems. The results of $G_3(s)$ match the experimental data for the first three cases very well, but they do not show good agreement with the fourth case. This is most likely due to the multiple eddy current sources present in the system.

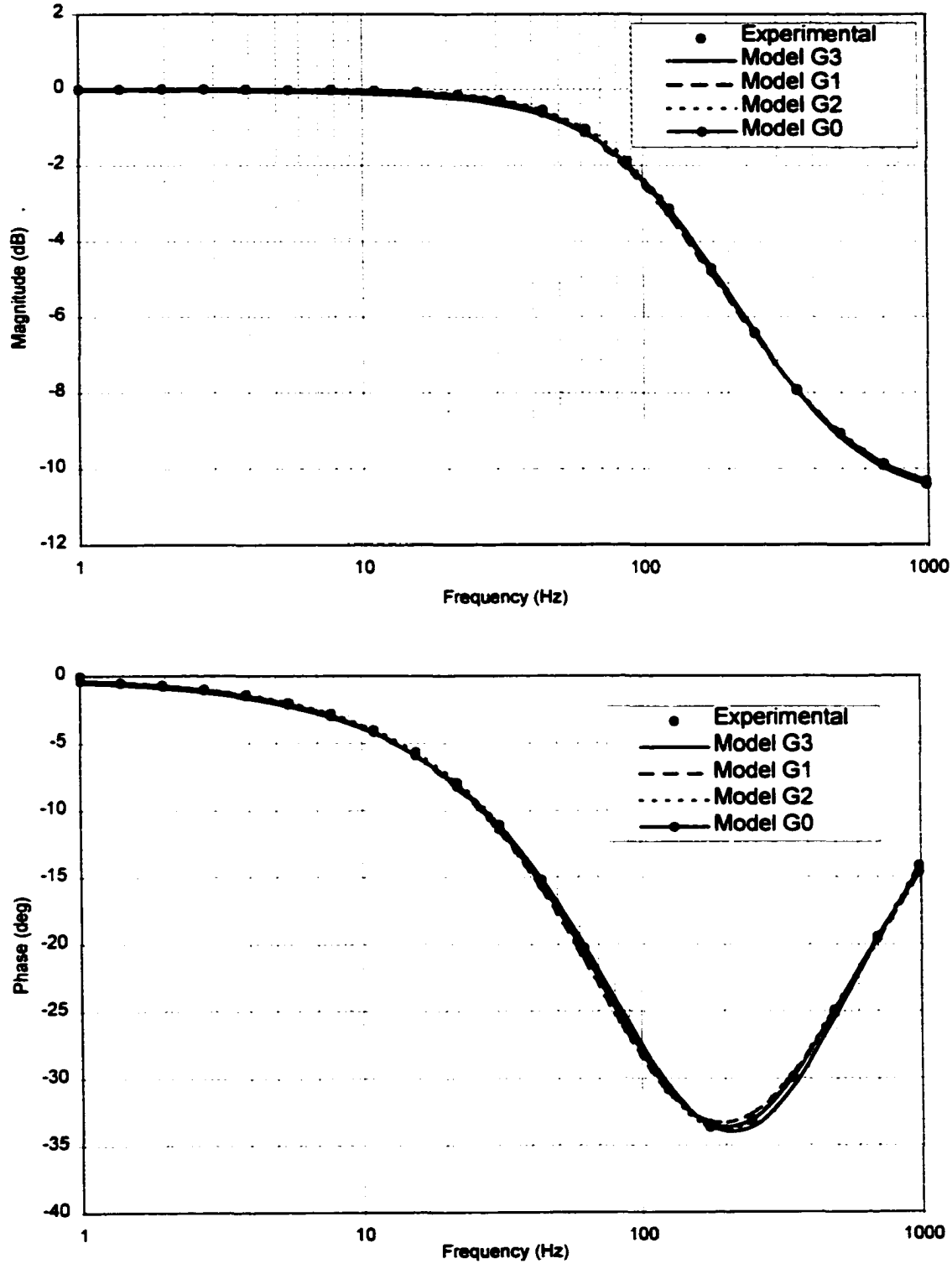

Figure 6.20: Comparison of Fractional Order Transformer Model and 6DOF-8C/2L System with Aluminum Plate Over Center Control Coil

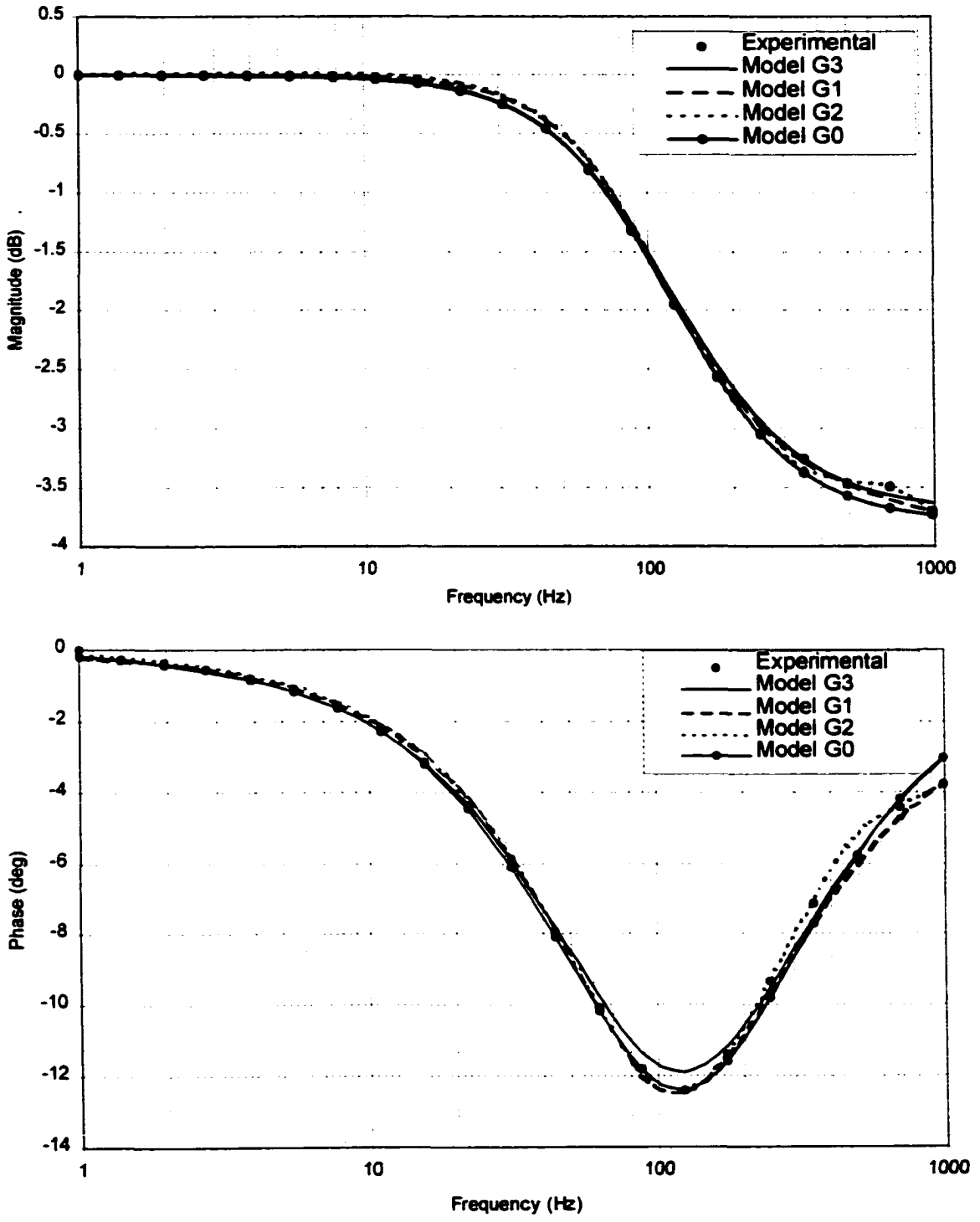

Figure 6.21: Comparison of Fractional Order Transformer Model and 6DOF-8C/2L System with Aluminum Plate Over Outer Control Coil

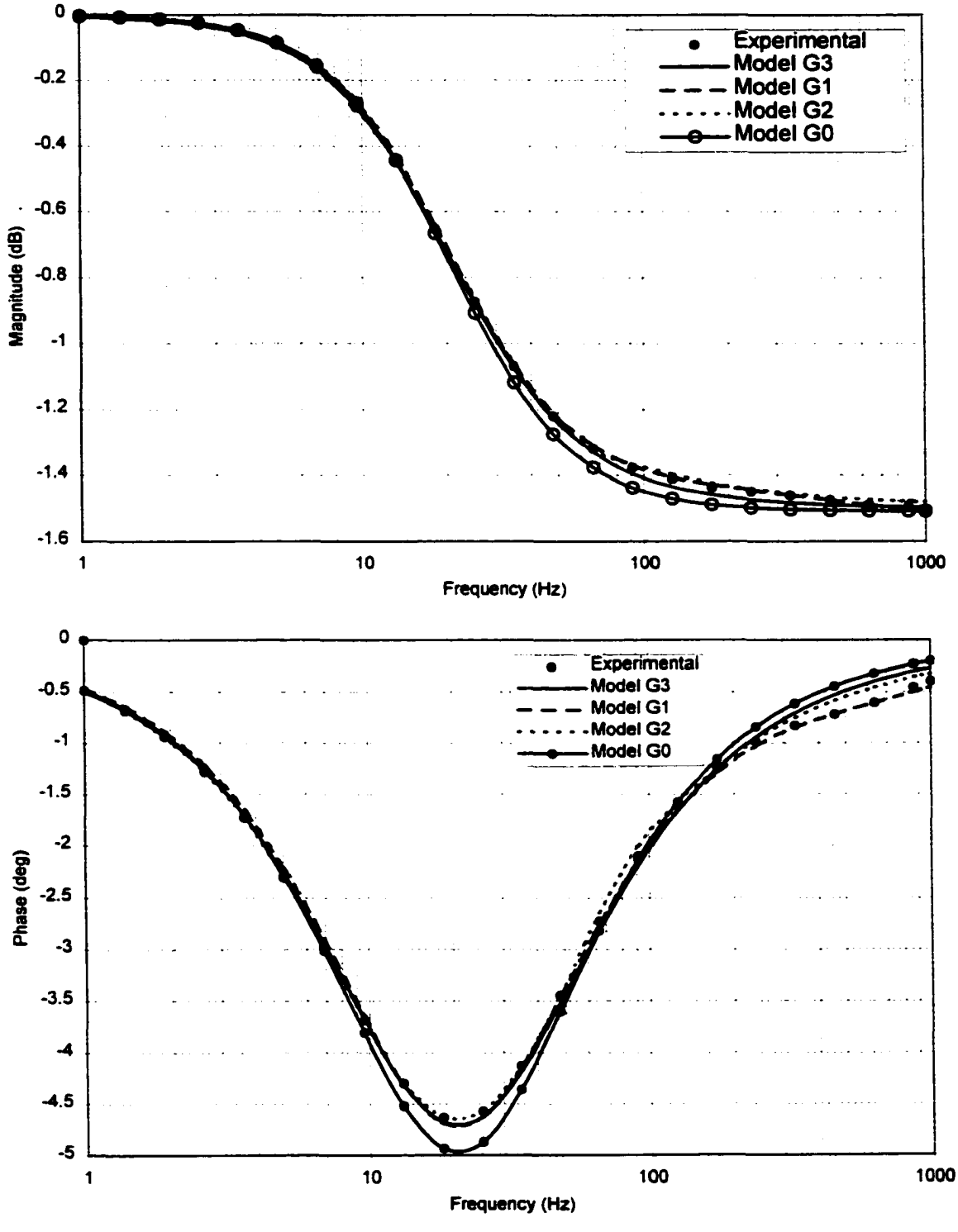

Figure 6.22: Comparison of Fractional Order Transformer Model and LAMSTF with Aluminum Plate Over Coil with No Steel Core

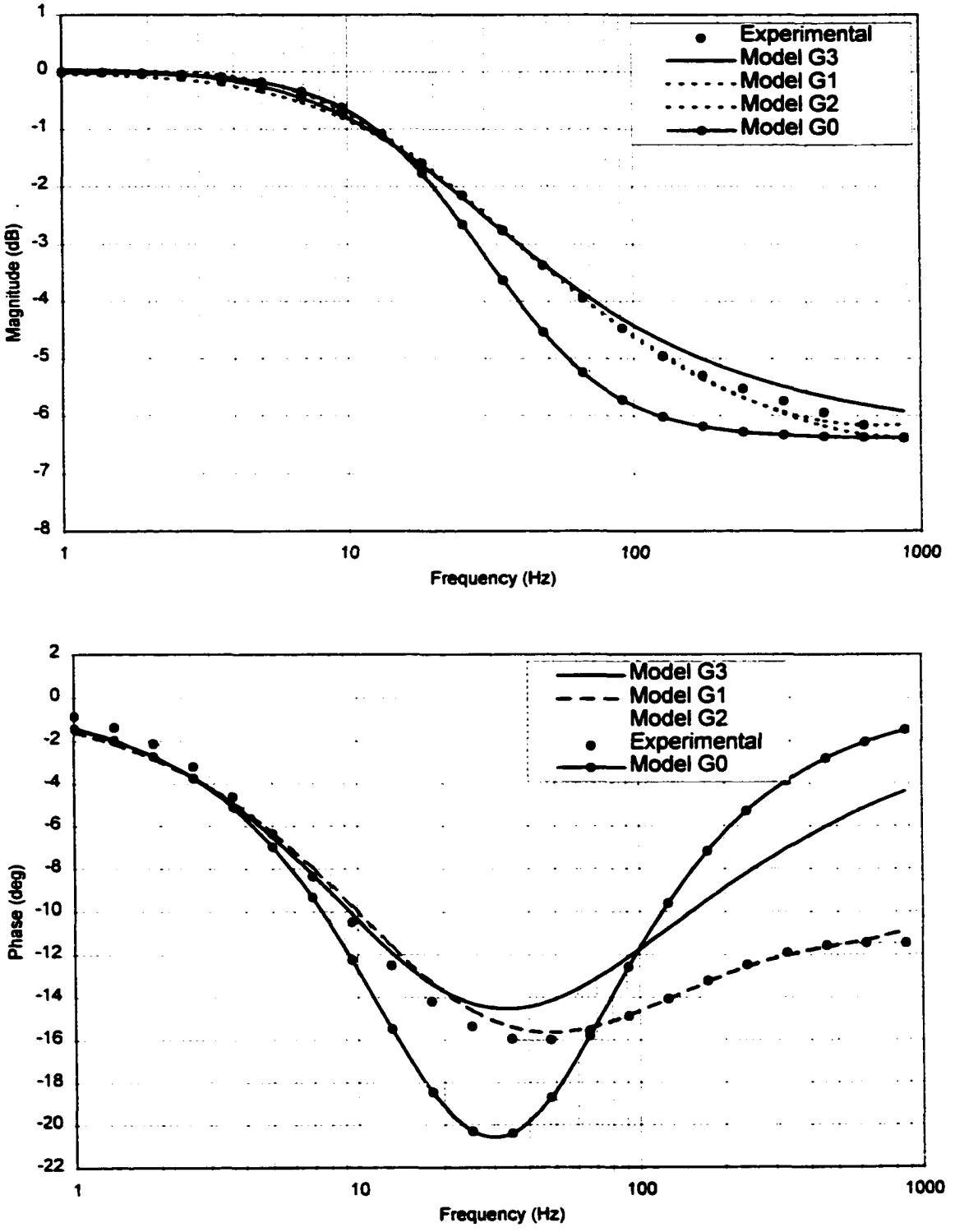

Figure 6.23: Comparison of Fractional Order Transformer Model and LAMSTF with Aluminum Plate Over Coil With Steel Core and Dummy Sensor Ring

The first two models are not only higher order, but they also have a larger number of coefficients. This allows the least-squares algorithm more freedom to match the data. The third model does not have this ability and is therefore only capable of modeling one of the two eddy current sources. This is important to note, even though $G_3(s)$ is capable of modeling the cases of single source eddy currents it is not capable of modeling multiple eddy currents. It is also important to note that effectiveness of $G_1(s)$ and $G_2(s)$ are aided by the least squares algorithm since the original derivation of these terms was for a single transformer pair.

The experimental results, along with the finite element results of the shorted loop and thin plate, prove that the single time constant model does a good job at modeling eddy currents in thin plates. The results also show that the single time constant model breaks down as the thickness of the plate is increased. This is primarily due to the skin depth effect. In the case of the thin plate, the skin depth is always larger than the thickness of the plate. For the thick plate, the skin depth actually becomes less than the thickness of the plate and the fractional resistance term becomes active. However, this fractional component only appears at higher frequencies.

The experimental tests on the LAMSTF and the 6DOF-8C/2L system showed that all three fractional order transformer models are capable of modeling the magnetic effects of the induced eddy currents. Th,e first two models were able to handle all four experimental test

configurations while the third model failed to model the last experiment. This was due to the effects of multiple eddy current sources.

6.4. Discussion of Results

The frequency dependent fractional order transformer model, or thickness dependent model, that was developed in Section 5 was expanded to encompass the entire frequency range. Three models were developed based on the frequency dependent resistance term. The models were compared to finite element results and experimental data. The results show that the fractional order behavior inherent in eddy current results can be attributed to the frequency dependent resistance term. For all cases, the fractional order eddy current models performed as well or better then the accepted integer order models.

7. CONCLUSIONS

Several different modeling tools were developed for small-gap systems, such as magnetic bearings and eddy current analysis, which is used for both small-gap and large-gap systems. Practical design information was also gained from the experimental analysis of the magnetic actuators and a reference data set was developed.

The analysis of the experimental results of the magnetic actuators clearly showed several trends. Firstly, when using a biasing permanent magnet, the location of the magnet has a significant effect on the performance of the system. Placing the magnets on the pole faces provides the highest level of performance. It reduces the flux fringing at the gap and flux leakage of the system. Sandwiching the magnet between two sections of high permeability material proved to be very inefficient. This is an important point to note because when systems are designed with the permanent magnets on the pole surfaces the magnets are generally covered by a thin piece of high permeability steel to protect the fragile magnetic material in case of contact. This research indicates that it might be more efficient to use non-magnetic materials to protect the permanent magnet, despite the increase in the effective air gap.

Actuator performance also proved to be sensitive to the location of the windings. Placing the windings on the poles provided for the most efficient configuration. When the windings were placed on the rear of the stator, flux leakage between the stator and the armature was significantly larger than when the windings were placed on the poles. This too is an

important finding because a significant proportion of commercially produced magnetic bearings place the windings on the rear of the stators. This is done for size and space constraints, but this practice inadvertently may be decreasing the efficiency of the magnetic bearings.

The separation distance of the poles only significantly affected the systems with the biasing permanent magnet in the armature and the systems with the windings on the rear of the stator. In this case, the increased distance between the poles provided more surface area for flux leakage to occur. When the windings or permanent magnets were placed on the poles, there was little difference due to the stator length. The differences that were measured always showed higher performance on the shorter actuator. These differences were due to iron losses. While these losses were not significant, they were larger than initially expected. Further analysis is needed in the understanding of the force generation when the driving current is attempting to cancel the permanent magnet mmf. Some experimental and finite element analysis suggests that not only are reluctance forces at work, but that some force is being transmitted between the armature and the windings via the Biot-Savart relationship of field leakage and ampere-turns. This area warrants further research.

Extended circuit theory showed a significant increase in accuracy over classical magnetic circuit theory. The information added to the analytical model from the finite element data, or experimental data, served to account for the violations in the fundamental assumptions. The

small number of finite element runs necessary to calculate the loss coefficients is well worth the additional effort in order to attain the high level of accuracy in the model.

The algorithm used to predict the loss factors showed that quadratic interpolation was more effective than linear interpolation. Thus, in order to quadratically model a system a total of $2^n + 1$ finite element runs must be performed. This number can be reduced slightly due to the least-squares best fit characteristics of the pseudo inverse. The practicality of using this method in an optimization routine is dependent upon the number of degrees-of-freedom. It should be noted that even if circumstances make it impractical to optimize the entire design space, this method can still be used to optimize specified degrees-of-freedom with only a slight increase in effort.

A quality factor was also introduced which accurately relates the performance of different magnetic actuators with respect to the permanent magnet thickness. It would be very helpful if the quality factor could relate systems with different permanent magnet thicknesses. In its current form, it is not possible. It may be possible to scale the quality factor with magnet thickness to provide an overall efficiency measurement, but this approach has not yet been explored.

One important point to note about the use of finite element analysis in extended circuit theory is the accuracy of material properties. The BH curves of the steel and the permanent magnet material greatly affect the outcome of the results. Even if specifications have been

provided by the manufacturer, it is strongly recommended that testing be used to verify the values.

A fractional eddy current model was also developed. It is based in part from the diffusion model, developed using Maxwell's equations, and the transformer model. The theory explains the "half-order" behavior of eddy currents and provides a unique analytical tool for the analysis of eddy currents and the development of control algorithms for magnetic suspension systems. Three fractional order eddy current models were developed. The models were compared to finite element results and experimental data. The results show that the fractional order behavior inherent in eddy current results can be attributed to the frequency dependent resistance term. For all cases, the fractional order eddy current models performed as well or better then the accepted integer order models.

REFERENCES

Beams, J. W., "High Rotation Speeds," J. Appl. Phys., 8, 795-806, 1937.

Beyer, W.H., "Standard Mathematical Tables and Formulae," 29th Edition, CRC Press, Boston, 1991.

Bloodgood, V.D. Jr, Groom, N.J., Britcher, C.P., "Further Development Of An Optimal Design Approach Applied To Axial Magnetic Bearings," Seventh International Symposium on Magnetic Bearings, Zurich, Switzerland, August 2000.

Bloodgood, V. D. Jr., "Design Optimization of Magnetic Bearings and Magnetic Suspension Systems." Masters Thesis, Old Dominion University, December 1998.

Bozorth, R. M., "Ferromagnetism," Sixth Edition, Van Nostrand Press, Princeton, NJ, 1951

Britcher, C.P., Gonzalez, O., Gray, S., Gomeiz, O., Barkley, J.E., Jafri, A., "Design of a Magnetic Suspension and Balance System for the Princeton/ONR High Reynolds Number Testing Facility," 5th International Symposium on Magnetic Suspension Technology, Santa Barbara, CA, December 1999. NASA/CP-2000-210291, July 2000.

Britcher, C. P., "Wind Tunnel Magnetic Suspension and Balance Systems with Transversely Magnetized Model Cores," 4th International Symposium on Magnetic Suspension Technology, Gifu, Japan, October 1997. NASA CP-1998-207654, May 1998(a).

Britcher, C.P., Bloodgood, V.D., "Eddy Current Influences on the Dynamic Behaviour of Magnetic Suspension Systems," 4th International Symposium on Magnetic Suspension Technology, Gifu, Japan, October 1997. NASA CP-1998-207654, May 1998(b).

Britcher, C. P., "Applications of Magnetic Suspension Technology to Large Scale Facilities- Progress, Problems, and Promises," AIAA 35th Aerospace Sciences Meeting, Reno, NV. AIAA 97-0346, January 1997.

Britcher, C.P., Foster, L.E., "Some Further Developments in the Dynamic Modeling and Control of the Large Angle Magnetic Suspension Test Fixture," 2nd International Symposium On Magnetic Suspension Technology, Seattle, WA, May 1994.

Britcher, C. P., Ghofrani, M., "A Magnetic Suspension System with a Large Angular Range," Rev. Sci, Instrum. 64 (7), July 1993.

Britcher, C. P., Alcorn, C. W., "Interference-Free Measurements of the Subsonic Aerodynamics of Slanted-Base Ogive-Cylinders," AIAA Journal, April 1991.

Britcher, C. P., Alcorn, C. W., "Subsonic Sting Interference on the Aerodynamic Characteristics of a Family of Slanted-Base Ogive-cylinders," NASA CR-4299, June 1990.

Coleman, T. F., Branch, M. A., Grace, A., "Optimization Toolbox for use with MATLAB," Users guide, Version-2, January 1999.

Connecticut Metals, Spec sheet for CMI-C Cold Drawn Rod and Wire for Electromagnetic Applications. 65 Burritt Street, New Britain, CT, 06053. 1-800-548-4770.

Davis, H. T., "The Theory of Linear Operators," Principia Press, Bloomington, Indiana, 1936.

Dexter Magnetic Technologies, http://www.dextermag.com, 1-800-566-4517, 2001.

Downer, J., Goldie, J., Gondhalekar, V., Hockney, R., "Aerospace Applications of Magnetic Bearings," 2nd International Symposium on Magnetic Suspension Technology, Seattle, Washington, August, 1993. NASA CP-3247, May 1994.

Earnshaw, S., "On the Nature of the Molecular Forces... ," Transactions of the Cambridge Philosophical Society, Vol. 7, pp 97-112, 1842.

Euler, L., "De Progressionibus Transcentibus, sev Quarum Termini Algebraice Dari Nequeunt," Comment, Acad. Sci. Imperialis Petropolitanae 5, 1738.

Gautheir, M., Roland, J.P., "An Advanced and Low Cost 2 Degrees of Freedom Magnetic Bearing Flywheel, AIAA, 1987.

Groom, N. J., Bloodgood,V. D. Jr., "A Comparison of Analytical and Experimental Data for A Magnetic Actuator", NASA/TM-2000-210328, September 2000.

Groom, N. J., "Expanded Equations for Torque and Force on a Cylindrical

Permanent Magnet Core in a Large Gap Magnetic Suspension System," NASA TM-3638, 1997 (a).

Groom, N. J., "Simplified Model of a Six-Degree-of-Freedom Large-Gap Magnetic Suspension System," NASA TM-1112868, June 1997 (b).

Groom, N. J., Britcher, C. P., "International Symposium on Magnetic Suspension Technology," NASA CP-3152, Parts 1 and 2, May 1992(a).

Groom, N. J., "Overview of Magnetic Suspension Research at Langley Research Center," 1st International Symposium on Magnetic Suspension Technology, Hampton, Virginia, August 1991. NASA CP-3152, 1992(b).

Groom, N. J., Britcher, C. P., "Aerospace Applications of Magnetic Suspension Technology," NASA CP-10066, Parts 1 and 2, March 1991(a).

Groom, N. J., "Description of the Large Gap Magnetic Suspension System (LGMSS) Ground-Based Experiment," Technology 2000, Washington, D.C., November 1990. NASA CP-3109, 1991(b).

Groom, N.J., "Analytical Model of an Annular Momentum Control Device (AMCD) Laboratory Test Model Magnetic Bearing Actuator," NASA TM-80099, August 1979.

Hildebrand, F. B., "Advanced Calculus for Applications," 2nd edition, Prentice Hall, New Jersey, 1976.

Hartley, T.T., Lorenzo, C.F., "A Solution to the Fundamental Linear Fractional Order Differential Equation," NASA/TP-1998-208693, December 1998.

Holmes, F. T., "Axial Magnetic Suspension," Rev. Sci. Inst. 8, 444-447, 1937.

Keckler, C.R., Groom, N.J., Britcher, C.P., "Magnetic Suspension Technology Workshop," NASA-CP-3202, 1993.

Klesen, C., Nordmann, R., Schönhoff, U., "Design of a Minimum Current Magnetic Bearing," 5th International Symposium On Magnetic Suspension Technology, Santa Barbara, CA, December 1999.

Kolm, H. H., Thornton, R. D., "Magneplane: Guided Electromagnetic Flight," Proceedings of the 5th International Applied Superconductivity Conference, IEEE Publication no. 72CH0682-5-TABSC, May 1972.

KWJ News, KWJ News Web Page, http://jin.jcic.or.jp/kidsweb/news/98-1/maglev.html, 1998.

Leibniz, G.W., Letter from Hanover, Germany, September 30, 1965 to G. A. L' Hôpital. Leibnizen Mathematische Schriften, Vol. 2, pp. 301-302, Olms Verlag., Hildesheim, Germany, 1962. First published in 1849.

Lorenzo, C. F., Hartley, T. T., "Initialization, Conceptualization, and Application in the Generalized Fractional Calculus," NASA Technical Paper, NASA/TP-1998-208415, December 1998.

Lorenzo, C.F., Hartley, T.T., "Generalized Functions for the Fractional Calculus," NASA/TP-1999-209424, October 1999.

Malone, C. L., "Power to Weight Optimization for Magnetic Bearings," Mag-93: Magnetic Bearings, Magnetic Drives and Dry Gas Seals Conference & Exhibition, Alexandria, Virginia, July 1993.

MECOS, Mecos Traxler AG company web page, http://www.mecos.ch, 2001.

Meirovitch, L., "Elements of Vibration Analysis," Second Edition, McGraw-Hill, Inc., New York, 1986.

Miller, K. S., Ross, B., "An Introduction to the Fractional Calculus and Fractional Differential Equations," John Wiley and Sons, Inc., New York, 1993.

Moon, F.C., "Superconducting Levitation, Applications to Bearings and Magnetic Transportation," John Wiley & Sons, Inc., New York, 1994.

Moon, P., Spencer, D.E., "Field Theory for Engineers," Van Nostrand, Princeton, New Jersey, 1961.

NASA, NIX-NASA Image eXchange, http://nix.larc.nasa.gov, Image # EL-1996-00077, 1996.

Oldham, K. B., Spanier, J., "The Fractional Calculus,"Academic Press, New York, 1974.

Oustaloup, A., "La Derivation Non Entiere: Thorie, Synthese et Applications, Hermes, Paris, 1995.

Penrose, R., "A Generalized Inverse for Matrices," Proc. Cambridge Philos. Soc., vol. 51, pp. 406-413, 1955.

Perry, M.P., "Low Frequency Electromagnetic Design," Marcel Dekker, Inc., New York, 1985.

Podlubny, I., "Fractional Differential Equations," Academic Press, San Diego, 1999.

Roters, H.C., "Electromagnetic Devices," John Wiley & Sons, New York, 1941.

Schoeb, R., Barletta, N., Fleischli, A., Foiera, G., Gempp, T., Reiter, H.G., Poirier, V.L., Gernes, D.B., Bourque, K., Loree, H.M., Richardson, J.S., "A Bearingless Motor for a Left Ventricular Assist Device (LVAD)," Seventh International Symposium on Magnetic Bearings, Zurich Switzerland, 2000.

Schweitzer, G., "1st International Symposium on Magnetic Bearings," Zurich, Switzerland, 1988.

Smits, A. J., "Needs for High Reynolds Number Facilities to Design the Next Generation of Sea and Air Vehicles," A workshop presented at the Arlington Hilton, June 18-19, 1997

Stoll, R.L., "The Analysis of Eddy Currents," Clarendon Press, Oxford, 1974.

Swann, M. K., "Magnetic Bearings - Fifty Years of Progress," Proceedings from the Magnetic Suspension Technology Workshop, Hampton, VA, 1988.

S2M, http://www.s2m.fr/g3/applications.html, 2001

Tanaka, H., "Change in Coil Distribution of Electrodynamic Suspension System," 1st International Symposium on Magnetic Suspension Technology, Hampton, Virginia, August 1991. NASA CP-3152, 1992.

Vector Fields, "PC-OPERA, Software for Electromagnetic Design," Vector Fields Reference Manual, Version 01-97-F4, 1997.

Vector Fields, "OPERA-3D User Guide," Vector Fields Reference Manual, Version 7.1, 1999.

APPENDIX A: EXPERIMENTAL DATA

Air Gap	Force (lb)					
(in)	Test 3	Test 8	Test 12	Test 16	Test 21	Test 25
0.150	1.602	0.468	2.473	1.741	0.698	2.723
0.145	1.680	0.475	2.570	1.823	0.712	2.812
0.140	1.769	0.491	2.684	1.918	0.737	2.919
0.135	1.871	0.506	2.811	2.023	0.757	3.048
0.130	1.984	0.526	2.955	2.141	0.783	3.194
0.125	2.110	0.546	3.107	2.270	0.812	3.355
0.120	2.245	0.571	3.275	2.414	0.847	3.535
0.115	2.394	0.594	3.458	2.571	0.885	3.731
0.110	2.562	0.624	3.659	2.744	0.928	3.943
0.105	2.744	0.657	3.876	2.932	0.969	4.176
0.100	2.945	0.694	4.116	3.140	1.019	4.428
0.095	3.169	0.730	4.379	3.378	1.076	4.709
0.090	3.420	0.777	4.673	3.640	1.138	5.014
0.085	3.700	0.827	4.991	3.930	1.207	5.353
0.080	4.009	0.885	5.348	4.257	1.288	5.735
0.075	4.361	0.952	5.742	4.630	1.377	6.147
0.070	4.760	1.031	6.188	5.049	1.486	6.612
0.065	5.214	1.116	6.682	5.525	1.608	7.138
0.060	5.727	1.221	7.241	6.069	1.746	7.723
0.055	6.318	1.346	7.867	6.703	1.917	8.389
0.050	7.003	1.495	8.593	7.431	2.116	9.146
0.045	7.794	1.674	9.413	8.284	2.358	10.022
0.040	8.721	1.899	10.363	9.286	2.653	11.023
0.035	9.818	2.181	11.461	10.497	3.021	12.193
0.030	11.141	2.539	12.775	11.939	3.495	13.568
0.025	12.753	3.015	14.326	13.716	4.112	15.223
0.020	14.723	3.664	16.210	15.941	4.939	17.217
0.015	17.256	4.591	18.539	18.846	6.113	19.713
0.010	20.575	5.993	21.570	22.769	7.892	22.915
0.005	25.256	8.419	25.572	28.372	10.884	27.305
0.000	31.956	13.877	30.991	36.888	17.218	33.342

Table A1: Data for tests 3, 8, 12, 16, 21, and 25

NI	Force (lbs)				
(Amps)	g = 0.02"	g = 0.04"	g = 0.05"	g = 0.06"	g = 0.07"
0	-*	0.000	0.000	0.000	0.000
200	-	0.221	0.167	0.148	0.134
400	-	0.866	0.588	0.428	0.322
600	-	2.843	1.937	1.405	1.053
800	-	5.746	3.949	2.892	2.196
1000	-	8.136	5.607	4.111	3.132
1200	-	12.549	8.628	6.339	4.856
1400	-	15.896	10.921	8.022	6.156
1600	-	21.590	14.919	10.938	8.400
1800	-	25.299	17.816	13.059	10.032
2000	-	30.178	22.542	16.576	12.763
2200	-	33.946	27.057	20.216	15.668

Table A2: Data for test 1

NI	Force (lbs)				
(Amps)	g = 0.02"	g = 0.04"	g = 0.05"	g = 0.06"	g = 0.07"
0	0.001	0.000	0.000	0.000	0.000
200	0.896	0.286	0.194	0.143	0.047
400	4.653	1.510	1.041	0.769	0.238
600	8.320	2.686	1.853	1.371	0.434
800	15.347	5.013	3.478	2.583	0.824
1000	19.844	6.738	4.714	3.514	1.131
1200	26.832	9.167	6.595	5.010	1.674
1400	29.587	10.260	7.537	5.818	2.035
1600	32.772	11.511	8.583	6.720	2.506
1800	35.668	12.486	9.372	7.382	2.840
2000	37.517	13.035	9.813	7.750	3.017
2200	39.775	13.797	10.416	8.251	3.255

Table A3: Data for test 10

NI	Force (lbs)				
(Amps)	g = 0.02"	g = 0.04"	g = 0.05"	g = 0.06"	g = 0.07"
0	-*	0.000	0.000	0.000	0.000
200	-	0.184	0.116	0.050	0.018
400	-	1.366	0.920	0.612	0.437
600	-	2.747	1.873	1.309	0.974
800	-	5.675	3.901	2.792	2.120
1000	-	8.139	5.592	4.043	3.091
1200	-	12.704	8.714	6.334	4.862
1400	-	18.222	12.477	9.079	6.988
1600	-	22.227	15.289	11.118	8.557
1800	-	27.732	19.981	14.600	11.247
2000	-	30.674	23.143	17.025	13.154
2200	-	34.204	27.430	20.773	16.220

Table A4: Data for test 14

NI	Force (lbs)				
(Amps)	g = 0.02"	g = 0.04"	g = 0.05"	g = 0.06"	g = 0.07"
0	0.000	0.000	0.000	0.000	0.000
200	1.257	0.395	0.273	0.185	0.056
400	4.837	1.542	1.057	0.738	0.223
600	10.755	3.354	2.316	1.619	0.494
800	19.142	5.822	4.046	2.813	0.867
1000	26.608	8.799	6.143	4.300	1.334
1200	31.463	11.660	8.354	5.967	1.896
1400	36.151	13.695	10.091	7.520	2.523
1600	39.448	15.527	11.592	8.862	3.229
1800	42.569	16.798	12.603	9.719	3.676
2000	45.816	17.963	13.534	10.479	4.046
2200	48.189	19.048	14.355	11.161	4.371

Table A5: Data for test 23

* The protective epoxy around the coils extended beyond the end of the pole face over 0.02", so this data could not be collected.

NI	Force (lbs)				
(Amps)	g = 0.02"	= 0.04"	g = 0.05"	g = 0.06"	g = 0.12"
-2200	1.723	1.280	0.983	0.970	0.585
-2000	1.623	1.059	0.765	0.845	0.487
-1800	1.728	1.020	0.707	0.772	0.391
-1600	1.983	1.141	0.761	0.808	0.369
-1400	2.688	1.356	0.901	0.998	0.395
-1200	3.368	1.894	1.288	1.219	0.453
-1000	4.737	2.689	1.893	1.701	0.609
-800	6.527	3.360	2.416	2.360	0.844
-600	7.938	4.596	3.389	2.899	1.050
-400	10.436	5.562	4.159	3.856	1.427
-200	12.286	7.235	5.501	4.591	1.723
0	15.385	8.480	6.505	5.828	2.232
200	17.606	10.508	8.157	6.736	2.614
400	21.393	12.766	9.995	8.230	3.253
600	24.087	14.368	11.304	9.290	3.716
800	28.545	16.963	13.438	11.010	4.471
1000	33.249	18.791	14.933	12.868	5.286
1200	36.410	21.768	17.359	14.158	5.855
1400	41.049	23.777	19.023	16.226	6.773
1600	43.688	26.943	21.660	17.638	7.406
1800	47.221	30.006	24.340	19.869	8.428
2000	49.294	31.868	26.063	21.329	9.121
2200	52.057	34.432	28.485	23.510	10.214

Table A6: Test 4 experimental results

NI	Force (lbs)				
(Amps)	g = 0.02"	g = 0.04"	g = 0.05"	g = 0.06"	g = 0.12"
-2200	1.864	1.258	1.085	0.986	0.407
-2000	1.906	1.256	1.067	0.962	0.379
-1800	2.021	1.281	1.069	0.957	0.334
-1600	2.202	1.349	1.110	0.975	0.310
-1400	2.710	1.589	1.279	1.105	0.307
-1200	3.206	1.845	1.470	1.262	0.351
-1000	4.281	2.430	1.921	1.637	0.419
-800	5.219	2.955	2.331	1.977	0.601
-600	7.062	3.995	3.152	2.673	0.761
-400	9.354	5.324	4.208	3.570	1.089
-200	11.093	6.343	5.025	4.272	1.354
0	13.924	8.049	6.402	5.460	1.819
200	15.835	9.244	7.387	6.314	2.172
400	18.872	11.104	8.923	7.658	2.753
600	20.838	12.323	9.935	8.546	3.361
800	23.595	14.178	11.492	9.923	3.772
1000	25.499	15.705	12.853	11.161	4.407
1200	26.369	16.410	13.512	11.784	4.794
1400	27.391	17.220	14.253	12.483	5.259
1600	27.961	17.637	14.629	12.829	5.486
1800	28.732	18.199	15.128	13.288	5.764
2000	29.179	18.517	15.409	13.541	5.991
2200	29.805	18.961	15.799	13.898	6.122

Table A7: Test 9 experimental results

NI	Force (lbs)				
(Amps)	g = 0.02"	= 0.04"	g = 0.05"	g = 0.06"	g = 0.12"
-2200	1.905	1.317	1.256	1.103	0.625
-2000	1.637	1.028	0.954	0.814	0.436
-1800	1.661	0.971	0.849	0.710	0.348
-1600	2.055	1.090	0.853	0.680	0.275
-1400	2.563	1.323	1.044	0.803	0.279
-1200	3.726	1.916	1.293	0.995	0.319
-1000	4.769	2.470	1.852	1.432	0.443
-800	6.757	3.553	2.337	1.827	0.579
-600	9.284	4.942	3.263	2.576	0.855
-400	11.261	6.035	4.006	3.179	1.085
-200	14.689	7.942	5.302	4.249	1.502
0	17.255	9.376	6.296	5.063	1.828
200	21.583	11.740	7.949	6.429	2.381
400	24.867	13.470	9.824	7.971	3.025
600	30.363	16.320	11.173	9.089	3.493
800	36.399	19.464	13.381	10.917	4.268
1000	40.449	21.703	14.939	12.210	4.821
1200	46.293	25.362	17.481	14.315	5.721
1400	49.160	27.816	19.225	15.773	6.346
1600		31.475	22.021	18.101	7.364
1800		33.696	24.822	20.497	8.440
2000		36.598	26.557	22.058	9.183
2200		39.127	28.952	24.319	10.358

Table A8: Test 17 experimental results

NI	Force (lbs)				
(Amps)	g = 0.02"	g = 0.04"	g = 0.05"	g = 0.06"	g = 0.12"
-2200	1.850	1.299	1.104	0.933	0.539
-2000	1.811	1.246	1.065	0.921	0.496
-1800	1.805	1.170	0.977	0.809	0.363
-1600	2.100	1.259	0.996	0.796	0.309
-1400	2.608	1.492	1.162	0.901	0.307
-1200	3.409	1.905	1.476	1.128	0.345
-1000	4.446	2.489	1.929	1.475	0.447
-800	5.766	3.240	2.523	1.935	0.603
-600	7.459	4.206	3.289	2.539	0.823
-400	9.883	5.633	4.440	3.401	1.170
-200	12.188	7.002	5.537	4.260	1.520
0	14.788	8.567	6.813	5.273	1.929
200	17.646	10.279	8.226	6.383	2.402
400	20.580	12.021	9.693	7.564	2.915
600	23.833	13.982	11.326	8.857	3.492
800	27.020	16.047	13.037	10.237	4.114
1000	29.708	17.988	14.723	11.643	4.773
1200	32.191	19.879	16.370	13.104	5.580
1400	33.693	21.015	17.457	14.031	6.175
1600	35.027	22.078	18.388	14.911	6.663
1800	36.259	23.000	19.121	15.600	7.144
2000	37.612	23.762	19.729	16.130	7.482
2200	38.210	24.300	20.166	16.515	7.736

Table A9: Test 22 experimental results

NI	Force (lbs)				
(Amps)	g = 0.02"	= 0.04"	g = 0.05"	g = 0.06"	g = 0.12"
-2200	10.945	7.758	5.776	4.499	3.595
-2000	7.885	5.523	4.123	3.205	2.553
-1800	6.064	4.243	3.165	2.461	1.959
-1600	3.708	2.590	1.931	1.498	1.188
-1400	2.463	1.716	1.275	0.991	0.785
-1200	1.051	0.722	0.535	0.416	0.327
-1000	0.226	0.147	0.107	0.086	0.069
-800	0.003	-0.003	0.001	0.007	0.012
-600	0.143	0.112	0.093	0.083	0.078
-400	0.561	0.427	0.334	0.270	0.231
-200	1.688	1.245	0.970	0.773	0.646
0	2.735	2.009	1.557	1.238	1.034
200	4.823	3.522	2.716	2.162	1.789
400	7.474	5.426	4.169	3.313	2.733
600	9.487	6.881	5.283	4.198	3.458
800	12.896	9.438	7.224	5.724	4.705
1000	15.108	11.315	8.644	6.844	5.615
1200	18.279	14.548	11.039	8.727	7.156
1400	22.118	18.127	13.713	10.811	8.852
1600	25.364	20.707	15.619	12.290	10.048
1800	29.492	24.858	18.691	14.724	12.023
2000	31.047	27.528	20.798	16.390	13.397
2200	33.174	31.228	23.963	18.975	15.526

Table A10: Test 7 experimental results

NI	Force (lbs)				
(Amps)	g = 0.02"	g = 0.04"	g = 0.05"	g = 0.06"	g = 0.12"
-2200					
-2000					
-1800					
-1600	3.196	1.584	1.213	0.954	0.352
-1400	2.000	0.980	0.744	0.580	0.222
-1200	1.073	0.533	0.401	0.316	0.130
-1000	0.419	0.229	0.182	0.146	0.089
-800	0.116	0.104	0.091	0.087	0.087
-600	0.252	0.189	0.166	0.153	0.134
-400	0.880	0.514	0.425	0.363	0.235
-200	2.040	1.094	0.873	0.728	0.395
0	3.713	1.917	1.514	1.239	0.613
200	5.787	2.950	2.314	1.884	0.885
400	8.726	4.409	3.451	2.802	1.276
600	11.394	5.722	4.472	3.637	1.636
800	14.212	7.129	5.571	4.526	2.018
1000	16.590	8.515	6.681	5.438	2.426
1200	18.267	9.622	7.621	6.255	2.827
1400	19.560	10.428	8.320	6.871	3.179
1600	20.645	11.067	8.861	7.341	3.446
1800	21.607	11.609	9.314	7.730	3.657
2000	22.581	12.180	9.790	8.131	3.869
2200	23.335	12.598	10.134	8.427	4.025

Table A11: Test 13 experimental results

NI	Force (lbs)				
(Amps)	g = 0.02"	= 0.04"	g = 0.05"	g = 0.06"	g = 0.12"
-2200	8.211	5.854	4.440	3.480	1.211
-2000	5.658	4.040	3.068	2.405	0.834
-1800	4.221	3.022	2.294	1.803	0.627
-1600	2.444	1.753	1.337	1.054	0.376
-1400	1.170	0.849	0.654	0.521	0.208
-1200	0.599	0.444	0.343	0.284	0.141
-1000	0.134	0.123	0.108	0.110	0.105
-800	0.099	0.113	0.107	0.113	0.132
-600	0.443	0.384	0.326	0.306	0.239
-400	0.947	0.768	0.628	0.554	0.356
-200	2.141	1.656	1.326	1.121	0.601
0	3.837	2.904	2.301	1.905	0.934
200	5.254	3.948	3.111	2.555	1.206
400	7.866	5.841	4.573	3.724	1.682
600	9.884	7.313	5.697	4.620	2.041
800	13.475	9.829	7.637	6.163	2.652
1000	16.189	11.726	9.072	7.298	3.101
1200	20.425	14.960	11.481	9.215	3.845
1400	22.590	17.317	13.227	10.589	4.380
1600	25.663	21.182	16.132	12.850	5.258
1800	28.354	25.333	19.242	15.321	6.216
2000	29.860	27.869	21.347	17.022	6.887
2200	31.519	31.489	24.473	19.636	7.956

Table A12: Test 20 experimental results

NI	Force (lbs)				
(Amps)	g = 0.02"	g = 0.04"	g = 0.05"	g = 0.06"	g = 0.12"
-2200					
-2000	3.223	1.668	1.248	0.965	0.298
-1800	2.094	1.066	0.786	0.599	0.169
-1600	1.129	0.563	0.411	0.314	0.073
-1400	0.445	0.213	0.149	0.116	0.020
-1200	0.028	0.000	0.001	0.006	0.004
-1000	0.013	0.002	0.008	0.019	0.029
-800	0.295	0.154	0.133	0.130	0.095
-600	0.911	0.487	0.400	0.353	0.204
-400	1.864	0.990	0.799	0.678	0.355
-200	3.155	1.665	1.333	1.112	0.550
0	4.780	2.520	2.001	1.654	0.788
200	7.135	3.752	2.961	2.431	1.124
400	9.455	4.930	3.889	3.185	1.448
600	12.098	6.271	4.921	4.017	1.808
800	15.071	7.741	6.054	4.934	2.202
1000	18.175	9.308	7.299	5.930	2.629
1200	20.866	10.944	8.580	6.992	3.084
1400	22.909	12.375	9.795	8.042	3.567
1600	24.614	13.459	10.769	8.914	4.045
1800	26.443	14.497	11.682	9.713	4.537
2000	27.719	15.245	12.325	10.263	4.846
2200	28.948	15.916	12.881	10.760	5.117

Table A13: Test 26 experimental results

NI	Force (lbs)				
(Amps)	g = 0.02"	= 0.04"	g = 0.05"	g = 0.06"	g = 0.12"
-2200	2.187	1.218	0.925	0.712	0.163
-2000	2.920	1.654	1.281	1.004	0.275
-1800	3.521	2.029	1.581	1.251	0.375
-1600	4.636	2.719	2.150	1.727	0.577
-1400	5.509	3.262	2.598	2.100	0.734
-1200	7.028	4.222	3.388	2.760	1.032
-1000	8.780	5.338	4.309	3.534	1.377
-800	10.058	6.157	4.991	4.106	1.637
-600	12.188	7.518	6.122	5.065	2.077
-400	13.729	8.490	6.933	5.753	2.396
-200	16.207	10.083	8.256	6.874	2.921
0	17.984	11.190	9.182	7.658	3.290
200	20.912	13.027	10.701	8.948	3.893
400	24.128	14.990	12.325	10.325	4.542
600	26.426	16.368	13.457	11.285	4.996
800	30.134	18.589	15.281	12.838	5.726
1000	32.689	20.126	16.540	13.905	6.227
1200	36.610	22.587	18.542	15.608	7.031
1400	40.290	25.125	20.635	17.390	7.872
1600	42.587	26.798	22.061	18.588	8.448
1800	45.686	29.323	24.224	20.452	9.358
2000	47.647	30.866	25.621	21.682	9.974
2200	50.219	33.060	27.624	23.478	10.934

Table A14: Test 6 experimental results

NI	Force (lbs)				
(Amps)	g = 0.02"	g = 0.04"	g = 0.05"	g = 0.06"	g = 0.12"
-2200	2.773	1.553	1.230	0.964	0.255
-2000	3.300	1.863	1.475	1.169	0.330
-1800	4.069	2.331	1.858	1.485	0.460
-1600	4.684	2.711	2.170	1.748	0.572
-1400	5.789	3.406	2.739	2.226	0.778
-1200	6.651	3.935	3.178	2.593	0.944
-1000	8.196	4.898	3.972	3.260	1.245
-800	9.331	5.613	4.561	3.755	1.472
-600	11.225	6.816	5.560	4.604	1.864
-400	13.341	8.158	6.672	5.550	2.311
-200	14.804	9.101	7.460	6.221	2.630
0	17.068	10.579	8.693	7.261	3.142
200	18.594	11.540	9.514	7.972	3.497
400	20.955	13.052	10.784	9.069	4.044
600	22.461	14.039	11.607	9.780	4.408
800	24.477	15.487	12.841	10.860	4.967
1000	25.868	16.620	13.856	11.778	5.502
1200	26.536	17.137	14.354	12.221	5.804
1400	27.371	17.757	14.920	12.738	6.160
1600	27.820	18.098	15.222	13.019	6.336
1800	28.429	18.564	15.623	13.386	6.565
2000	28.787	18.830	15.859	13.594	6.694
2200	29.298	19.200	16.185	13.889	6.871

Table A15: Test 11 experimental results

NI	Force (lbs)				
(Amps)	g = 0.02"	= 0.04"	g = 0.05"	g = 0.06"	g = 0.12"
-2200	2.234	1.265	0.986	0.769	0.251
-2000	2.939	1.707	1.340	1.069	0.377
-1800	3.513	2.071	1.642	1.322	0.488
-1600	4.567	2.742	2.198	1.789	0.707
-1400	5.819	3.556	2.875	2.359	0.969
-1200	6.780	4.175	3.388	2.796	1.173
-1000	8.427	5.231	4.267	3.541	1.522
-800	9.621	6.015	4.919	4.091	1.779
-600	11.637	7.322	6.014	5.016	2.215
-400	13.072	8.260	6.799	5.686	2.530
-200	15.503	9.803	8.090	6.777	3.051
0	18.121	11.459	9.480	7.963	3.614
200	20.037	12.656	10.473	8.804	4.015
400	23.173	14.588	12.077	10.163	4.668
600	25.430	15.960	13.199	11.124	5.125
800	29.008	18.152	15.019	12.647	5.852
1000	31.516	19.681	16.273	13.714	6.358
1200	35.286	22.118	18.299	15.428	7.170
1400	37.807	23.787	19.660	16.590	7.725
1600	41.256	26.348	21.829	18.423	8.605
1800	44.265	28.831	23.984	20.302	9.525
2000	46.118	30.355	25.378	21.530	10.149
2200	48.648	32.500	27.321	23.319	11.125

Table A16: Test 19 experimental results

NI	Force (lbs)				
(Amps)	g = 0.02"	g = 0.04"	g = 0.05"	g = 0.06"	g = 0.12"
-2200	2.457	1.290	0.984	0.747	0.101
-2000	2.487	1.307	1.016	0.787	0.116
-1800	3.640	2.162	1.617	1.293	0.351
-1600	4.557	2.746	2.186	1.774	0.565
-1400	5.549	3.409	2.740	2.252	0.798
-1200	6.685	4.158	3.366	2.791	1.059
-1000	7.960	5.003	4.075	3.398	1.353
-800	9.400	5.970	4.885	4.092	1.686
-600	11.017	7.028	5.777	4.859	2.067
-400	12.799	8.187	6.749	5.691	2.476
-200	15.115	9.660	8.001	6.767	3.007
0	17.126	10.969	9.135	7.731	3.484
200	19.275	12.353	10.312	8.744	3.997
400	21.457	13.756	11.524	9.780	4.519
600	23.791	15.262	12.801	10.887	5.078
800	25.995	16.792	14.115	12.020	5.663
1000	27.783	18.176	15.341	13.108	6.261
1200	29.070	19.275	16.326	14.012	6.832
1400	30.424	20.279	17.233	14.852	7.410
1600	31.511	21.105	18.015	15.561	7.831
1800	32.401	21.838	18.637	16.108	8.232
2000	33.176	22.417	19.128	16.553	8.511
2200	33.567	22.768	19.439	16.856	8.690

Table A17: Test 24 experimental results

APPENDIX B: EXPERIMENTAL DETERMINATION OF PERMANENT MAGNET PROPERTIES

Traditionally, one of the most difficult parameters to characterize when modeling a magnetic system is the magnetic moment of the biasing permanent magnet, m. The accuracy of the model is highly dependent upon knowing the true magnetic moment. Once the magnetic moment has been determined, the residual induction, B_r, can be found.

$$m = \frac{B_r v}{\mu_0} \tag{B.1}$$

Because of its importance, three different measurement techniques were used to determine the residual induction of the permanent magnets used on the magnetic actuators discussed in Section 3. The first method is based on the magnetic dipole model. The second method is based on a formulation by Richard M. Bozorth [Bozorth, 1951]. The third method uses a bifilar pendulum and a magnetic stiffness formulation. Each method is described and the experimental results are discussed.

B.1. Experimental Methods

B.1.1. Dipole Measurement Method

A simple field source such as a permanent magnet wafer can be modeled as a magnetic dipole as long as the region under consideration is a good distance away from the dipole. The magnetic moment of a permanent magnet can be determined using this model. The value of B_r can be determined directly using mathematical models for a rectangular magnet and a cylindrical magnet, given in Eq. B.2 [Dexter, 2001],

$$B_{cyl} = \frac{B_r}{2}\left(\frac{l+x}{\sqrt{r^2+(l+x)^2}} - \frac{x}{\sqrt{r^2+x^2}}\right)$$

$$B_{rec} = \frac{B_r}{\pi}\left(tan^{-1}\left(\frac{x+l}{ab}\sqrt{(x+l)^2+a^2+b^2}\right) - tan^{-1}\left(\frac{x}{ab}\sqrt{x^2+a^2+b^2}\right)\right) \quad \text{(B.2)}$$

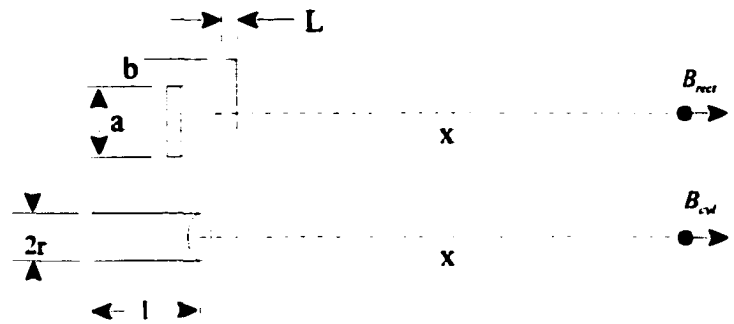

Figure B1: Geometry for Eq. B.2

The distance x is measured from the outer-most surface of the permanent magnet. The rule of thumb for the dipole assumption to be accurate is that the probe should be placed at a minimum distance of 10 times the largest magnet dimension, with the probe and magnet both on nonmagnetic supports. It is very difficult to properly line up the probe with the magnet; to account for this problem the measurements should be taken with the permanent magnet facing the probe and rotated 180°. By doing this, the stronger field, at say +0.5 degrees offset, and the weaker field, at - 0.5 degrees offset, can be averaged to remove any biasing error due to misalignment. The flux density should be measured at various distances from the permanent magnet and inserted into Eq. B.2 to solve for the magnetic moment and residual induction flux.

B.1.2. Bozorth's Method

Bozorth introduces a measurement technique based on the field intensity of a permanent magnet. The magnetic field produced by a permanent magnet varies with distance and offset angle. Bozorth developed an equation relating the magnetic field strength at a point a distance x from the center of the permanent magnet and at an offset angle θ from the magnetization orientation of the magnet. The formulation is given in Eq. B.3.

$$H = \frac{1}{4\pi}\frac{m}{r^3}\sqrt{1-3\cos^2\theta} \tag{B.3}$$

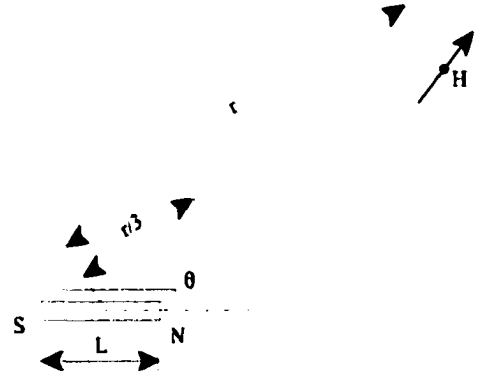

Figure B.2: Geometry for Eq. B.3

Substituting for the magnetic moment and H,

$$H = \mu_0 \mu_r B \tag{B.4}$$

Rearranging for B_r results in,

$$B_r = \frac{4\pi r^3}{v}\frac{B}{\sqrt{1-3\cos^2\theta}} \tag{B.5}$$

The orientation of the magnet can be varied by rotating the magnet to different angles with respect to the gauss probe, θ, or by changing the distance between the magnet and the gauss probe, r. The results of the tests can be inserted into Eq. B.3 to determine B_r and the magnetic moment. This method is similar to the dipole method. Thus, as was the case for

the magnetic dipole model, the probe should be placed a minimum distance of 10 times the largest permanent magnet dimension.

B.1.3. Magnetic Stiffness Technique

The magnetic moment of a permanent magnet can be determined experimentally using a bifilar pendulum and a Helmholtz coil pair. When a permanent magnet is placed within a magnetic field the magnet will try to align itself with the magnetic field. This is the same as a magnetized compass needle aligning itself with the earth's magnetic field. When the magnetization vector of the magnet is misaligned with the magnetic field a restoring force is introduced that will attempt to realign the magnet. The restoring force is proportional to the magnetic stiffness of the system. The system can be excited within the field produced by the Helmholtz coil pair and the frequency of oscillation can be measured and used to calculate the magnetic moment of the permanent magnet.

The pendulum set up is shown in Fig. B.3. The permanent magnet is attached to the suspended element such that the magnetization vector points through the center of both Helmholtz coils. The length of the support strings, H, should be large as compared to the string separation distance, L. The string separation distance should be carefully chosen. If too short a distance is chosen the frequency of oscillation will be high and will be

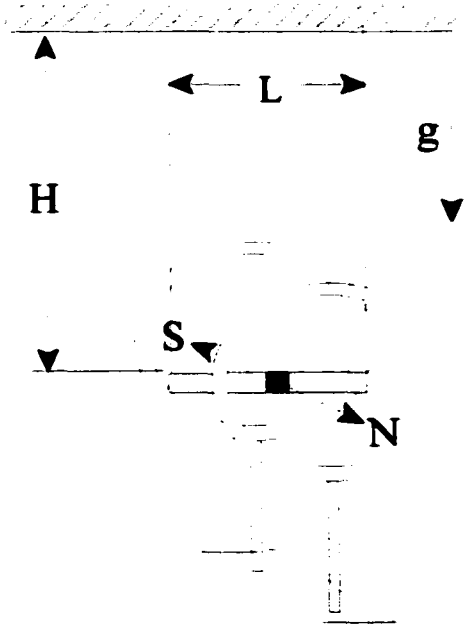

Figure B.3: Bifilar pendulum setup

heard to accurately measure. If the distance is too long then the effect of the magnetic moment will be small as compared to the inertia of the support.

The equation for this system can be determined by examining the free-body diagram of the system when the pendulum is offset from equilibrium. There are three forces to be considered. The restoring force of the support strings, the magnetic torque, and the aerodynamic drag forces act on the pendulum. The free-body diagram is shown in Fig. B.4.

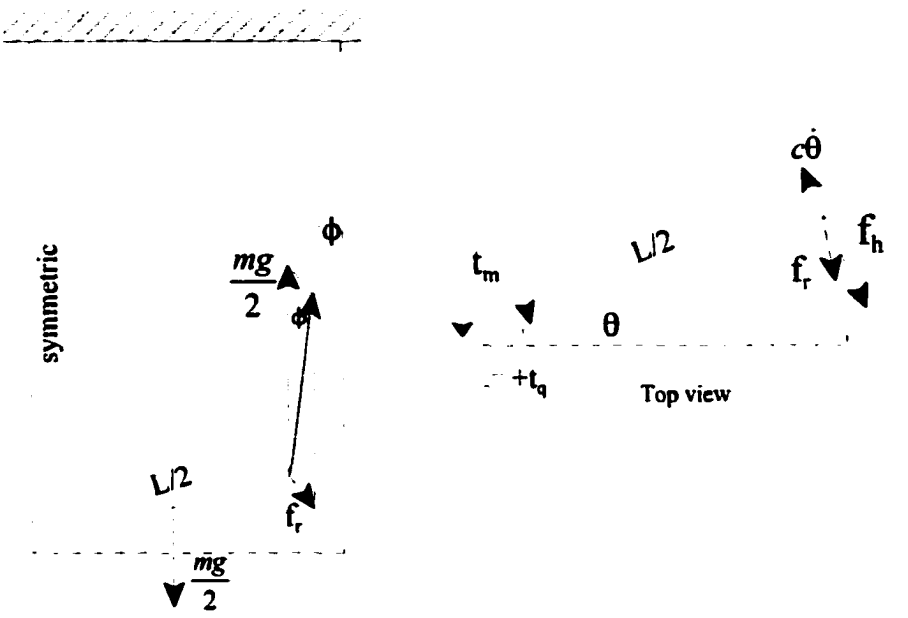

Figure B.4: Free-body diagram of bifilar pendulum

Summing the torques about the center of the pendulum results in,

$$\sum t_q = -2\frac{L}{2} f_h - t_m - 2c\dot{\theta} = I\ddot{\theta} \qquad \text{(B.6)}$$

Where f_h is the horizontal restoring force, t_m is the magnetic torque, and c is the damping coefficient. The horizontal force due to twisting of the pendulum, the horizontal restoring

force, and the relation between ϕ and θ are,

$$f_r = \frac{mg}{2}\tan(\phi) \quad f_h = f_r \cos\left(\frac{\theta}{2}\right) \quad \sin(\phi) = \frac{L}{H}\sin\left(\frac{\theta}{2}\right) \tag{B.7}$$

If the length of the string is long compared to the string separation distance then the vertical angle, ϕ, will always be very small, so the small angle assumption will always be met. Substituting and applying the small angle assumption to ϕ results in,

$$f_h = \frac{mgL}{2H}\sin\left(\frac{\theta}{2}\right)\cos\left(\frac{\theta}{2}\right) \tag{B.8}$$

The volume of the permanent magnet is small so the flux density can be assumed constant within the volume. With this assumption, the magnetic torque is given by,

$$t_q = \int_v (\bar{M} \times \bar{B}) dv \approx MvB\sin(\theta) \tag{B.9}$$

Substituting Eqs. B.8 and B.9 into Eq. B.6 results in the governing nonlinear differential equation describing the behavior of the pendulum.

$$\ddot{\theta} + \frac{2c}{I}\dot{\theta} + \frac{mgL^2}{2IH}\cos\left(\frac{\theta}{2}\right)\sin\left(\frac{\theta}{2}\right) + \frac{MvB}{I}\sin(\theta) = 0 \tag{B.10}$$

This equation can be linearized by applying the small angle assumption to the horizontal rotation angle, θ.

$$\ddot{\theta} + \frac{2c}{I}\dot{\theta} + \left(\frac{mgL^2}{4IH} + \frac{MvB}{I}\right)\theta = 0 \tag{B.11}$$

This can be written in the more standard form,

$$\ddot{\theta} + 2\zeta\omega_n\dot{\theta} + \omega_n^2 = 0 \tag{B.12}$$

Assuming a solution of the form $\theta = Ae^{st}$ results in the solution of,

$$\theta(t) = Ae^{-\zeta\omega_n t}\cos(\omega_d t - \psi) \qquad \omega_d = \omega_n\sqrt{1-\zeta^2} \tag{B.13}$$

The value of ζ can be determined from experimental data using the logarithmic decrement [Meirovitch, 1986]. The pendulum is excited with the magnet facing East-West with the Helmholtz coil pair turned off. The number of oscillations, j, and the angular distance, θ_j, are recorded and used to solve for the damping ratio.

$$\zeta = \frac{\delta}{\sqrt{(2\pi)^2 + \delta^2}} \qquad \delta = \frac{1}{j}ln\left(\frac{\theta_1}{\theta_{1+j}}\right) \tag{B.14}$$

The bifilar pendulum can be set up between a pair of Helmholtz coils to provide a uniform magnetic field. By varying the magnetic field and measuring the period of oscillation, the damped natural frequency can be determined as a function of *B*.

$$B_r = M\mu_0 = \frac{I\mu_0}{vB}\left(\frac{\omega_d^2}{1-\zeta^2} - \omega_{n_0}^2\right) \tag{B.15}$$

Where the initial damped natural frequency of the pendulum (the natural frequency of with no magnetic field) can be calculated analytically from Eq. B.11, $\omega_{n0} = (mgL^2/4IH)^{1/2}$, or can be determined from experimental data,

$$\omega_{n_0} = \frac{\omega_{d_0}}{\sqrt{1-\zeta^2}} \tag{B.16}$$

B.2. Experimental Results

The tests were performed on a set of NdFeB permanent magnet purchased from Dexter Magnetic Technologies in the spring of 1999. The magnets were quoted to have a residual induction of 1.35 Tesla. Each magnet has dimensions of 0.5"×0.5"×0.1" and a weight of 8.75×10^{-3} lb.

B.2.1. Dipole Method Experimental Results

The magnetic field produced by the permanent magnet was measured using a 3-D Gauss probe. The field was measured at 0.25 inch increments. After each measurement was taken, the magnet was rotated 180 degrees and the field recorded again. The two data sets were then averaged to determine the flux density. The experimental results are given in Table B.1 and Fig. B.5. The average B_r was calculated to be 1.27 Tesla.

Distance	Flux Density (Tesla)			Br
(mm)	0°	180°	Average	(Tesla)
194.6	3.15E-05	3.32E-05	3.24E-05	1.293
188.2	3.47E-05	3.64E-05	3.56E-05	1.289
181.9	3.79E-05	3.97E-05	3.88E-05	1.272
175.5	4.25E-05	4.41E-05	4.33E-05	1.279
169.2	4.73E-05	4.88E-05	4.81E-05	1.274
162.8	5.30E-05	5.44E-05	5.37E-05	1.273
156.5	5.91E-05	6.14E-05	6.03E-05	1.271
150.1	6.74E-05	6.88E-05	6.81E-05	1.273
143.8	7.63E-05	7.80E-05	7.72E-05	1.271
137.4	8.79E-05	8.90E-05	8.85E-05	1.277
131.1	9.98E-05	1.01E-04	1.00E-04	1.263
124.7	1.16E-04	1.17E-04	1.17E-04	1.273

Table B.1: Dipole Model Test Results

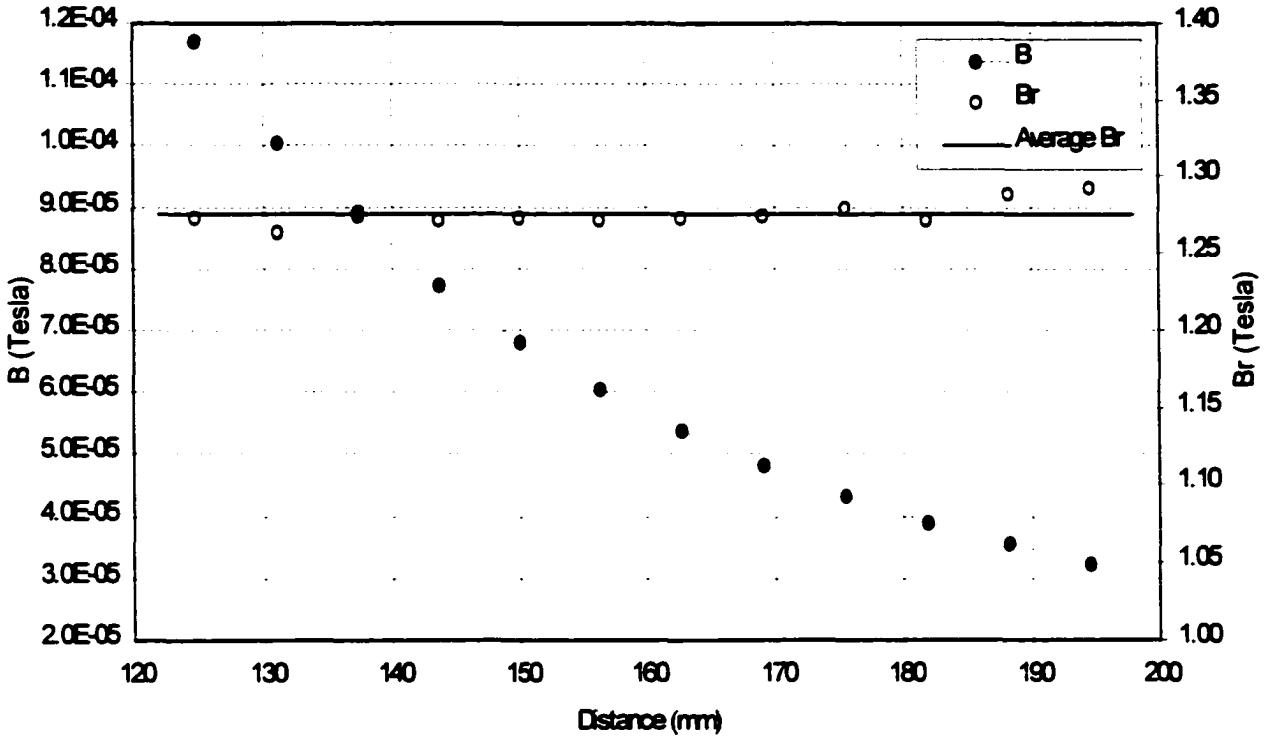

Figure B.5: Dipole Test Experimental Results

B.2.2. Bozorth's Method Experimental Results

The magnetic field produced by the permanent magnet was again measured using a 3-D Gauss probe. The magnet was rotated in 10° increments from -90° to 90°. Any misalignment is canceled out by measuring the flux density from both the positive and negative angles. The probe was placed 180 mm from the center of the magnet. The two data sets were then averaged to determine the flux density. The experimental results are given in Table B.2 and Fig. B.6. The average B_r was calculated to be 1.21 Tesla.

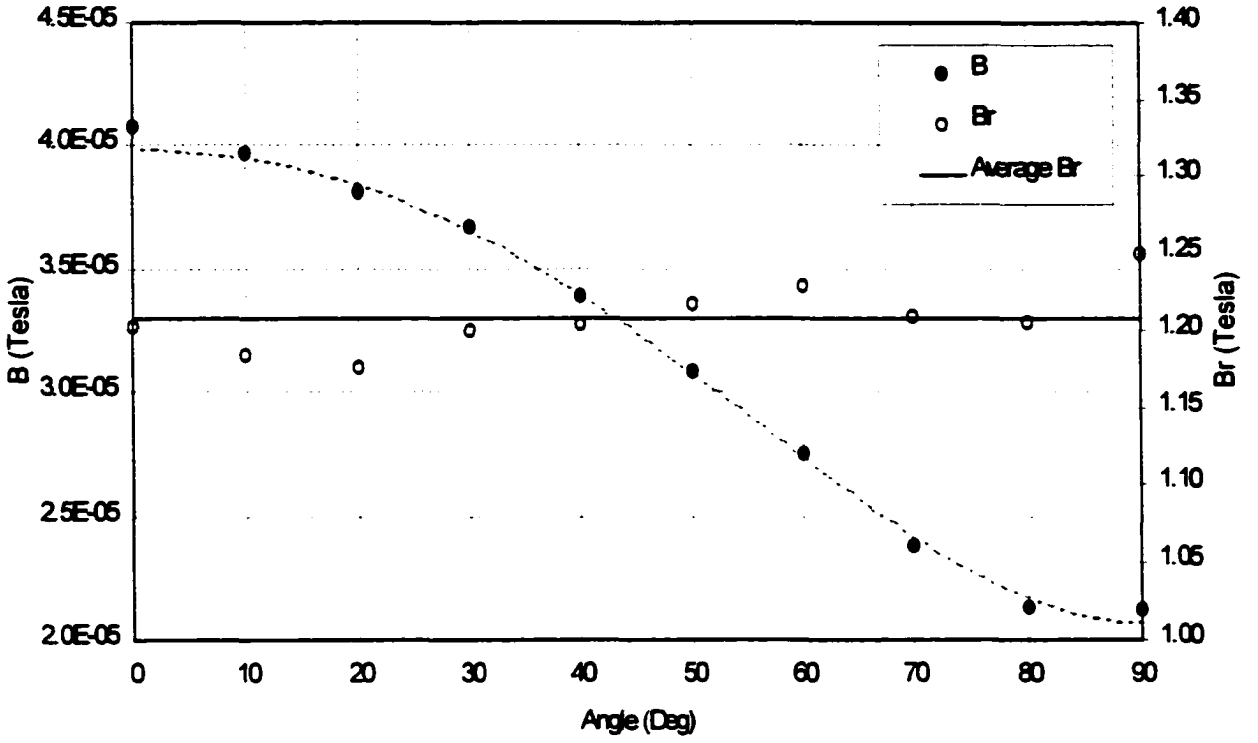

Figure B.6: Bozorth's Test Experimental Results

Angle	Bz (Tesla)			Br
(deg)	(+θ)	(-θ)	Average	(Tesla)
90	2.12E-05	2.12E-05	2.12E-05	1.251
80	2.14E-05	2.13E-05	2.13E-05	1.205
70	2.33E-05	2.44E-05	2.38E-05	1.209
60	2.69E-05	2.82E-05	2.76E-05	1.229
50	3.09E-05	3.08E-05	3.09E-05	1.217
40	3.37E-05	3.41E-05	3.39E-05	1.204
30	3.62E-05	3.72E-05	3.67E-05	1.200
20	3.73E-05	3.89E-05	3.81E-05	1.177
10	3.99E-05	3.95E-05	3.97E-05	1.184
0	4.08E-05	-	4.08E-05	1.203

Table B.2: Bozorth Model Test Results

B.2.3. Magnetic Stiffness Experimental Results

The pendulum was set up with a string length of 55.25" and a string separation of 5.75". The total weight of the pendulum was 1.81×10^{-2} lb. The inertia was measured to be 8.174×10^{-4} slug in^2. The system was tested with the magnetic field turned off with the permanent magnet facing East-West, West-East, North-South, and South-North. The results are given in Table B.3.

		Time (Sec)					Frequency
Direction	Cycles	1	2	3	4	5	(Hz)
West	12	13.3	13.3	13.3	13.2	13.3	0.904
East	12	13.2	13.1	13.3	13.2	13.3	0.908
South	12	13.7	13.6	13.7	13.7	13.6	0.878
North	12	12.9	12.9	12.9	12.9	12.9	0.930

Table B.3: Oscillation Measurements With No Magnetic Field

The system was tested with a magnetic field produced by a Helmholtz coil pair. The flux density varied between 0 and 6.3×10^{-2} Tesla. The damping ratio was measured using the logarithmic decrement. The pendulum was set into motion and the number of cycles was recorded for the pendulum to reach 1/2 the amplitude and 1/4 the amplitude. The logarithmic decrement was measured to be $\delta = 0.126$, and the damping ratio was calculated to be $\zeta = 0.020$. The average value of B_r was 1.23 Tesla. The results are shown in Fig. B.7 and tabulated in Table B.4.

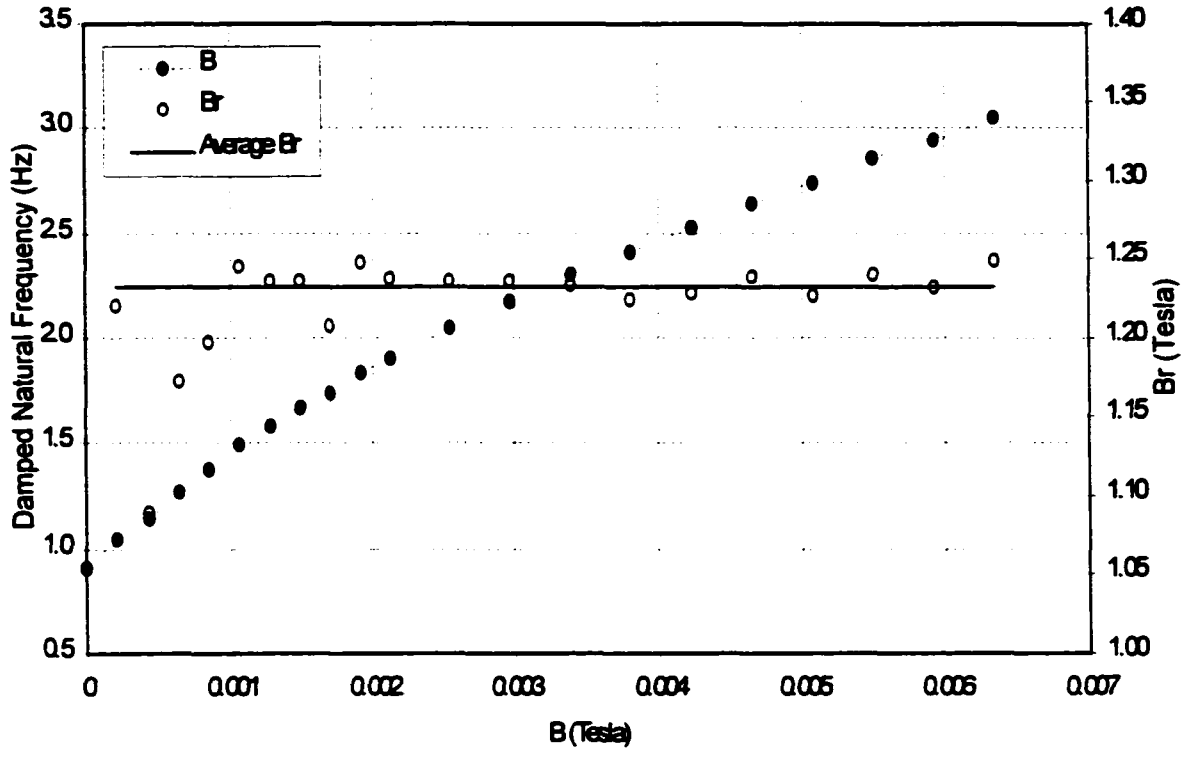

Figure B.7: Magnetic Stiffness Test Results

B.3. Discussion of Experimental Procedures

All three test methods yielded similar, but not identical, results. The dipole method and Bozorth's method are the easiest experiments to perform. The only assumptions used in calculating B_r are involved in the models themselves. The effects of the modeling errors are minimized by placing the Gauss probe away from magnet material. The dipole and Bozorth methods yielded results of B_r = 1.27 Tesla and 1.21 Tesla, respectively.

Current (A)	Flux (Tesla)	Cycles	Time (Sec) 1	2	3	4	5	Damp. Nat. Freq. (Hz)	Natural Freq (Hz)	Br (Tesla)
0	0	12	13.25	13.2	13.3	13.2	13.3	0.906	0.906	-
0.05	0.000212	15	14.3	14.3	14.4	14.3	14.3	1.047	1.048	1.220
0.1	0.000423	15	13.1	13.1	13.1	13	13.1	1.147	1.147	1.090
0.15	0.000635	20	15.7	15.7	15.7	15.7	15.8	1.272	1.273	1.173
0.2	0.000846	20	14.5	14.5	14.4	14.5	14.5	1.381	1.381	1.198
0.25	0.001058	20	13.3	13.4	13.4	13.4	13.4	1.495	1.495	1.246
0.3	0.001269	25	15.9	15.8	15.7	15.8	15.8	1.582	1.583	1.236
0.35	0.001481	25	15	14.9	15	15	15	1.669	1.669	1.237
0.4	0.001693	25	14.4	14.4	14.4	14.4	14.4	1.736	1.736	1.208
0.45	0.001904	30	16.4	16.4	16.3	16.3	16.3	1.836	1.836	1.249
0.5	0.002116	35	18.3	18.4	18.4	18.4	18.4	1.905	1.905	1.237
0.6	0.002539	35	17.1	17.1	17.1	17.0	17.2	2.047	2.047	1.237
0.7	0.002962	35	16.1	16	16.1	16	16.1	2.179	2.180	1.236
0.8	0.003385	35	15.2	15.2	15.2	15.1	15.3	2.303	2.303	1.234
0.9	0.003808	35	14.5	14.5	14.5	14.6	14.4	2.414	2.414	1.225
1	0.004231	35	13.9	13.9	13.8	13.8	13.8	2.529	2.529	1.228
1.1	0.004655	35	13.2	13.1	13.2	13.3	13.3	2.648	2.648	1.239
1.2	0.005078	40	14.6	14.6	14.6	14.7	14.5	2.740	2.740	1.227
1.3	0.005501	40	14	14.1	14	14	14	2.853	2.854	1.240
1.4	0.005924	40	13.6	13.6	13.6	13.5	13.7	2.941	2.942	1.232
1.5	0.006347	40	13.1	13.1	13.1	13.0	13.2	3.053	3.054	1.249

Table B.4: Magnetic Stiffness Test Results

The advantage of the pendulum method is that no Gauss meter is needed. Only a Helmholtz coil pair and amplifier is needed. The drawback is in the complexity. The method is derived on a significant amount of theory and has several assumptions embedded within. These assumptions can influence the results if proper care is not taken while performing the tests. Using the pendulum method, the resulting B_r was found to be 1.23 Tesla. This agrees well with the other two tests.

Each of the three tests are subject to a certain amount of experimental uncertainty. To minimize the effect of any one set of experiments the average between the three was used to model the permanent magnets. The average of the three tests was 1.24 Tesla.

APPENDIX C: OPERA FINITE ELEMENT METHOD

Vector Fields OPERA-3D and PC-OPERA are the finite element packages that were used to perform the analysis in Sections 4 and 6. It is not the purpose of these sections to describe in detail the finite element methods used in Vector Fields' 2-D and 3-D versions; instead, the purpose is to briefly discuss some of the aspects unique to the OPERA finite element package. The finite element formulation for both OPERA-3D and PC-OPERA was developed using the Galerkin weighted residual method.

OPERA-3D is a pre-processor designed by Vector Fields to interface with its electromagnetic field analysis programs. Two packages were used for this research: TOSCA was used to perform the magnetostatic analysis and ELEKTRA was used to perform the magnetodynamic analysis.

PC-OPERA uses similar algorithms as OPERA-3D except that the analysis packages have been simplified for 2-D analysis. This allows for quicker analysis of problems that contain certain symmetries.

C.1. TOSCA Algorithm

TOSCA is based on a program developed by the Rutherford Appleton Laboratory in England. The analysis package can be used to solve for current flow and magnetostatic fields and electrostatic fields in 3D nonlinear materials. TOSCA was used in Section 4 to compute the forces acting on the armature of the magnetic actuators.

Stationary magnetic fields consist of solenoidal and rotational components, which give rise to multi-valued solutions. To avoid this, TOSCA implements a combination of reduced and total potentials. The total field intensity is defined in terms of the total potential or as the sum of the reduced field intensity H_m and the conductor field intensity H_s.

$$\bar{H} = \bar{H}_m + \bar{H}_s \tag{C.1}$$

The reduced field intensity can be written in terms of the reduced scalar potential while the conductor field intensity can be calculated directly using the Biot-Savart law. These formulations are given in Eqs. C.2 and C.3.

$$\bar{H}_m = -\nabla\phi \tag{C.2}$$

$$\bar{H}_s = \int_{\Omega_J} \frac{\bar{J} \times \bar{R}}{|R|^3} d\Omega_J \tag{C.3}$$

Substituting these three equations into Maxwell's flux divergence equation results in an equation which can be easily solved using the finite element method.

$$\begin{aligned} \nabla \cdot \bar{B} &= 0 \\ \nabla \cdot \mu\left(\bar{H}_m + \bar{H}_s\right) &= 0 \\ \nabla \cdot \mu\nabla\phi - \nabla \cdot \mu\left(\int_{\Omega_J} \frac{\bar{J} \times \bar{R}}{|R|^3} d\Omega_J\right) &= 0 \end{aligned} \tag{C.4}$$

The formulation given by Eq. C.4 can introduce significant errors because H_m is solved using the derivative of the shape function while H_s is solved directly from integration, introducing spatial variations between the two terms as well as cancellation errors. This problem is bypassed in TOSCA by using the total magnetic scalar potential, $\bar{H} = -\nabla\psi$, in volumes where no current is flowing. Applying the flux divergence condition results in,

$$\nabla \cdot \mu \nabla \psi = 0 \qquad \text{(C.5)}$$

Defining regions in terms of reduced potential where currents are flowing, Eq. C.4, and regions where no current is flowing as total potential, Eq. C.5, eliminates the cancellation errors. The two regions are connected by applying the condition of normal B and tangential H continuity on the interface surfaces.

This combination of reduced and total potentials does not prevent multi-valued solutions. To avoid multi-valued solutions the total potential field must be "cut" by a region of reduced potential. This is illustrated in a 2-D sense in Fig. C1.

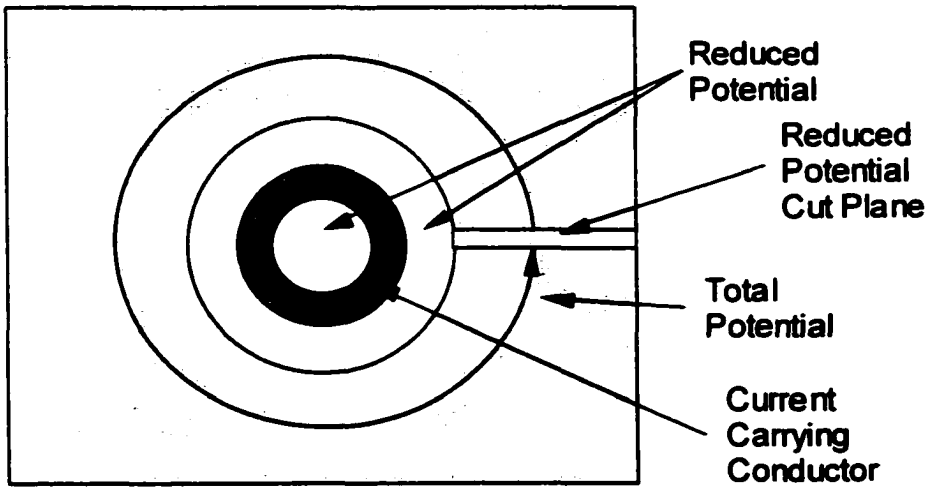

Figure C.1: Example Of A Reduced Potential Cut Plane
Used To Ensure A Single Valued Solution

C.2. ELEKTRA Algorithm

ELEKTRA is the finite element program that is used to analyze time varying fields. It was used to analyze the eddy-currents in Section 6. ELEKTRA uses an algorithm similar to that of TOSCA in that the finite element region must be subdivided into reduced and

total scalar potentials. However, ELEKTRA also requires that conductive materials be defined as vector potentials. The final solution is found by solving the three different regions with the normal flux and tangential field intensity conditions applied at the interface of the boundaries.

In regions of free space that do not include any source currents, the field is specified as total potential. The field intensity is defined as $\bar{H} = -\nabla\psi$ and the governing equation is given in Eq. C.5.

In regions where the media is non-conducting but there are source currents, the field intensity is broken up into three components, H_s, H_m, and H_e, where H_e is the field due to eddy-currents. The component H_s is defined in Eq. C.3, and H_m and H_e are defined in terms of the magnetic scalar potential.

$$\bar{H}_m + \bar{H}_e = -\nabla\phi \tag{C.6}$$

In regions of conducting materials all of Maxwell's equations are used along with the vector potential, A. The magnetic flux density is related to the vector potential according to Eq. C.7.

$$\bar{B} = \nabla \times \bar{A} \tag{C.7}$$

When Eq. C.6 is combined with Maxwell's equations Eqs. 5.1-5.3 a non-unique solution arises which introduces the electric scalar potential V. To eliminate the non-uniqueness the vector potential must be gauged, ELEKTRA uses the Coulomb gauge, $\nabla \cdot \bar{A} = 0$. This results in the governing equation,

$$\nabla \times \frac{1}{\mu} \nabla \times \vec{A} - \nabla \frac{1}{\mu} \nabla \cdot \vec{A} + \sigma \left(\frac{\partial \vec{A}}{\partial t} + \nabla V \right) = 0 \tag{C.8}$$

The introduction of the electric scalar potential requires one addition equation to be solved to determine the complete solution

$$\nabla \cdot \sigma \nabla V + \nabla \cdot \sigma \frac{\partial \vec{A}}{\partial t} = 0 \tag{C.9}$$

Explicit details for the formulations given in Sections C.1 and C.2 are discussed in [Vector Fields, 1999].

C.3. PC-OPERA

PC-OPERA is a scaled down version of OPERA-3D; it is limited to solving 2-D problems, which allows it to be implemented on a standard personal computer. It is used to solve systems that possess either radial symmetry or x-y symmetry. This software was used to analyze the variable resistance model in Section 6.

The steady-state AC analysis package was used to solve for the eddy-current solutions. This package solves for eddy-currents when the driving currents are sinusoidal in time. Using the vector potential and Maxwell's equation, Eq. 5.3, the governing partial differential equation is,

$$\nabla \cdot \frac{1}{\mu} \nabla A_z = \vec{J}_s + \vec{J}_v - \sigma \frac{\partial A_z}{\partial t} \tag{C.10}$$

Where the current density has been split into three components, the source currents J_s, the current in the windings of external circuits J_v, and the induced currents $-\sigma \partial A/\partial t$.

PC-OPERA allows the user to specify whether or not the induced eddy-current fields will diminish the driving current or if the driving current will be specified. For the analysis in Section 6, the driving current was specified. This results in an additional equation which must be solved and relates the total current to the induced current and the potential gradient.

$$\int_{\Omega} \sigma \left(\frac{\partial A_z}{\partial t} + \nabla v \right) d\Omega = I \tag{C.11}$$

Eqs. C.10 and C.11 are solved using the real part of the complex functions, $A_z = A_c e^{j\omega t}$. Explicit details for the formulations given in this section are discussed in [Vector Fields, 1997].

APPENDIX D: Curve Fitting Formulations For Section 6

The formulations which were derived in Section 6.2 to determine the least squares best fit between a set of data, either finite element or experimental, and the respective frequency response functions are described in detail in this appendix.

The transfer functions that were analyzed in Section 6 are given in Eq. D.1.

$$G_1(s)=\frac{a_3s^2+a_2s^{3/2}+a_1s+a_0}{s^2+b_2s^{3/2}+b_1s+b_0}$$
$$G_2(s)=\frac{a_5s^{5/2}+a_4s^2+a_3s^{3/2}+a_2s+a_1s^{1/2}+a_0}{s^{5/2}+b_4s^2+b_3s^{3/2}+b_2s+b_1s^{1/2}+b_0} \tag{D.1}$$
$$G_3(s)=\frac{a_2s+a_1s^{1/2}+a_0}{s+b_1s^{1/2}+b_0}$$

The end conditions are specified by examining Eqs. D.1 at $\omega = 0$ and ∞. This results in the following relationships.

$$G(0)=G^0_{1,2,3}=\frac{a_0}{b_0}$$
$$G(\infty)=\begin{cases}G_1^\infty=a_3\\G_2^\infty=a_5\\G_3^\infty=a_2\end{cases} \tag{D.2}$$

The respective error functions for the three formulations are,

$$e_i^1=\left(G_\infty s_i^2+a_2s_i^{3/2}+a_1s_i+G_0b_0\right)-G_i\left(s_i^2+b_2s_i^{3/2}+b_1s_i+b_0\right) \tag{D.3}$$

$$e_i^2=\left(G_\infty s_i^{5/2}+a_4s_i^2+a_3s_i^{3/2}+a_2s_i+a_1s_i^{1/2}+G_0b_0\right)- G_i\left(s_i^{5/2}+b_4s_i^2+b_3s_i^{3/2}+b_2s_i+b_1s_i^{1/2}+b_0\right) \tag{D.4}$$

$$e_i^3=\left(G_\infty b_2s_i^{3/2}+a_1s_i+G_0\right)-G_i\left(b_2s_i^{3/2}+b_1s_i+1\right) \tag{D.5}$$

The quadratic error function, J, is defined by multiplying e_i by its complex conjugate. The derivative of J is taken with respect to each of the unknown coefficients, resulting in m equations for m unknowns at each data point. The set of equations can be written as $[M]\{x\}=\{r\}$ at each data point.

The minimized matrix formulation for $G_1(s)$ is given in Eq. D6.

$$\begin{bmatrix} 2s^{3/2}\bar{s}^{3/2} & -s\left(s^{3/2}-\bar{s}^{3/2}\right) & -s^{3/2}\bar{s}^{3/2}\left(G+\bar{G}\right) & -s\left(G\bar{s}^{3/2}-\bar{G}s^{3/2}\right) & G_0\left(s^{3/2}-\bar{s}^{3/2}\right)-\left(G\bar{s}^{3/2}+\bar{G}s^{3/2}\right) \\ & 2s^2 & s\left(Gs^{3/2}-\bar{G}\bar{s}^{3/2}\right) & s^2\left(G+\bar{G}\right) & s^2\left(G-\bar{G}\right) \\ & & 2s^{3/2}\bar{s}^{3/2}\bar{G}G & -s\bar{G}G\left(s^{3/2}-\bar{s}^{3/2}\right) & -G_0\left(Gs^{3/2}+\bar{G}\bar{s}^{3/2}\right)+\bar{G}G\left(s^{3/2}+\bar{s}^{3/2}\right) \\ & & & 2s^2\bar{G}G & -sG_0\left(G-\bar{G}\right) \\ & & & & 2\left(G_0^2-G_0\left(G+\bar{G}\right)+\bar{G}G\right) \end{bmatrix} \begin{Bmatrix} a_2 \\ a_1 \\ b_2 \\ b_1 \\ b_0 \end{Bmatrix} = \begin{Bmatrix} -s^2\left(G_\infty\left(s^{3/2}+\bar{s}^{3/2}\right)-\left(G\bar{s}^{3/2}+\bar{G}s^{3/2}\right)\right) \\ -s^3\left(G-\bar{G}\right) \\ -s^2\left(\bar{G}G\left(s^{3/2}+\bar{s}^{3/2}\right)-G_\infty\left(Gs^{3/2}+\bar{G}\bar{s}^{3/2}\right)\right) \\ s^3G_\infty\left(G-\bar{G}\right) \\ -s^2\left(\left(2G_0G_\infty+2\bar{G}G-\left(G+\bar{G}\right)\left(G_0+G_\infty\right)\right)\right) \end{Bmatrix} \tag{D.6}$$

The minimized formulation for $G_2(s)$ is given by Eqs. D.7 and D.8.

$$\left[\begin{array}{cccc:cccc:c} q_{44} & \cdots & \cdots & q_{41} & l_{44} & \cdots & \cdots & l_{41} & \left(l_{40}+G_0q_{40}\right) \\ \vdots & & & \vdots & \vdots & & & \vdots & \vdots \\ \vdots & & & \vdots & \vdots & & & \vdots & \vdots \\ q_{14} & \cdots & \cdots & q_{11} & l_{14} & \cdots & \cdots & l_{11} & \left(l_{10}+G_0q_{10}\right) \\ \hdashline m_{44} & \cdots & \cdots & m_{41} & n_{44} & \cdots & \cdots & n_{41} & \left(n_{40}+G_0m_{40}\right) \\ & & & & & & & & \\ \vdots & & & \vdots & \vdots & & & \vdots & \vdots \\ & & & & & & & & \\ m_{04} & \cdots & \cdots & m_{00} & n_{04} & \cdots & \cdots & n_{11} & \left(n_{00}+G_0m_{00}\right) \end{array}\right] \begin{Bmatrix} a_4 \\ a_3 \\ a_2 \\ a_1 \\ \hdashline b_4 \\ b_3 \\ b_2 \\ b_1 \\ b_0 \end{Bmatrix} = -\begin{Bmatrix} G_\infty q_{45}+l_{45} \\ G_\infty q_{35}+l_{35} \\ G_\infty q_{25}+l_{25} \\ G_\infty q_{15}+l_{15} \\ \hdashline G_\infty m_{45}+n_{45} \\ G_\infty m_{35}+n_{35} \\ G_\infty m_{25}+n_{25} \\ G_\infty m_{15}+n_{15} \\ G_\infty m_{05}+n_{05} \end{Bmatrix} \tag{D.7}$$

where,

$$\begin{aligned} q_{ij} &= \left(\bar{s}^{i/2}s^{j/2}+\bar{s}^{j/2}s^{i/2}\right) & l_{ij} &= -\left(G\bar{s}^{i/2}s^{j/2}+\bar{G}\bar{s}^{j/2}s^{i/2}\right) \\ m_{ij} &= -\left(\bar{G}\bar{s}^{i/2}s^{j/2}+G\bar{s}^{j/2}s^{i/2}\right) & n_{ij} &= \bar{G}G\left(\bar{s}^{i/2}s^{j/2}+\bar{s}^{j/2}s^{i/2}\right) \end{aligned} \tag{D.8}$$

Eqs. D.7 and D.8 can be used to derive both $G_1(s)$ and $G_3(s)$ with the cancellation of the appropriate rows and columns.

The minimized matrix formulation for $G_3(s)$ is given in Eq. D.9.

$$\begin{bmatrix} -2s^2 & s^2(G+\bar{G}) & s\left(G_\infty\left(\bar{s}^{3/2}-s^{3/2}\right)+\left(Gs^{1/2}-\bar{G}\bar{s}^{1/2}\right)\right) \\ & -2s^2\bar{G}G & s\left(\bar{G}G\left(\bar{s}^{1/2}-s^{1/2}\right)-G_\infty\left(G\bar{s}^{1/2}-\bar{G}s^{1/2}\right)\right) \\ sym & & -2s^{3/2}\bar{s}^{3/2}\left(G_\infty^2+\bar{G}G-G_\infty(G+\bar{G})\right) \end{bmatrix} \begin{Bmatrix} a_1 \\ b_1 \\ b_2 \end{Bmatrix} = \begin{Bmatrix} -s(G-\bar{G}) \\ sG_0(G-\bar{G}) \\ \left(\bar{s}^{3/2}+s^{3/2}\right)\left(\bar{G}G+G_0G_\infty\right)+G_\infty\left(G\bar{s}^{1/2}+\bar{G}s^{1/2}\right)+G_0\left(\bar{G}\bar{s}^{1/2}+Gs^{1/2}\right) \end{Bmatrix} \tag{D.9}$$

In order to solve for the best-fit coefficients for all the data points the set of matrix equations must be solved simultaneously. This is done using the pseudo inverse, illustrated for $G_1(s)$ in Eq. D.10.

$$\underbrace{\begin{Bmatrix} a_2 \\ a_1 \\ b_2 \\ b_1 \\ b_0 \end{Bmatrix}}_{5\times1} = \underbrace{\begin{bmatrix} M_1 \\ M_2 \\ \vdots \\ M_q \end{bmatrix}^{\#}}_{5\times5q} \underbrace{\begin{Bmatrix} r_1 \\ r_2 \\ \vdots \\ r_q \end{Bmatrix}}_{5q\times1} \tag{D.10}$$

Once the coefficients have been determined, they are plugged back into Eq. D.1 and compared against the reference data. Because the end points are specified, it is not necessary to include them in the solution of Eq. 10. Additionally, since the end points are specified and the general form is contingent upon the form of the transfer function, relatively few data points are necessary to provide for an adequate solution for the vector of coefficients.

VITA

Vernon Dale Bloodgood, Jr.
Combat Direction Systems Activity, NAVSEA-Dam Neck
1922 Regulus Avenue, Virginia Beach, VA 23461-2097
(757) 492-6958, Fax (757) 492-6397, Email bloodgoodD@navseadn.navy.mil

EDUCATION

PhD in Engineering Mechanics, May 2002
Old Dominion University

Master of Science in Engineering Mechanics, December 1998
Old Dominion University

Bachelor of Science in Mechanical Engineering, December 1995
Aerospace option, Minor in Mathematics
Old Dominion University

EXPERIENCE

NASA Graduate Student Researcher
NASA Langley Research Center & Old Dominion University (8/97-12/01)

Instructor
Old Dominion University, Aerospace Engineering Dept. (5/01-8/01)

Old Dominion University Research Foundation
NASA Langley Research Center & Old Dominion University (1/96-8/97)

Virginia Space Grant Consortium Undergraduate Research Scholarship
NASA Langley Research Center & Old Dominion University (5/95-12/95)

Mechanical Engineering Co-op, Naval Surface Warfare Center Dahlgren Division, Dahlgren, VA (5/92-8/92),(1/94-8/94)

HONORS, AWARDS, & PRIZES

Engineering Mechanics Faculty Award, College of Engineering and Technology, 2001
Phi Kappa Phi Engineering Mechanics Faculty Award, 2001
Dean's list: Fall '90, '92, '93, '94, '95, Spring '91, '92, '93, '95
Chairman's List: Fall '92 and Fall '94
ODU-AIAA Student Of The Year 1994-95

MEMBERSHIP IN PROFESSIONAL SOCIETIES

Tau Beta Pi, American Institute of Aeronautics and Astronautics, America Helicopter Society, American Society of Mechanical Engineers

PRINCIPAL RESEARCH AREAS

Magnetic Suspension Systems, Developed fractional order eddy-current models.
Modified magnetic circuit theory for magnetic actuators and magnetic bearings.
Analyzed eddy current effects using finite-element codes.
Analyzed eddy current effects experimentally.
Developed design procedures for power efficient magnetic bearings.

Mechanical Vibration Analysis
Taught experimental vibration analysis at Old Dominion University.

Lidar & Wake Vortex Interaction, Developed FORTRAN code to simulate the Lidar signature for a vortex pair interacting with the ground.

PUBLICATIONS

• Bloodgood Jr, V. D., Groom, N. J., Britcher, C.P., "Further Development of an Optimal Design Approach Applied to Axial Magnetic Bearings," 7th International Symposium on Magnetic Bearings, Zurich, Switzerland, August 2000.

• Groom, N. J., Bloodgood Jr., V. D., "A Comparison of Analytical and Experimental Data for a Magnetic Actuator," NASA-TM-2000-210328, August 2000.

• Bloodgood Jr, V. D., "New Design Methods for Magnetic Suspension Systems," Proceedings of the Virginia Space Grant Consortium-2000 Student Research Conference, Hampton, VA, March 2000.

• Bloodgood Jr, V. D., Britcher, C.P., "Design Optimization of Magnetic Suspension Systems," 37th Aerospace Sciences Meeting and Exhibit, Reno, NV. AIAA_99_0832, January 1999.

• Bloodgood Jr, V. D., "Design Optimization of Magnetic Bearings and Magnetic Suspension Systems," MS Thesis, Old Dominion University, December 1998.

• Britcher, C.P., Bloodgood Jr, V.D., "Eddy Current Influences on the Dynamic Behavior of Magnetic Suspension Systems," 4th International Symposium On Magnetic Suspension Technology, Gifu, Japan, October 1997. NASA CP-1998-207654, May 1998.

PRESENTATIONS

"Further Development of an Optimal Design Approach Applied to Axial Magnetic Bearings," 7th International Symposium on Magnetic Bearings, Zurich, Switzerland, August 2000.

"New Design Methods for Magnetic Suspension Systems," Virginia Space Grant Consortium-2000 Student Research Conference, Hampton, VA. March 2000.

"Design Optimization of Magnetic Suspension Systems," 37th Aerospace Sciences Meeting and Exhibit, Reno, NV. January 1999.

"Design Optimization of Magnetic Bearings and Magnetic Suspension Systems," MS Thesis Defense, Old Dominion University, December 1998.

"Optimization of Force and Efficiency of Iron Core Electromagnets," AIAA Regional Conference, Norfolk, VA, Spring 1997.

"Computer Simulation of LIDAR as an Aircraft Wake Vortex Detection System," ASME Regional Conference, Raleigh, NC, Spring 1996.